S2S4E

Climate Services for Clean Energy

Research and Innovation action

H2020-SC5-2017

Modes of variability in Europe and their impact on the energy indicators

Deliverable D3.2

Version N°2

This project received funding from the Horizon 2020 programme under the grant agreement n°776787.

Authors: Wei Yang (SMHI), Kean Foster (SMHI), Llorenç Lledó (BSC), Veronica Torralba (BSC), Nicola Cortesi (BSC), Nathalie Schaller (CICERO), Irene Cionni (ENEA), Matteo De Felice (ENEA), David Brayshaw (UREAD), Hannah Bloomfield (UREAD).

Disclaimer

Document Information

Grant Agreement	776787
Project Title	Sub-seasonal to Seasonal climate forecasting for Energy
Project Acronym	S2S4E
Project Start Date	01/12/2017
Related work package	WP 3- Observational datasets
Related task(s)	Task 3.3 - Characterization of the main modes of variability affecting Europe and their impact on the essential climate variables
Lead Organisation	SMHI
Submission date	30/11/2018
Dissemination Level	PU

History

Date	Submitted by	Reviewed by	Version (Notes)
30/11/2018	Wei Yang (SMHI)	Irene Cionni (ENEA), David Brayshaw (UREAD), Hannah Bloomfield (UREAD).	Version 1
10/01/2020	Irene Cionni (ENEA)		Version2: revised version according to the Review Report from the EC.

Table of content

List of figures

List of tables

Summary

Atmospheric variability is known to affect the energy system as a whole in many aspects, and the importance of this dependency is only to keep growing with higher shares of renewable energy entering the electricity mix. Therefore it is crucial to understand the impacts that atmospheric variability at climatic scales can have to electricity production and demand. In this document the atmospheric variability is described in terms of different climate oscillations or variability modes, and the relative importance of each of these modes of variability for the wind power, solar power, hydro power generation and demand are evaluated. The atmospheric variability has been studied from reanalysis datasets employing Euro-Atlantic teleconnections and weather regimes methodologies. Both Essential Climate Variables (ECVs) (e.g. wind speed or temperature) and impact indicators derived from those ECVs (e.g. wind power capacity factor or energy demand) have been considered.

The skill of sub-seasonal and seasonal forecasting models at predicting the teleconnection indices and weather regimes, and the usability of the teleconnection indices and weather regimes to anticipate the energy generation and energy demand at sub-seasonal to seasonal will be employed later on in the project (WP4). Therefore, it is important to use methodologies that can be applied also for prediction systems.

First, time-series of monthly Euro-Atlantic teleconnection (EATc) indices have been produced using ERA-interim reanalysis for the period of 1981-2016. The reproduced EATc patterns show high similarities to the Climate Prediction Center patterns with only a few exceptions. Then Pearson correlation analysis has been employed to analyze the impact of identified main variability modes on the ECVs and energy indicators. The results show that for all the ECVs and energy indicators not only NAO is important but also the other modes have substantial correlations. Additionally, two long-term products, ERA-20C and the 10 ensemble members of CERA-20C have been used to investigate the long-term variability of atmospheric teleconnections since 1900. The relative contributions of the four main patterns are found to vary similarly over the period 1900-2010, but the range is larger at the beginning of the 20st Century.

Secondly, weather regimes (WRs) have been classified using different machine learning techniques. Three different classifications have been produced: one for atmospheric variability over Europe, another for impact-indicator variability over European country aggregates, and another one for hydrological assessments of snow-driven hydropower production in Sweden. The impact of a monthly weather regime on wind-power and solar-power generation have been assessed by averaging the ECVs and energy indicators for all days associated with a given weather regime and month. For hydrology two skill scores have been used to assess the performance of synthetic inflows that are conditioned using climate variability modes. The energy-impact regimes illustrate how difficult it is to match supply and demand on a particular day, i.e., the stress on the system.

The impact of EATcs/WRs on energy sectors exhibit strong inter-annual variations. For wind generation the impact in winter months (i.e., Dec-Mar of EATc and Sept-Mar of WRs) is much higher compared to that in summer months. The corresponding energy capacity factor looks very similar to their impact on wind speed. For solar generation the SSRD is highly correlated with the leading atmospheric variability mode in almost all the months with a predominant effect of NAO in winter, EA/WR in winter and spring, SCAND and EA in summer. The patterns of correlation of solar power capacity factor are identical to the pattern of correlation of solar radiation, with temperature having almost no effect. For hydropower generation both teleconnections and weather regimes outperform the traditional ensemble streamflow predictions (ESP) but show strength in different aspects. Teleconnections and weather regimes complement each other quite well and this helps to characterize part of the climate variability in different areas and different time periods.

The impact regimes are able to reproduce features consistent with the weather regimes; they however have much stronger connections to the surface impacts of interest (demand, demand-net-wind, etc.) than the pure weather regimes. Due to time constraints, the development of impact-pattern technology has focused on the daily regimes timescale. This is consistent with the patterns being most relevant to sub-seasonal forecasting given such forecasts typically offering greater immediate opportunities for skillful forecasts (see Deliverable 4.1). Initial analysis has been conducted for monthly-to-seasonal impact teleconnections (not shown), though the methodology remains under development. It is expected that impact-teleconnections it will be discussed further in subsequent deliverables (Deliverable 4.2 and Deliverable D4.3).

Keywords

Teleconnections. Weather regimes. Weather-impact regimes. Energy-relevant essential climate variables. Wind-power generation. Solar-power generation. Hydro-power generation. Energy demand. Renewable energy.

1 Background and motivation

European climate variability is often assessed through the role of atmospheric teleconnection indices. They are typically derived from the first few principal components of seasonal-mean, or monthly-mean upper-atmosphere geopotential height or mean-sea level pressure (Barnston and Livesy, 1987). The first four modes of European climate variability are commonly referred to as North Atlantic Oscillation (NAO), East Atlantic Pattern (EA), Scandinavian pattern (SCAND) and East-Atlantic West Russian Pattern (EA/WR). Each of these patterns is known to imprint different surface temperature, wind speed and precipitation conditions which can, in turn, be associated with particular impacts on the European energy system (Brayshaw et al., 2011, Cradden et al., 2017, Zubiate et al., 2017).

Indices for those teleconnections are regularly published by NCEP's Climate Prediction Center (CPC), and have gained popularity in the climate arena to describe and monitor climate variability. These teleconnections are computed at CPC with a Rotated Empirical Orthogonal Function (REOF) analysis: the 10 leading EOF modes of northern hemispheric 500 hPa geopotential height anomalies are computed for each month and then a Varimax rotation is applied (Barnston and Livezey 1987). However, the associated teleconnection patterns are only made available as images by CPC. This prevents computing the indices from seasonal predictions or other reanalysis datasets through a projection. Moreover, selecting the four Euro-Atlantic Teleconnections from the ten rotated modes is challenging as they do not appear always in the same order, and CPC removes the spurious modes and then does a Least Squares regression to obtain the indices. To overcome these limitations, a similar methodology has been employed here to recreate those teleconnection indices and patterns (see section 3.1). This is a crucial step for the work to follow in WP4.

Another limitation of the REOF methodology to assess climate variability is that it enforces symmetric variability patterns (i.e. the positive and negative patterns of an oscillation need to be identical). However this is not the case sometimes, and an alternative description of variability that does not enforces symmetry is provided by classifying synoptic-scale "weather regimes" on time-scales of ~days. These regimes were historically calculated based on professional knowledge of atmospheric motions such as GrossWetterlagen (Baur et al., 1944). However more recently it has become common practice to calculate regimes objectively, e.g., using machine learning techniques such as clustering or fuzzy logics. As with low frequency teleconnection patterns, it is reasonable to expect a close link between the circulation patterns associated with weather regimes and European energy system impacts (Brayshaw et al., 2012,

Gramms et al., 2017, Thornton et al., 2017, Bloomfield et al., 2018). The impact of each weather regime is assessed through composite maps (also known as stratifications).

A key property of both approaches (i.e., teleconnections and weather regimes) is that they begin from a standpoint of atmospheric variability and then evaluate the impact of those modes in the energy sector. Another approach has been also studied in S2S4E: rather than dissect variability at atmospheric level and then evaluate its response in the impacted system, a set of energy-impact regimes directly computed from indicator variability are investigated. This method begins by identifying regimes in the impacted system (e.g., in maps of national daily demand or demand-minus-wind across Europe) and only then seeks to associate these to meteorological circulation patterns. The resulting patterns are thus by construction closely associated with significant impacts on the power system and are sensitive to the structure of the power system itself (e.g., deployments of renewable technologies). Impact regimes are therefore expected to provide a complementary view to the traditional meteorological analysis (teleconnections, weather regimes), highlighting the patterns of weather which most strongly characterize variations in the properties of the impacted system.

2 Dataset and methods

2.1 Energy-relevant Essential climate variables

Essential Climate Variables (ECVs) that heavily impact the energy sectors include 2 meters temperature (T2m) for electricity demand, surface solar radiation downward (SSRD) for solar power generation, 10 meters surface wind speed (sfcWind) for wind power generation, and adjusted precipitation (P) and adjusted 2 meters temperature (T) for hydropower generation.

	Wind-power	Solar-power	Hydro-power	Demand
ECVs	sfcWind	T2m & SSRD	P & T	T2m
Temporal resol.	6-hourly	6-hourly	Daily	Daily
Spatial resol.	Gridded	Gridded	River basin	Country-level
Dataset	ERA-interim	ERA-interim	HydroGFD2.0	MERRA2

Table 1: Overview of ECVs in energy models

Table 1 shows the datasets, the temporal and spatial resolution employed for each ECV for investigating the link between climate variability and a number of energy subsectors in Europe. For wind and solar energy sectors the ECVs come from a reanalysis product, the ECMWF ERA-interim (Dee et al., 2011). Hydro-power generation highly relies on the quality of precipitation and temperature, but precipitation is poorly simulated by most reanalysis products. An adjusted global dataset that builds upon ERA-Interim, the HydroGFD2.0 (Berg et al., 2018), is therefore used to drive hydrological models for better representation of water balance simulations. The reanalysis that has been used in the Demand modelling to complete the impact regimes analysis is MERRA2 (Gelaro et al., 2017). A comparison of several reanalyses in terms of those ECVs has been undertaken in D3.1 Although the MERRA2 and ERA-Interim reanalyses differ in some aspects, the qualitative synoptic scale circulation patterns in both reanalysis are very similar – particularly over Europe where the reanalyses are strongly constrained by observations. The results presented here are therefore believed to be qualitatively insensitive to the choice of reanalysis dataset.

2.2 Energy indicators

We focus on three energy generation models (i.e., wind power generation, solar power generation and hydropower generation) and one energy balance model (i.e., demand model). Here, a brief overview of each model is given. Full details of models can be found in ANNEX A: Energy models, while the impacts coming from climate variability are presented in section 4-7.

Wind power is calculated using 6-hourly 10m surface wind speed with BSC wind-power model (Lledó 2017, Lledó et al. in prep.). The model estimates capacity factor (CF) at each grid point

through three different power curves corresponding to three turbine classes suitable for low, medium and high wind speed. The daily and monthly averaged sfcWind and CF are used to evaluate the impact of the teleconnection indices and weather regimes on the wind power sector.

Solar power is calculated using 2m temperature and incoming surface solar radiation with a model from Bett and Thornton (2016), which is a modified version of Evans and Florschuetz, 1975. The model estimates hourly solar power capacity factors at each grid point. Again, the monthly averaged T2m, SSRD and CF are used to evaluate the impact of climate variability on the solar power sector.

Hydropower inflow volumes (synthetic observations) are calculated using a hydrological model, which is typically the Hydrologiska Byråns Vattenbalansavdelning model (HBV) within the hydropower sector in Sweden. HBV (Bergström, 1995, Linström et al., 1997) is initialized by driving it, for a spin-up period, up to the forecast initialisation date with observed meteorological inputs. Historical daily precipitation and temperature time series in the period from the initialisation date to the end of the analysis period, from previous years going back to 1961 are then used as input to HBV. This results in an ensemble of forecasts that are climatological in their evolution from the initial conditions. Here, the Ume river system in the northern Sweden is to be used as a case study. The impact of the Euro-Atlantic teleconnections and weather regimes on the ability to model the seasonal inflow volumes to hydropower reservoirs, using analogue forcing data, will be described by two scores, the mean absolute error skill scores (MAESS) and the frequency of years score (FY^+). The MAESS score and the FY^+ score measure whether the conditioned forcing data (CFD) outperforms the reference or not. Improved performance is indicative of the Euro-Atlantic teleconnections and weather regimes having a non-trivial impact on the inflow volumes.

Electricity demand is calculated with a country-level multiple-linear regression model containing parameters to capture both meteorological- and human-behavior. Each country has a unique regression model, which is trained on two years of measured demand data (2016-2017) from the ENTSOe transparency platform (https://transparency.entsoe.eu), and is then applied retrospectively full reanalysis period (1980-2017). Two versions of the model output are created, the "full" demand (using all of the available regression parameters) and the "weather-dependent" demand (which includes only the heating-degree and cooling degree terms – i.e., removes the impacts of the day-of-week term and long term-trends). The temporal resolution of the demand data is reported differently depending on the country, but all datasets are converted into daily-mean demand for model training.

3 Climate variability over Europe

3.1 Teleconnections

3.1.1 Euro-Atlantic teleconnections

Geopotential height anomalies at 500 hPa from the ERA-interim reanalysis (Dee et al. 2011) for the period 1981-2016 have been employed to compute the four Euro-Atlantic teleconnections NAO, EA, SCAND and EA/WR. Here the analysis has been restricted to the Euro-Atlantic domain [90ºW-60ºE; 20-80ºN] and only the first four REOF modes have been considered. For each month, the monthly anomalies of the previous and next month are also included in the REOF analysis, although only the index for the central month is used. These three months are included to increase the sample size and the robustness of the analysis.

The four obtained REOF modes have been reordered and their sign has been adjusted so that the correlation patterns resemble as much as possible the positive phases of the NAO, EA, EA/WR and SCAND patterns (in this order) as computed by CPC. The correlation patterns obtained for the twelve months of the year can be seen in Figure 1 and Figure 2.
The results have been compared with the CPC patterns for each month, as illustrated for January in Figure 3. The correlation maps of the teleconnection indices with the anomalies of 500 hPa geopotential height are very similar. However, given the differences in period, region, dataset and methodology used, it is not surprising to find differences for some months and modes, namely:

- mode 2 differs from CPC EA pattern in April and May
- mode 3 does not resemble CPC EA/WR for February and March (weak patterns in CPC) and December (similar pattern to November)
- mode 4 differs from CPC SCAND in October

The impacts of those four variability modes have been assessed through correlation analysis of the teleconnection indices with the ECVs and the energy indicators at monthly scale from 1981-2016. The correlation is based on the Pearson correlation coefficient at lag 0 and the statistical significance is calculated by the two–tailed probability of the Student-t distribution at 99% of confidence. In section 4-6 a detailed explanation is given for the central month of each season (i.e. January, April, July, and October) so as to present impacts coming from Euro-Atlantic teleconnections on sfcWind, SSRD, T2m and precipitation from the HydroGFD. For the sake of readability January is used as an example to illustrate the dependence amongst climate variability, ECVs and energy indicators, while the figures for the other months are available in the Annexes.

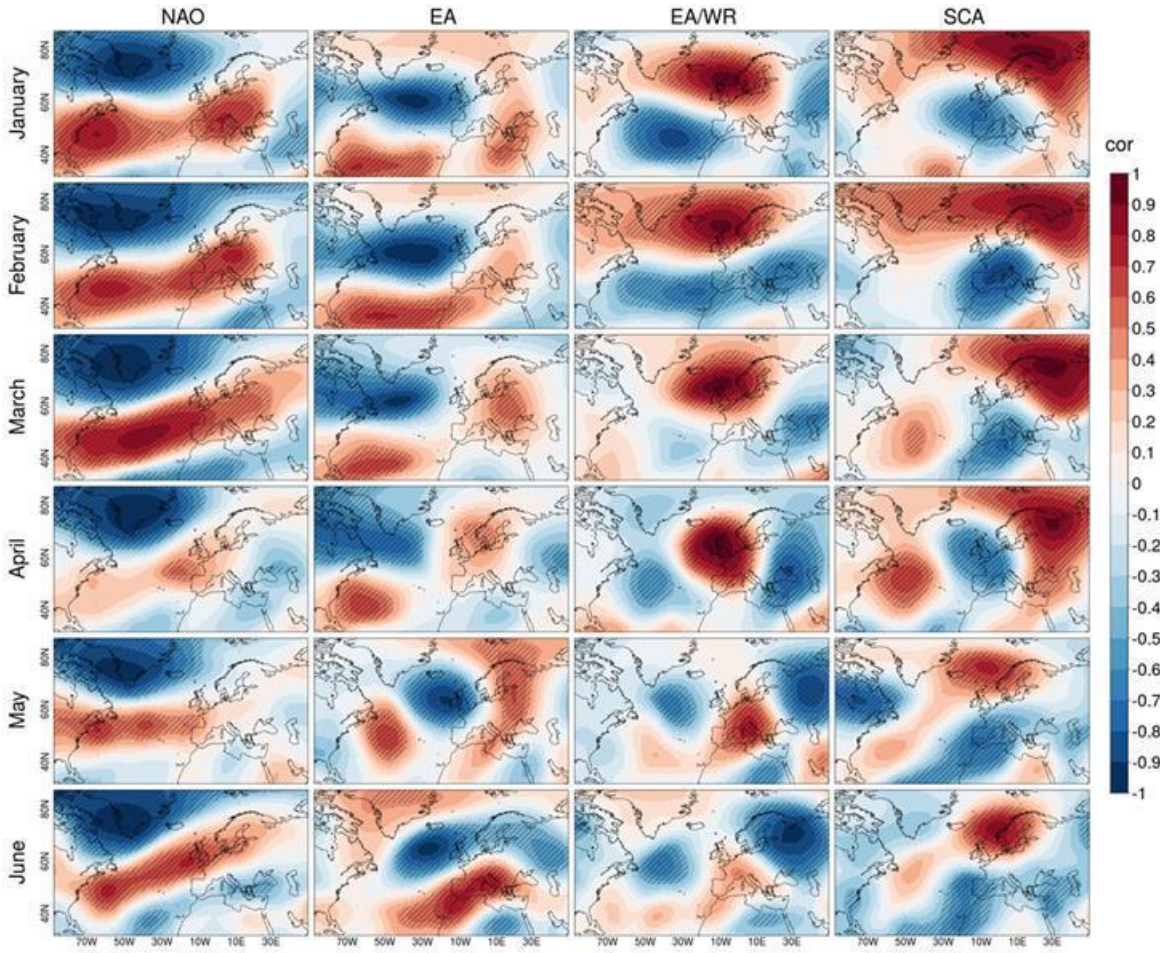

Figure 1: Correlation patterns between 500 hPa Geopotential heights and the four Euro-Atlantic Teleconnection indices (columns) as computed in S2S4E, for the first six months of the year (rows). Scratched area indicates statistical significance at 99% confidence level. Source: ERA-interim.

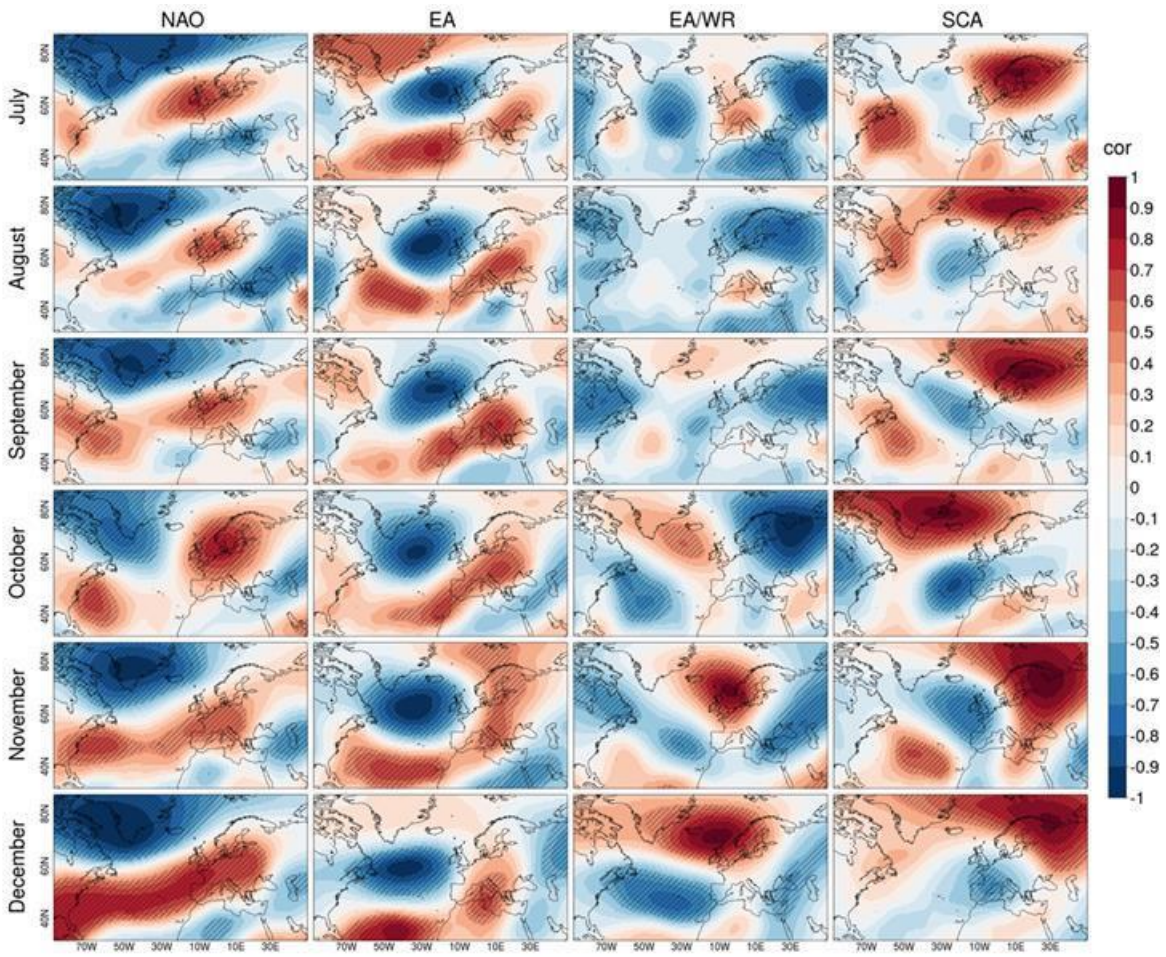

Figure 2: Correlation patterns between 500 hPa Geopotential heights and the four Euro-Atlantic teleconnection indices (columns) as computed in S2S4E, for the last six months of the year (rows). Scratched area indicates statistical significance at 99% confidence level. Source: ERA-interim.

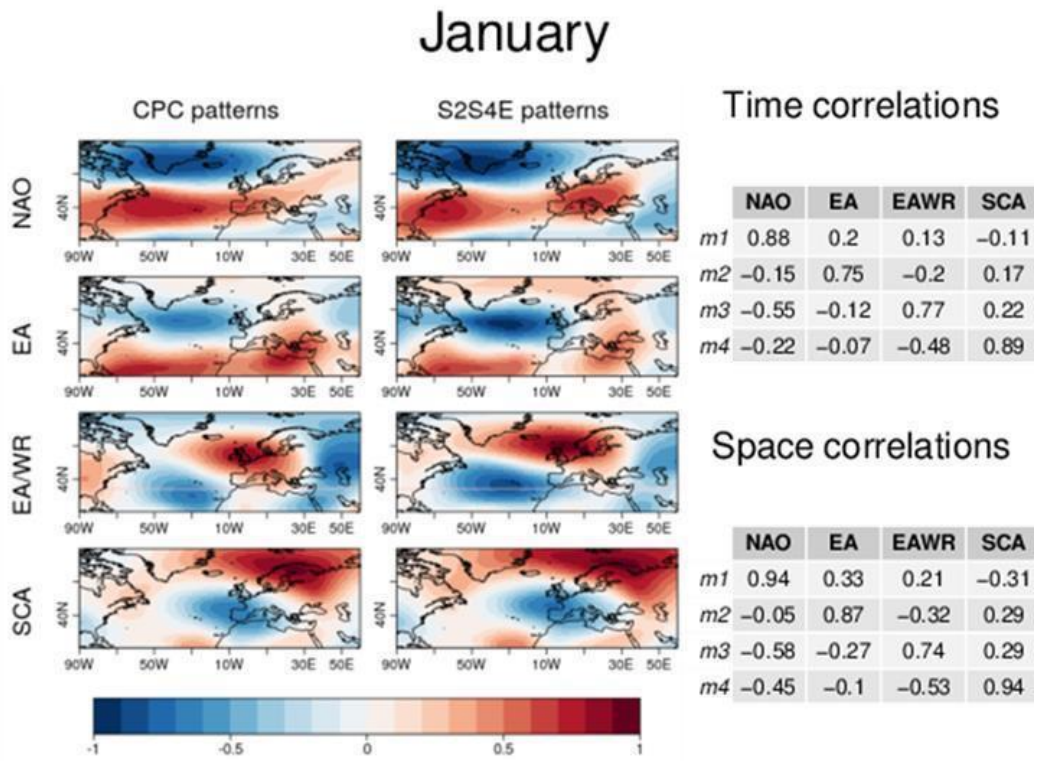

Time correlations

	NAO	EA	EAWR	SCA
m1	0.88	0.2	0.13	−0.11
m2	−0.15	0.75	−0.2	0.17
m3	−0.55	−0.12	0.77	0.22
m4	−0.22	−0.07	−0.48	0.89

Space correlations

	NAO	EA	EAWR	SCA
m1	0.94	0.33	0.21	−0.31
m2	−0.05	0.87	−0.32	0.29
m3	−0.58	−0.27	0.74	0.29
m4	−0.45	−0.1	−0.53	0.94

Figure 3: Comparison of patterns obtained correlating geopotential height at 500 hPa anomalies with CPC and S2S4E indices for January in the period 1981-2016. The tables on the right summarize time and space correlations between the two methods.

3.1.2 Long-term variability of Euro-Atlantic teleconnections

Two long-term reanalysis products, the ERA-20C reanalysis (Poli et al. 2013, 2015) and the 10 ensemble members of the CERA-20C reanalysis (Laloyaux et al. 2018) have been used to investigate the long-term variability of atmospheric teleconnections. While ERA-20C was produced using an atmosphere-only model, CERA-20C is a reanalysis produced by a coupled model, which also provides 10 ensemble members. For this analysis, mean sea level pressure (MSLP) instead of geopotential height at 500 hPa (g500) is used, because the g500 for the period 1900-2010 shows a trend due to global warming. We focus on December-January-February (DJF).

Figure 4 shows the correlation patterns between MSLP and the four main teleconnection pattern for the three months average of DJF and the whole period from 1900 to 2010.

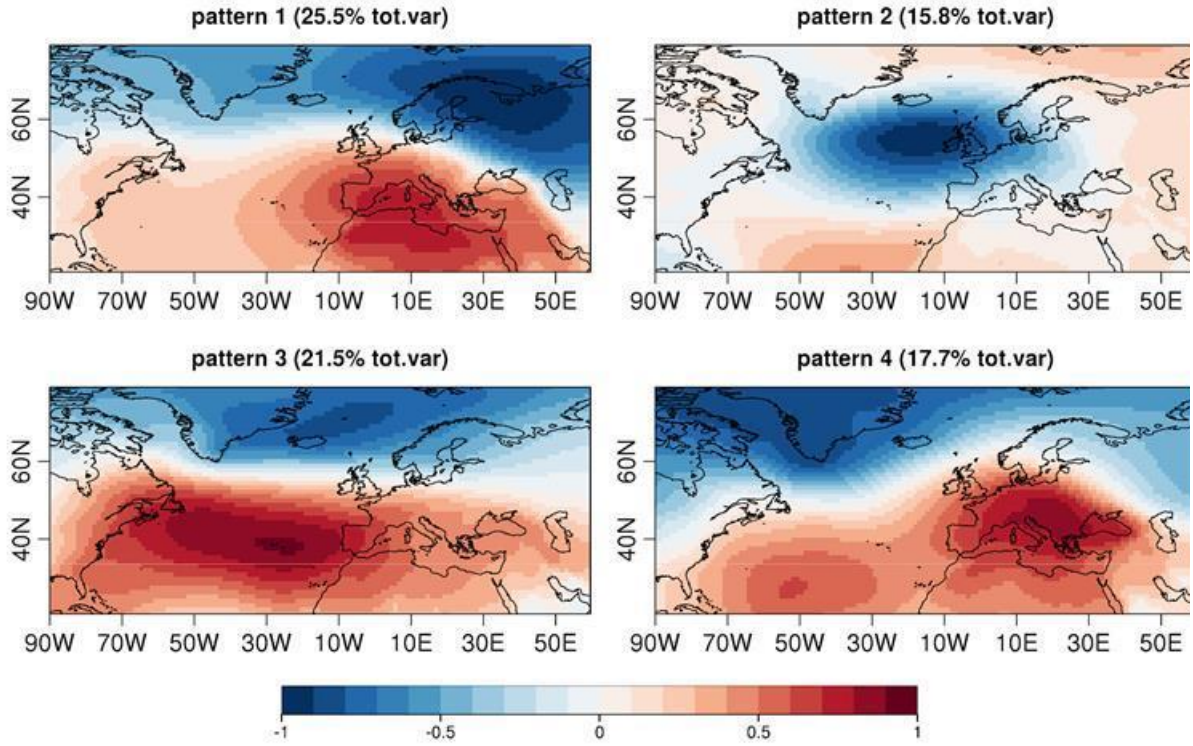

Figure 4: Correlation patterns between mean sea level pressure anomalies (DJF from 1900-2010) and the four Euro-Atlantic teleconnection indices as computed in ERA-20C.

Pattern 1 resembles the negative phase of the Scandinavian (SCAND) pattern, pattern 2 the positive phase of the East Atlantic (EA) pattern, pattern 3 the positive phase of the NAO and pattern 4 does not resemble any particular pattern.

The same analysis for each of the 10 ensemble members of CERA-20C has been done. Apart from reversed signs patterns, they all look very similar to each other, and to ERA-20C, but somewhat different from what is obtained with ERA-interim. When the patterns are calculated considering only the 1980-2010 period, the patterns are more similar (not shown here).

The evolution over time of these 4 teleconnection patterns in ERA-20C and CERA-20C was therefore considered (see Figure 5).

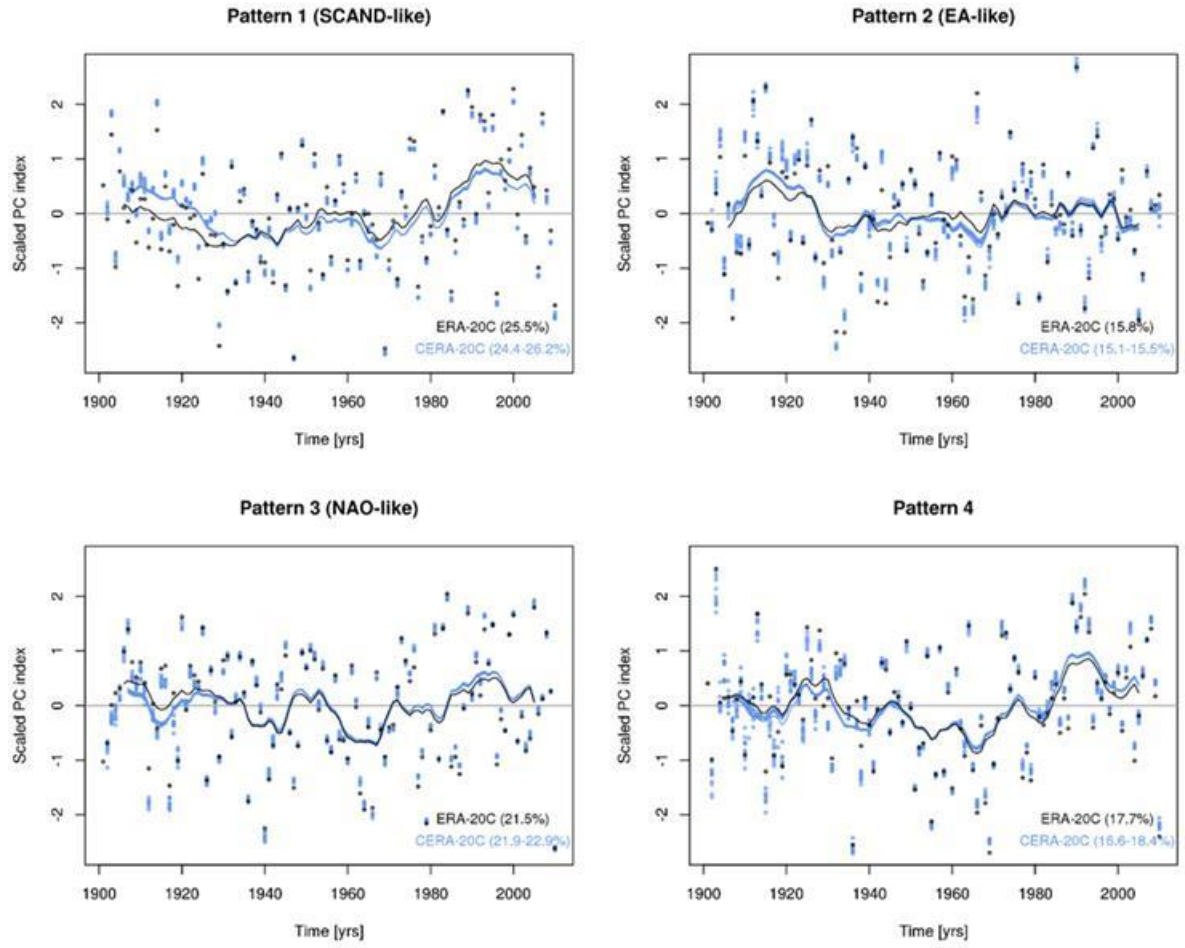

Figure 5: Time evolution of the four main teleconnection patterns in the ERA-20C (black) and CERA-20C (blue) reanalyses. Each dot represents DJF for the winters 1902-2010 and the lines are the 10 years running average time series.

While the range across the 10 ensemble members of CERA-20C is relatively narrow, the differences with ERA-20C, especially for pattern 1 and in general at the beginning of the 20th century, can be more substantial. However, the year-to-year and decadal variability in both re-analyses varies in a similar way. In Deliverable 4.2 the skill of seasonal hindcasts will be assessed in the ASF-20C dataset, and since this was produced using a similar modelling setup to the ERA-20C reanalysis, ERA-20C will be the reference dataset (Weisheimer et al., 2017).

Next, the relationship between the main teleconnection patterns and temperature extreme in Europe are investigated, as days with extreme cold/warm weather would be related to high demand events in the model for different situations (e.g., heating/cooling systems). Extreme temperature indices during the period 1981-2010 were calculated in ERA-20C and the Euro-Atlantic teleconnection patterns are re-calculated for this period (Figure 6). Pattern 1 now resembles the positive phase of the Scandinavian pattern, pattern 2 the negative of the EA, pattern 3 the positive phase of the NAO and pattern 4 again does not correspond to any particular known pattern.

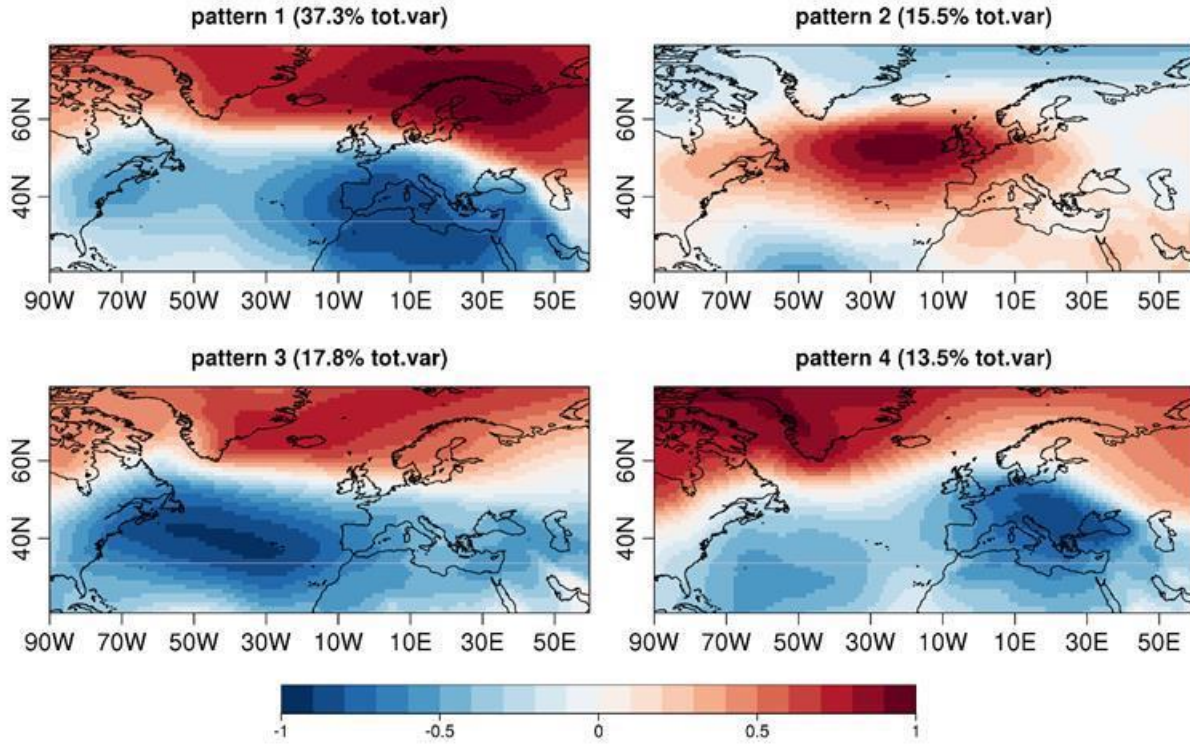

Figure 6: Correlation patterns between mean sea level pressure anomalies (DJF from 1981-2010) and the four Euro-Atlantic teleconnection indices as computed in ERA-20C.

The daily Heat Wave Magnitude Index (HWMId) (Russo et al. 2015) and the daily Cold Wave Magnitude Index (CWMId) are calculated similarly as in Brunner et al. (2018). At each grid point, each day is classified either as a warm or cold extreme (obtains a value of 1), or as a "normal" day (obtains a value of 0). Then for each DJF three months period, we obtain the sum of warm and cold extremes at each grid point. The Spearman's rank correlation coefficient between these two time series and the patterns indices is then calculated and shown in Figure 7 and Figure 8. The positive phase of the two patterns explaining most of the total variance, pattern 1 (SCAND) and 3 (NAO), are associated with more cold extremes in Northern Europe, and less warm extremes in these regions. The EA is associated with less cold extreme in the Scandinavian Peninsula but not necessarily with more hot extremes. It is however associated with less cold extremes in parts of France, Portugal, Spain, Italy and the Balkans, and more cold extremes in Portugal, Spain, Italy and the Balkans. How these extreme temperature indices relate to energy demand will be investigated in Deliverable 4.2.

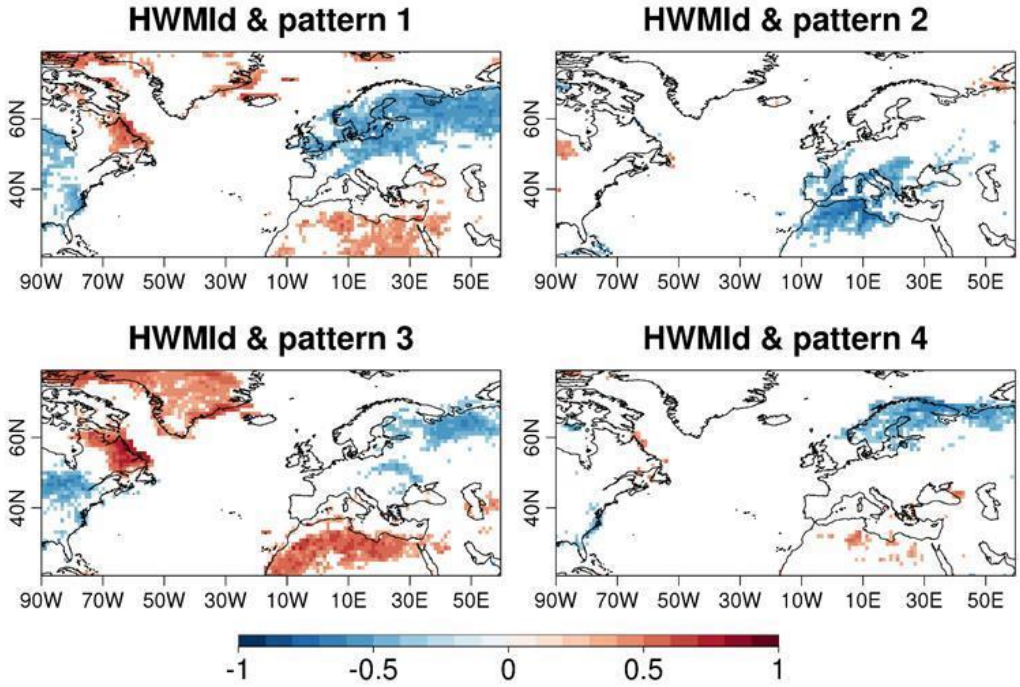

Figure 7: Maps of the Spearman's rank correlation coefficient between the teleconnection index of each of the four main patterns in ERA-20C and the sum of heat wave days during DJF for the period 1981-2010. Only correlation coefficients significant at the 5% level are shown.

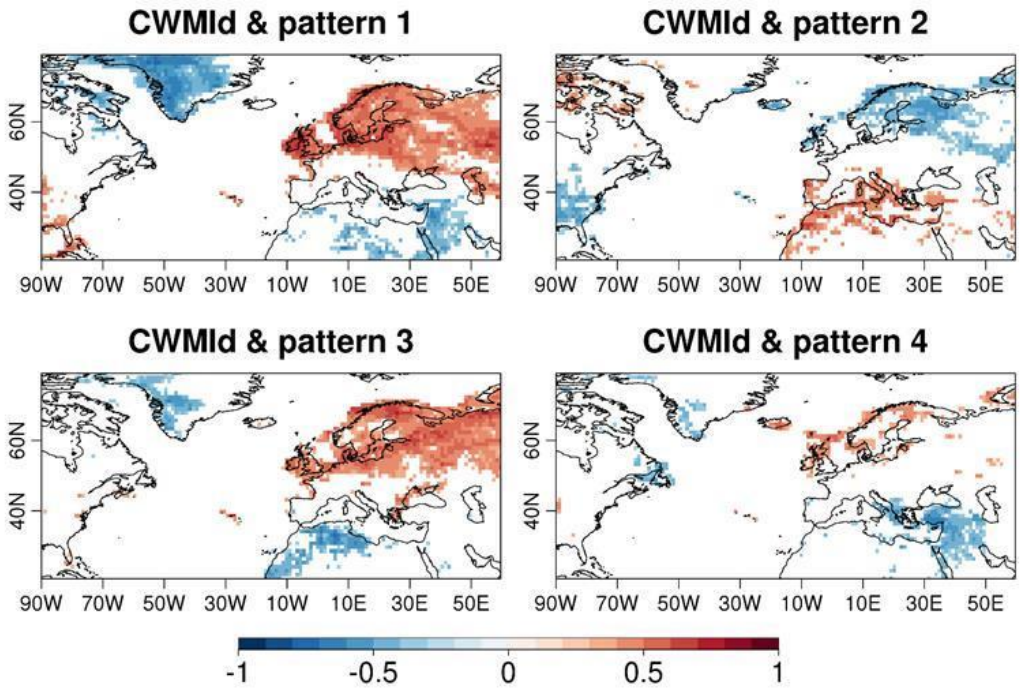

Figure 8: Maps of the Spearman's rank correlation coefficient between the teleconnection index of each of the four main patterns in ERA-20C and the sum of cold

wave days during DJF for the period 1981-2010. Only correlation coefficients significant at the 5% level are shown.

3.2 Weather Regimes

3.2.1 Weather regimes

Weather regimes (WRs) have been computed with the sea level pressure (SLP) from ERA-interim (Dee et al. 2011) during 1981-2016 periods (see Figure 9 and Figure 10).

Daily-mean SLP was computed as an average of 6-hourly raw data (00, 06, 12 and 18 UTC). The daily anomalies at each grid have been computed as deviations from the climatology which have been filtered with a LOESS polynomial regression with a degree of smoothing α = 1 to take into account the annual cycle and minimize the short-term variability of the climatological estimates (Mahlstein et al. 2015). Before classifying the WRs, daily gridded SLP anomalies were weighted by the cosine of the latitude, in order to ensure equal area weighting at each grid point. Principal Components Analysis (PCA) filtering was not applied in this work, to take into account extreme SLP values.

For each individual month of the year, four regimes were classified, by clustering daily SLP anomalies with the k-means algorithm (Hartigan and Wong 1979) with 30 random starts and a maximum of 100 iterations over the Euro-Atlantic region (27°-81°N, 85.5°W-45°E). The k-means algorithm minimizes the sum over all clusters of the within-cluster SLP variance. Its main caveat is that the optimal number of clusters (k) is not defined a priori. The number of regimes k=4 was chosen in this work as it corresponds to the more robust regime partition during winter months (Michelangeli et al 1995).

The impact of a monthly WR on energy production and demand are to be assessed by averaging the ECVs and energy indicators for all days associated to a given weather regime and month. A t-test is performed to assess the level of significance of the anomalies at 99% level. In section 4-6 a detailed explanation is given to the middle month of each season (i.e. January, April, July, and October) so as to present impacts coming from weather regimes on sfcWind, SSRD, T2m and precipitation from the HydroGFD. Again, January is used as an example to illustrate the dependence of ECVs and energy indicators under the influence of weather regimes.

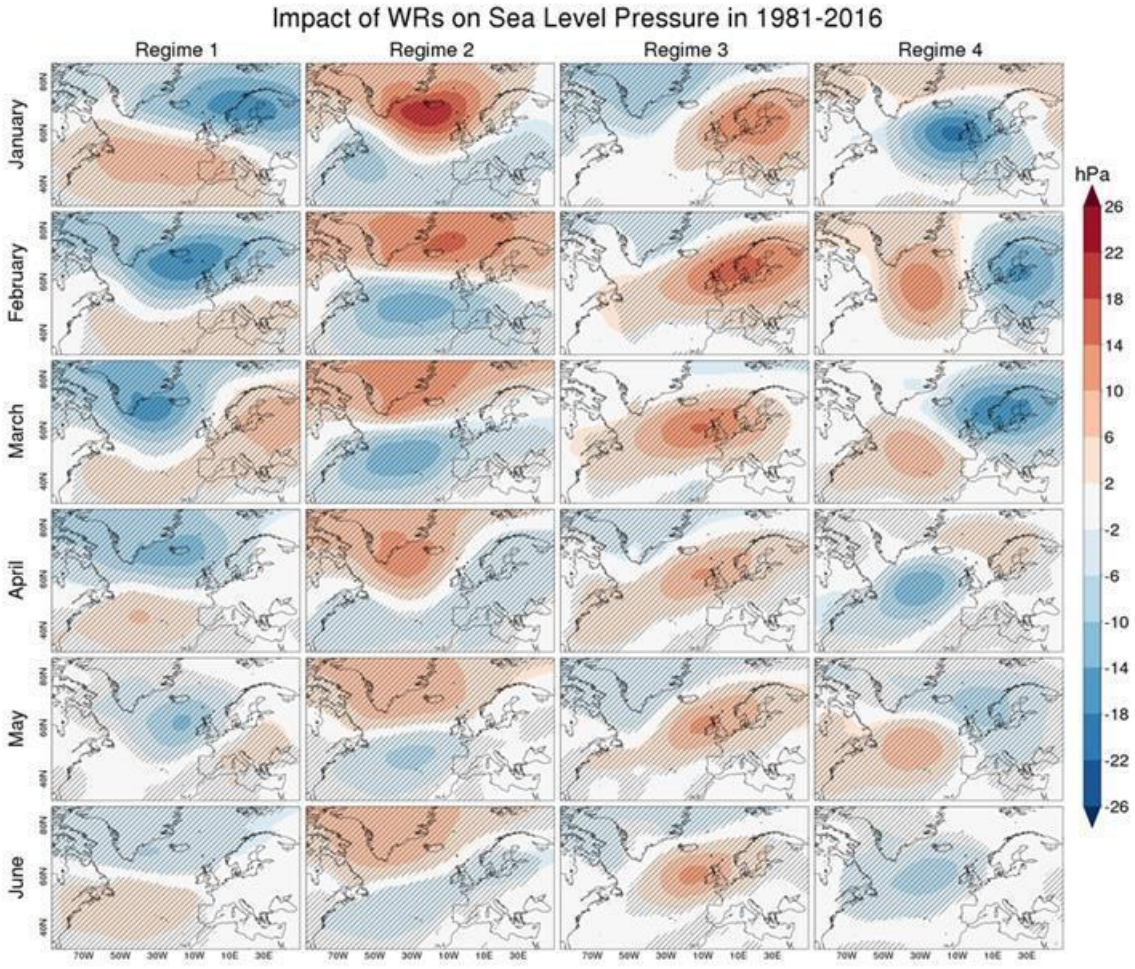

Figure 9: WRs (columns) derived from k-means clusters using SLP during 1981-2016, for the first six months of the year (rows). Scratched area indicates statistical significance at 99% confidence level. Source: ERA-interim.

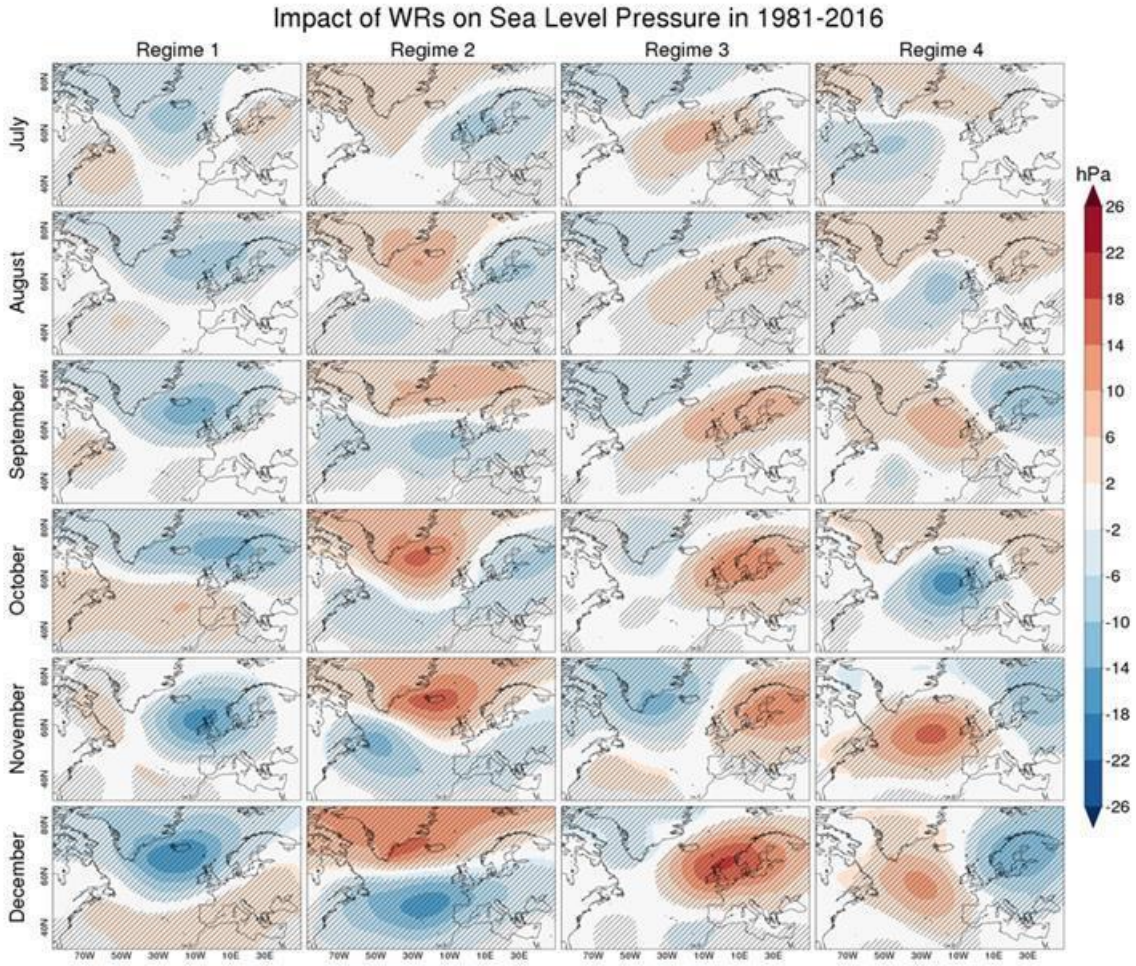

Figure 10: WRs (columns) derived from k-means clusters using SLP during 1981-2016, for the last six months of the year (rows). Scratched area indicates statistical significance at 99% confidence level. Source: ERA-interim.

3.2.2 Hydrological WRs

Hydrological WRs have been classified based on the concept of fuzzy sets (Zadeh, 1965), using imprecise statements to describe a certain system (in this case the climate system). The classification scheme follows four steps: 1) the transformation of large-scale data, e.g., the MSLP; 2) the definition of the fuzzy rules; 3) the optimization of the fuzzy rules and 4) the classification of hydrological weather regimes. A detailed description of the methodology can be found in Bárdossy et al., 2002.

The anomalies of daily mean sea level pressure (MSLP) from reanalysis data (i.e., ERA-interim) serve as a predictor to derive precipitation-induced WRs. Daily-mean SLP was computed as an average of 6-hourly raw data (00, 06, 12 and 18 UTC) at 3° resolution over Euro-Atlantic region (27°-75°N, 100.5°W-73.5°E). Precipitation records, measured in the Ume river basin during 1981-2016 are used as local observations to optimize each fuzzy rule that describes a type of "average" variability of local climate in terms of the frequency and magnitude of precipitation

events (normal events and extreme events) via an iteration optimization process. In total, twelve hydrological WRs for the whole year are classified at a daily scale (see Figure 11).

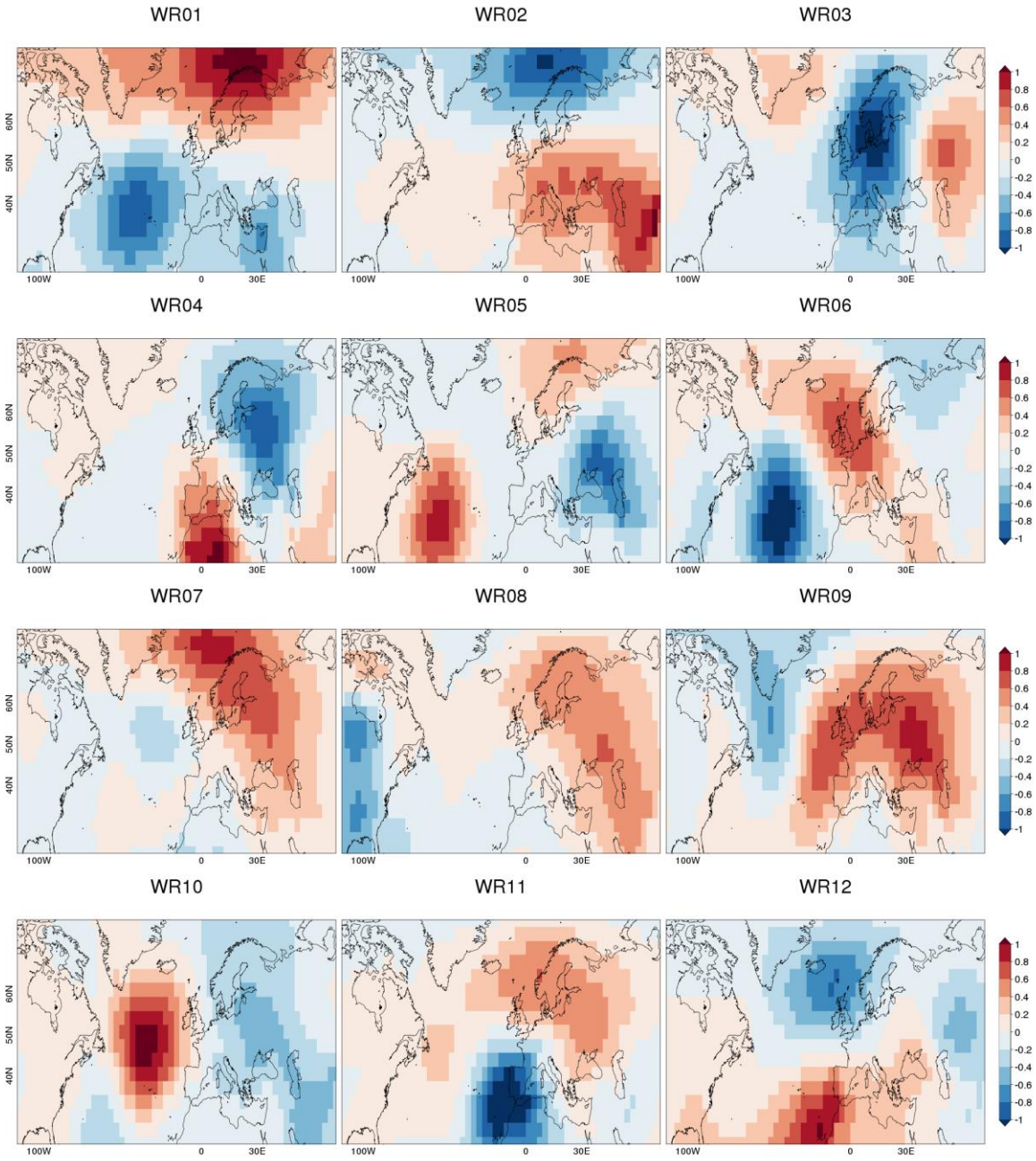

Figure 11: Anomaly maps of hydrological WRs derived from fuzzy classification using the MSLP during 1981-2016. Source: ERA-interim.

A number of hydrological WRs show similarities to identified leading atmospheric variability modes but with shifts in the location of cyclonic and anti-cyclonic centres and strength of MSLP gradients.

A wetness index is used to evaluate the impact of individual hydrological WR on precipitation amount and occurrence. Wet hydrological WRs (wetness index >1) indicates high precipitation amount but with low frequency and dry WRs (wetness index >1) indicates opposite conditions.

Seen from the wetness indices, WR02, WR06 and WR12 are therefore likely to cause more extreme wet situations for the Northern Sweden, while WR02 and WR03 and WR12 are dominant drivers for the wet situations in summer for the same area (not shown here).

3.2.3 Impact regimes

Impact regimes provide an alternative perspective on the meteorological drivers of the power system compared to traditional teleconnection or weather regime analysis. Impact regimes are constructed analogously to weather regimes (i.e., using clustering techniques), but with input time-series corresponding to daily maps of a nationally-aggregated energy variable (i.e., demand, wind power generation or demand-net-wind) rather than a gridded meteorological data set. As with the weather regime analysis, a unique set of clusters is constructed for each calendar month.

By construction, the impact regimes are sensitive to the nature of the energy variable being considered, with important implications for their interpretation. For example, an impact regime based on raw national energy data time-series in Europe identifies the patterns associated with the largest absolute energy fluctuations (in GW) by country across Europe. However, while this might be of interest to a hypothetical pan-European network operator running a 'copper plate' network without transmission constraints, it fails to represent capture the variability of concern to individual regional or national TSOs. In simple terms: a 1GW swing in France (representing ~2% of their annual-average demand) is likely to be less important to the French TSO than a 1GW swing in Romania is to the Romanian TSO (representing ~15% of their average demand).

Each energy variable is therefore normalized prior to the calculation of impact regimes to reduce the over-dominance of larger national energy systems. A LOESS filter is first applied to each country-aggregated daily energy variable time series to calculate a smoothed seasonal cycle (the orange line in Figure 12), which is then removed to calculate the time-varying energy variable anomaly. Each country's anomaly time-series is then divided by its own standard deviation. A value of +1 in the resulting time-series therefore indicates a +1 standard deviation departure above the seasonal cycle norm for that country. For demand or demand-net-renewables, the normalized anomaly time series can therefore be considered to be an indicator of the 'system stress' (how difficult it is to match supply and demand on a particular day). Hereafter, the de-seasonalised, normalized energy variable time series are referred to as "normalized energy anomalies" (e.g., normalized demand anomaly, normalized demand-net-wind anomaly).

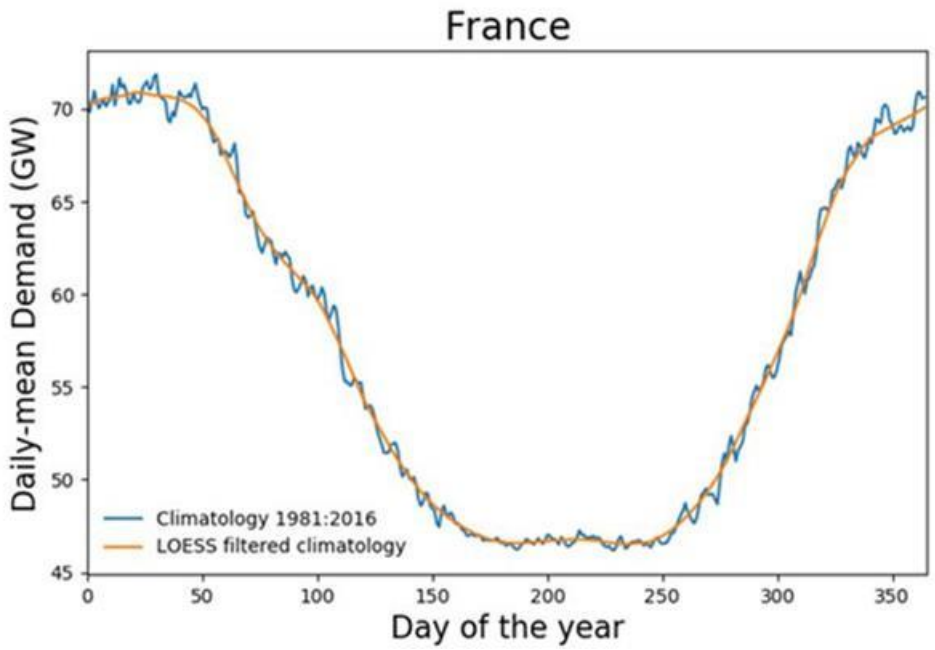

Figure 12: 36-year mean daily demand for France (blue) and the corresponding LOESS filter (orange).

Impact regimes have been calculated for demand, demand-net-wind (DNW; demand – wind power generation). Demand-net-solar, demand-net-wind-net-solar impact regimes were also calculated however, these were not included in the deliverable as the relatively modest amount of installed solar generation across Europe (compared to wind power generation) results in the patterns looking very similar to those for demand and demand-net-wind respectively. It is noted here that it should be recalled that the demand data used in this analysis is modelled demand – and depends only on temperature (heating/cooling degree days): the 'days of week' and long term trend terms are removed to reduce noise. In this analysis, each countries installed wind power and solar power capacities are taken from those reported on the ENTSOe transparency platform. Future work will also investigate if the impact regimes are significantly different if plausible future installed wind and solar capacities are used. This data is available data from the eHighway2050 (2015) scenarios.
For each energy variable, weather-impact regimes are calculated separately for each calendar month using data from 1981-2016. The regimes are calculated using the k-means clustering algorithm with 4 clusters. The choice of 4-clusters is arbitrary and is chosen to be comparable with the weather regimes previously discussed, but further research will seek to apply quantitative measures to determine optimal cluster numbers.

Each month's clusters are examined individually, and composites of MSLP, 2m temperature and 10m wind speed are made from the data corresponding to the days allocated to each cluster, and can be compared with equivalent composites for the weather regimes. This report will exclusively focus on January but analysis from other calendar months can be found in the ANNEX F: Influence of climate variability on energy demand.

4 Wind power generation

4.1 Impact of Euro-Atlantic Teleconnections

Figure 13 and Figure 14 show the impact of Euro-Atlantic teleconnections on surface wind speed for every calendar month. The analysis follows the methodology described in section 3.1.1.

In general, the Euro-Atlantic teleconnections and wind speed variability appear to be related, with correlation coefficients as high as r=±0.9 in some specific areas and months. The more significant correlations are observed in northern, central and western Europe for a period from December to March.

In January NAO significantly influences the wind speed over most part of Europe, with positive influence in northern Europe (in particular in the British Isle, the southern Scandinavia, and the Baltic Sea countries) and negative influence in southern Europe. EA has a strong influence on wind speed over Southern Europe (i.e., positive correlation in the Iberian Peninsula and negative correlation in the Balkan Peninsula). EA/WR's influencing area appears to be Ireland, the UK, most part of France and Germany and the northern Scandinavia, in which positive correlation is observed in contrast to the negative correlation in other influencing regions. The correlations between SCAND and wind speed are mostly negative and significant in Eastern Europe and positive and significant in the Iberian Peninsula.

In April only EA/WR and SCAND show correlations higher than ±0.3 over the whole European region. The former has a widespread negative impact over Western Europe and a positive one over Scandinavia. The latter has a spatial correlation distribution similar to EA/WR, but with opposite sign.

In July NAO exhibits negative and significant correlations over central and Western Europe. On the contrary, EA has limited impact that is restricted to positive and significant correlations over the UK, southern Scandinavia and Denmark. EA/WR show impacts on South Europe, with negative correlations over southwestern Europe and positive ones over southeastern Europe, even if rarely significant. SCAND is characterized by an area with negative and significant correlations over northern Europe.

In October NAO shows negative correlations over most part of Europe (except Scandinavia, Greece and northern UK) but they only appear to be significant in central Europe. EA presents negative and significant correlations over Italy and Greece, and positive over UK. EA/WR only exhibits significant anomalies over Eastern Europe. SCAND presents a clear north-south gradient, with negative and significant correlations over northern Europe and positive and significant ones over Iberian Peninsula.

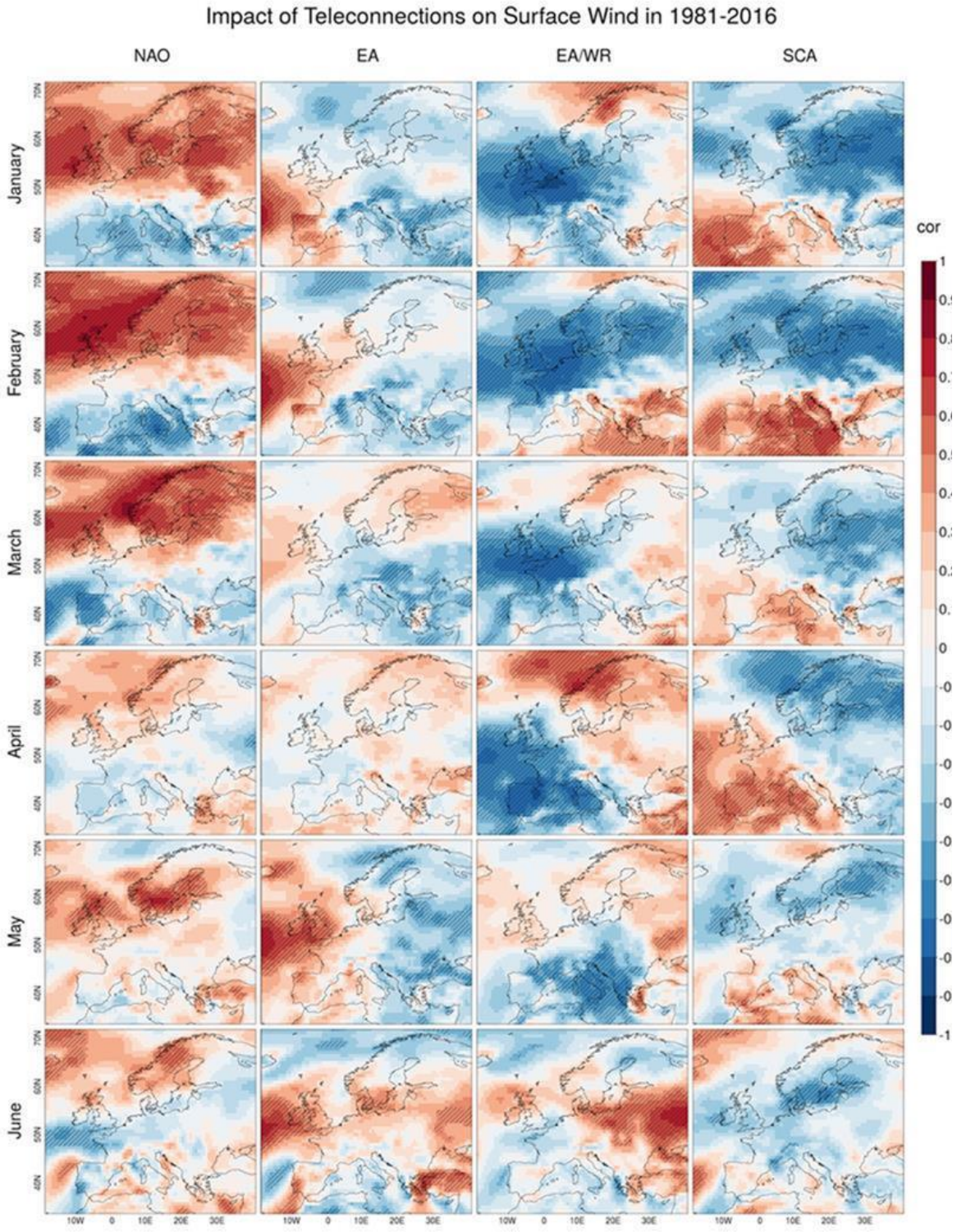

Figure 13: Impact of Euro-Atlantic Teleconnections (columns) on surface wind speed in the first 6 months (rows) in 1981-2016.

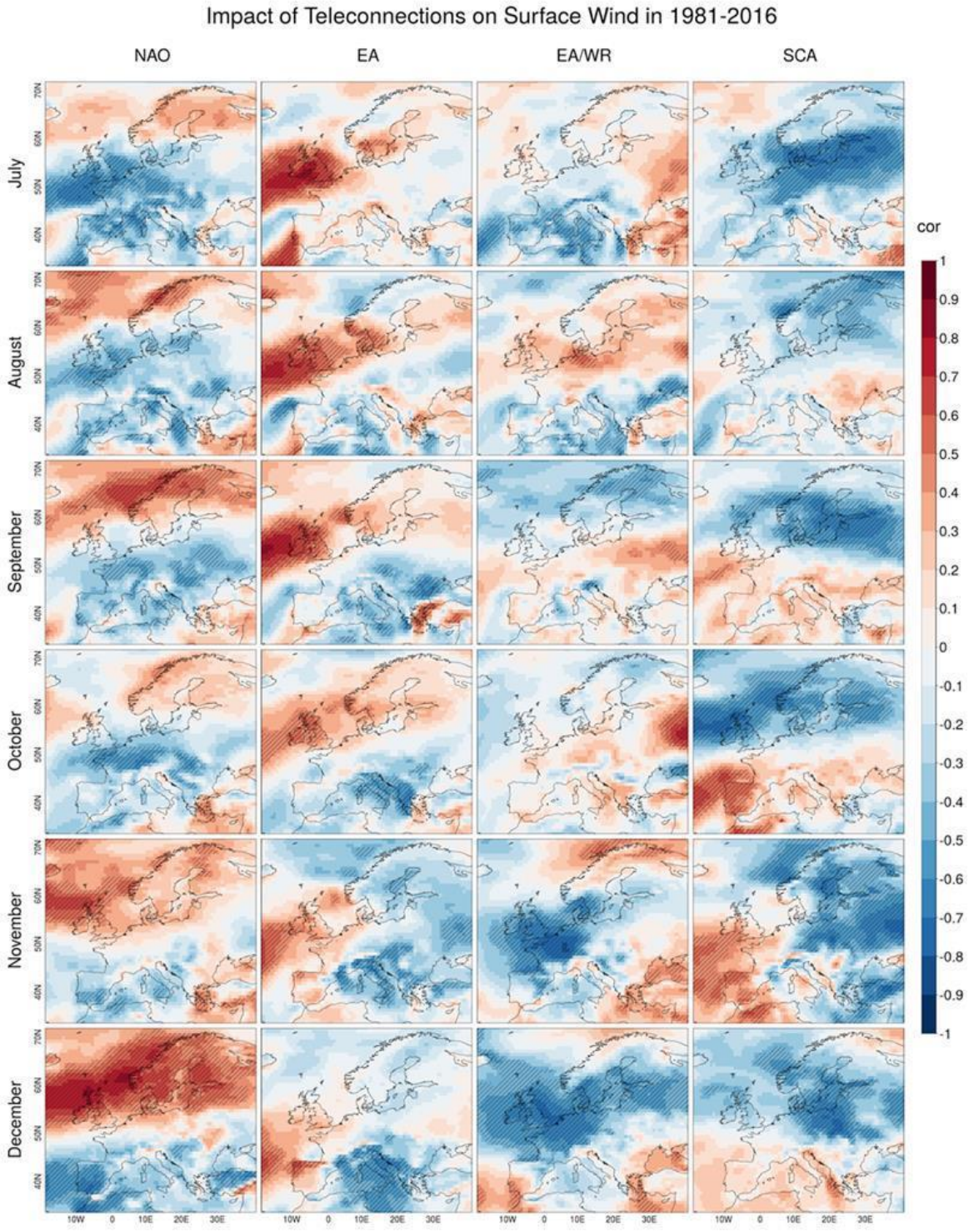

Figure 14: Impact of Euro-Atlantic Teleconnections (columns) on surface wind speed in the first 6 months (rows) in 1981-2016.

The spatial distribution of the impact of teleconnections on capacity factor is very similar to their impact on wind speed, regardless of the type of turbine installed. The calculated correlation maps for each month are included in B.1: Impact of EATc on wind speed and

capacity factors. The most striking differences are observed for the indicator CF iec3[1] indicator in January (see figures in Figure 15) where CF iec3 correlations with all the four teleconnection indices are of opposite sign of those of the other two indicators CF iec1 and CF iec2 in the north Atlantic region close to north-western UK and in the North Sea.

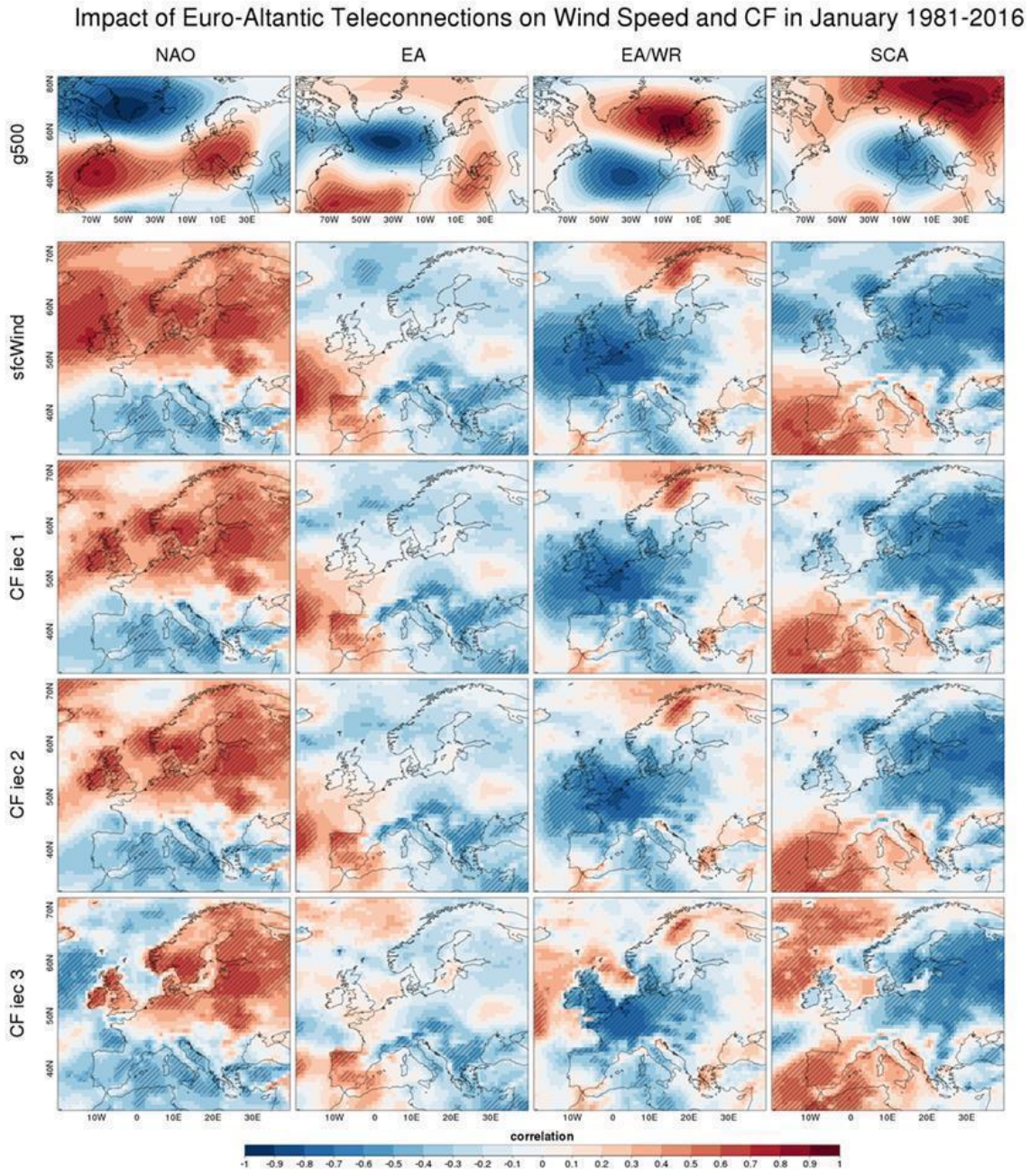

Figure 15: Impact of January teleconnection indices on wind speed and wind power generation. Each image shows the correlation between the four Euro-Atlantic Teleconnection indices (columns) and 500 hPa geopotential height (g500), surface wind speed (sfcWind) and the three capacity factor indicators. Hatches indicate statistical

1

significance at 99% confidence level.

4.2 Impact of weather regimes

The impact of a monthly WR on wind speed and CF was measured following the methodology described in section 3.2.1. Wind speed anomalies were normalized with the climatological wind speed value (i.e. averaging wind speed at a given point in 1981-2016). This allows to better discern the impact of the WRs over land, where wind speed is usually lower (in absolute value) than over the sea.

Like teleconnections, the impact of WRs on wind speed exhibits strong inter-monthly variations (see Figure 16 and Figure 17). WRs can significantly influence average wind speed in Europe, locally up to ±50% of its climatological value for certain WRs and months, especially in winter months. From September to March the WR impact on wind speed is high, significant and more widespread, particularly in Northern, Central and Western Europe.

Northern, western and southeastern Europe wind speed is often affected in a different way by WRs. Their spatial impact patterns often exhibit a bipolar structure with a mostly north-south gradient, when the SLP patterns of the WR resembles those of the wintertime NAO+ or NAO- regime (as in case of regimes 1 and 2 in winter months). Regime 3 is characterized by a higher than normal SLP over Scandinavia and for this reason its impact from August to March patterns usually show a significant decrease of wind speed over central Europe. Regime 4 greatly varies its impact patterns through the year.

In January all regimes have a strong impact on wind speed. Regime 1 influence exhibits a north-south gradient over a widespread area of positive and significant wind anomalies over central and northern Europe, that can be locally very intense (>26% average wind speed). Negative and significant anomalies are observed mostly over the Iberian Peninsula. Regime 2 shows another spatial gradient of its impact on wind speed, with negative and significant anomalies over UK and positive and significant ones over the Mediterranean basin. Regime 3 is characterized by widespread negative and significant wind anomalies over most part of Europe. By contrast, areas with positive and significant wind anomalies are measured over Greece, Adriatic Sea and northern Scandinavia. Regime 4 exhibits mostly positive and significant anomalies over the Iberian Peninsula and western France, and weak negative anomalies over the rest of continental Europe.

In April regime influence on wind speed is very low over continental Europe: regime 1 and 3 show significant anomalies almost only over the British Isle. The influence of regime 2 over the wind speed is restricted to Iberian Peninsula and Greece. Lastly, regime 4 presents weak but widespread negative anomalies over most part of Europe.

In July regime influence over the wind speed in Europe is determined mainly by regime 1 and 2: the former presents mostly negative and significant anomalies over most part of Europe, the latter mostly positive and significant ones.

In October all regimes have a strong influence on wind speed. Regime 1 exhibits widespread positive and significant wind anomalies over central and northern Europe and negative and significant over the Iberian Peninsula. Regime 2 is characterized by positive and significant anomalies over Eastern Europe and negative and significant ones over the UK. Regime 3 leads to a significant reduction of wind speed over most part of central, western and northern Europe, except Greece and northern Scandinavia, where the impact has the opposite sign. Regime 4 shows positive and significant anomalies over Iberian Peninsula, western France and the UK and weak negative anomalies elsewhere.

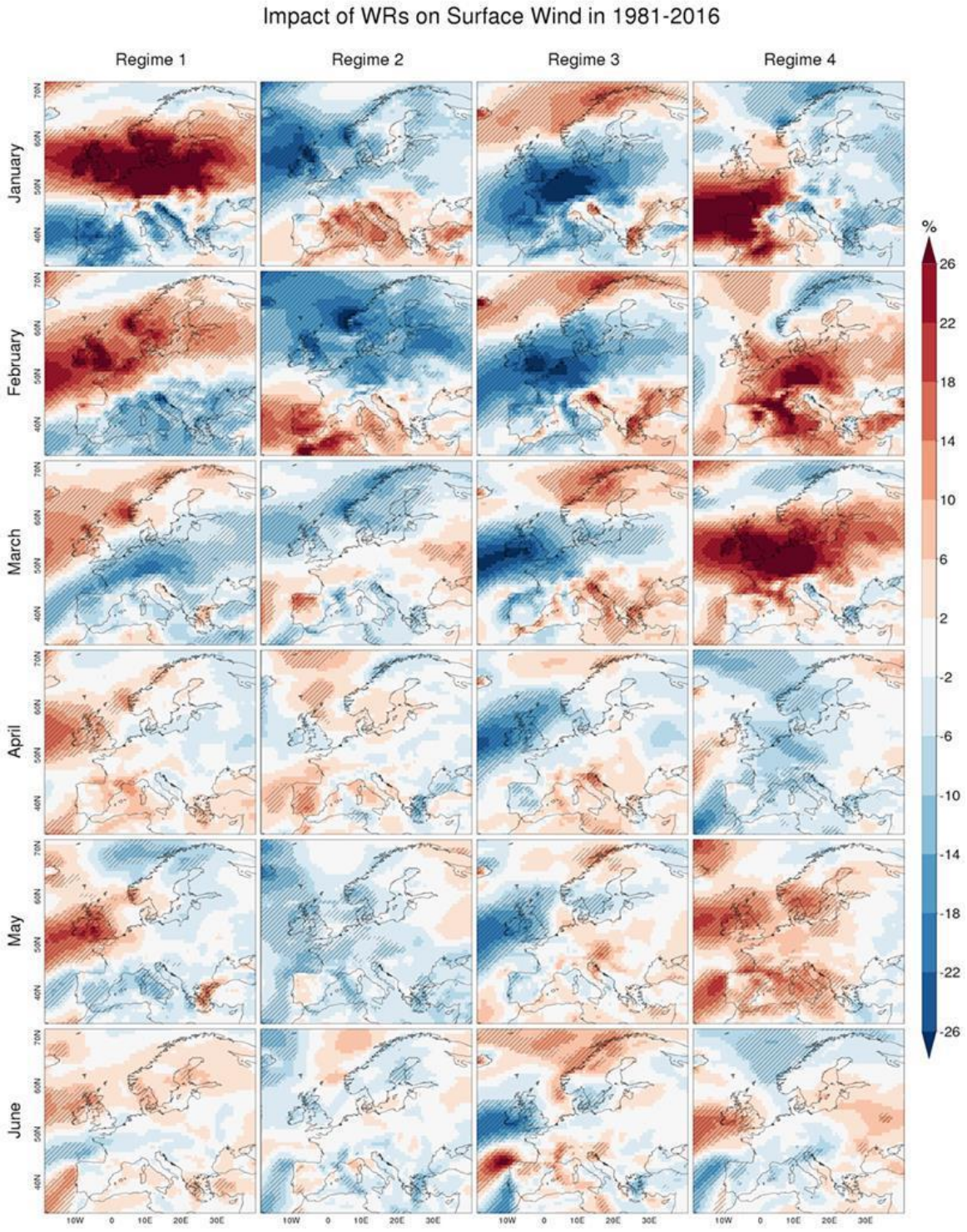

Figure 16: Impact of weather regimes (columns) derived from k-means on surface wind speed in the first 6 months (rows) in 1981-2016. Source: ERA-interim.

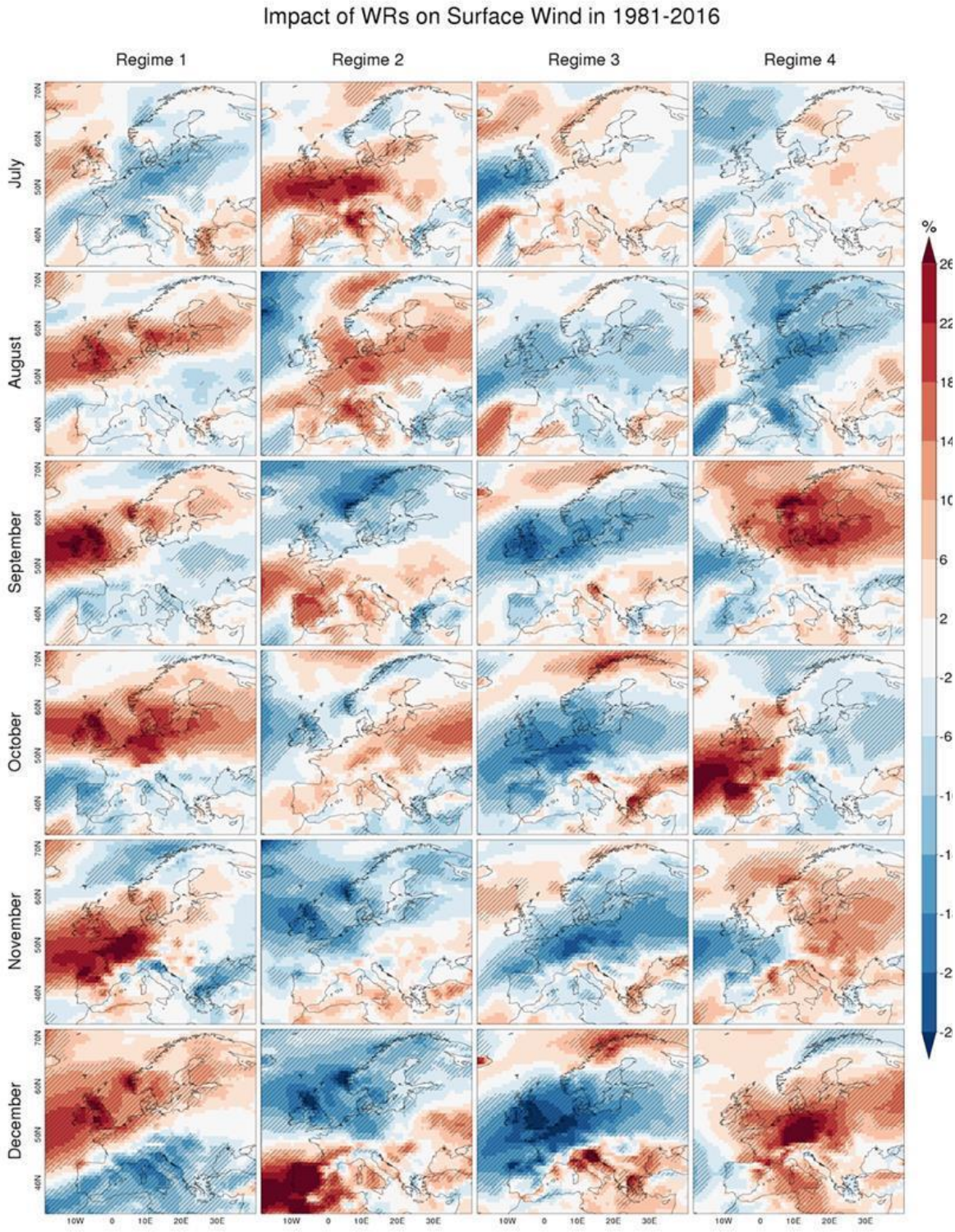

Figure 17: Impact of weather regimes (columns) derived from k-means on surface wind speed in the last 6 months (rows) in 1981-2016. Source: ERA-interim.

It is found that the spatial distribution of the impact of WRs on capacity factor is very similar to their impact on wind speed. However, the similar discrepancies were also detected in the case of the relationships between weather regimes and *CF iec3* in January (see Figure 18),

where the positive impact observed in the North Sea for wind speed and *CF iec1* and *CF iec2* are negative. The analytical maps for other calendar months are included in B.2: Impact of WRs on wind speed and capacity factors.

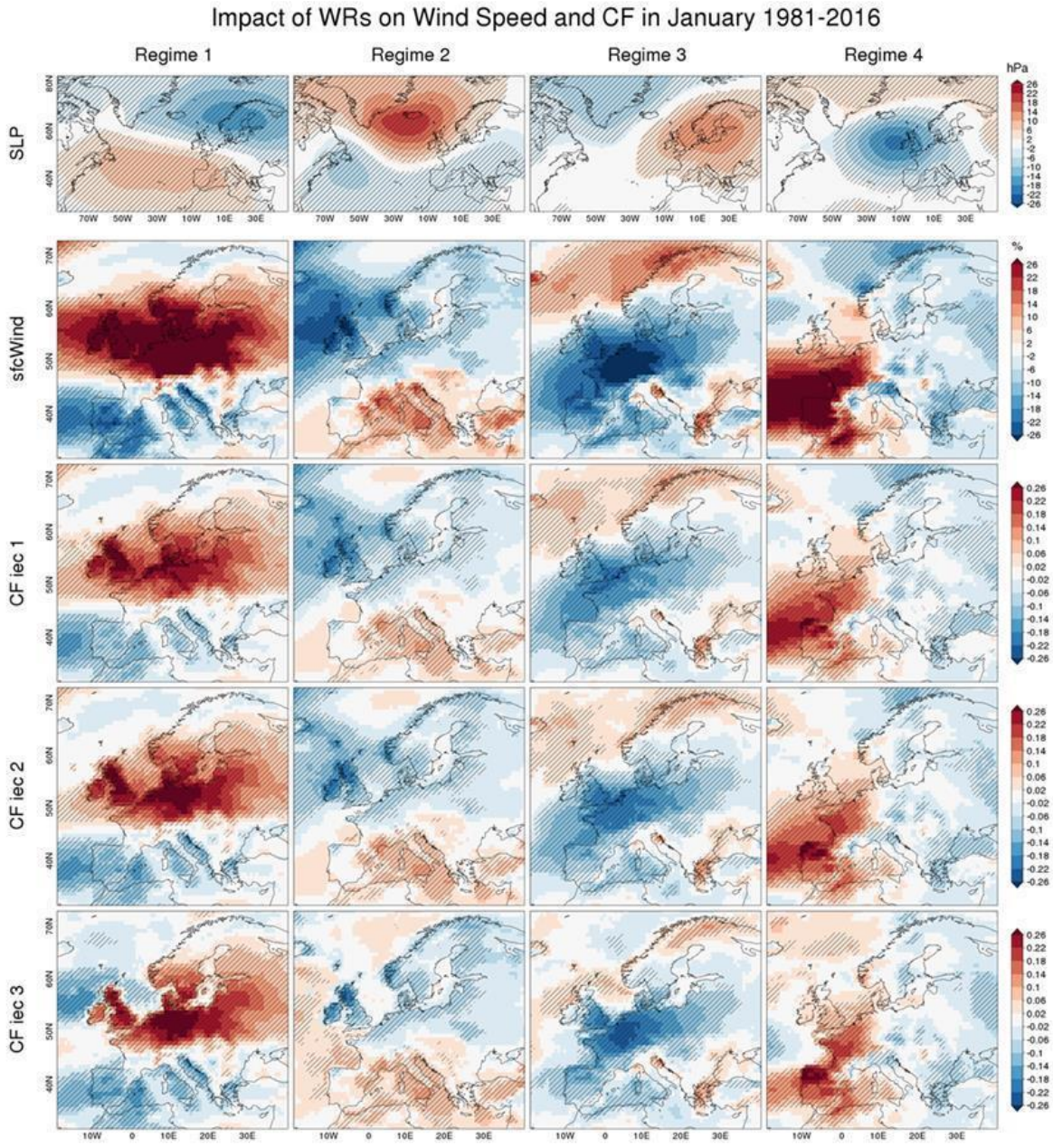

Figure 18: Impact of weather regimes (columns) derived from k-means on surface wind speed (sfcWind) and capacity factors (CFs) during January 1981-2016. Values ranges from -1 to 1 for both wind speed and CF. Impact on surface wind speed is expressed in relative anomalies (with respect to the average wind speed).

5 Solar power generation

5.1 Impact of Euro-Atlantic Teleconnections

The photovoltaic capacity factor mainly depends on the amount of the surface solar radiation downward (SSRD) available, but is also influenced by other atmospheric variables that affect the efficiency of the photovoltaic cells, which diminishes as their temperature increases (see A.2: Solar-power model). Therefore, the correlation of the main four teleconnection indices (NAO, EA, EAWR and SCAND) with SSRD, T2m and photovoltaic capacity factor (CF PV) has been investigated expecting possible small effects of temperature on the photovoltaic capacity factor during summer, with no effects in the other seasons. Figure 19 - Figure 22 show the monthly correlation between the main teleconnection indices and ECVs.

In January the correlation between NAO and SSRD is significant and up to 0.6 over Mediterranean region and over part of the Iberian Peninsula. Significant negative values of correlation are located over Norway. The way the NAO influence the solar radiation variability is mainly by controlling the storm track and the associated cloud cover (Pozo-Vazquez et al. 2004). NAO is positively correlated with cloud cover anomalies over the North of the British Isles and the Scandinavian area, and maximum negative correlated with cloud cover anomalies over Southern Europe (Trigo et al., 2002). The NAO-associated spatial pattern of correlation of solar radiation is opposite to the pattern of correlation of precipitation (see Figure 29 and Figure 30). Temperature correlation patterns are high and significant over Northern and Central Europe, with almost no correlation in the Mediterranean basin. EA is mainly significantly anti-correlated with solar radiation and significantly correlated with the surface temperature over Iberian and Mediterranean basin. In Northern Europe, EA/WR is strongly correlated (up to 0.8) with solar radiation and anti-correlated with the temperature. The correlation between SCAND and solar radiation is negative over Southern Europe.

In April there are no significant regions of correlation over Europe between NAO and SSRD, temperature or PV CF. Solar radiation and PV CF are not affected by the EA, instead, temperature is correlated (up to 0.5) positively over British Isles and Norway. In Northern and Central Europe, SSRD and temperature show high values of correlation with EA/WR. SSRD is anti-correlated with SCAND over Central Europe and Scandinavia. Temperature is anti-correlated with SCAND over Western Europe.

In July there are significant regions of correlation over Scandinavia and British Isles between NAO and SSRD. Solar radiation and temperature are significantly anti-correlated with EA over the British Isles. Temperature is positively correlated with EA in the eastern part of the Mediterranean basin. Low values of significant positive correlation (up to 0.3) between EA/WR index and solar radiation are found over Continental Europe. The highest pattern of positive correlation with SSRD (up to 0.8) and temperature (up to 0.9) are shown over Northern Europe for SCAND index.

In October surface solar radiation is positively correlated with NAO over North of France, temperature is positively correlated over British Isles and Scandinavia. Small patch of negative correlation between solar radiation and EA exists over Great Britain, Ireland and Southern Scandinavia. Temperature is positively correlated with EA over Northern Europe. There are not significant regions of correlation between EA/WR and surface solar radiation. The temperature is strongly anti correlated with EA/WR over Northern Scandinavia. SCAND index and solar radiation are positively correlated over Northern Western Scandinavia and negative correlated over Iberian Peninsula.

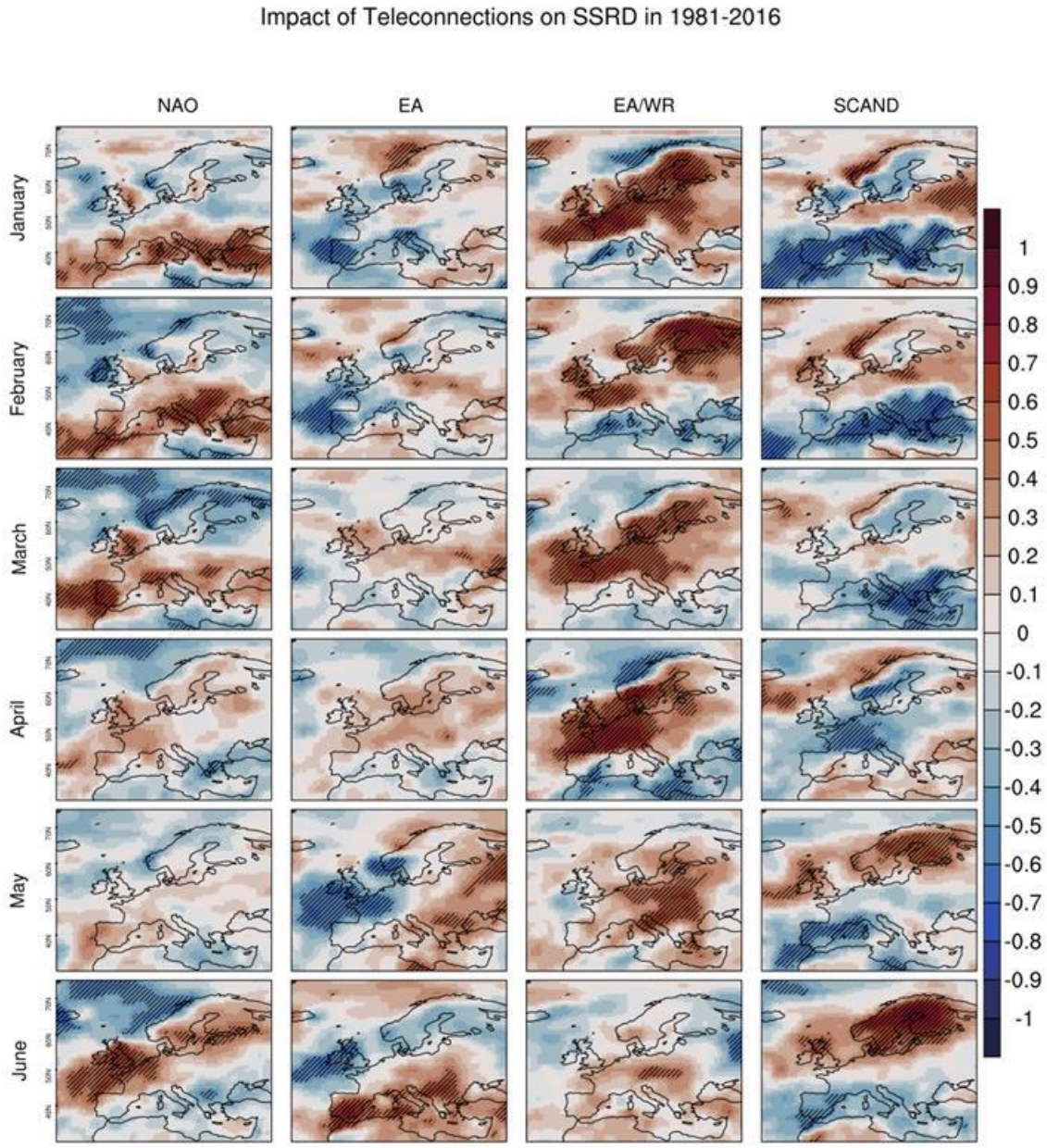

Figure 19: Impact of Euro-Atlantic Teleconnections (columns) on SSRD in the first 6 months (rows) in 1981-2016.

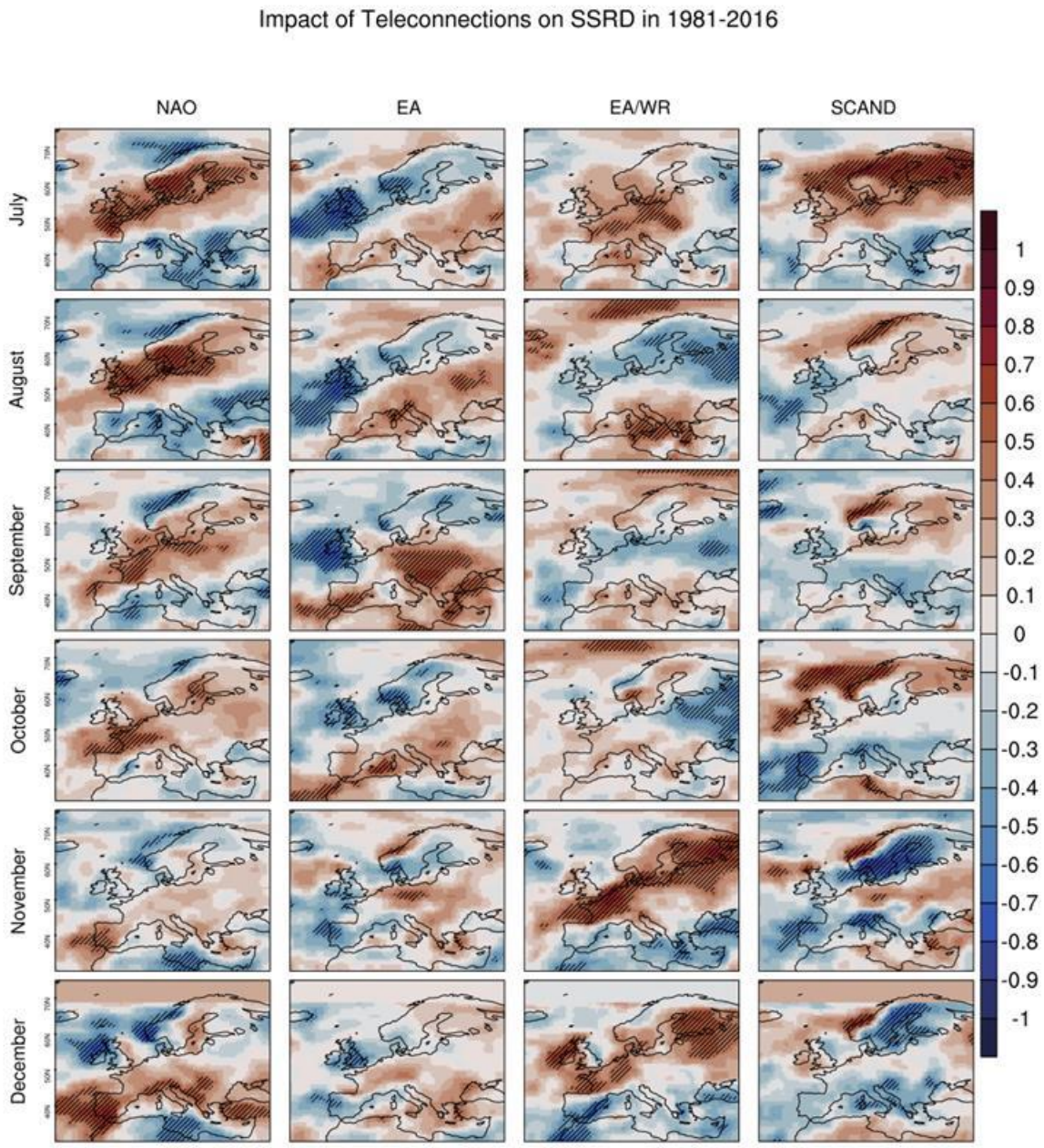

Figure 20: Impact of Euro-Atlantic Teleconnections (columns) on SSRD in the last 6 months (rows) in 1981-2016.

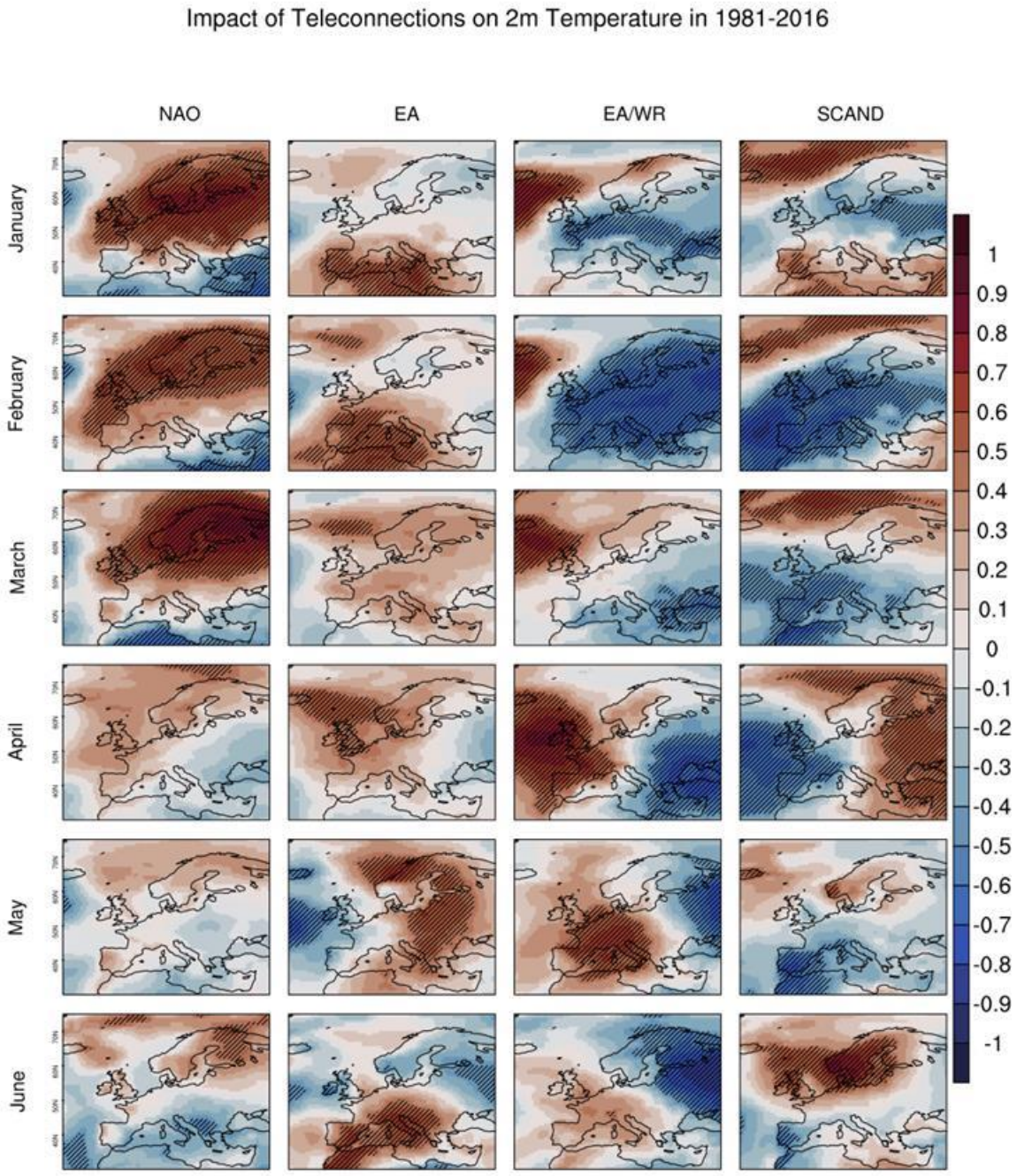

Figure 21: Impact of Euro-Atlantic Teleconnections (columns) on 2 meters temperature in the first 6 months (rows) 1981-2016.

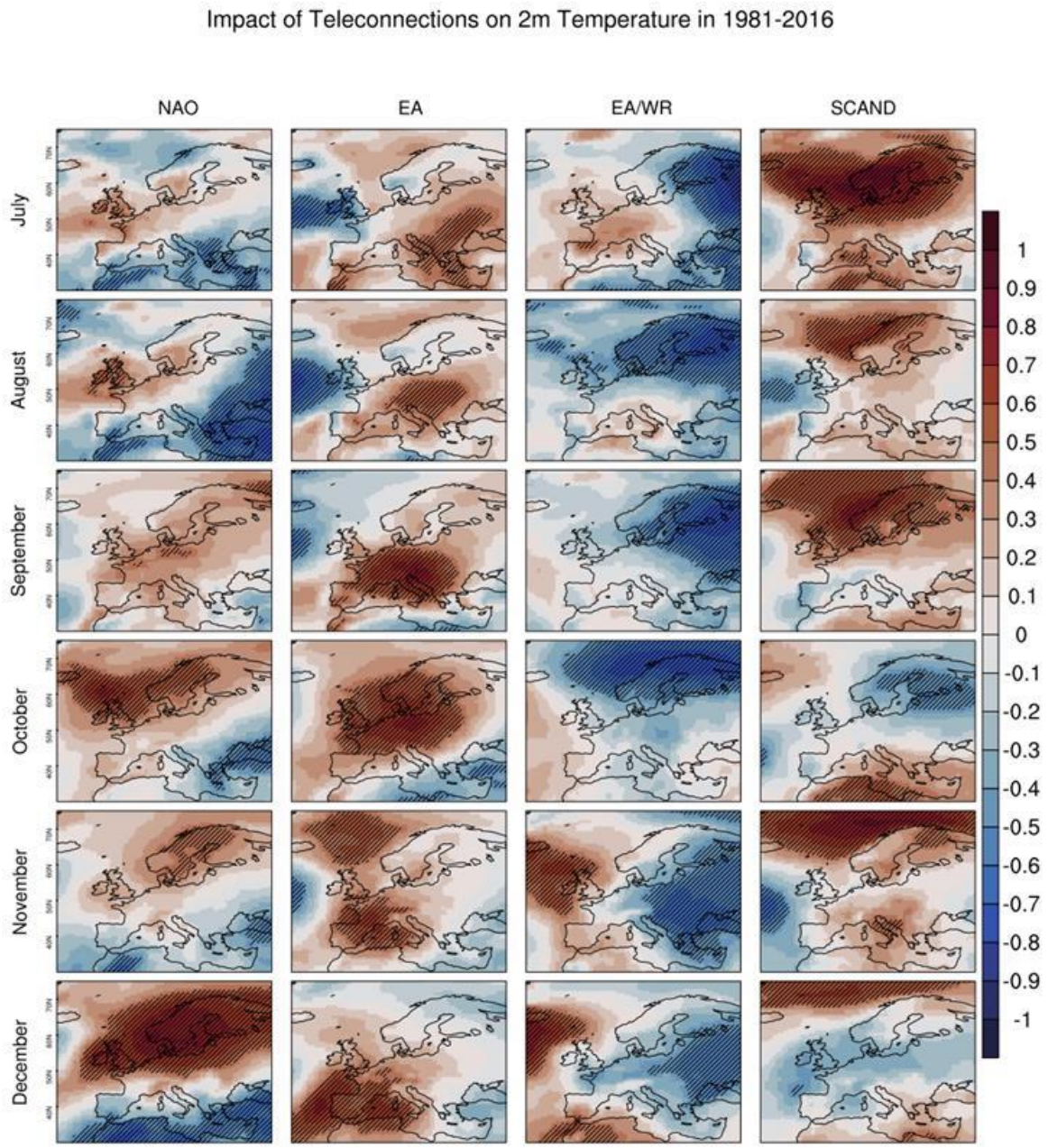

Figure 22: Impact of Euro-Atlantic Teleconnections (columns) on 2 meters temperature in the last 6 months (rows) in 1981-2016.

For all the months and teleconnection indices, it is found that the pattern of correlation of CF PV is identical to the pattern of correlation of solar radiation, with temperature having almost no effect. For example, in January (see Figure 23) pattern of correlation between NAO, EA, EA/WR and SCAND indices and CF PV fully reflect in terms of amplitude and significance patterns of correlation with SSRD. Pattern of SSRD generally show a dipolar structure with gradient that is the same of temperature in spring and summer, but is opposite in winter and

autumn. The correlation maps for other calendar month can be found in C.1: Impact of EATc on solar generation related variables and capacity factors.

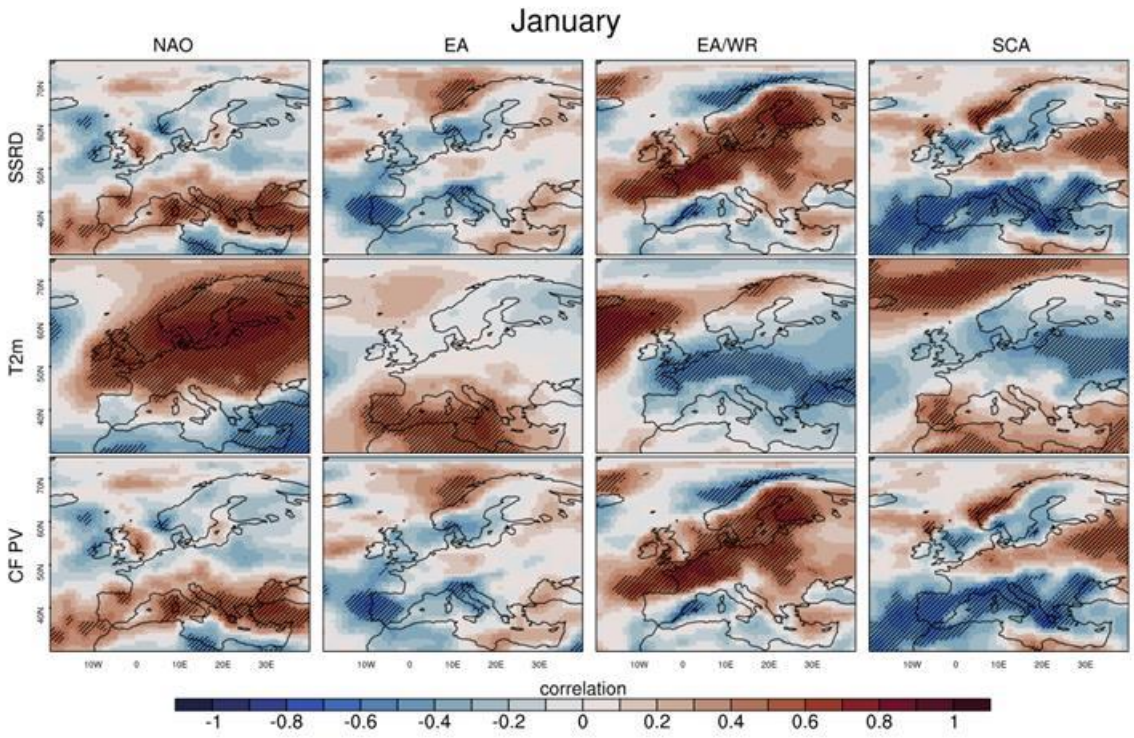

Figure 23: Impact of January teleconnection indices on surface solar radiation, 2 meters temperature and solar power capacity factor. Each image shows the correlation between the four Euro-Atlantic Teleconnection indices (columns) and surface solar radiation (SSRD), 2 meters Temperature (T2m), the capacity factor indicator (CF PV). Hatches indicate statistical significance at 99% confidence level.

5.2 Impact of weather regimes

The photovoltaic capacity factor depends on the amount of the surface solar radiation downward (SSRD) available and, in a limited manner, on the ambient air temperature (see A.2: Solar-power model). The main factor of meridional variations of surface solar radiation is the cloud cover variability, associated, for instance with the precipitation. The concept of weather regimes is based on the idea of an earth atmosphere evolving between a limited numbers of states that have specific consequences for local weather. Several studies over the North Atlantic-European domain, demonstrate that weather regimes are highly correlated to anomalies of local surface temperature and precipitation (Plaut and Simonnet, 2001, Yiou and Nogaj, 2004, Herting et al.2014). Therefore, it is expected that clear spatial patterns of solar radiation and photovoltaic capacity factor (PV CF) associated with those regimes.

Daily anomalies of SSRD, T2m and CF are calculated by removing the seasonal cycle from 1981 to 2016. The impact of a monthly weather regime (as calculated in Section 3.2.1) on surface solar radiation downward, temperature and CF PV was measured following the methodology

described in section 3.2.1. A t-test is performed to assess the level of significance of the anomalies. Figure 24 - Figure 27 show the correlation between the weather regimes and ECVs for each calendar month.

In January (see Figure 25 and Figure 27), averaged composite of SSRD anomalies relative to Regime 1 has a dipole structure with north-south gradient. Anomalies are positive and significant over Mediterranean basin (about 10 W m-2) and Iberian Peninsula (up to 20 W m-2). Negatives significant values over Northern Europe are below 8 W m-2. Temperature anomalies are positive over Northern Europe with values up to 5 °C. The influence of Regime 2 leads to negative anomalies over Balkan region and positive anomalies over British Isles. Northern Europe temperature is largely affected by Regime 2 (negative anomalies up to 4 °C). Positive significant anomalies of about 10 W m-2 over Central Europe and Portugal are due to Regime 3, that influences mainly Eastern Europe temperatures. Regime 4 largely influences SSRD negative values over Iberian Peninsula, (about -20 W m-2), Alps region (about -12 W m-2) and Balkan region (about -8 W m-2). Instead, positive surface changes in temperature are localized over Northern France and Balkan.

In April (see Figure 25 and Figure 27), strong negative and significant anomalies of SSRD related with Regime 1 are localized over Ireland, Great Britain and Scandinavia. Positive anomalies are significant only over Iberian Peninsula. Temperature is influenced significantly by Regime 1 only over Northern Eastern Europe. Negative SSRD anomalies over Iberian region and Alps region and positive SSRD anomalies over Ireland and Eastern Mediterranean basin are associated with Regime 2. The averaged composite of SSRD anomalies associated with Regime 3 has a dipole structure with a gradient oriented from North-West to South-East similarly to the gradient of temperature anomalies. Regime 4 influences Western European SSRD with positive anomalies in the South and negative anomalies in the North.

In July (see Figure 26 and Figure 28), the averaged composite of SSRD anomalies associated to Regime 1 is positive over Northern Central and Eastern Europe (up to 16 W m-2) and negative (about 8 W m-2) over Southern Eastern Europe. Significant temperature anomalies below 2 K are localized over Northern Continental Europe. SSRD anomalies associated with Regime 2 have a large dipolar structure with a gradient of about 35 W m-2 from North to South. Temperature anomalies reflect the same dipolar structure with the amplitude of the anomalies below 2/3°C. Changes in temperature follow the same South–East to North-West structure and are less than 1 °C.

In October (see Figure 26 and Figure 28), the SSRD positive and significant anomalies over Southern Europe are always below 12 W m-2, except over Iberian Peninsula (up to 20 W m-2). Regime 2 influences SSRD over Central Europe (negative anomalies) and Temperature over British Isles and Scandinavia. The averaged composite of SSRD anomalies associated with Regime 3 is positive and significant over Northern Europe and negative over Mediterranean basin. The low changes in temperature are significant over all Europe except Iberian Peninsula. Regime 4 impacts SSRD over Western Europe with negative anomalies below 20 W m-2.

The averaged anomalies of the photovoltaic capacity CF PV resembles the averaged anomalies of SSRD. For instance, and associated change in CF PV of about 0.018 over Iberian Peninsula. In January (see Figure 29), CF PV anomalies associated with Regime 1 are larger over Iberian Peninsula (about 0.02) where the SSRD is larger. The Regime 2 leads to lower values of solar radiation over over Balkan region as well as lower CF PV. The positive variations of CF PV (below 0.01) due to Regime 3 are localized over Central Europe and Portugal, where the SSRD anomalies are larger. The most relevant changes in CF PV are over Iberian Peninsula (about -/+ 0.020) and are due to Regime 1 and Regime 4, associated with anomalies of SSRD of about 20 W m-2.

The influence of WRs on the surface solar radiation downward can be greater than 20 W m-2per day and the CF anomalies can reach up to 0.03. Changes in solar radiation associated with WR are due to the enhanced cloudiness with consequent dimming (Chiacchio and Wild 2010; Pozo-Vazquez et al. 2011). Regime 1 during winter and autumn is associated with above-normal temperature over northern Europe and Scandinavia and above-normal solar radiation over Southern Europe. Regime 2 is associated with Solar radiation lower than normal in Central Europe and above than normal over Balkan region in spring and summer. Regime 3 is associated with solar radiation above than normal in Northern Europe and lower than normal in Mediterranean basin, especially in summer and spring. Regime 4 mainly affects Solar radiation in the Iberian Peninsula with values below than normal in winter and autumn and above than normal in spring.

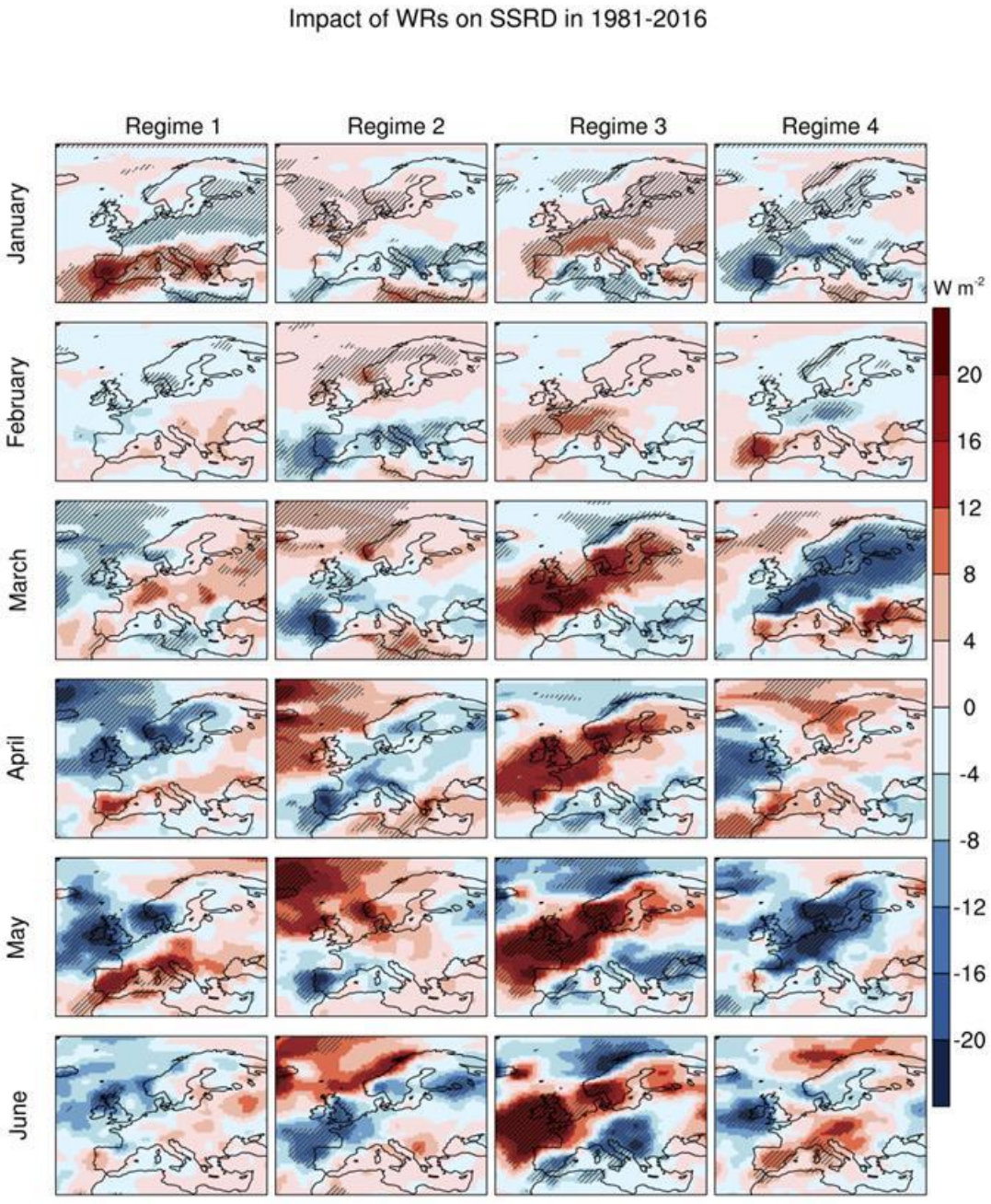

Figure 24: Impact of weather regimes (columns) derived from k-means on SSRD in the first 6 months in 1981-2016

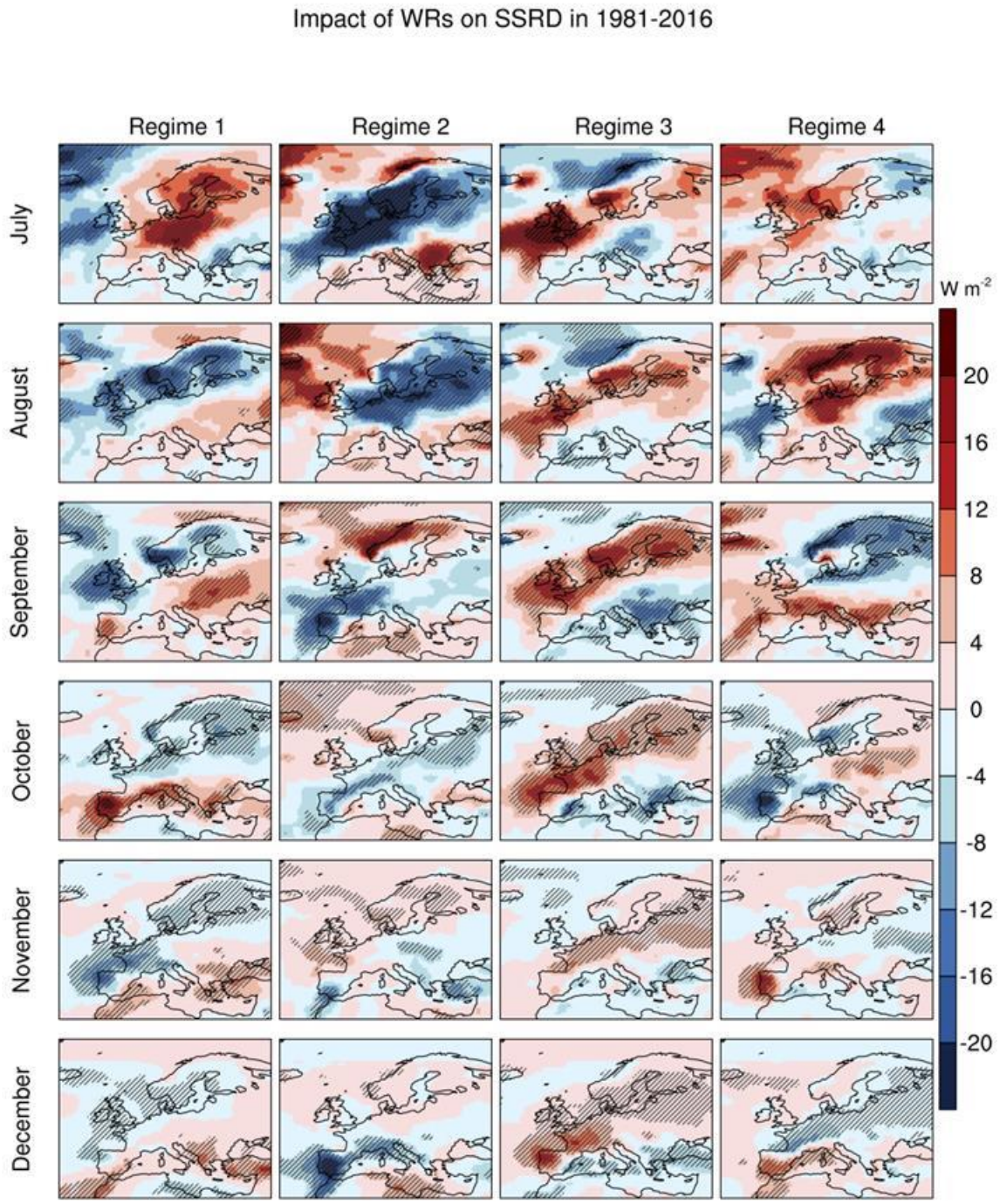

Figure 25 Impact of weather regimes (columns) derived from k-means on SSRD in the last 6 months in 1981-2016

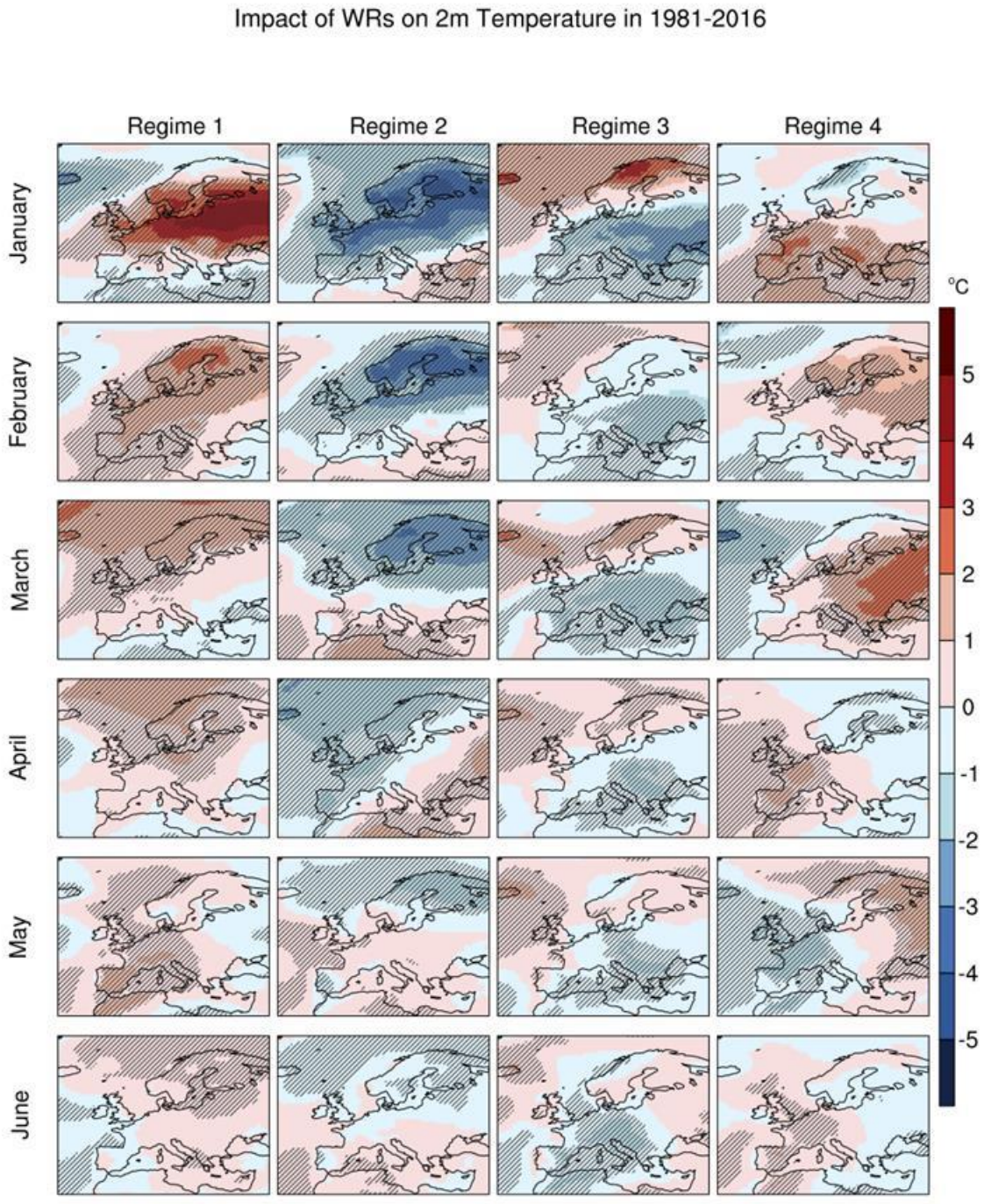

Figure 26: Impact of weather regimes (columns) derived from k-means on 2 meters temperature in the first 6 months in 1981-2016

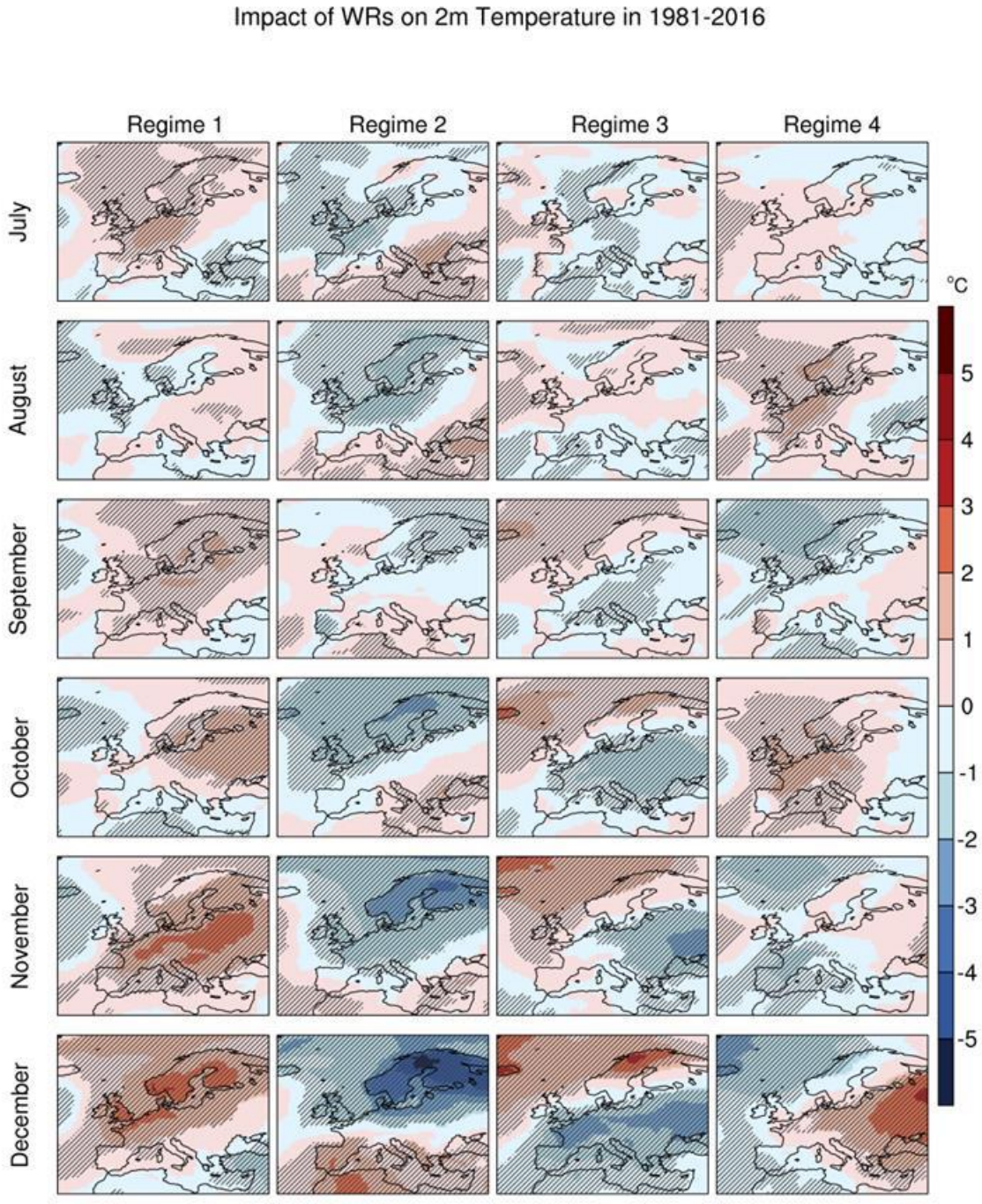

Figure 27: Impact of weather regimes (columns) derived from k-means on 2 meters temperature in the last 6 months in 1981-2016

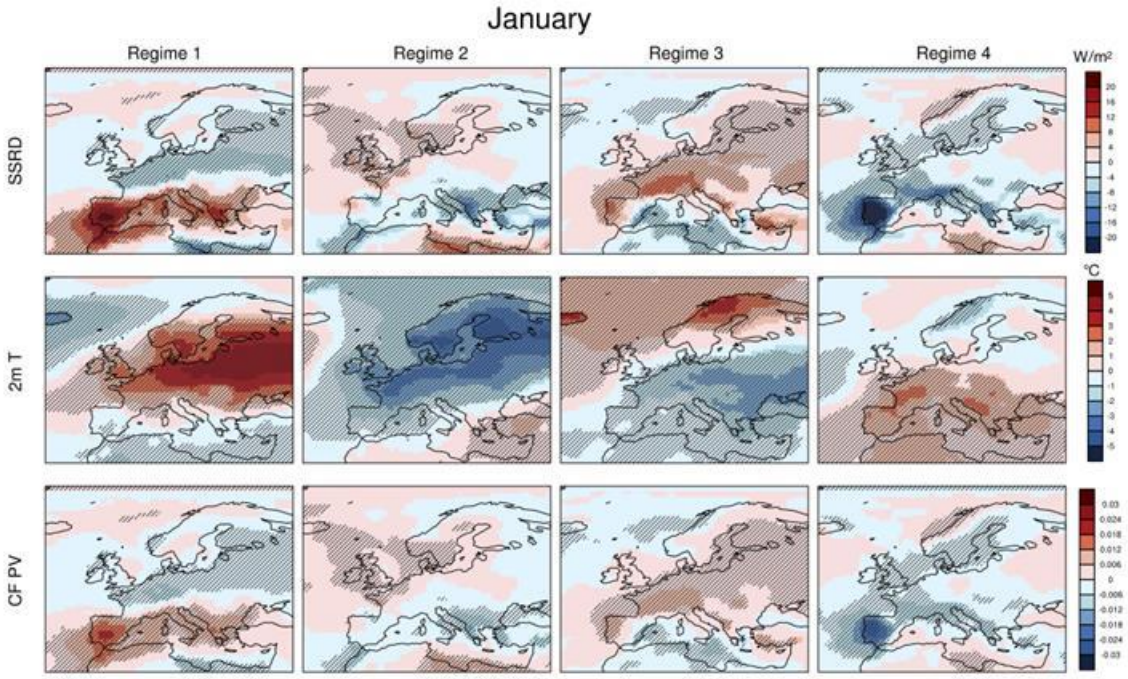

Figure 28: Impact of weather regimes (columns) derived from k-means on SSRD (first row), 2 meters temperature (second row) and CF (third row) during January 1981-2016. Hatches indicate that anomalies are significant at the 95% confidence level.

6 Hydropower generation

6.1 Impact of Euro-Atlantic Teleconnections

Precipitation data from the HydroGFD has been used to investigate the impact of Euro-Atlantic teleconnections on precipitation over the European domain. The analysis follows the methodology described in section 3.1.1 and the results are presented in Figure 29 and Figure 30.

In January NAO has a positive and significant correlation on precipitation over parts of northern Europe while showing negative and significant correlations over the Mediterranean region and to the north of the Black Sea. EA has a weaker influence on precipitation across the domain. However, there are a few areas where the influence is significant i.e. positive correlation over the western part of the Iberian and negative correlations over southern Germany, Czech Republic, and Austria. EA/WR has a negative and significant correlation over the British Isles, Southern Scandinavia, France, and the northern parts of Germany and Poland. Two small regions of strong positive correlations are found over the northern Norwegian coast and the Spanish Mediterranean coast. SCAND has a negative and significant correlation over the northern Scandinavia, Finland, the Baltic States, and parts of northern Russia, while it has a negative and significant impact on precipitation over the Iberian Peninsula, southern France, and Italy.

In April only EA/WR and SCAND show correlations higher than ±0.3 over any substantial area of the European domain. The former has a widespread negative impact over the northern parts of Western Europe, southern Scandinavia, Finland, and the Baltic States. Additionally, it has a positive impact over the northern coast of Norway. The latter has a spatial correlation distribution similar to EA/WR, but with opposite sign.

In July NAO exhibits negative and significant correlations over central and Western Europe. EA has limited impact that is restricted to positive and significant correlations over the UK, southern Scandinavia and Denmark. EA/WR shows negative correlations over most of Western Europe and positive and significant correlations over central western Russia. SCAND shows negative and significant correlations over the north eastern coast of Sweden, Finland, and north eastern Russia, while showing positive and significant correlations over the western seaboard of the Black Sea.

In October NAO shows negative correlations over most part of Europe (except the northern coast of Norway and the Spanish Mediterranean coast) but they only appear to be significant in central Europe. EA presents negative and significant correlations over Eastern Europe and positive over the British Isles and southern Norway. EA/WR only exhibits significant anomalies over Eastern Europe and western Russia. SCAND shows negative and significant correlations over northern Scandinavia and positive and significant ones over Iberian Peninsula.

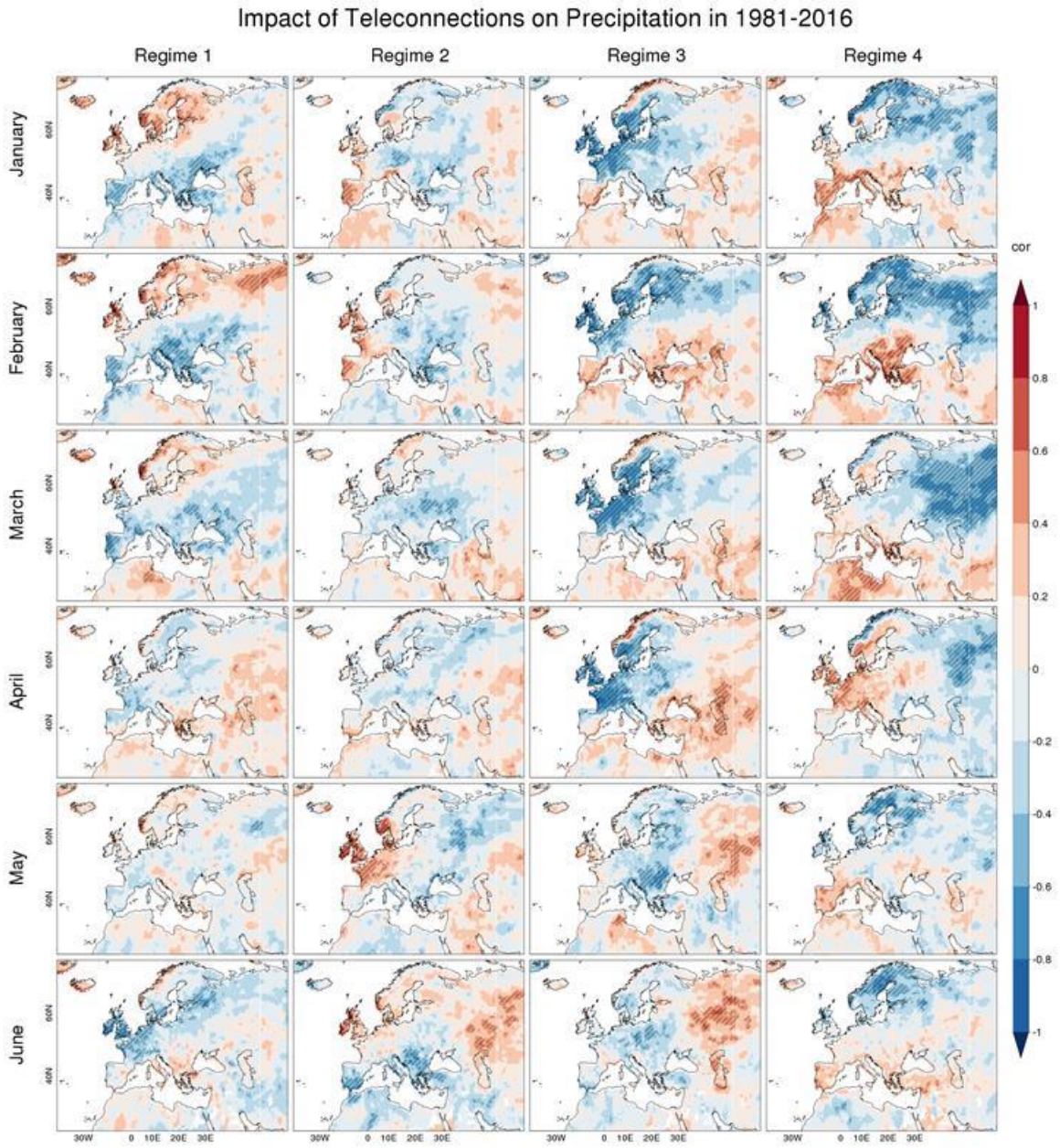

Figure 29: Impact of Euro-Atlantic Teleconnections (columns) on precipitation from HydroGFD in the first 6 months (rows) in 1981-2016.

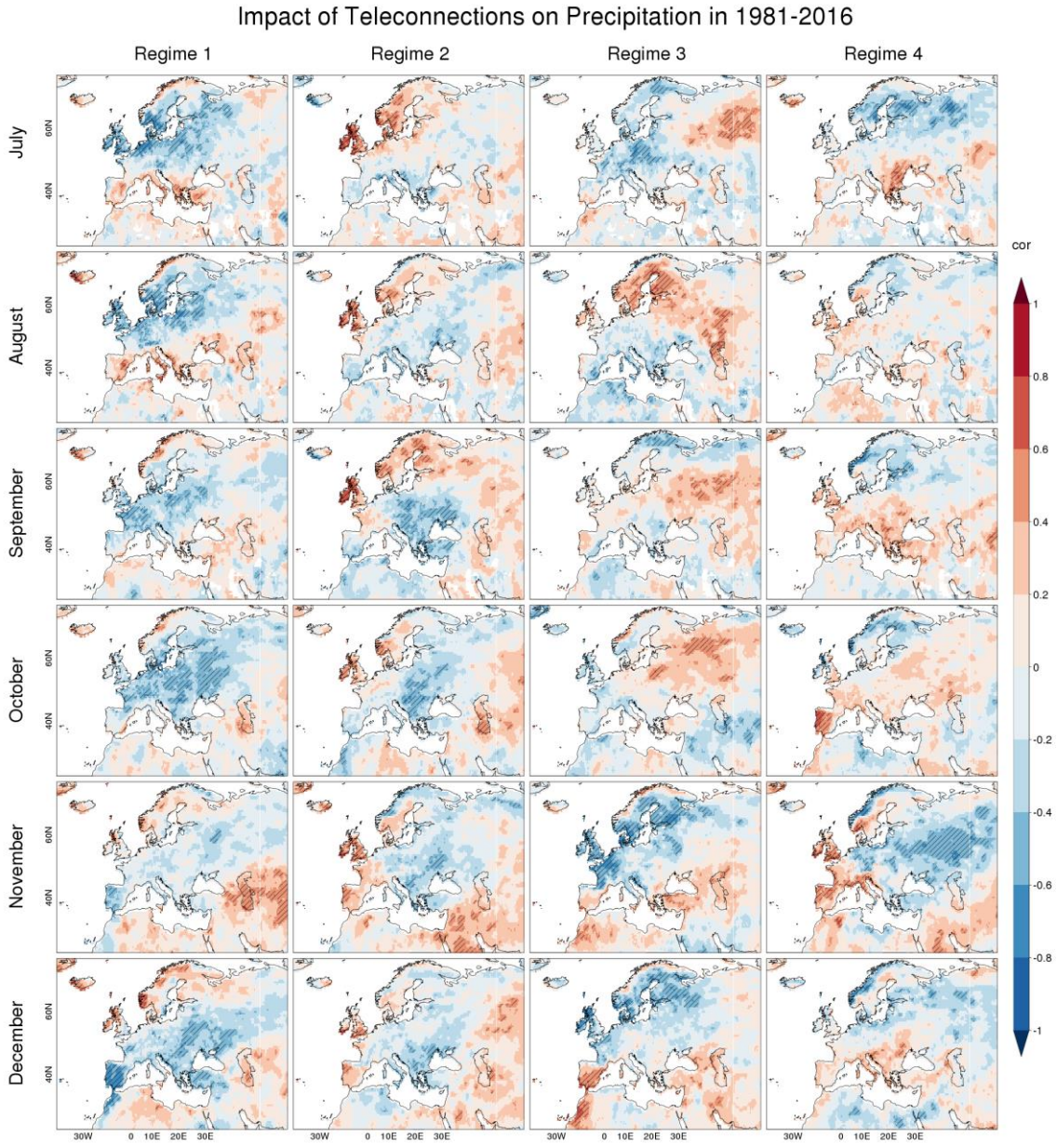

Figure 30: Impact of Euro-Atlantic Teleconnections (columns) on precipitation in the last 6 months (rows) in 1981-2016.

6.2 Impact of weather regimes

The impact of a monthly WR on precipitation was measured by averaging the precipitation anomalies for all days associated to a given regime and month. Precipitation anomalies were normalized with the climatological precipitation value (i.e. averaging precipitation at a given point in 1981-2016). The monthly maps are available in Figure 31 and Figure 32.

In January regime 1 has a mild negative impact on precipitation over the northern parts of Europe and the Iberian Peninsula and a somewhat stronger positive impact over southern Europe particularly over the Balkans and Greece. Regime 2 shows a predominantly weak

negative impact over most of Europe with scattered stronger anomalies over Eastern Europe. There is a mild positive anomaly over Iberian Peninsula. Regime 3 exhibits a similar pattern to regime 3 but with the opposite sign. Regime 4 has a weak to mild positive impact over much of Scandinavia, Finland, the Baltic States, northern Russia, whilst the opposite impact is found for the rest of Europe.

In April all the regimes have a low impact on precipitation is over continental Europe. Regime 1 has a positive impact over most of Europe and a weak negative impact over Italy, Greece, southern Bulgaria, and northern Scandinavia. Regime 2 has a negative impact over France, Germany, Poland, and the Baltic region and a weak positive impact over the rest of Europe. The impact of Regime 3 is predominantly positive with a weak negative impact over Eastern Europe and western Russia. Regime 4 has a negative impact over the British Isles, France, southern Norway, Eastern Europe and western Russia.

In July there is a noticeable increase in the impact of all regimes on precipitation over the Iberian Peninsula. Regime 1 has a positive impact over the Iberian Peninsula, southern Scandinavia, Eastern Europe, and most of Italy. Regime 2 has a positive impact over the Iberian Peninsula and much of northern Europe. Regime 3 exhibits a similar pattern to regime 2 but with the opposite sign. Regime 4 has a strong negative impact over the Iberian Peninsula and weaker negative impact over northern France, the British Isles, Greece, and parts of Eastern Europe.

In October Regime 1 has a weak positive impact over much of Europe with pockets of negative impact over parts of the Iberian Peninsula, Northern Scandinavia, norther Russia, and around the Black Sea. Regime 2 has a positive impact over much of the Iberian Peninsula, Central and Eastern Europe (especially around Greece), and northern Scandinavia. Regime 3 has a mild negative impact over much of central Europe, southern Scandinavia, and western Russia. Regime 4 has a similar but opposite pattern to regime 3.

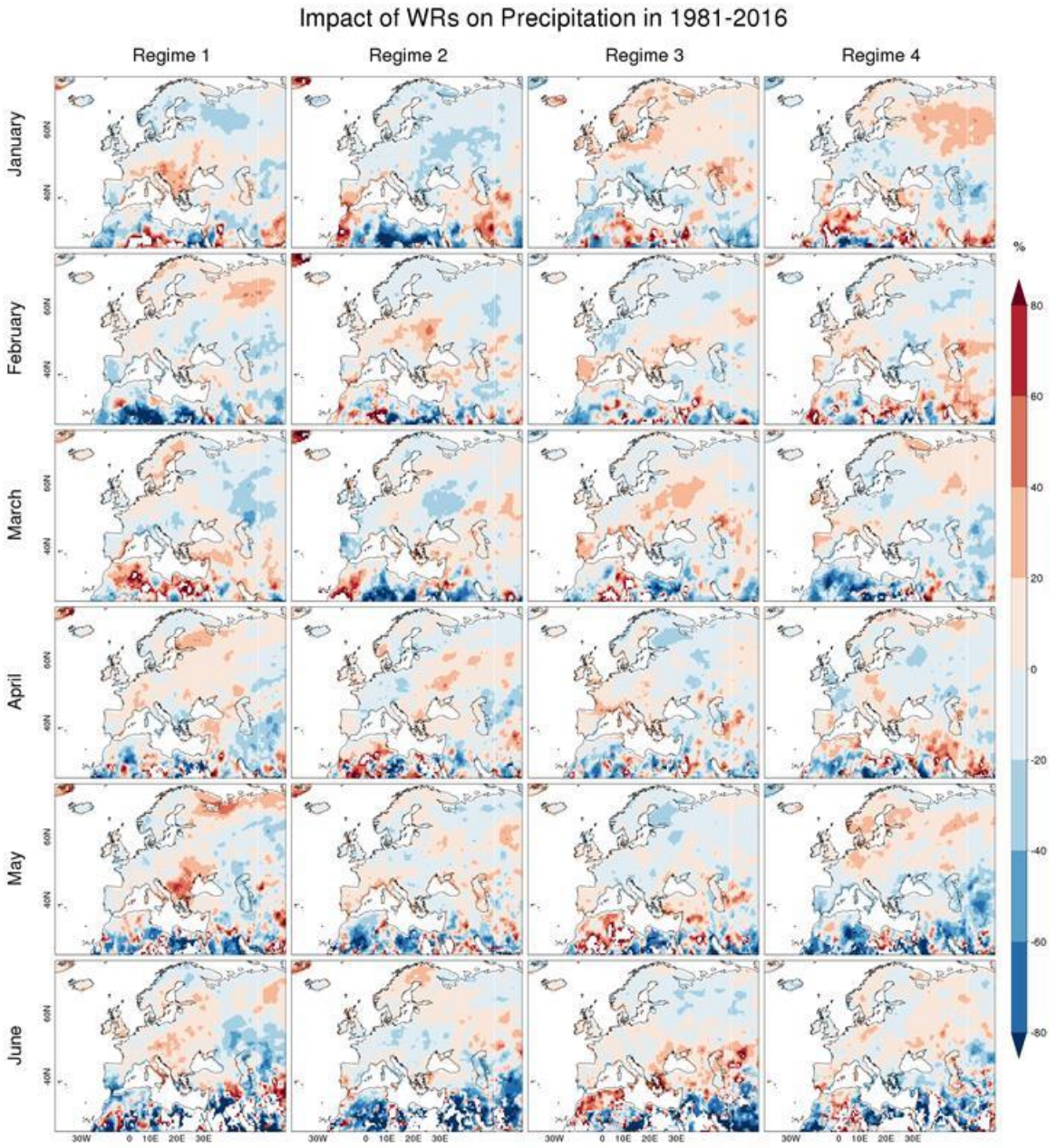

Figure 31: Impact of weather regimes (columns) derived from k-means on precipitation in the first 6 months (rows) in 1981-2016.

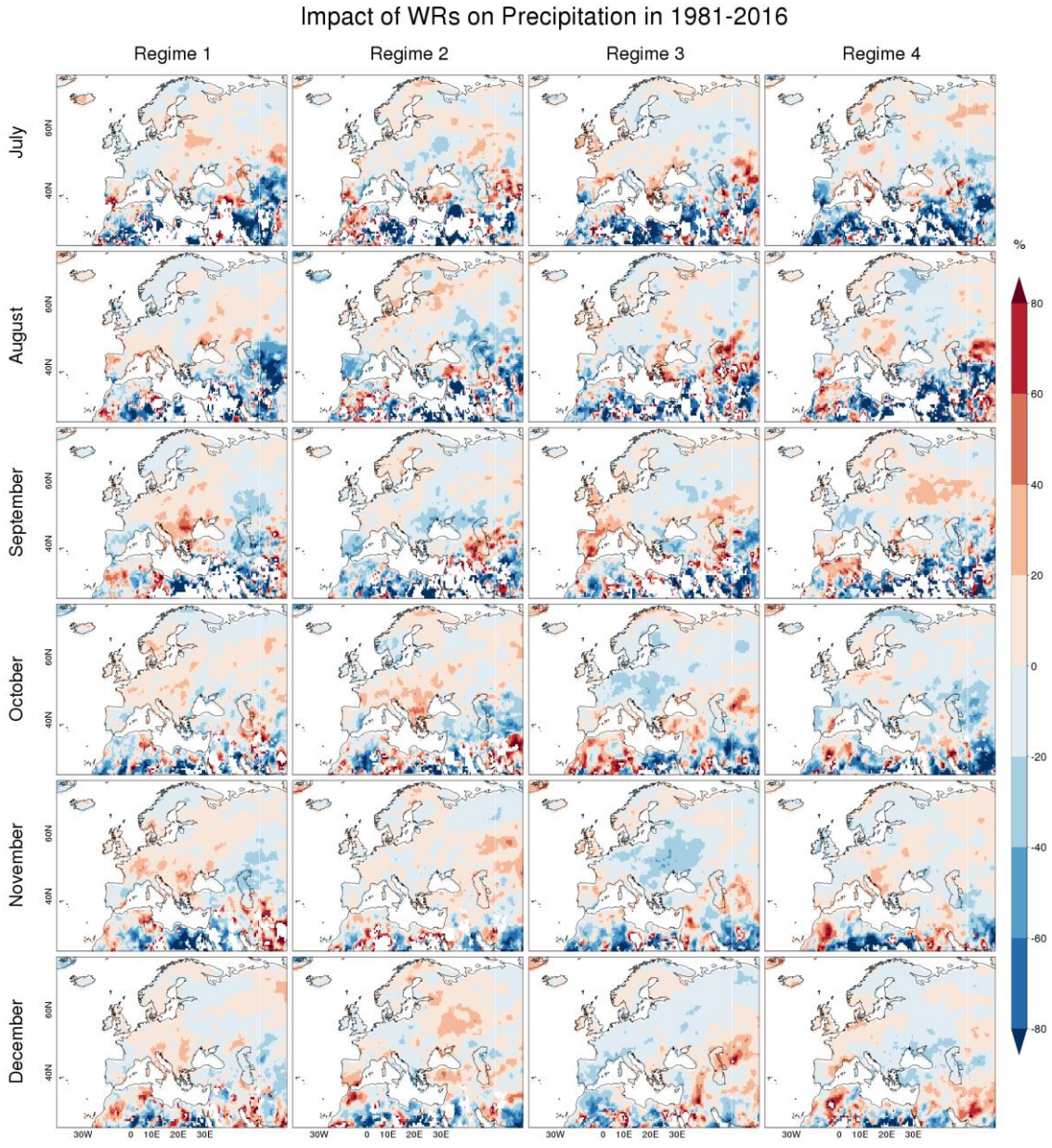

Figure 32: Impact of weather regimes (columns) derived from k-means on precipitation in the last 6 months (rows) in 1981-2016.

6.3 Inflows to hydropower reservoirs in the Ume River system

6.3.1 Impact of Euro-Atlantic Teleconnections

A simple correlation analysis identified NAO and SCAND as the two teleconnection patterns that typically have the greatest impact on streamflow in the Ume River. The former is having a positive correlation with inflow volumes and the latter a negative correlation. This is supported by work done by Foster et al. (2018) amongst others.

Table 2 summarises the results for all 12 sub-basins in the Ume River. For more detailed results the reader is referred to D.1 Impacts of modelled seasonal inflow volumes conditioned using teleconnections. These results show that modelled inflow volumes conditioned using teleconnection analysis tends to show skill over an approach that uses climatology (hereafter referred to as the reference). On average, modelled inflow volumes made using teleconnection index conditioned forcing data (CFD) outperform the reference 62% of the time. Furthermore, the mean absolute error skill scores (MAESS) suggest that the conditioned forcing data (CFD) shows skill at reducing error in inflow volumes too. The average MAESS is modest but positive for all initialisation months suggesting that the teleconnections have an impact on the inflow volumes for most of the sub-basins throughout the year..

The CFD approach tends to outperform the reference least often for simulations initialised early in the year and most often in the later months of the year. The largest improvements in the volume error appear to be achieved for forecasts initialised around the middle of the year. This implies that the teleconnection impact of NAO and SCA on inflow volumes is greatest then.

Table 2: Skill scores for seasonal inflow volumes made using forcing data conditioned using teleconnection analysis. The scores are calculated using synthetic inflow made with the current industry standard modelling approach as the reference. The lead-time indicates the number of months prior to the initialisation date analysed to condition the forcing data.

	Lead time	FY⁺	MAESS
Jan	7	50.0	0.005
Feb	8	55.6	0.007
Mar	8	55.6	0.010
Apr	4	55.6	0.014
May	6	61.1	0.054
Jun	1	61.1	0.048
Jul	6	55.6	0.030
Aug	7	61.1	0.013
Sep	7	61.1	0.012
Oct	3	72.2	0.060
Nov	5	83.3	0.017
Dec	4	72.2	0.010
Avg.		**62.04**	**0.023**

6.3.2 Impact of hydrological weather regimes

The results shown in Table 3 are very similar to those presented in the previous sub-section. They are similar in both magnitudes and trends and such this section will concentrate on the differences with respect to those in section 6.3.1 rather than repeating what has already been presented. For more detailed results the reader is referred to D.2 Impacts of modelled seasonal inflow volumes conditioned using hydrological weather regimes. The most striking difference is that the modelled inflow volume made using the hydrological weather regime CFD tend to reduce the magnitude of the error more than the teleconnection CFD, however this is reversed with respect to the frequency with which the CFD outperform the reference. This suggests that with the hydrological weather regime CFD may have a greater impact on the inflows for specific sub-basins, especially those where the reference has larger errors, whilst the other approach is more of a generalist. Furthermore, the lead-times used for the conditioning tends to be shorter for the 2nd half year for the hydrological weather regime based approach. This suggests that this approach is more efficient at discriminating between different events, albeit marginally so.

Table 3: Skill scores for seasonal inflow volumes made using forcing data conditioned using the hydrological weather regimes. The scores are calculated using synthetic inflow made with the current industry standard modelling approach as the reference. The lead-time indicates the number of months prior to the initialisation date analysed to condition the forcing data.

	Lead time	FY^{+}	MAESS
Jan	8	50.0	0.007
Feb	8	55.6	0.009
Mar	8	55.6	0.011
Apr	3	55.6	0.033
May	2	61.1	0.054
Jun	3	55.6	0.073
Jul	5	55.6	0.018
Aug	4	55.6	0.037
Sep	3	61.1	0.080
Oct	1	66.7	0.003
Nov	1	77.8	0.018
Dec	4	77.8	0.015
Ave		**60.68**	**0.030**

7 Energy demand

7.1 Impact of climate variability

7.1.1 Electricity demand

Figure 33 shows the normalized demand anomalies present during each of the four weather regimes for January (as presented previously in section 3.2.1). For convenience, the MSLP patterns associated with the regimes are shown in Figure 33, as well as the 2m temperature and 10m surface wind speed anomalies.

During the positive NAO (NAO+), negative normalized demand anomalies up to one standard deviation of the mean are seen over Europe. This is consistent with anomalously high temperatures over the region caused by warm air being transported from the North Atlantic by prevailing westerly winds (Figure 33, first column). The lowest normalized demands are seen over regions with warmest temperatures (note that in January, a "warm" temperature does not lead to the need for air conditioning, just a reduction in the need for heating). In contrast, the negative NAO (NAO-) leads to positive demand anomalies of up to one standard deviation. This is associated with anomalously cold temperatures consistent with an increasing requirement for heating (Figure 33, second column).

The third regime, resembling Scandinavian blocking (Figure 33 third column), results in a dipole structure in the demand anomalies, with Northern Europe experiencing anomalously low normalized demand (with corresponding high temperatures) and Southern Europe experiencing anomalously high demand (consistent with anomalously cold temperatures). These temperature anomalies are consistent with the near-surface circulation associated with the area of high pressure, centred over southern Scandinavia.

The fourth regime for January is an area of low pressure to the west of Ireland analogous to the East Atlantic Pattern (Figure 33 fourth column). This also leads to a dipole structure with somewhat opposite impact to that seen in the Scandinavian blocking regime (in the sense of cold to the north, warm to the south). The temperature dipole is, however, slightly rotated towards a SW-NE axis and consequently, the clearest power system impact is in south-western Europe (France, Iberia) rather than eastern and northern Europe.

In summary, the January weather regimes are associated with normalized demand anomalies across the European domain (typically up to 0.5 to 1 standard deviation from the seasonal norm). The patterns of the demand anomalies are consistent with the regimes' imprint on surface air temperature. Though results are presented for January only, somewhat similar results are found for the entire extended winter period (November-March; see online Appendix). The normalized demand anomalies associated with of the weather-regimes from April-September are, in contrast, rather smaller (generally less than 0.5 standard deviation from the seasonal norm) suggesting that during these months the weather regimes provide less

information on demand conditions over Europe. Further details and examples for other months can be found in the ANNEX F: Influence of climate variability on energy demand.

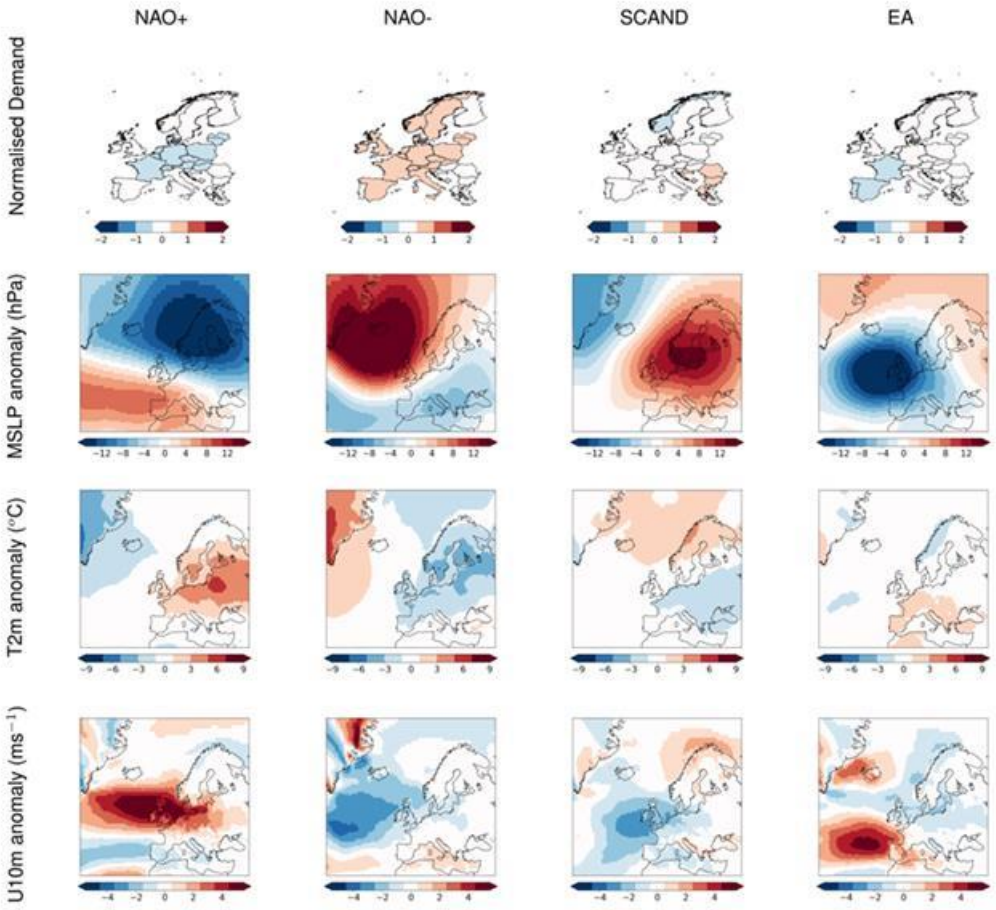

Figure 33: January normalized demand anomalies associated with each of the traditional weather regimes: The two phases of the North Atlantic Oscillation (NAO+, NAO-), Scandinavian Blocking (SCAND) and the East Atlantic Pattern (EA). MSLP, 2m temperature and 10m surface wind speed anomalies for each regime are also presented (expressed as composites of fields relative to the 1981-2016 mean).

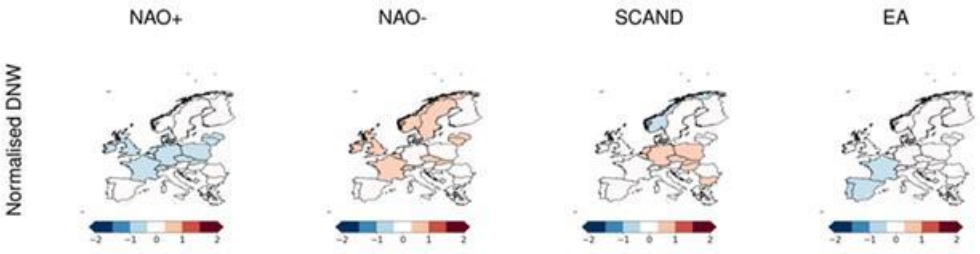

Figure 34: January normalized demand-net-wind anomalies for each of the traditional weather regimes: The two phases of the North Atlantic Oscillation (NAO+, NAO-), Scandinavian Blocking (SCAND) and the East Atlantic Pattern (EA).

7.1.2 Demand-net-wind

This section discusses the response of demand-net-wind (i.e. daily demand minus daily mean wind power generation) to the weather regimes for January (equivalent figures for other calendar months can be found in the online Appendix). In general, it is expected that a day of high demand-net-wind (DNW) will have a combination of anomalously high demand and anomalously low wind power generation: thus typically a mixture of low temperatures and low wind speeds.

Figure 34 shows the normalized demand-net-wind anomalies associated with the traditional weather regimes for January, and can be contrasted to the equivalent plots for normalized demand-only anomalies (top row of Figure 33). Some key differences emerge.

In the NAO+ state the warm temperatures correspond with area of average or above average wind speeds (both of which lead to low values of DNW). In this case, the pattern of demand (or demand-net-wind) impact is therefore relatively unchanged, though on closer inspection, the response becomes stronger over western/coastal Europe (where the wind anomalies are more marked).

Previously (for demand-only) the NAO- resulted in anomalously high normalized demand over almost the whole of Europe due to lower than normal temperatures (Figure 33, second column). For DNW, however, the NAO- is associated with anomalously high demand over a much smaller extent. This is due to some of the countries which are experiencing cold temperatures also experiencing near-average wind speeds, thereby limiting the "response" on DNW (e.g. Germany, Spain and Portugal). In this case, inclusion of wind power therefore mitigates against this weather-regime strongly influencing DNW in those countries.

In the Scandinavian blocking (SCAND), the pattern of change between the demand-only and DNW response is more marked. Central European countries (Germany, Netherlands, Romania; Figure 33 third column) that experienced very weak anomalies (<0.5 standard deviations) compared to the climatological norm) experience more strongly positive DNW anomalies (> 0.5 standard deviations). The slightly cooler-than-average conditions (which one might expect to slightly increase January demand) are therefore exacerbated by low wind speeds, leading to a stronger DNW footprint.

The introduction of wind power generation into the power system therefore leads to a change in the power system response to a given weather regime, where the magnitude of this change is influenced by the amount of wind power capacity which is installed. The growth of this impact with increasing installed capacity is illustrated in Figure 35 where the correlation between 2m temperature and DNW, and 10m wind speed and DNW is shown for a selection of European power systems across a range of scenarios with 0-50GW of installed wind power capacity. The response is not uniform across countries, but generally there is typically a level of installed wind power capacity at which the wind speed becomes more important than temperature for understanding system operation (see Bloomfield et al., 2018 for further discussion).

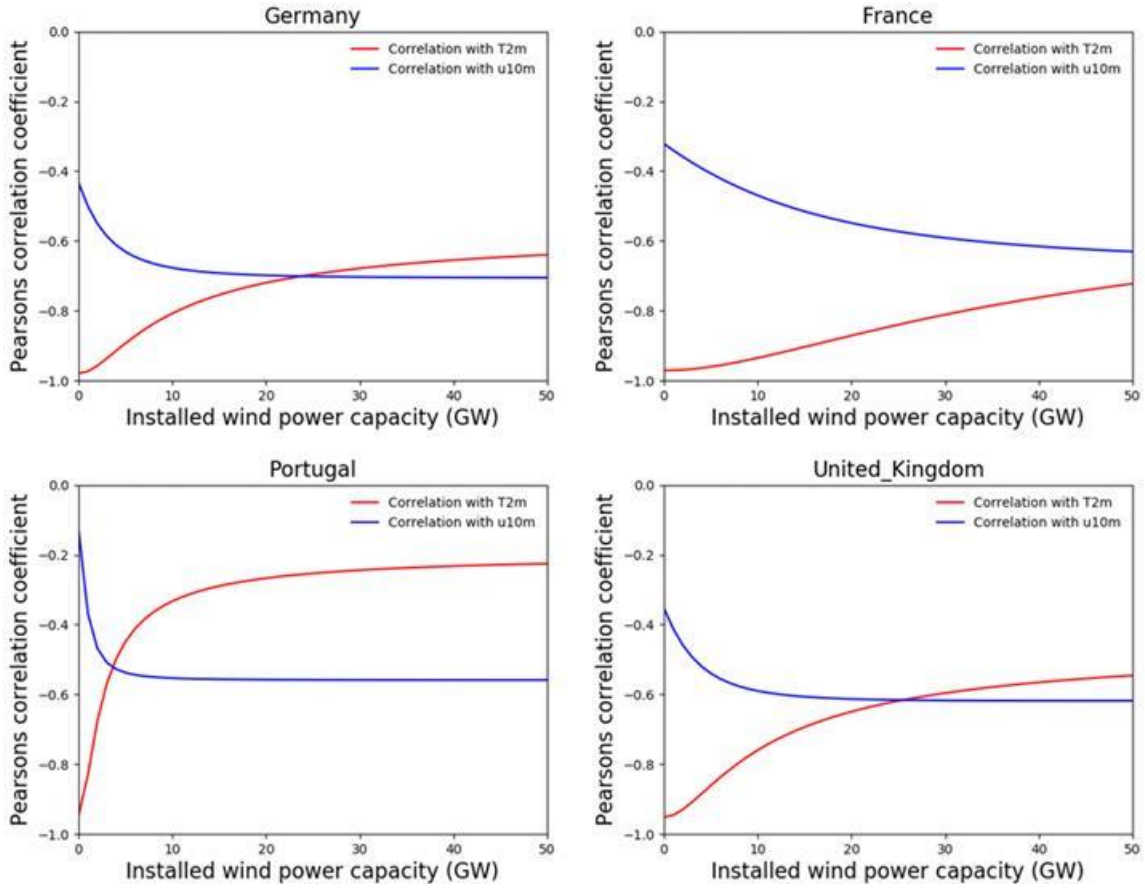

Figure 35: The correlation between daily 2m temperature and demand-net-wind (red) and 10m wind speed and country aggregate demand-net-wind (blue) for a selection of case study countries.

7.2 Impact of impact regimes

7.2.1 Electricity demand

The impact regimes for the normalized demand anomalies in January are shown in Figure 36, along with the associated MSLP, 2m temperature and 10m wind speed composites. As expected, the meteorological composites are, in gross terms, similar to the traditional weather regimes (Figure 33 and Figure 34) but there are important differences. Each of the four impact regimes is therefore discussed in turn in terms of its similarities and differences with respect to the weather regimes.

Regime A from Figure 36 (closest to the NAO+ weather regime) results in strong low normalized demand anomalies over central and South-East Europe (Figure 36). These are comparable in magnitude to those seen in the NAO+ weather regime (Figure 33; up to ~1 standard deviations) but over a larger area. This is consistent with the impact regime having a more widespread temperature impact than the corresponding weather regime, associated with

a much weaker pressure gradient anomaly across central Europe in the weather-impact regime, as well as smaller increases in wind speed over a larger number of countries.

Regime B has some similarities to both the NAO+ and Scandinavian blocking weather regimes, though in neither case is there a direct equivalent (compare Figure 36 column 2 to Figure 33 columns 1 and 3). In this impact regime, significantly stronger positive normalized demand anomalies are seen over central Europe than those associated with any individual weather regime. This is consistent with a very strong temperature anomaly over the whole of continental Europe, leading to very low anomalous normalized demands.

Regime C also has similarities to the NAO+ and Scandinavian blocking weather regimes in terms of the MSLP pattern but, again, neither of the weather regimes is directly equivalent to the impact regime. A dipole structure of normalized demand anomalies is seen in this regime with centers over Norway and Greece, but generally *opposite in sign* compared to the SCAND weather regime (compare Figure 33 SCAND with Figure 36 Regime C), despite some apparent similarities in the MSLP pattern. Anomalously high pressure over Scandinavia and anomalously low pressure over the Mediterranean are associated with anomalously cold temperatures over Scandinavia (therefore increased demand) and anomalously warm temperatures over Greece (therefore reduced demand).

The MSLP pattern associated with regime D (Figure 36, column 4) superficially resembles the Scandinavian blocking pattern weather regime (see Figure 33, column 3), and has somewhat similar associated impacts (anomalously colder temperatures, therefore anomalously higher normalized demand to north and vice-versa). The extent of the normalized demand anomalies is, however, different between the two regimes: the impact regimes demand signal covers a broader area than that from the weather regime.

This analysis demonstrates that although the weather regimes are associated with impacts on the demand for power, a similarly constructed set of regimes based directly on the demand itself can provide significantly more information and therefore potentially explanatory power. It is particularly notable that in some cases, superficially similar MSLP anomaly patterns can lead to quite different regional demand responses. Moreover, the fourth weather-regime from January (low pressure to the West of Ireland, associate with the East-Atlantic pattern) does not feature at all in the corresponding set of impact regimes - suggesting it has perhaps minimal relevance for forecasting European demand – whereas a new pattern (regime C) emerges. Further details and examples for other months can be found in the G.1: Normalized demand anomalies.

.

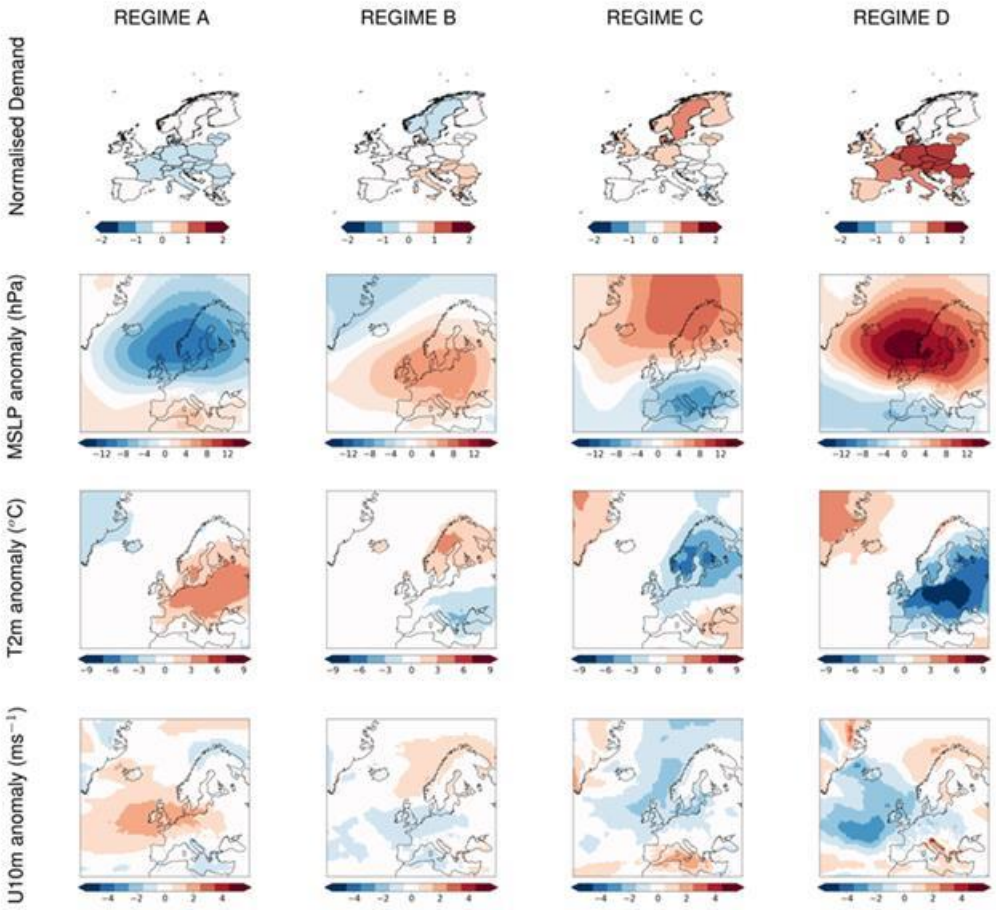

Figure 36: Impact regimes constructed from January normalized daily demand anomalies (see text for details). Corresponding anomaly composites of meteorological fields relative to the climatological mean (1981-2016) for MSLP, 2m temperature, 10m surface wind speed are given below the relevant regime.

7.2.2 Demand-net-wind

The impact regimes calculated from normalized demand-net-wind (DNW) anomalies for January are shown in Figure 37. These regimes are contrasted to the impact regimes generated from normalized demand-only anomalies to show how current day wind power generation has influenced the weather sensitivity of the European power system. The resulting impact regimes have been subjectively re-ordered to best match the impact regimes from Figure 36.

The MSLP composite associated with DNW regime A (Figure 37) is similar in structure to demand impact regime A (Figure 36) though the pressure anomaly is generally stronger for DNW. The normalized demand-net-wind anomalies are stronger in some countries (up to 1.5 standard deviations, particularly Germany, Poland) than for normalized demand-only, though weaker in others (e.g., Italy). This is due to the dependence of normalized DNW on both wind speeds and temperatures. Comparing Figure 36 and Figure 37 we see that the first DNW regime

has anomalously high wind speeds in a band over Great Britain and into Europe. These exacerbate the anomalously high temperatures in producing low demand-net-wind conditions.

DNW impact regime B has similarities to the demand impact regime B in terms of the MSLP composites (compare Figure 37 vs Figure 36). The normalized DNW anomaly pattern is, however, somewhat different. Anomalously high demand-net-wind is still seen over central Europe (due to anomalously low temperatures and anomalously low wind speeds), though the strength of the anomaly is weaker than for the demand-only regime. The presence of average-to-high wind speeds in some areas of Scandinavia and Southern Europe in the DNW regime, however, compensates for the lower temperatures and therefore these areas no longer exhibit strong DNW anomalies. In general, it is also possible to see a change in emphasis between the relative 'strength' of temperature vs wind anomalies between the two regime sets: as expected, the demand-only focuses exclusively on temperature whereas wind is emphasizes in the demand-net-wind regimes – thus subtlety different meteorological conditions occur.

The results for DNW impact regimes C and D have similarities to the demand impact regimes C and D. For regime C, the main difference is the introduction of negative normalized DNW anomalies over Southern Europe, consistent with to the high wind speeds over this region, leading to anomalously low normalized DNW.

In summary, the patterns associated with the normalized DNW impact regimes (Figure 37) are generally consistent with the normalized demand-only impact regimes (Figure 36) but with important subtle differences between the associated meteorological patterns and their surface impacts (temperature, wind, demand, wind-power), particularly for the first three regimes (A, B and C). These changes are consistent with the DNW-impact regimes becoming sensitive to a mixture of temperatures and wind speeds rather than temperatures alone.

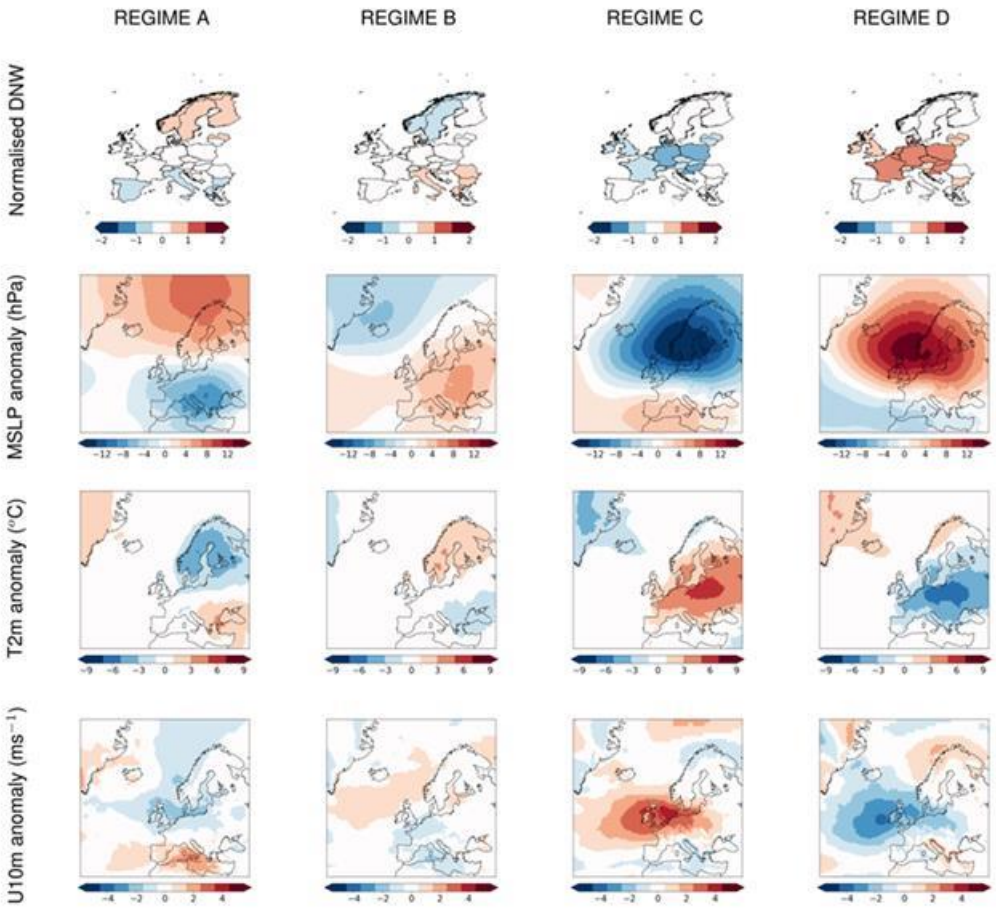

Figure 37: Impact regimes constructed from January normalized daily demand-net-wind anomalies (see text for details). Corresponding anomaly composites of meteorological fields relative to the climatological mean (1981-2016) for MSLP, 2m temperature, 10m surface wind speed are given below the relevant regime.

8 Conclusions

A methodology to compute Euro-Atlantic teleconnection patterns and indices has been developed and applied to ERA-interim 500 hPa geopotential heights for the 1981 to 2016 period. The monthly Euro-Atlantic Teleconnections patterns and indices have been compared to the well-known CPC teleconnections, and only minor differences have been found. The main advantage of this methodology is that it can be employed to compute seasonal and sub-seasonal forecasts of those indices from ensemble prediction systems.

Two methodologies have been also developed to compute weather regimes and classify the atmospheric general circulation for different focusing studies: 1) weather regimes for energy generation over the Europe and 2) hydrological weather regimes for snow-driven hydropower production in Sweden. With these methods some of the obtained clusters or regimes are similar to the main Euro-Atlantic teleconnections, e.g., NAO, EA, EA/WR, SCAND, although other patterns are also obtained.

The impact of EATc/WRs on energy sectors exhibits strong inter-annual variations. Notable patches of significant correlation with energy indictors can be found for the NAO, EA, EAWR, and SCAND in almost all the months, but influencing areas differ from month to month as well as the specific EATc/WRs. For wind generation the spatial distribution of the impacts is similar from one month to the next but it follows an annual cycle, varying from a maximum of intensity during winter months (i.e., Dec-Mar of EATc and Sept-Mar of WRs) and a minimum during summer months. The spatial distribution of the leading atmospheric variability mode on capacity factor looks very similar to their impact on surface wind speed. For solar generation the SSRD is found to be highly correlated with the leading atmospheric variability mode in almost all the months with a predominant effect of NAO in winter, EA/WR in winter and spring, SCAND and EA in summer. Teleconnection-associated spatial pattern of correlation of solar radiation is always opposite to the pattern of correlation of precipitation. This indicates that the teleconnections impact the solar radiation (and PV CF) mainly by controlling the storm track position and the associated cloud cover. For all the months and indices, the patterns of correlation of CF PV are identical to the pattern of correlation of solar radiation, with temperature having almost no effect. For hydropower generation both of the teleconnection indices and hydrological weather regimes have been shown to impact the inflow volumes to hydropower reservoirs year round and could provide support to improve hydrological streamflow forecasting. The teleconnections exhibit a stronger impact by increasing performance in the second half year, while the weather regimes do so in the first half year. In all cases, it is important to notice that not only NAO is important to represent variability at the European scale, but also EA, SCAND and EA/WR can have important contributions in the energy sector atmospheric impacts.

It is important to point out that teleconnections and weather regimes complement each other quite well, e.g., their influence on wind speed and hydrological streamflow forecasting. This is a useful feature as there are some areas where teleconnections have no impact, while weather

regimes show a high impact (and vice versa). Thus, in these cases at least one of the two atmospheric analyses (teleconnections or weather regimes) can be employed to characterize part of the climate variability.

In addition to the weather regimes a novel "impact-oriented" impact regimes framework has been developed. In gross terms, the regimes calculated from country-aggregate impact data are able to reproduce features consistent with the traditional weather regimes. However, the impact regimes have much stronger connections to the surface impacts of interest (demand, DNW etc.) than the pure weather regimes. The subtle differences can mainly be associated with shifts in the location and strength of MSLP gradients, which are associated in changes in surface temperature (therefore demand) and wind speed (therefore wind power generation) over European countries. The impact regimes are dependent on the structure of the European power system, therefore the growth in renewable energy has (and will continue to) change the structure of the impact regimes to which the European power systems is most sensitive to.

This method has highlighted that the impact regimes produce a stronger "impact-signature" than the pure weather regimes (suggesting that weather-days within a particular weather regime may have very different outcomes for European energy compared to the contrasting impact regime). Also, this method has highlighted that not all weather regimes are likely to be equally useful in forecasting the energy-system impact of weather. For example, the East Atlantic pattern does not resemble any of the weather-impact regimes calculated for January; conversely a "new" weather pattern of interest emerges from the impact-regime analysis.

It should be recognised that there is likely to be a trade-off in terms of predictability between impact regimes and weather regimes. One would, in general, expect the latter to be more readily predictable by numerical weather tools simply insofar as the patterns correspond to the natural weather evolution in some sense (whereas this link is less direct for the impact regimes). In contrast, however, the impact regimes clearly offer greater explanatory power (in terms of power system impact) if the occurrence of the weather pattern associated with the impact regime can be adequately forecast. Further work will therefore investigate whether this methodology does offer an increased ability to predict power system properties (demand, DNW etc.) as opposed to using the traditional weather regimes.

Bibliography

Barnston, A. G., & Livezey, R. E. (1987). Classification, seasonality and persistence of low-frequency atmospheric circulation patterns. Monthly weather review, 115(6), 1083-1126.

Bárdossy, A., Stehlík, J., & Caspary, H. (2002). Automated objective classification of daily circulation patterns for precipitation and temperature downscaling based on optimized fuzzy rules. Climate Research, 23:11–22.

Baur, F., Hess, P., & Nagel, H. (1944). Kalender der Grosswetterlagen europas 1881-1939. Bad Homburg, 35.

Berg, P., Donnelly, C., & Gustafsson, D. (2018). Near-real-time adjusted reanalysis forcing data for hydrology. Hydrol. Earth Syst. Sci., 22, 989-1000, https://doi.org/10.5194/hess-22-989-2018.

Bergström, S. (1995). The HBV model. In Singh, V.P. (ed.) *Computer Models of Watershed Hydrology*, Water Resources Publications, Littleton, Colorado, 443-476.

Bett, P. E., & Thornton, H. E. (2016). The climatological relationships between wind and solar energy supply in Britain. Renewable Energy, 87, 96-110.

Bloomfield, H. C., Brayshaw, D. J., Shaffrey, L. C., Coker, P. J., & Thornton, H. E. (2018). The changing sensitivity of power systems to meteorological drivers: a case study of Great Britain. Environmental Research Letters, 13(5), 054028

Brayshaw, D. J., Troccoli, A., Fordham, R., & Methven, J. (2011). The impact of large scale atmospheric circulation patterns on wind power generation and its potential predictability: A case study over the UK. Renewable Energy, 36(8), 2087-2096.

Brayshaw, D. J., Dent, C., & Zachary, S. (2012). Wind generation's contribution to supporting peak electricity demand–meteorological insights. Proceedings of the Institution of Mechanical Engineers, Part O: Journal of Risk and Reliability, 226(1), 44-50.

Chiacchio, M., and M. Wild, 2010: Influence of NAO and clouds on long-term seasonal variations of surface solar radiation in Europe. J. Geophys. Res., 115, D00D22, doi: 10.1029/ 2009JD012182.

Cradden, L. C., McDermott, F., Zubiate, L., Sweeney, C., & O'Malley, M. (2017). A 34-year simulation of wind generation potential for Ireland and the impact of large-scale atmospheric pressure patterns. Renewable energy, 106, 165-176.

Dee, D. P., Uppala, S. M., Simmons, A. J., Berrisford, P., Poli, P., Kobayashi, S., ... & Bechtold, P. (2011). The ERA-Interim reanalysis: Configuration and performance of the data assimilation system. Quarterly Journal of the royal meteorological society, 137(656), 553-597.

e-highway2050 2015: e-highway2050 (e-HW2050). Europe's future secure and sustainable electricity infrastructure, Final project report, available at: http://www.e-highway2050.eu/fileadmin/documents/e_ highway2050_booklet.pdf (last access: 25 February 2018), 2015.

Evans, D. L., & Florschuetz, L. W. (1977). Cost studies on terrestrial photovoltaic power systems with sunlight concentration. Solar Energy, 19(3), 255-262.

Foster, K., Bertacchi Uvo, C., & Olsson, J. (2018). The development and evaluation of a hydrological seasonal forecast system prototype for predicting spring flood volumes in Swedish rivers. Hydrol. Earth Syst. Sci., 22, 2953-2970, https://doi.org/10.5194/hess-22-2953-2018.

Grams, C. M., Beerli, R., Pfenninger, S., Staffell, I., & Wernli, H. (2017). Balancing Europe's wind-power output through spatial deployment informed by weather regimes. Nature climate change, 7(8), 557.

Gelaro, R., McCarty, W., Suárez, M. J., Todling, R., Molod, A., Takacs, L., ... & Wargan, K. (2017). The modern-era retrospective analysis for research and applications, version 2 (MERRA-2). Journal of Climate, 30(14), 5419-5454.

Hartigan, J., & Wong, M. (1979). Algorithm AS 136: A K-Means Clustering Algorithm. Journal of the Royal Statistical Society. Series C (Applied Statistics), 28(1), 100-108. doi:10.2307/2346830.

Herting et Jacobeit, 2014. Variability of weather regimes in the North Atlantic-European area: past and future Atmos. Sci. Let. 15: 314–320 (2014). doi: 10.1002/asl2.505.

Laloyaux, P., de Boisseson, E., Balmaseda, M., Bidlot, J.-R., Broennimann, S., Buizza, R., Dalhgren, P., Dee, D., Haimberger, L., Hersbach, H., Kosaka, Y., Martin, M., Poli, P., Rayner, N., Rustemeier, E. & Schepers, D. (2018). CERA-20C: A Coupled Reanalysis of the Twentieth Century. JAMES 10 (5), 1172-1195.

Lindström, G., Johansson, B., Persson, M, Gardelin, M. & Bergström, S. (1997). Development and test of the distributed HBV-96 hydrological model. Journal of Hydrology 201(1997) 272-288.

Lledó, Ll. (2017). CLIM4ENERGY technical note no.1: computing capacity factor. BSC-ESS Technical Memorandum 2017-001, 9 pp.

Mahlstein, I., Spirig, C., Liniger, M.A., & Appenzeller, C. (2015). Estimating daily climatologies for climate indices derived from climate model data and observations. J. Geophys. Res. Atmos., 120, 2808–2818. doi: 10.1002/2014JD022327.

Michelangeli, P. A., Vautard, R., & Legras, B. (1995). Weather regimes: Recurrence and quasi stationarity. Journal of the atmospheric sciences, 52(8), 1237-1256.

Plaut G, Simonnet E. 2001. Large-scale circulation classification, weather regimes, and local climate over France, the Alps and Western Europe. Climate Research 17: 303–324.

Poli, P., Hersbach, H., Tan, D., Dee, D., Thepaut, J.-N., Simmons, A., Peubey, C., Laloyaux, P., Komori, T., Berrisford, P., Dragani, R., Treemolet, Y., Holm, E., Bonavita, M., Isaksen, L., & Fisher, M. (2013). The data assimilation system and initial performance evaluation of the ECMWF pilot reanalysis of the 20thcentury assimilating surface observations only (ERA-20C). ECMWF ERA Report Series 14: Reading, UK.

Poli, P., Hersbach, H., Berrisford, P., Dee, D., Simmons, A. & Laloyaux, P. (2015). ERA-20C deterministic. ECMWF ERA Report Series 20: Reading, UK.

Pozo-Vazquez, D., J. Tovar-Pescador, S. R. Gamiz-Fortis, M. J. Esteban-Parra, and Y. Castro-Dıez, 2004: NAO and solar radiation variability in the European North Atlantic re- gion. Geophys. Res. Lett., 31, L05201, doi:10.1029/2003GL018502.

Pozo-Vazquez , F. J. Santos-Alamillos, V. Lara-Fanego, J. A. Ruiz-Arias, and J. Tovar-Pescador, 2011: The impact of the NAO on the solar and wind energy resources in the Mediterranean area. Ad- vances in Global Change Research: Hydrological, Socioeco- nomic and Ecological Impacts of the North Atlantic Oscillation in the Mediterranean Region, S. M. Vicente-Serrano and R. M. Trigo, Eds., Springer, 213–231

Russo, S., Sillmann, J., & Fischer, E. M. (2015). Top ten European heatwaves since 1950 and their occurrence in the coming decades. Environmental Research Letters 10(12), 124003.

Thornton, H. E., Scaife, A. A., Hoskins, B. J., & Brayshaw, D. J. (2017). The relationship between wind power, electricity demand and winter weather patterns in Great Britain. Environmental Research Letters, 12(6), 064017.

Trigo RM, Osborn TJ, Corte-Real JM (2002) The North Atlantic Oscillation influence on Europe: climate impacts and associated physical mechanisms. Clim Res 20:9–17

Weisheimer, A., Schaller, N., O'Reilly, C., MacLeod, D. A., & Palmer, T. N. (2017). Atmospheric seasonal forecasts of the twentieth century: multi-decadal variability in predictive skill of the winter North Atlantic Oscillation (NAO) and their potential value for extreme event attribution. QJ. RMetSoc, 143 (703), 917-923.

Yiou P, Nogaj M. 2004. Extreme climatic events and weather regimes over the North Atlantic: when and where? Geophysical Research Letters 31: L07202

Zadeh, L. (1965). Fuzzy sets. Information and control, 8:338–353.

Zubiate, L., McDermott, F., Sweeney, C., & O'Malley, M. (2017). Spatial variability in winter NAO–wind speed relationships in western Europe linked to concomitant states of the East Atlantic and Scandinavian patterns. Quarterly Journal of the Royal Meteorological Society, 143(702), 552-562.

ANNEX

ANNEX A: Energy models

A.1: Wind-power model

The BSC wind-power model takes 6 hourly ERA-interim 10m wind speeds and a power law is used to extrapolate the wind speeds to 100m of the form:

$$\frac{u_{100m}}{u_{10m}} = (\frac{100}{10})^{\alpha}$$

Equation 1

where α is 1/7. Once the wind speeds have been extrapolated they are passed through three different power curves in order to give 3 estimations of capacity factor (CF) at each grid box, where wind power capacity factor is just a normalization of the total generation dividing by the maximum generation that would be achieved if the turbine operated at full capacity all time:

$$CF = \frac{actual\ generation}{maximum\ possible\ generation}$$

Equation 2

This normalization enables a fair comparison between wind farms of different size (i.e. different installed capacity). It is important to stress that this CF estimates do not consider any kind of losses (electrical, curtailments, maintenance, etc) that any wind farm experiences.

This data can then be aggregated to the required (weekly/monthly/seasonal) timescale. The three power curves used in this study are chosen to represent three types of turbine (described in Table 4: Selected turbine models (source IEC-61400-1)) which would be built in different wind climates. Example power curves from the three turbines are given in Figure 2. The output of the grid-point wind power model is wind power potential for a set of three power curves.

Turbine Class	Annual-mean wind speed range	Turbine Name	Rotor Diameter (m)	Cut in speed (m/s)	Rated speed (m/s)	Cut out speed (m/s)
1	>10 m/s	Enercon E70 2.3MW	70	2.0	16.0	25.0
2	>8.5 m/s	Games G87 2.0 MW	87	4.0	16.0	25.0
3	>7.5 m/s	Vestas V110 2.0MW	110	3.0	11.5	20.0

Table 4: Selected turbine models (source IEC-61400-1)

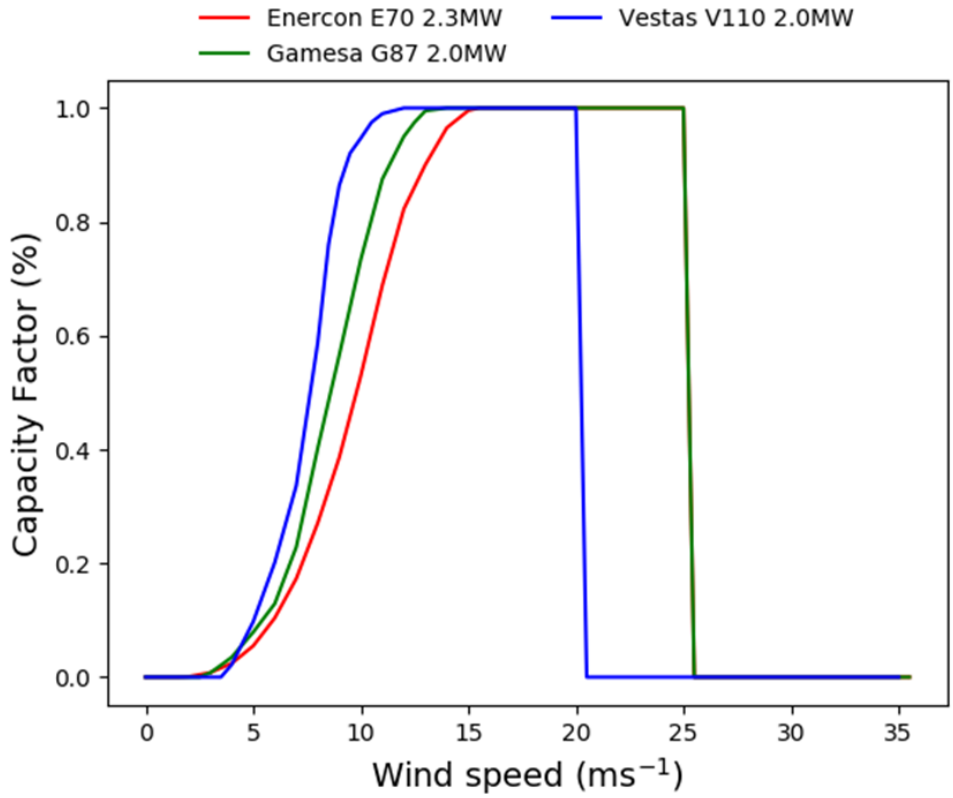

Figure 38: The three normalized power curves used in S2S4E

In order to calculate country-aggregate wind power generation, assumptions about the turbine classes installed to each grid box are made based on the long term (1980-2017) mean wind speed at each grid box for selecting the appropriate power curve (see Table 4). The resulting distribution of wind power CFs in Figure 39a is then weighted by the installed capacity in each grid box as a fraction of the national-total (see Figure 39b for an example for Germany), and summed over the country domain.

The final output is therefore a 6-hourly time series of country-aggregated wind power capacity factor. Country-aggregated wind power capacity factor has been created for the 28 countries which data is available for on the ENTSOe transparency platform. Figure 40 shows that the wind power models annual-mean capacity factor averaged over the 36 year period is comparable to the measured data from ENTSOe, and to other datasets (such as renewables.ninja; Staffell and Pfenninger, 2016) for a selection of European countries. It also shows that picking an "optimal turbine class" in each grid box gives better representation of country-average capacity factor than using a single type 1, 2 or 3 turbines for a whole country.

This has been created for the 28 countries which data is available for on the ENTSOe transparency platform. Figure 4 shows that the wind power models annual-mean capacity factor averaged over the 36 year period is comparable to the measured data from ENTSOe, and to other datasets (such as renewables.ninja; Staffell and Pfenninger, 2016) for a selection of European countries. It also shows that picking an "optimal turbine class" in each grid box

gives better representation of country-average capacity factor than using a single type 1, 2 or 3 turbines for a whole country.

The RMSE of the optimal turbine model (validated at daily timescales) is quite variable dependent on the country chosen (see Appendix 1). This is impacted heavily by the quality of the ENTSOe dataset. In countries such as France the installed capacity from 2016 is significantly below the output of the wind power generation time series (implying the capacity and generation data from ENTSO are not self-consistent). It is therefore likely that the discrepancies seen between the observed generation and modelled generation are due to these inconsistencies (e.g., the generation data corresponding to nationally metered generation connected to the high voltage transmission grid whereas the capacity data including an estimate of so-called "embedded" small scale generations connecting to the lower voltage distribution network).

The resulting daily country-aggregated generation estimates have an R^2 of ~0.9 in all countries (see Appendix 1) showing that it captures the weather-driven variability of the capacity factor well. With accurate information on the installed capacities in each country this model could therefore simulate country-aggregate wind power generation potential extremely well (note: this is formally an estimate of generation potential and network constraints leading to, e.g., wind power curtailment would require additional modelling components to estimate). This will be confirmed in future work for some case study countries of which accurate generation data and installed capacities are available from alternative sources.

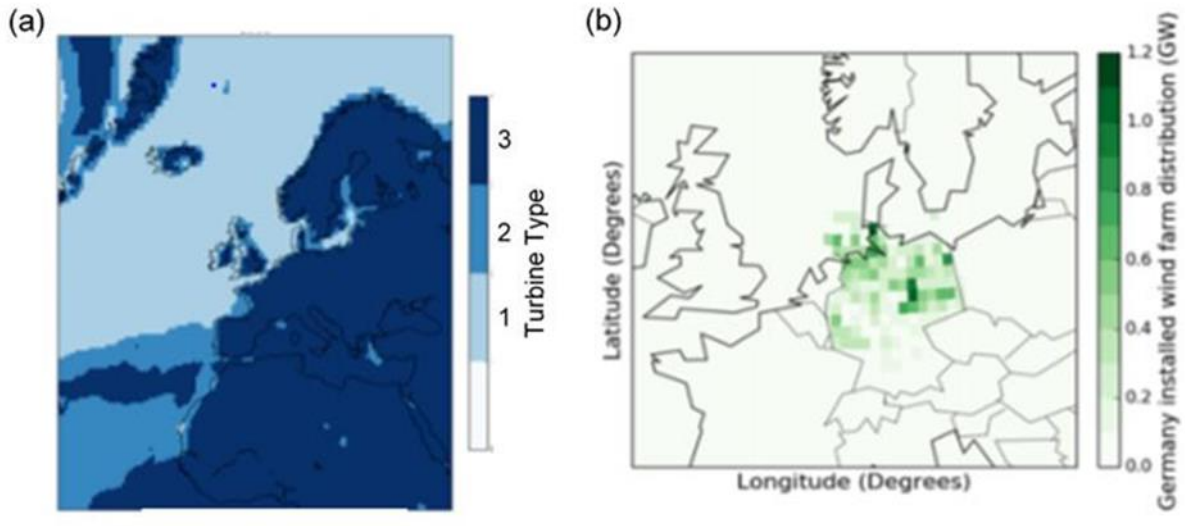

Figure 39: (a) optimal turbine classes allocated to each grid box based on the 1980-2017 mean 10m wind speed. (b) grid-box level distribution of installed wind power capacity in Germany, using data from thewindpower.ne

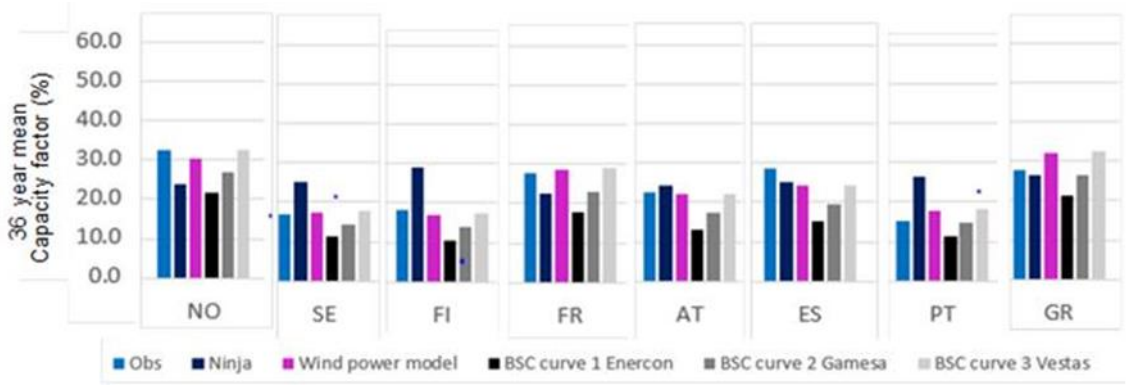

Figure 40: Validation of the country-aggregate annual-mean wind power capacity factors averaged over the 36 year period for a selection of European countries. Modelled data from this project (pink) compared to renewables.ninja (Staffell and Pfenninger 2016; dark blue) and recorded power system data (source https://transparency.entsoe.eu; light blue). Also shown are the corresponding values for the three individual power curves corresponding to the three turbine classes (grey).

The RMSE of the optimal turbine model (validated at daily timescales) is quite variable dependent on the country chosen (not shown here). This is impacted heavily by the quality of the ENTSOe dataset. In countries such as France the installed capacity from 2016 is significantly below the output of the wind power generation time series (implying the capacity and generation data from ENTSO are not self-consistent). It is therefore likely that the discrepancies seen between the observed generation and modelled generation are due to these inconsistencies (e.g., the generation data corresponding to nationally metered generation connected to the high voltage transmission grid whereas the capacity data including an estimate of so-called "embedded" small scale generations connecting to the lower voltage distribution network).

The resulting daily country-aggregated generation estimates have an R^2 of ~0.9 in all countries (see Appendix 1) showing that it captures the weather-driven variability of the capacity factor well. With accurate information on the installed capacities in each country this model could therefore simulate country-aggregate wind power generation potential extremely well (note: this is formally an estimate of generation potential and network constraints leading to, e.g., wind power curtailment would require additional modelling components to estimate). This will be confirmed in future work for some case study countries of which accurate generation data and installed capacities are available from alternative sources

A.2: Solar-power model

The solar power model calculates capacity factor in each reanalysis grid box at each time step from the equation:

$$CF = \frac{Power}{Power_{STC}} = \eta_{rel}(G,T)\frac{G}{G_{STC}}$$

Equation 3

Where G is the incoming surface solar radiation and T is the grid box 2m temperature. STC stands for standard test conditions (T=25 °C, G = 1000Wm^{-2}) and η_{rel} is the relative efficiency of the panel. The equation for this is given as:

$$\eta_{rel}(G,T) = \eta_r[\,1 - \beta_r(T_c - T_r\,)]$$

Equation 4

Where η_r is the photovoltaic cell efficiency evaluated at the reference temperature (T_r) and β_r is the fractional decrease of cell efficiency per unit temperature increase. T_c is the cell temperature (i.e. the grid box temperature).

This model is designed for the calculated of solar power yield at a specific site, rather than over a large grid-box area as is present in a reanalysis (~ 100km x 100 km) and Evans and Florschuetz, 1975 suggest a value of η_r based on detailed panel-level observations. This however yields very low capacity factors when using reanalysis and evaluating against the ENTSOe data. These changes are potentially consistent with marked improvements in solar panel technology over the last 40 years. Therefore, instead of using their value, a new estimate of η_r at standard test conditions is derived. To do so, a more complex empirical relationship for η_r is first considered, as shown in Figure 41 and used by Bett and Thornton (2016). In this case, η_r varies with irradiance and temperature but the change in η_r is modest for irradiances in excess of 100 Wm^{-2} (~0.85 to ~0.92 at 25 °C). This complex η_r dependency is therefore simplified to an average value (averaged over irradiances 0-1000Wm^{-2}) at the standard test conditions temperature (25°C, see Figure 5). η_r is thus set to a constant value of 0.90 and β_r to 0.00042K^{-1}.

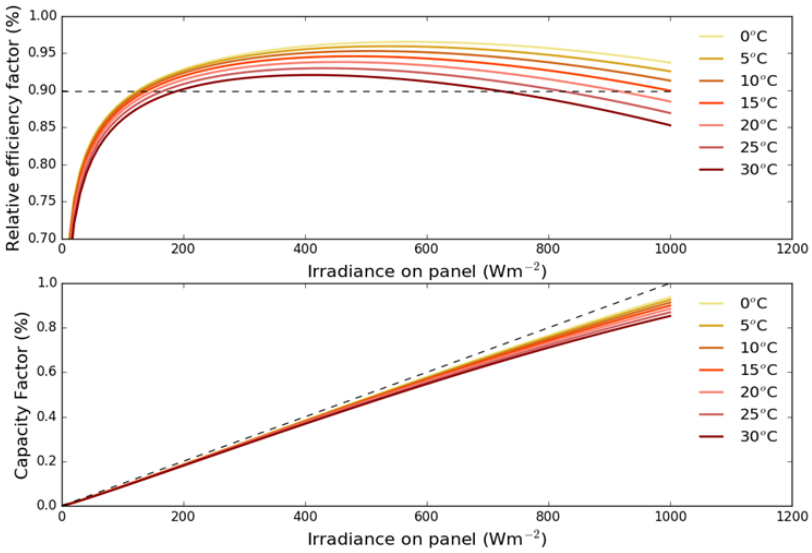

Figure 41: (top) the relationship between the irradiance incident on a solar panel and the efficiency of a panel at multiple temperatures (note: 25°C is considered to be standard test conditions in the present context). (bottom) The relationship between

irradiance on a panel and solar power capacity factor for a range of temperatures. Based on Bett and Thornton, (2016).

The long-term average capacity factors of country-aggregated solar power capacity factor produced by the model perform well compared to measured data from ENTSOe, renewables.ninja and the model from Bett and Thornton (2016) (see Figure 42). At the daily level, all countries have an R^2 of ~0.9 (see Appendix 1), showing that the model is capturing the overall behaviour of the country-level solar power generation well. A similar problem to the wind power model is, however, found when trying to validate the solar power model. For countries in which we have accurate data for the installed capacity of solar power and the time series of generation the absolute values produced by the model validates well (e.g. Austria and France). However, when the recorded installed capacity does not agree well with the observed generation time-series (both taken from ENTSOe's transparency portal), although the model correlates well (R^2 ~ 0.9 as discussed above) with recoded ENTSOe data, the absolute values contain biases and consequently a larger RMSE is found (e.g. Germany and Italy; see Appendix 1). This highlights the importance of maintaining accurate metadata and records if they are to be used in climate services projects.

Figure 42: Example validation of the country-aggregate annual-mean solar power capacity factors averaged over the 36 year period from the UREAD model (pink) compared to renewables Ninja (Staffell and Pfenninger, 2016; dark blue) and measured data (source https://transparency.entsoe.eu; blue) and the model from Bett and Thornton (2016; grey).

A.3: Hydrological model

The inflows to the 12 reservoirs are modelled using the rainfall-runoff model HBV. It is a semi-distributed conceptual rainfall-runoff model which includes numerical descriptions of hydrological processes at basin scale. It was originally developed at SMHI in the early 1970s (Bergström, 1995) to assist hydropower operations and it is still the hydrological model of choice for the industry in Sweden. The model has also proved itself to be a useful for work related to dam safety, water supply, flood warnings and climate change studies (SMHI. 2014).

Applications of the HBV model have been reported from more than 40 countries around the world (SMHI, 2016). The general water balance in the HBV-96 model can be expressed as:

$$P-E-Q=d/dt\ (SP+SM+UZ+LZ+LV)$$

Equation 5

where,

P = precipitation	E = evapotranspiration
Q = runoff	SP = snow pack
SM = soil moisture	UZ = upper groundwater zone
LZ =lower groundwater zone	LV = lake volume

The model is normally forced with daily observations of precipitation and temperature and monthly estimates of potential evapotranspiration. The model consists of subroutines for meteorological interpolation, snow accumulation and melt, evapotranspiration estimation, soil moisture accounting procedure, routines for runoff generation and finally, a simple routing procedure between sub-basins and in lakes. Basins with considerable elevation ranges can be subdivision into elevation zones which, if needed, divided into different vegetation zones (e.g., forested and non-forested areas). These subdivisions are made for the snow and soil moisture routines only. The model structure of HBV-96, with the most important characteristics, is presented schematically in Figure 43. For a more comprehensive model description readers are referred to Lindström et al. (1997).

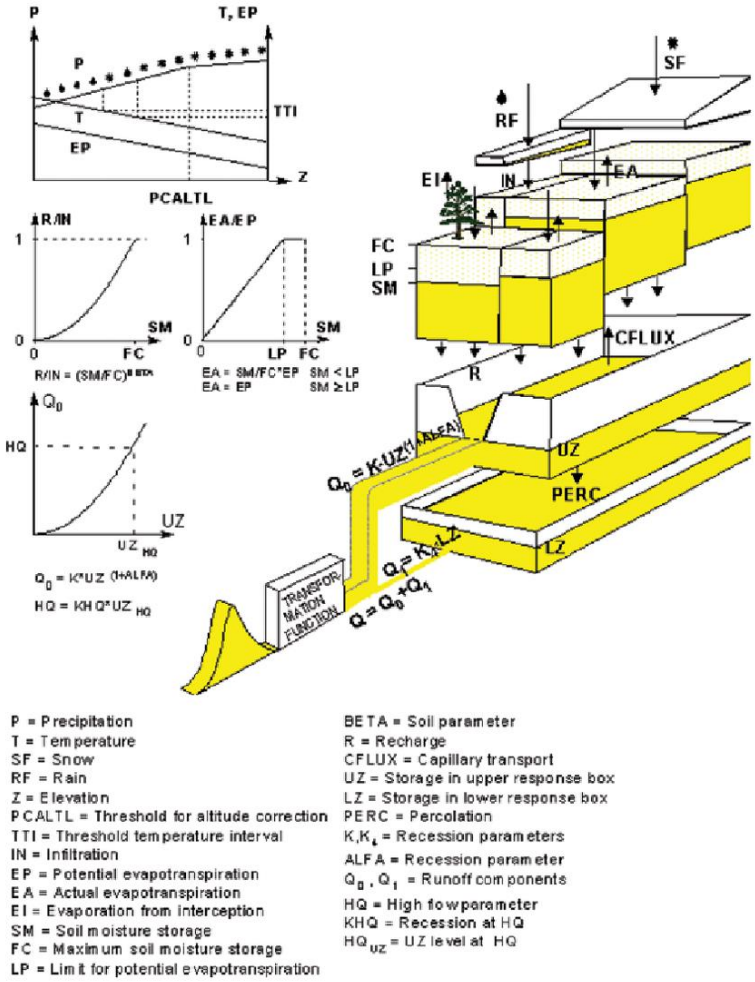

Figure 43. Schematic presentation of the HBV-96 model for a single basin (Lindström et al., 1997).

A.4: Demand model

The daily-mean demand is estimated using a multiple linear regression model of the form:

$$\boldsymbol{Demand(t)} = \boldsymbol{\alpha_1 LTT(t)} + \sum_{i=2}^{7} \boldsymbol{\alpha_i Weekday(t)} + \sum_{i=8}^{9} \boldsymbol{\alpha_i Weekend(t)} + \boldsymbol{HD(t) + CD(t)}$$

Equation 6

is created both weather-dependent (blue) and non-weather dependent (black) terms. Here t is the daily time step (where t=0 represents 1st January year 0000AD). The LTT term allows for the representation of long-term trends. These may be due to energy efficiency improvements, changes in GDP or changes in embedded renewable generation. The Weekday and Weekend terms are a series of five dummy variables which are 1 when it is the relevant day of the week. The heating degree (HD) and cooling degree (CD) terms represent the demand for either heating or cooling needs respectively for each country. These are time series of the form:

$$If\ T(t) \leq 15 : HD[t] = 15.5 - T(t)$$
$$If\ T > 15.5 : HD[t] = 0$$

$$If\ T(t) \geq 22: CD[t] = T(t) - 22$$
$$If\ T < 22: CD[t] = 0$$

In these Equations 15.5 degrees and 22 degrees are thresholds used by the European Environment Agency for heating degree day and cooling degree day assessment (https://www.eea.europa.eu/data-and-maps/indicators/heating-degree-days) and are also used by working group 3 of the IPCC report (IPCC 2014a, IPCC 2014b). T is the country average, daily-mean temperature from the MERRA2 reanalysis. This is calculated as an average over all reanalysis grid boxes within a country (using shapefiles downloaded from https://www.naturalearthdata.com/downloads/).

ANNEX B: Influence of climate variability on monthly wind power generation

B.1: Impact of EATc on wind speed and capacity factors

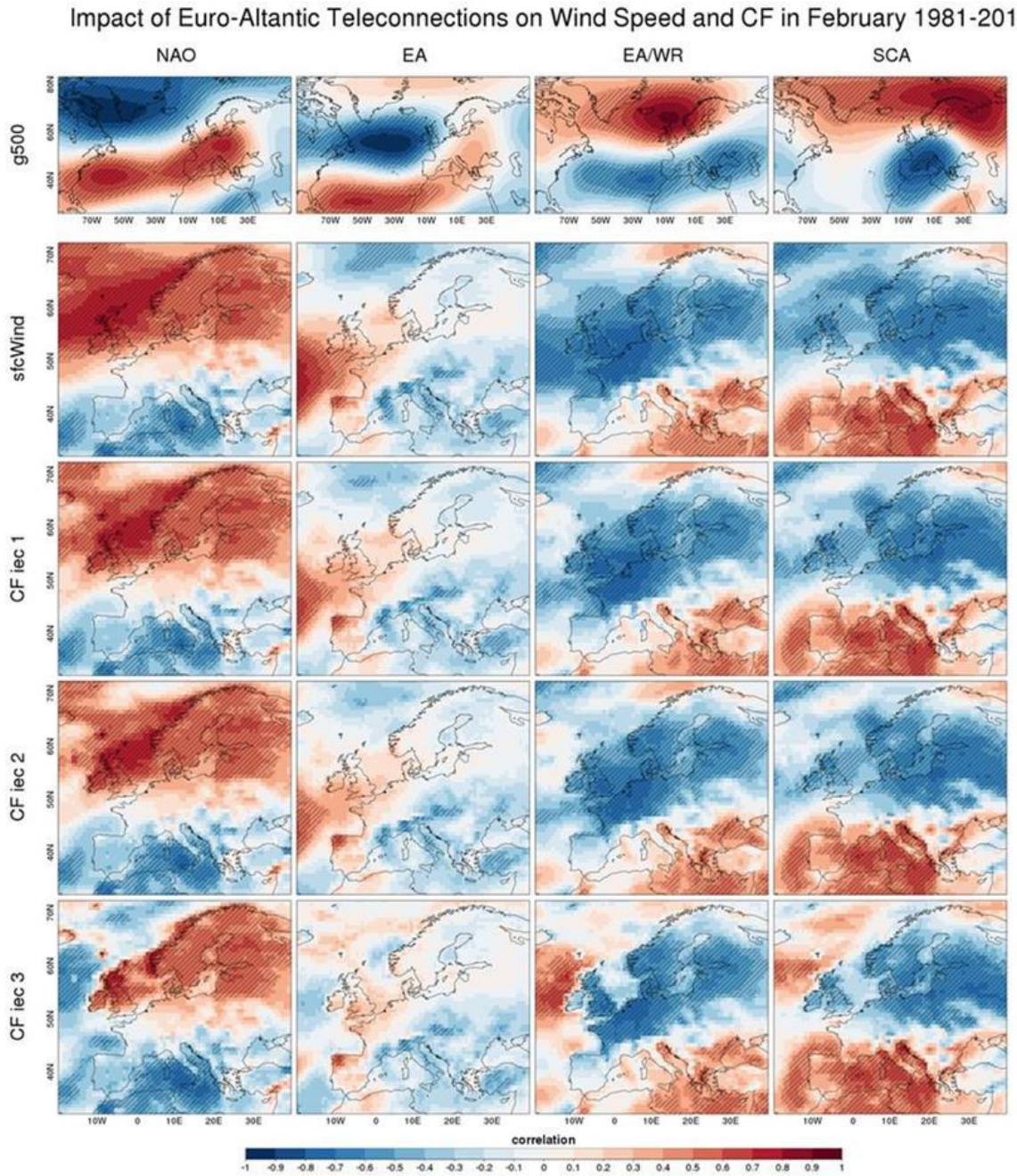

Figure 44: Impact of February teleconnection indices on wind speed and wind power generation. Each image shows the correlation between the four Euro-Atlantic Teleconnection indices (columns) and 500 hPa geopotential height (g500), surface wind speed (sfcWind) and the three capacity factor indicators. Hatches indicate statistical significance at 99% confidence level.

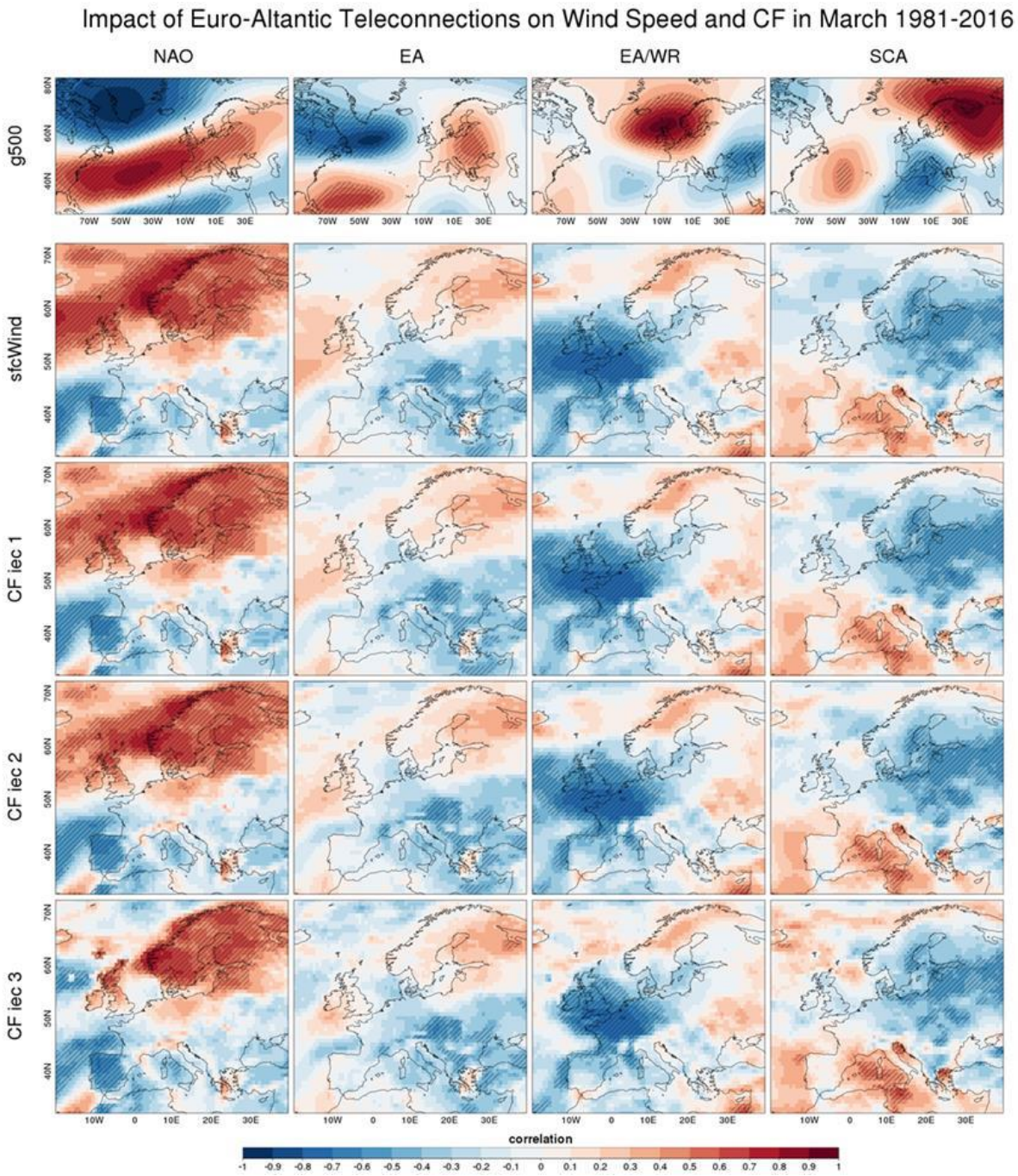

Figure 45: Impact of March teleconnection indices on wind speed and wind power generation. Each image shows the correlation between the four Euro-Atlantic Teleconnection indices (columns) and 500 hPa geopotential height (g500), surface wind speed (sfcWind) and the three capacity factor indicators. Hatches indicate statistical significance at 99% confidence level.

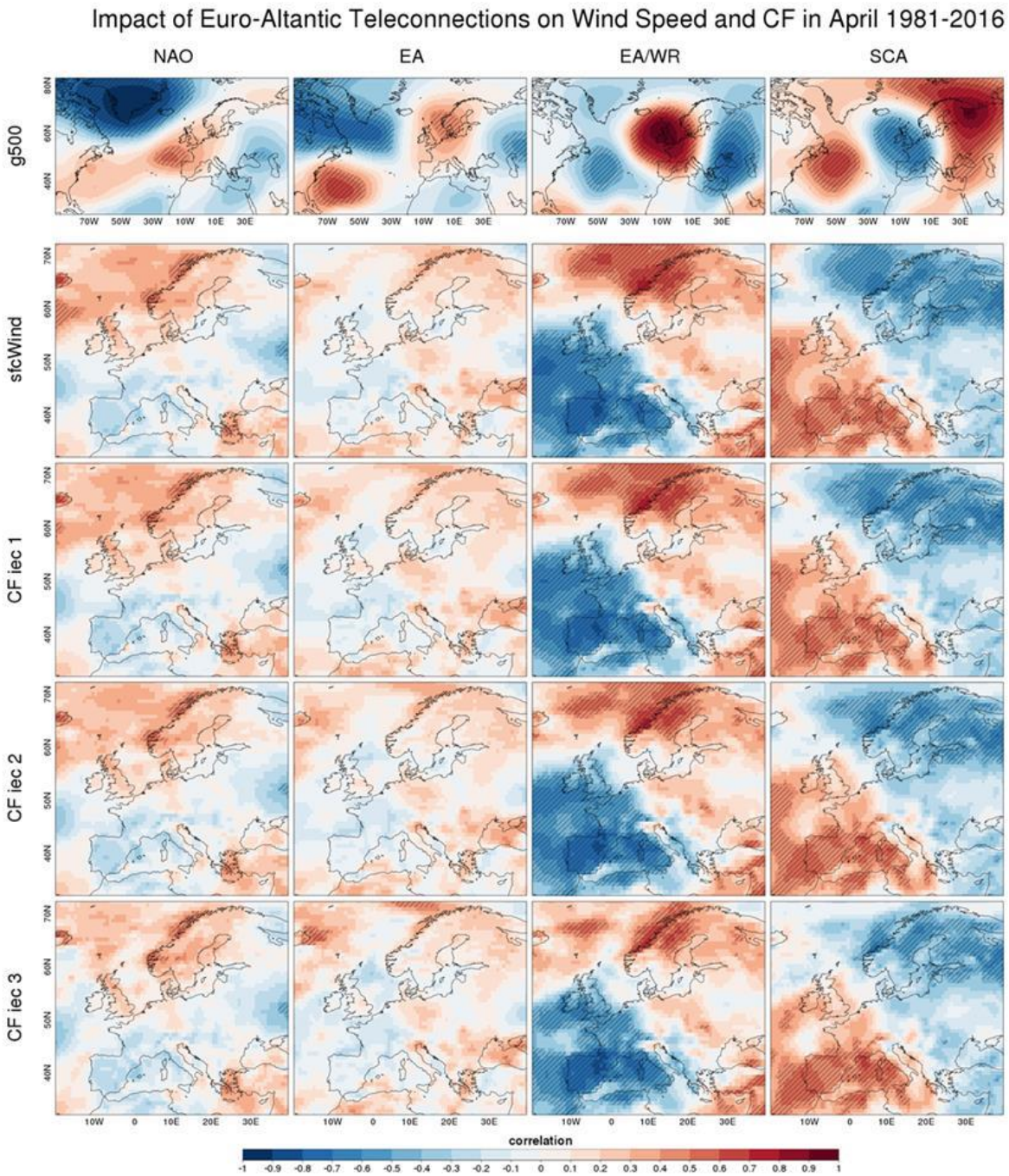

Figure 46: Impact of April teleconnection indices on wind speed and wind power generation. Each image shows the correlation between the four Euro-Atlantic Teleconnection indices (columns) and 500 hPa geopotential height (g500), surface wind speed (sfcWind) and the three capacity factor indicators. Hatches indicate statistical significance at 99% confidence level.

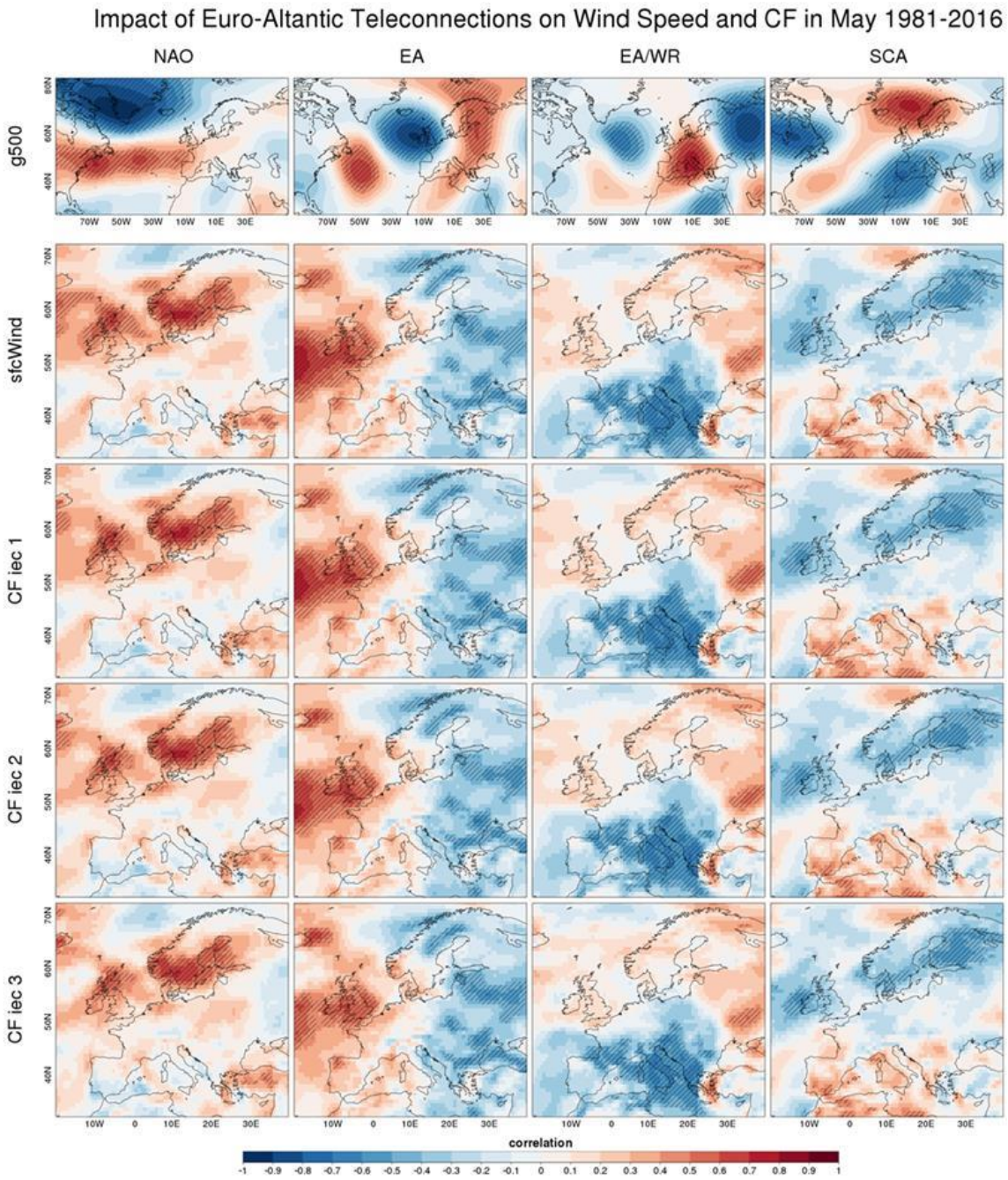

Figure 47: Impact of May teleconnection indices on wind speed and wind power generation. Each image shows the correlation between the four Euro-Atlantic Teleconnection indices (columns) and 500 hPa geopotential height (g500), surface wind speed (sfcWind) and the three capacity factor indicators. Hatches indicate statistical significance at 99% confidence level.

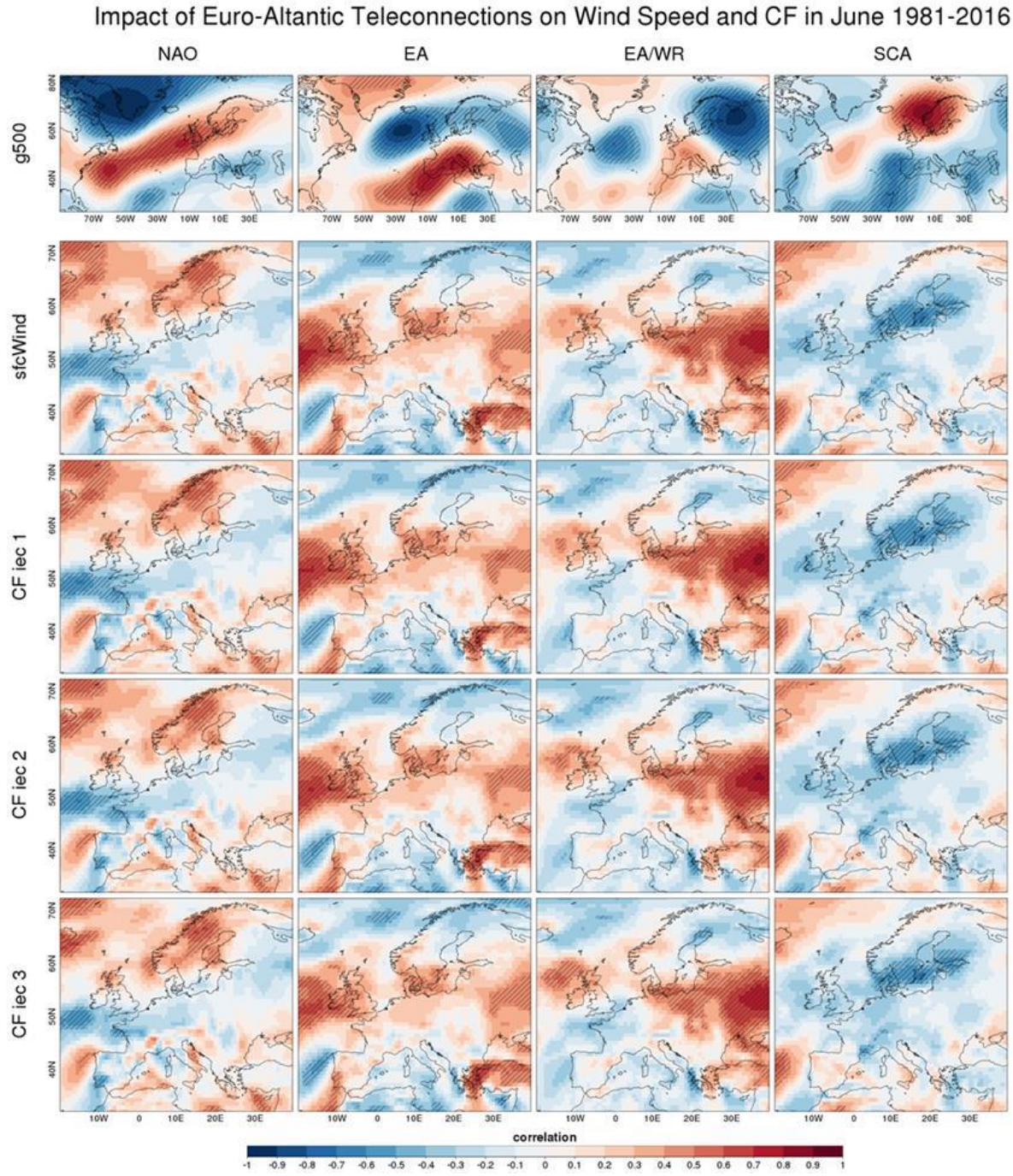

Figure 48: Impact of June teleconnection indices on wind speed and wind power generation. Each image shows the correlation between the four Euro-Atlantic Teleconnection indices (columns) and 500 hPa geopotential height (g500), surface wind speed (sfcWind) and the three capacity factor indicators. Hatches indicate statistical significance at 99% confidence level.

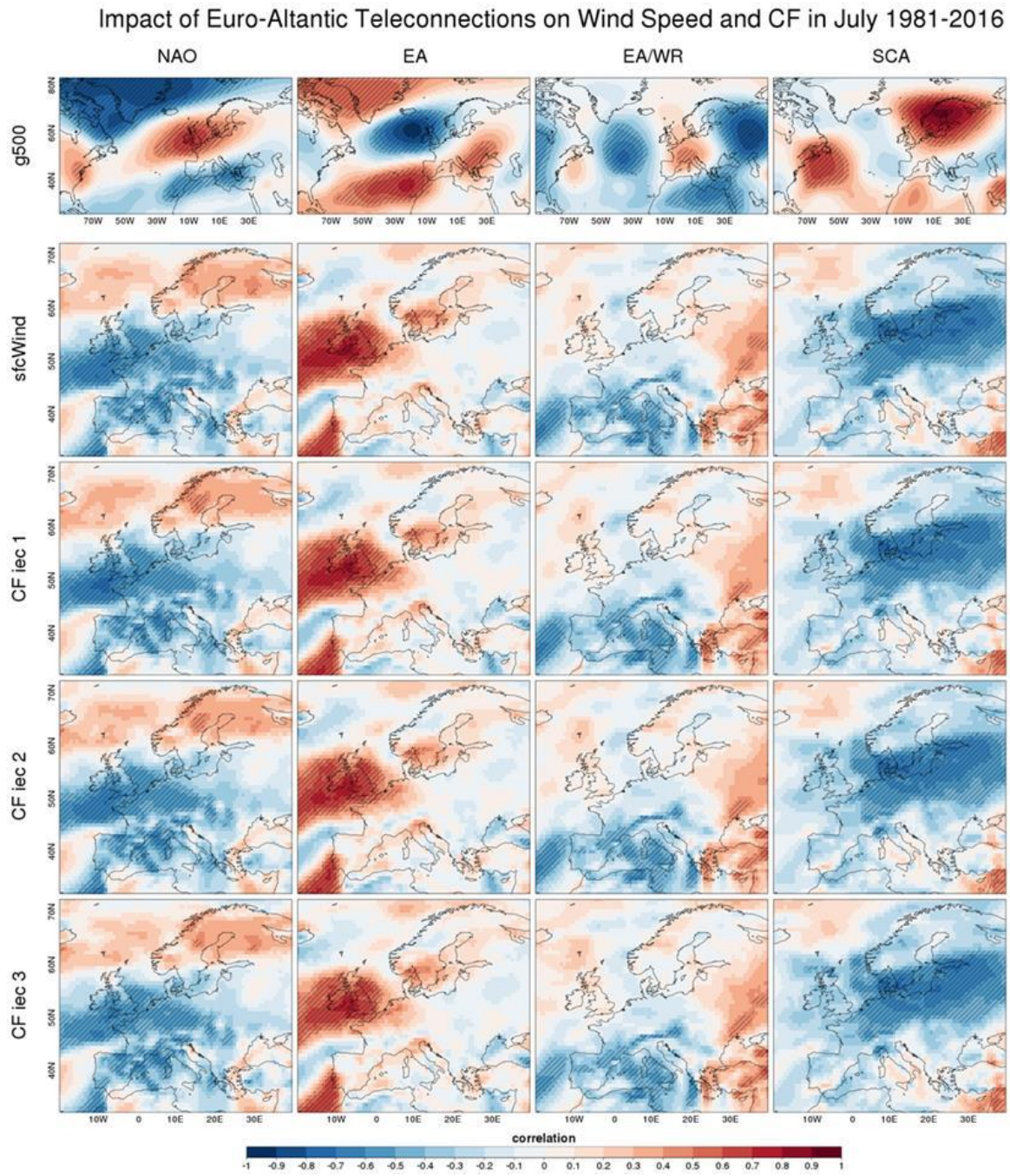

Figure 49: Impact of July teleconnection indices on wind speed and wind power generation. Each image shows the correlation between the four Euro-Atlantic Teleconnection indices (columns) and 500 hPa geopotential height (g500), surface wind speed (sfcWind) and the three capacity factor indicators. Hatches indicate statistical significance at 99% confidence level.

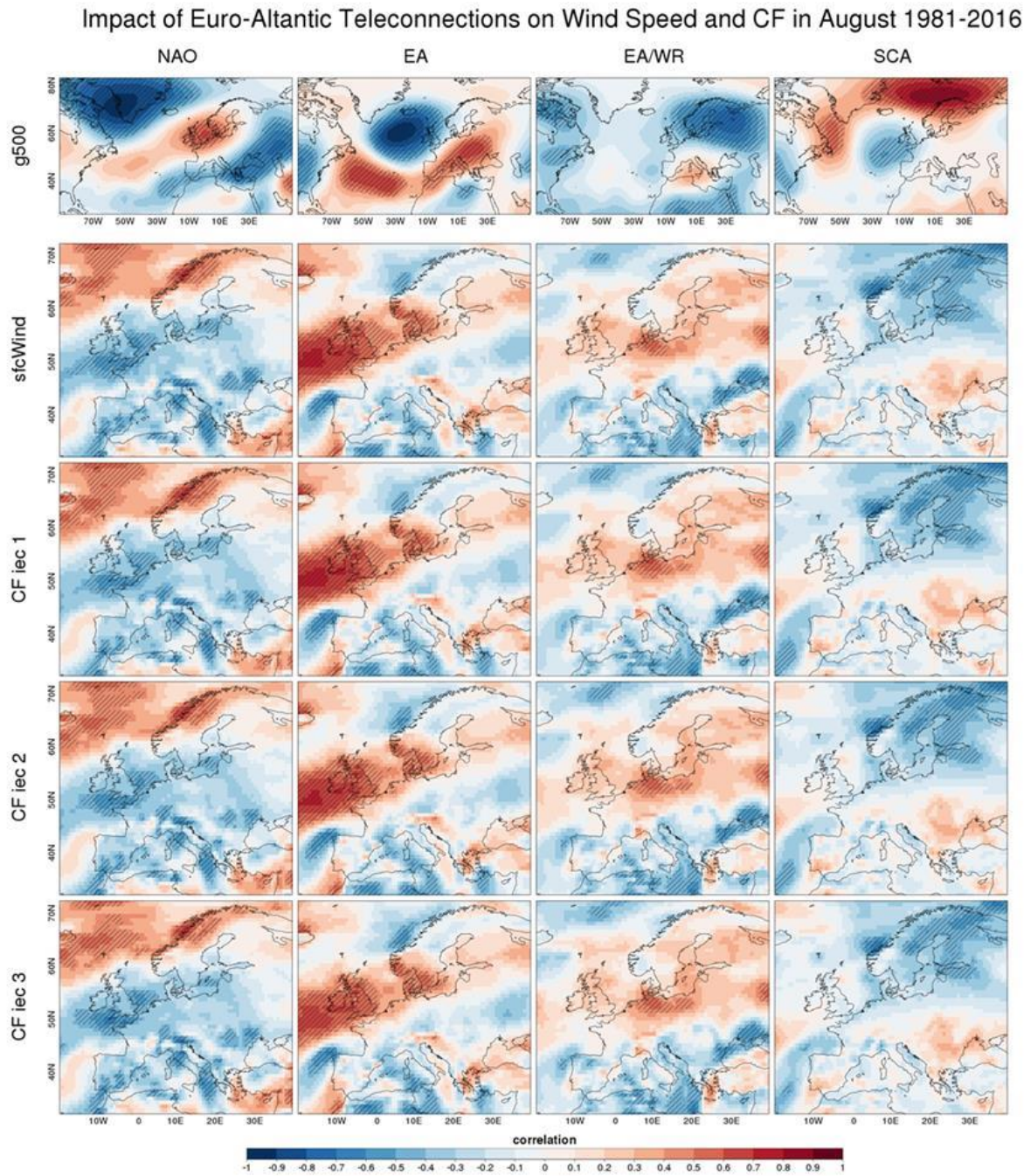

Figure 50: Impact of August teleconnection indices on wind speed and wind power generation. Each image shows the correlation between the four Euro-Atlantic Teleconnection indices (columns) and 500 hPa geopotential height (g500), surface wind speed (sfcWind) and the three capacity factor indicators. Hatches indicate statistical significance at 99% confidence level.

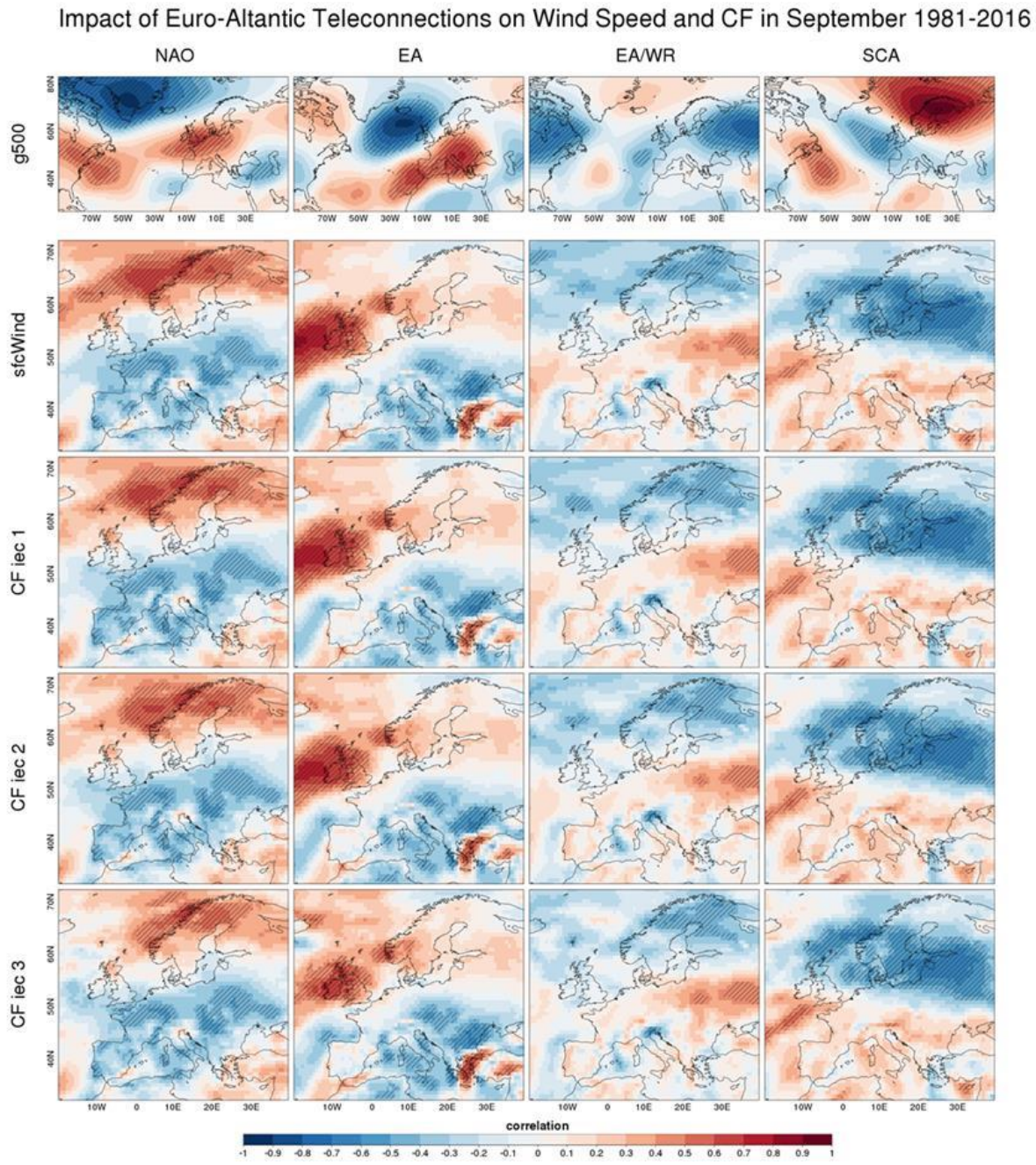

Figure 51: Impact of September teleconnection indices on wind speed and wind power generation. Each image shows the correlation between the four Euro-Atlantic Teleconnection indices (columns) and 500 hPa geopotential height (g500), surface wind speed (sfcWind) and the three capacity factor indicators. Hatches indicate statistical significance at 99% confidence level.

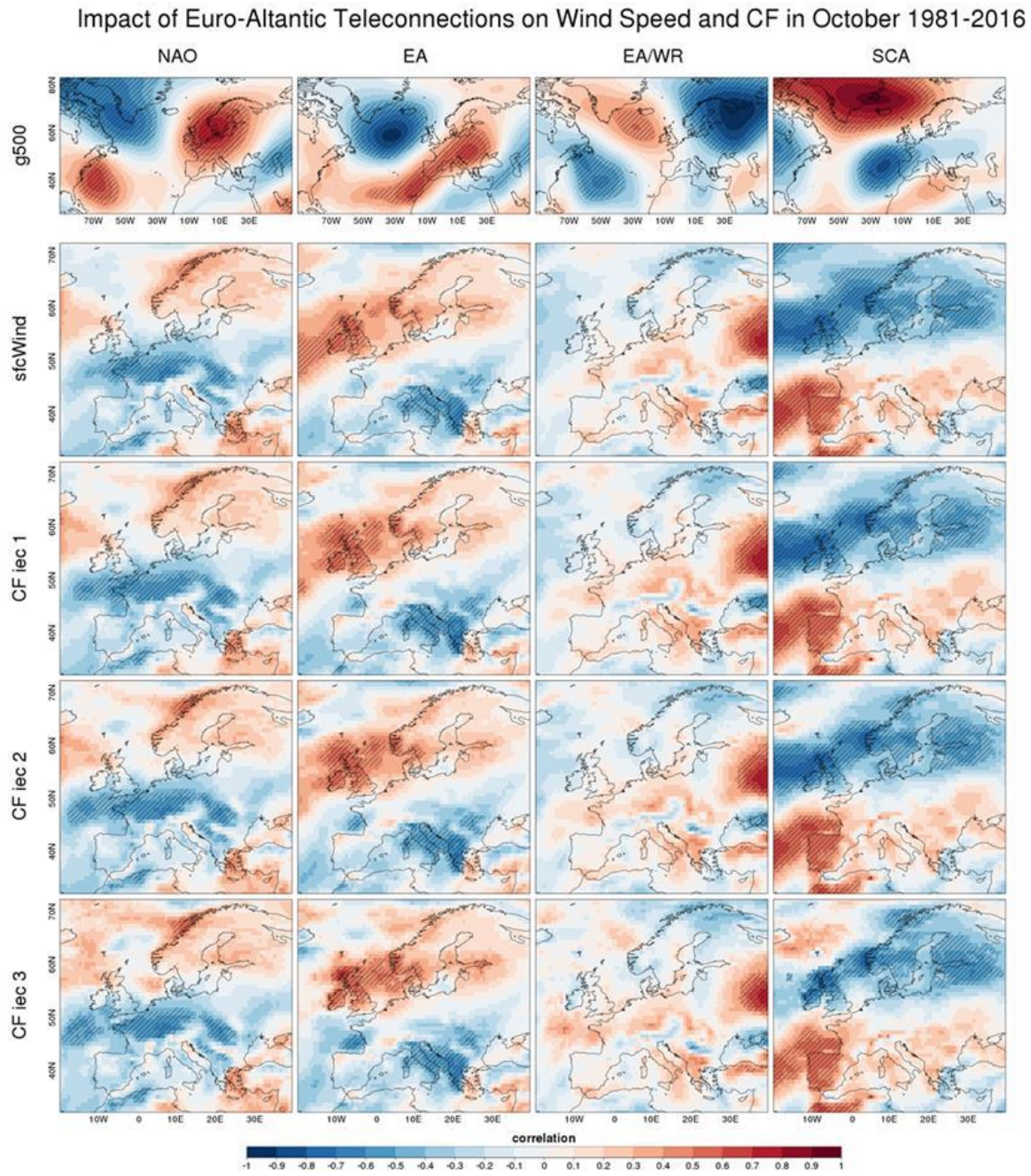

Figure 52: Impact of October teleconnection indices on wind speed and wind power generation. Each image shows the correlation between the four Euro-Atlantic Teleconnection indices (columns) and 500 hPa geopotential height (g500), surface wind speed (sfcWind) and the three capacity factor indicators. Hatches indicate statistical significance at 99% confidence level.

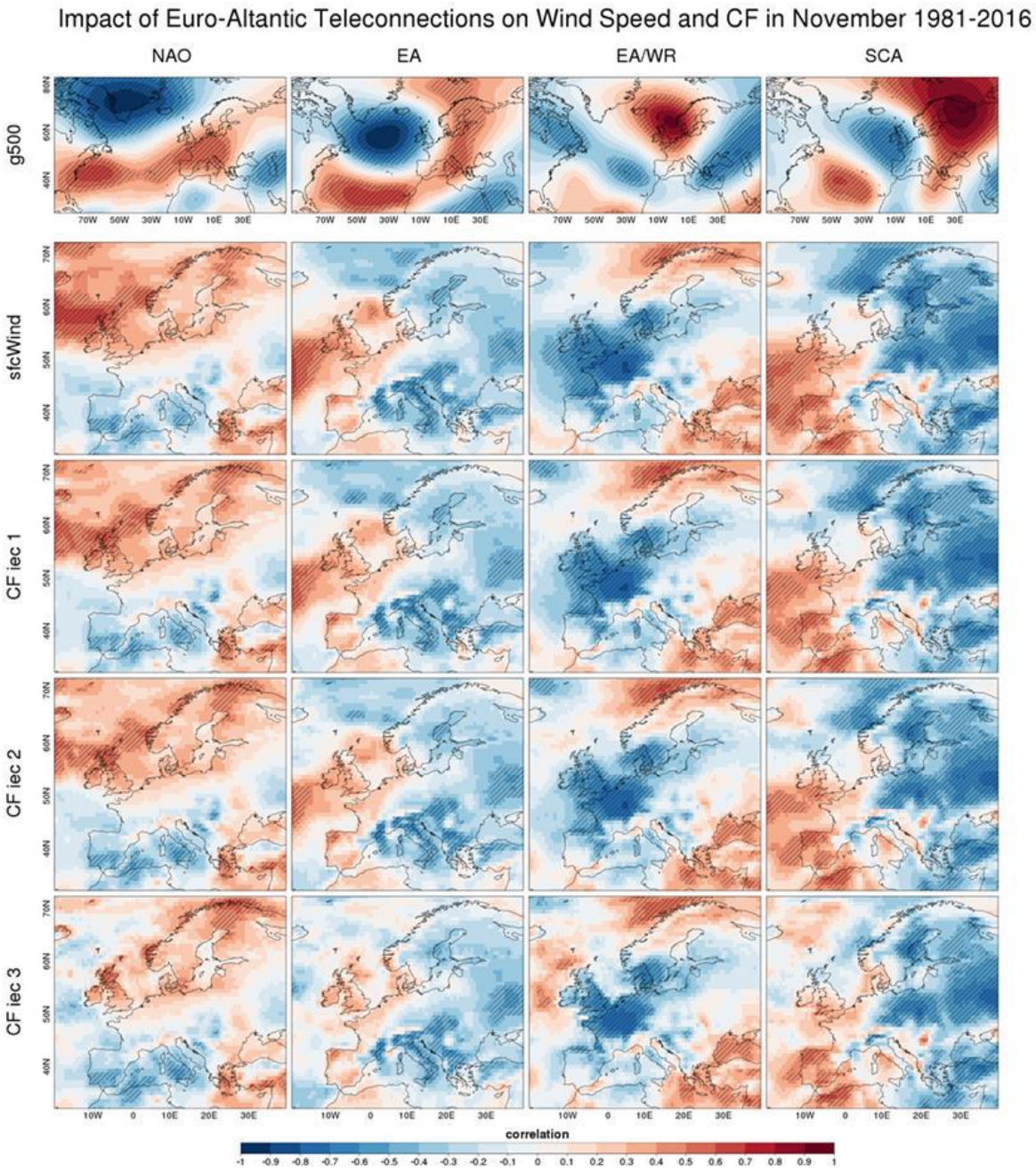

Figure 53: Impact of November teleconnection indices on wind speed and wind power generation. Each image shows the correlation between the four Euro-Atlantic Teleconnection indices (columns) and 500 hPa geopotential height (g500), surface wind speed (sfcWind) and the three capacity factor indicators. Hatches indicate statistical significance at 99% confidence level.

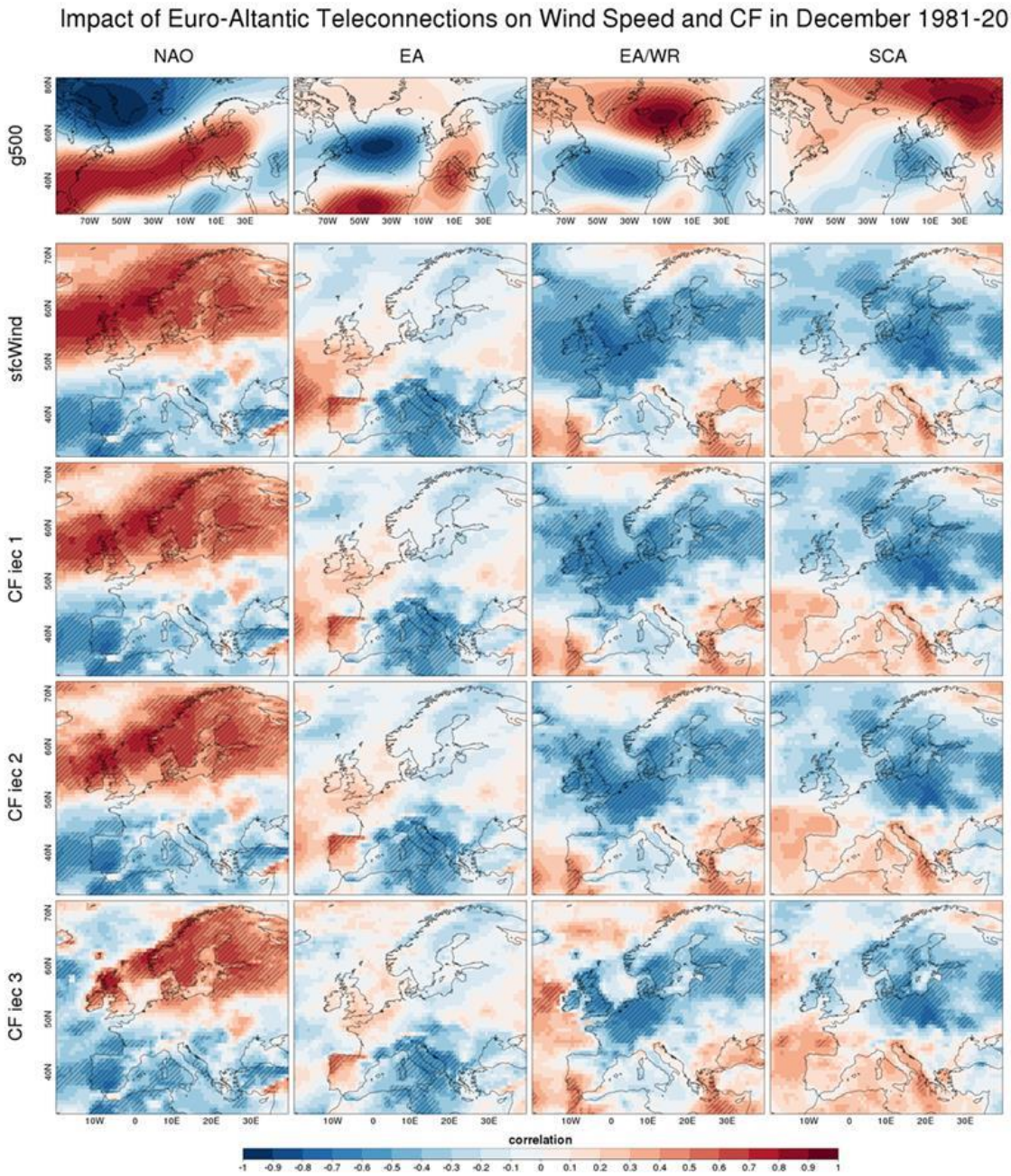

Figure 54: Impact of December teleconnection indices on wind speed and wind power generation. Each image shows the correlation between the four Euro-Atlantic Teleconnection indices (columns) and 500 hPa geopotential height (g500), surface wind speed (sfcWind) and the three capacity factor indicators. Hatches indicate statistical significance at 99% confidence level.

B.2: Impact of WRs on wind speed and capacity factors

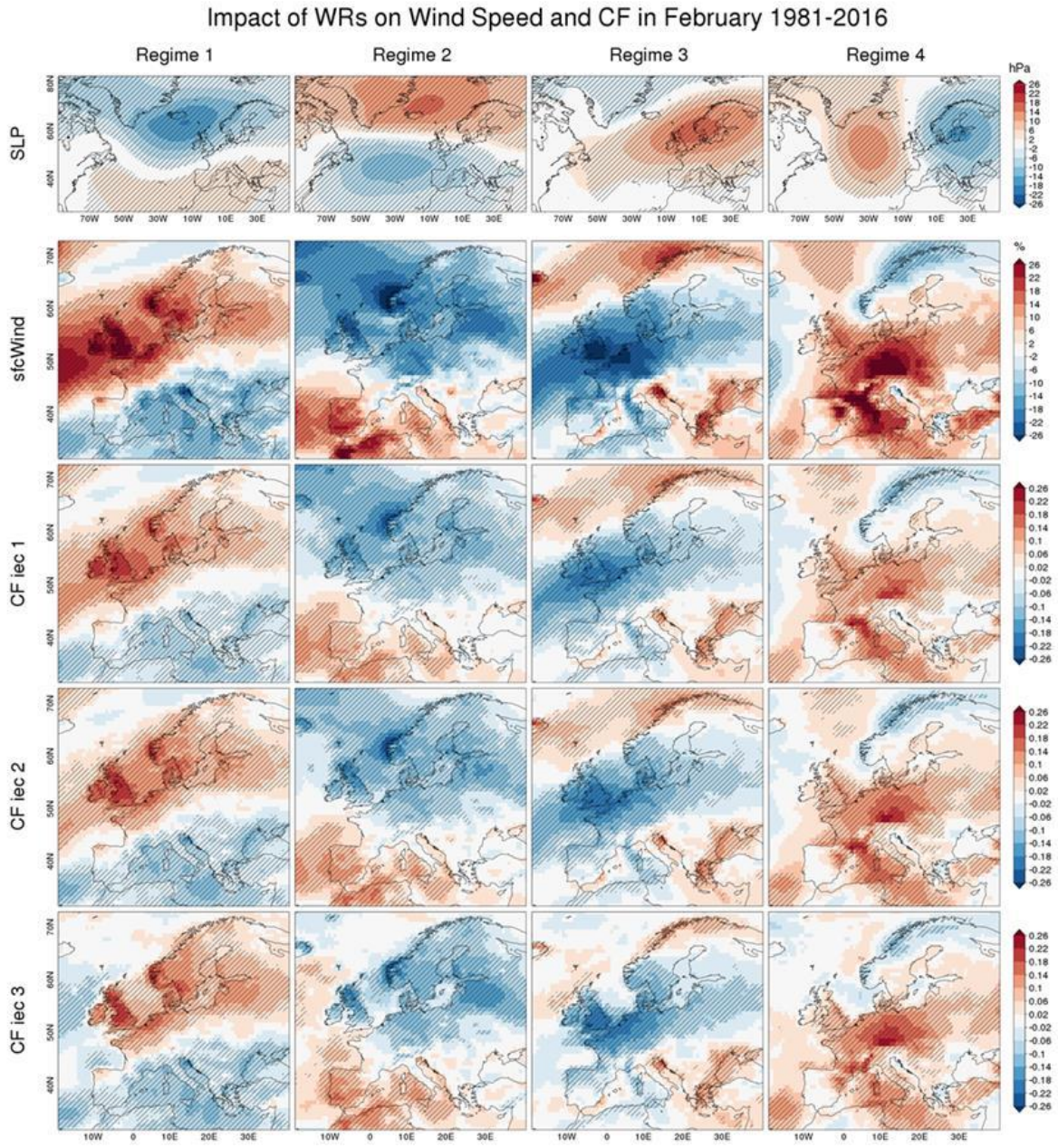

Figure 55: Impact of weather regimes (columns) derived from k-means on surface wind speed (sfcWind) and capacity factors (CFs) during February 1981-2016. Values ranges from -1 to 1 for both wind speed and CF. Impact on surface wind speed is expressed in relative anomalies (with respect to the average wind speed).

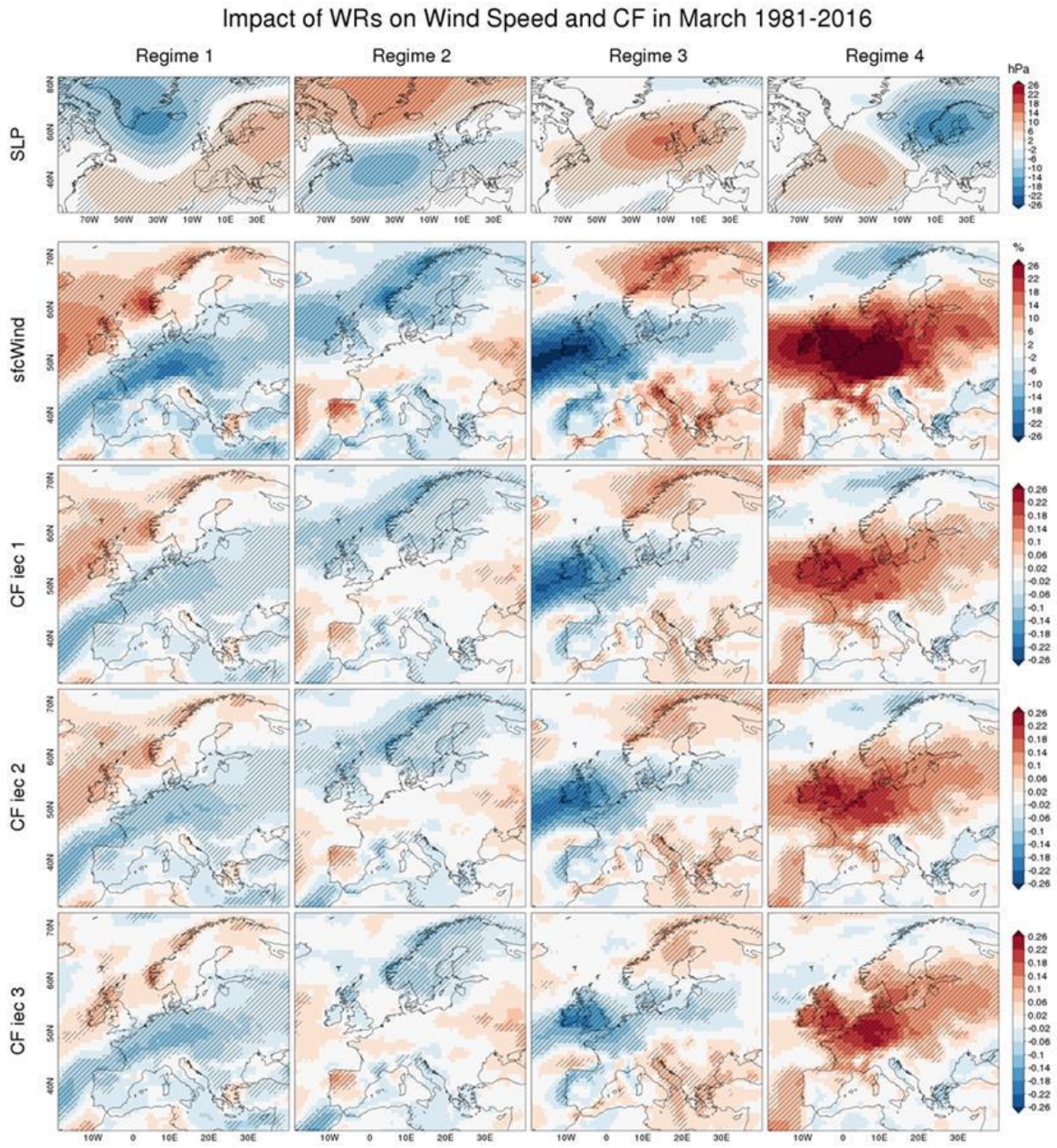

Figure 56: Impact of weather regimes (columns) derived from k-means on surface wind speed (sfcWind) and capacity factors (CFs) during March 1981-2016. Values ranges from -1 to 1 for both wind speed and CF. Impact on surface wind speed is expressed in relative anomalies (with respect to the average wind speed).

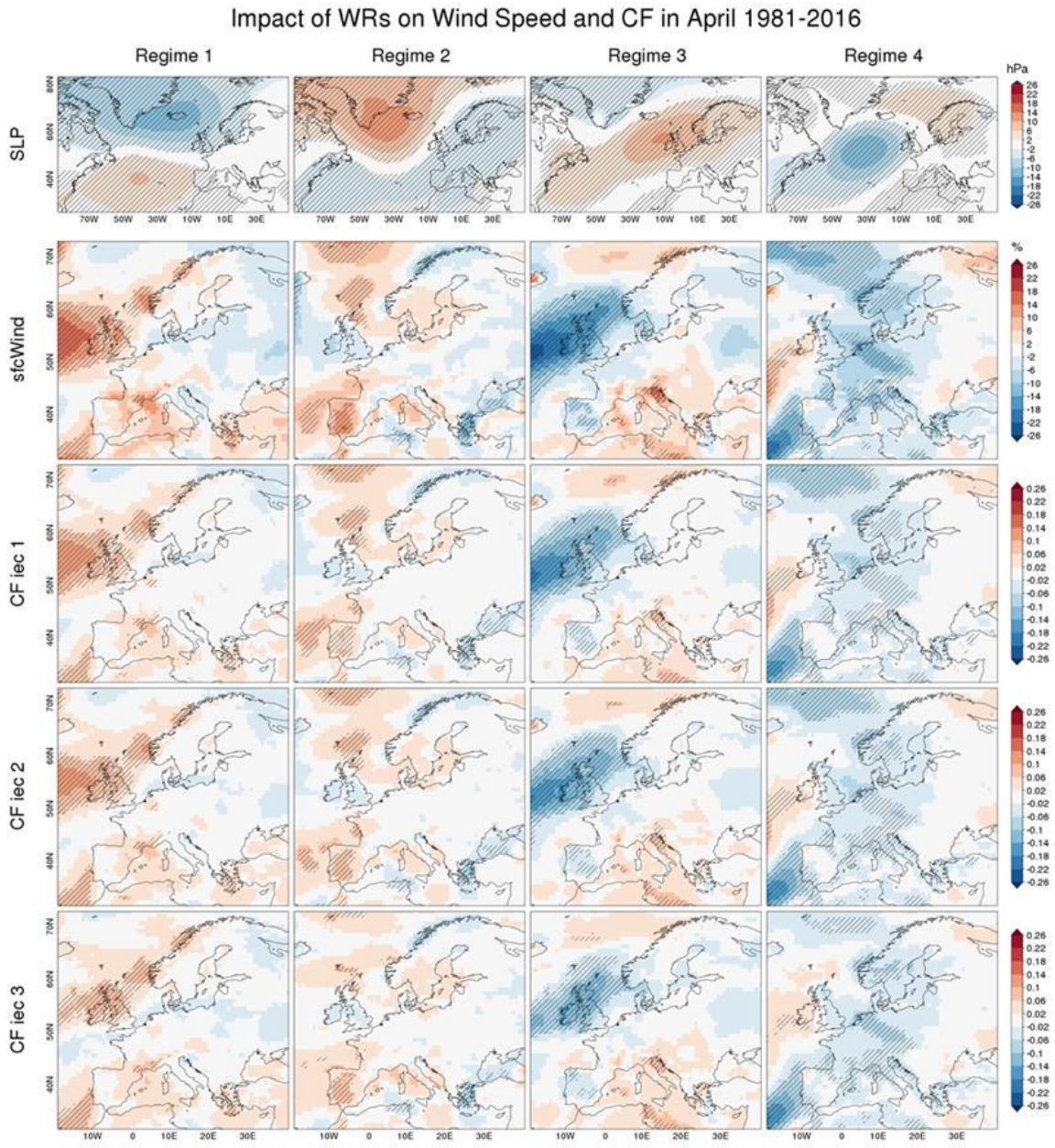

Figure 57: Impact of weather regimes (columns) derived from k-means on surface wind speed (sfcWind) and capacity factors (CFs) during April 1981-2016. Values ranges from -1 to 1 for both wind speed and CF. Impact on surface wind speed is expressed in relative anomalies (with respect to the average wind speed).

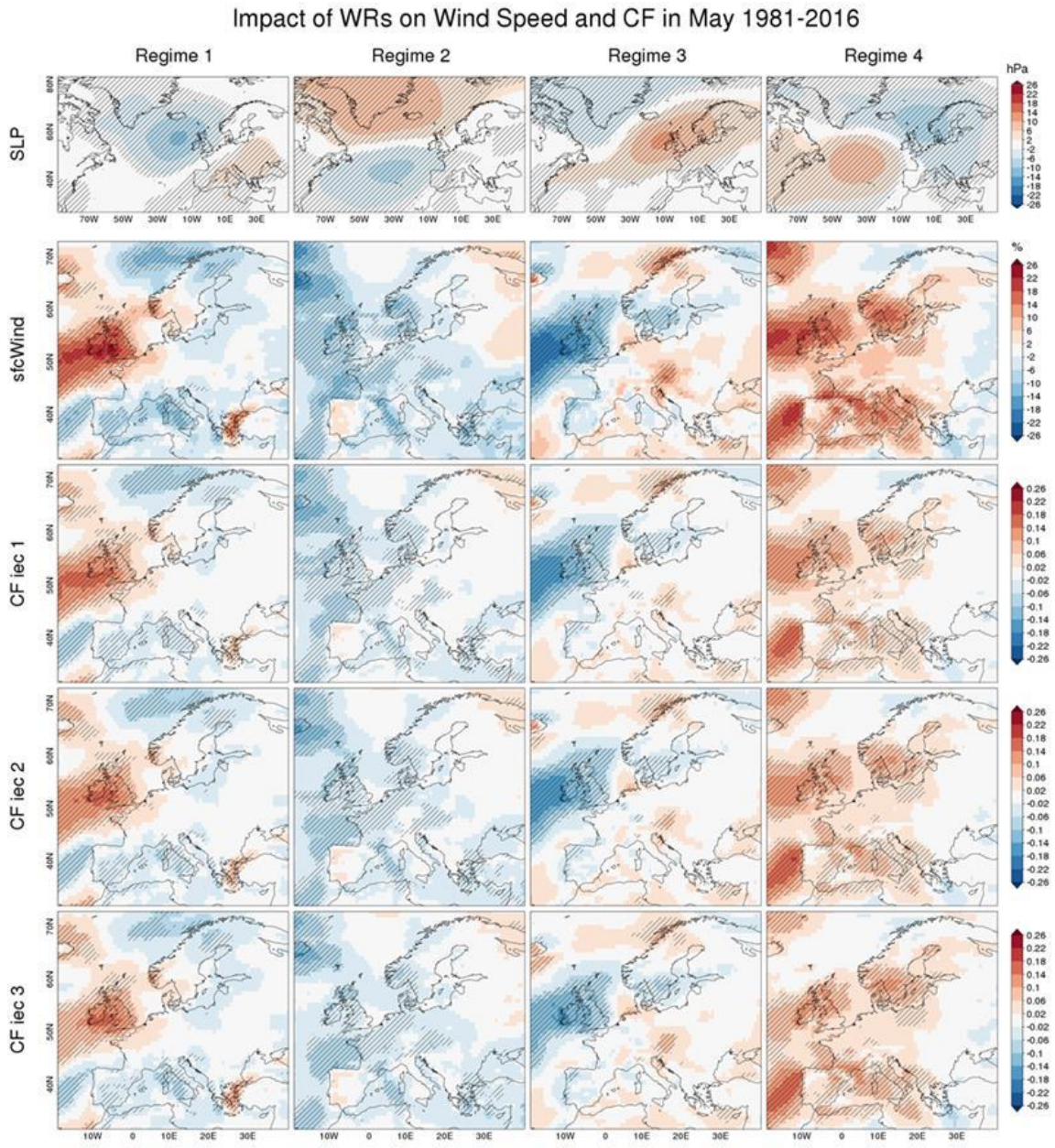

Figure 58: Impact of weather regimes (columns) derived from k-means on surface wind speed (sfcWind) and capacity factors (CFs) during May 1981-2016. Values ranges from -1 to 1 for both wind speed and CF. Impact on surface wind speed is expressed in relative anomalies (with respect to the average wind speed).

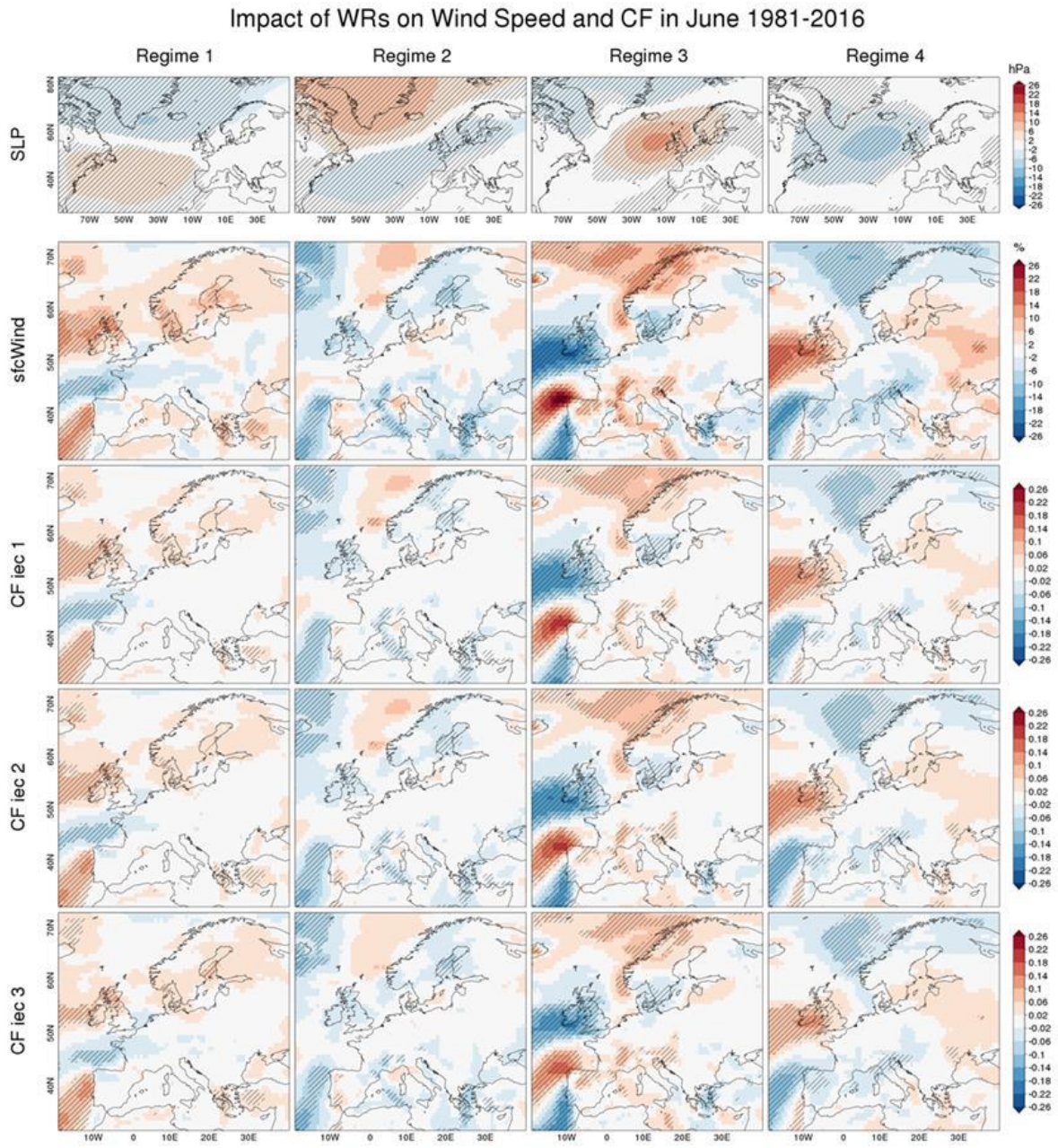

Figure 59: Impact of weather regimes (columns) derived from k-means on surface wind speed (sfcWind) and capacity factors (CFs) during June 1981-2016. Values ranges from -1 to 1 for both wind speed and CF. Impact on surface wind speed is expressed in relative anomalies (with respect to the average wind speed).

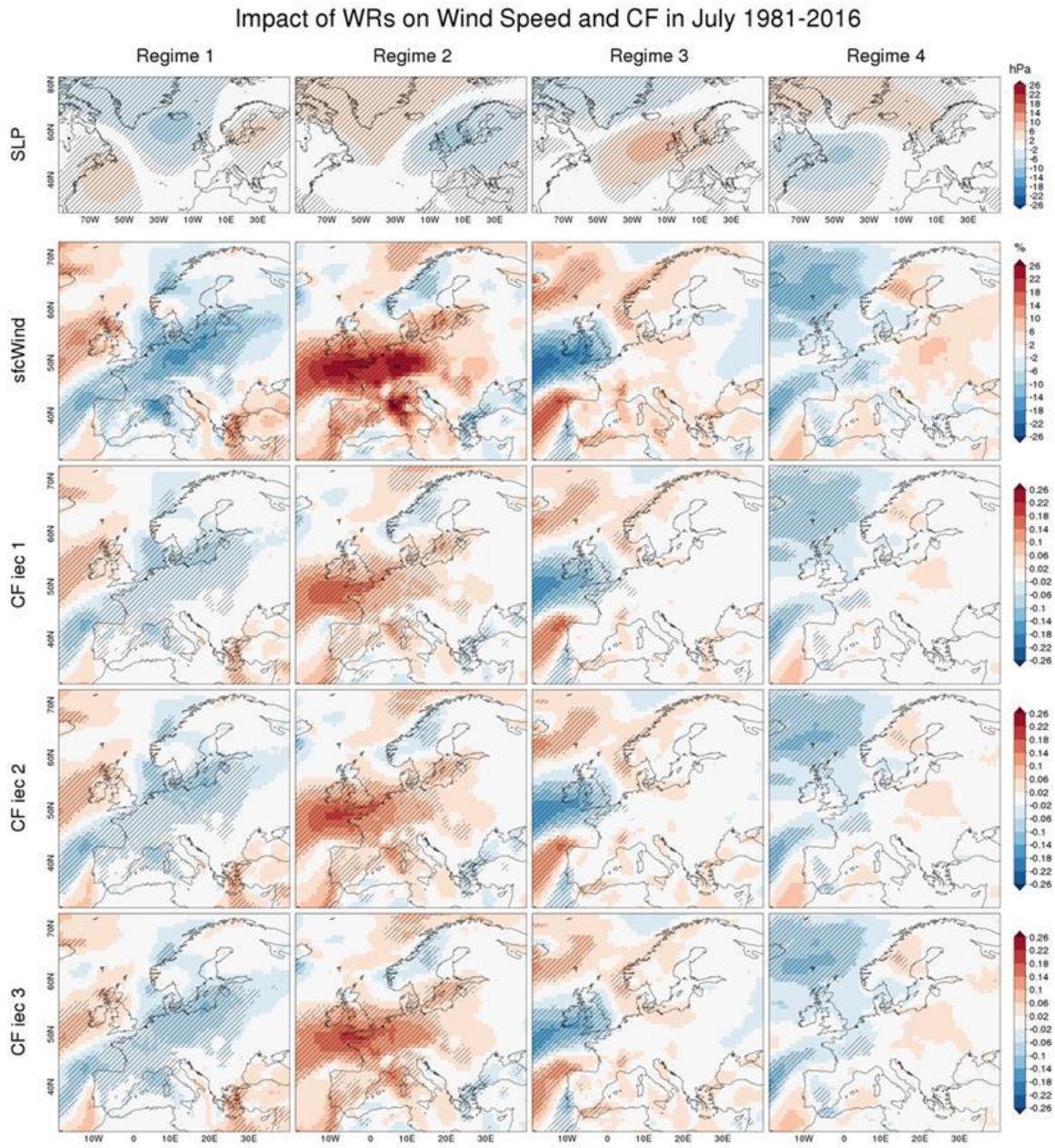

Figure 60: Impact of weather regimes (columns) derived from k-means on surface wind speed (sfcWind) and capacity factors (CFs) during July 1981-2016. Values ranges from -1 to 1 for both wind speed and CF. Impact on surface wind speed is expressed in relative anomalies (with respect to the average wind speed).

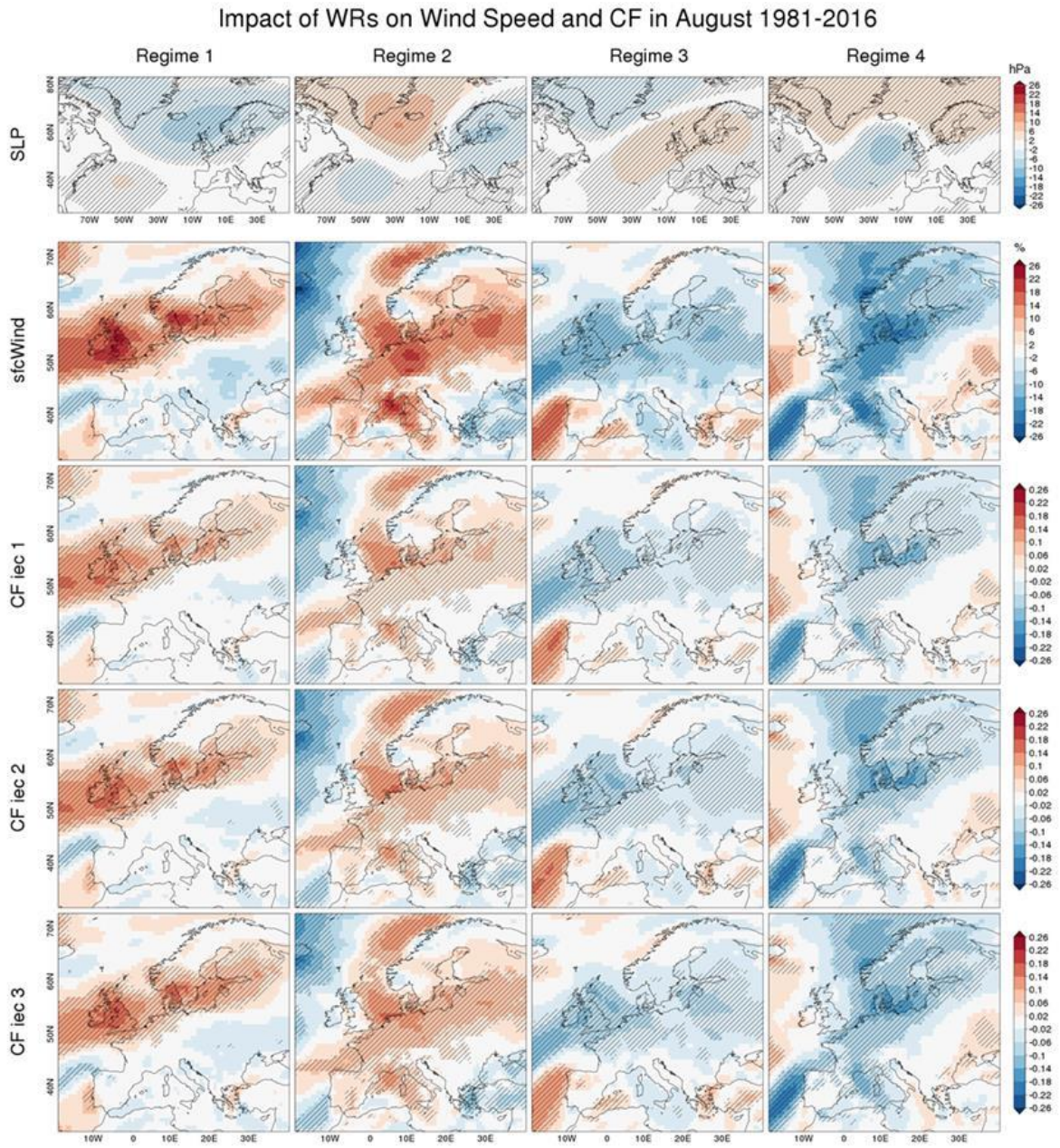

Figure 61: Impact of weather regimes (columns) derived from k-means on surface wind speed (sfcWind) and capacity factors (CFs) during August 1981-2016. Values ranges from -1 to 1 for both wind speed and CF. Impact on surface wind speed is expressed in relative anomalies (with respect to the average wind speed).

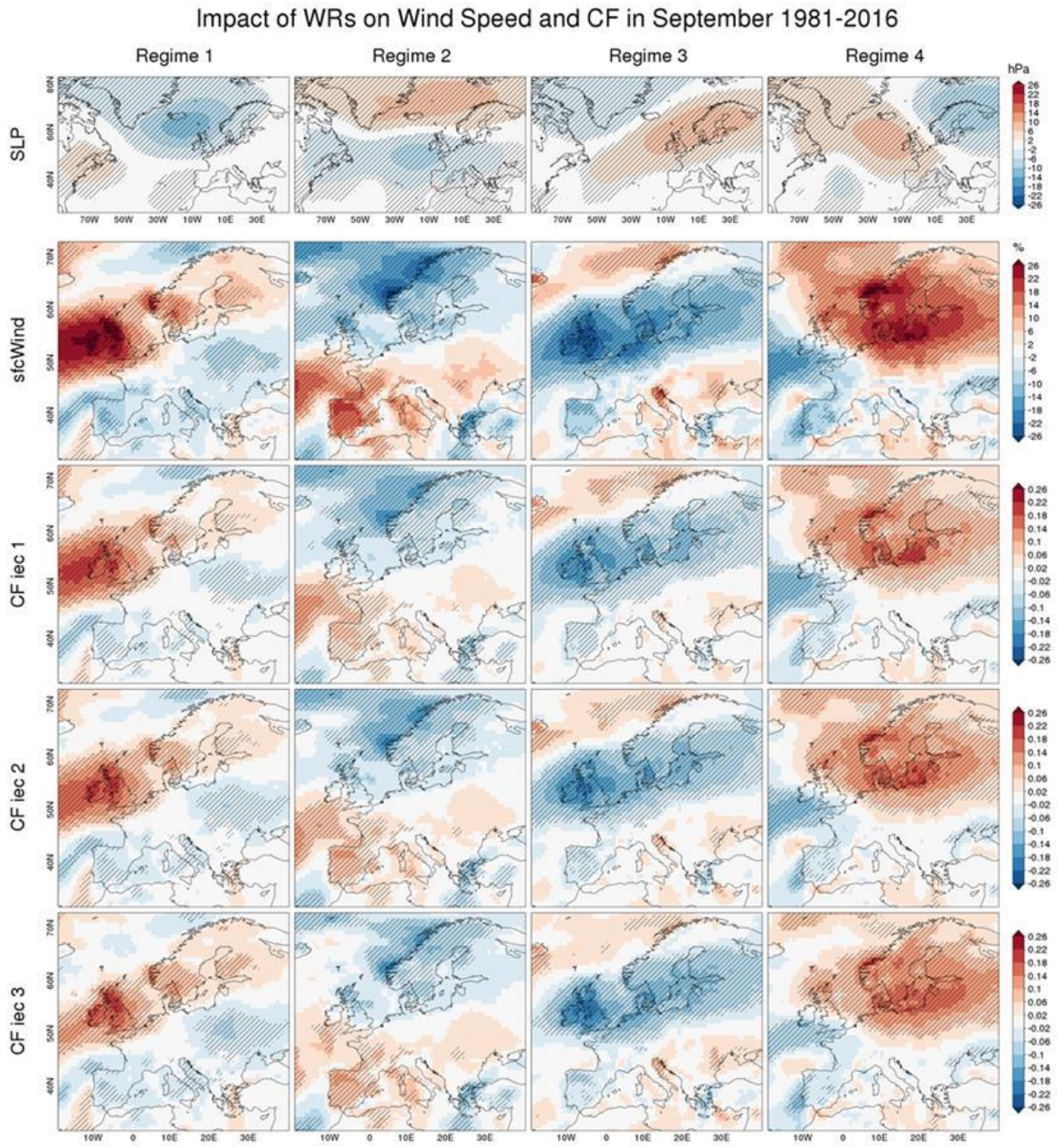

Figure 62: Impact of weather regimes (columns) derived from k-means on surface wind speed (sfcWind) and capacity factors (CFs) during September 1981-2016. Values ranges from -1 to 1 for both wind speed and CF. Impact on surface wind speed is expressed in relative anomalies (with respect to the average wind speed).

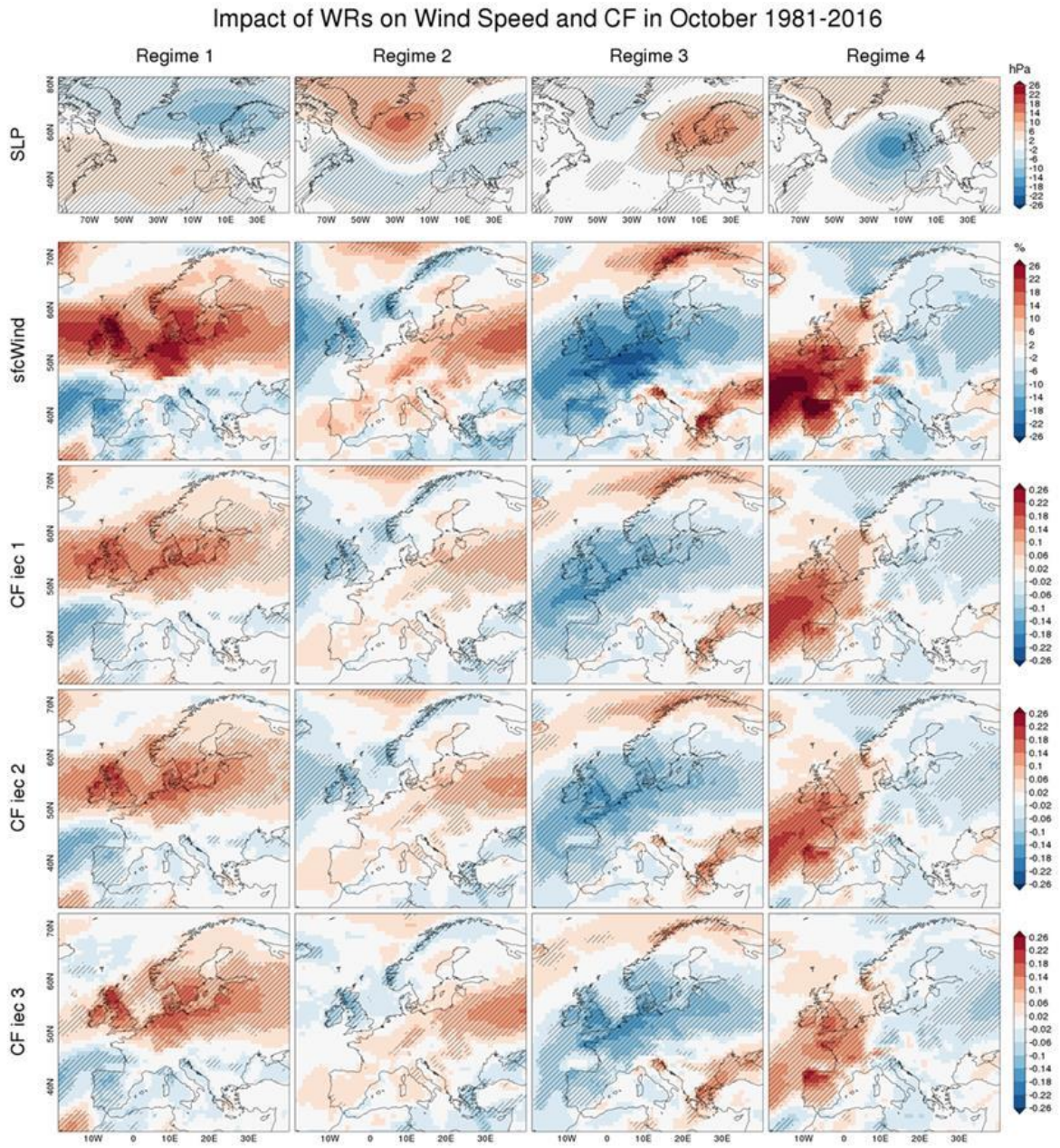

Figure 63: Impact of weather regimes (columns) derived from k-means on surface wind speed (sfcWind) and capacity factors (CFs) during October 1981-2016. Values ranges from -1 to 1 for both wind speed and CF. Impact on surface wind speed is expressed in relative anomalies (with respect to the average wind speed).

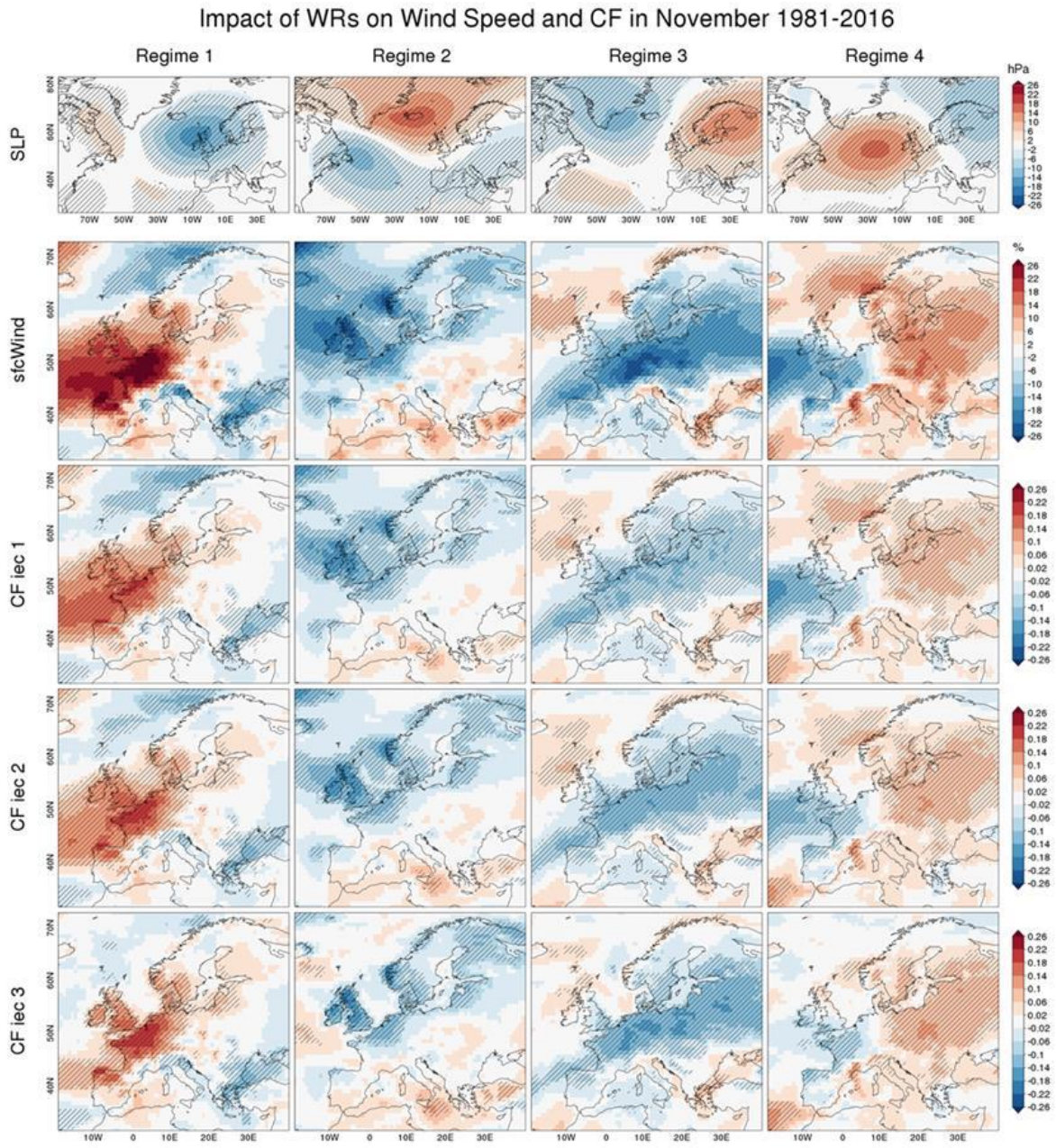

Figure 64: Impact of weather regimes (columns) derived from k-means on surface wind speed (sfcWind) and capacity factors (CFs) during November 1981-2016. Values ranges from -1 to 1 for both wind speed and CF. Impact on surface wind speed is expressed in relative anomalies (with respect to the average wind speed).

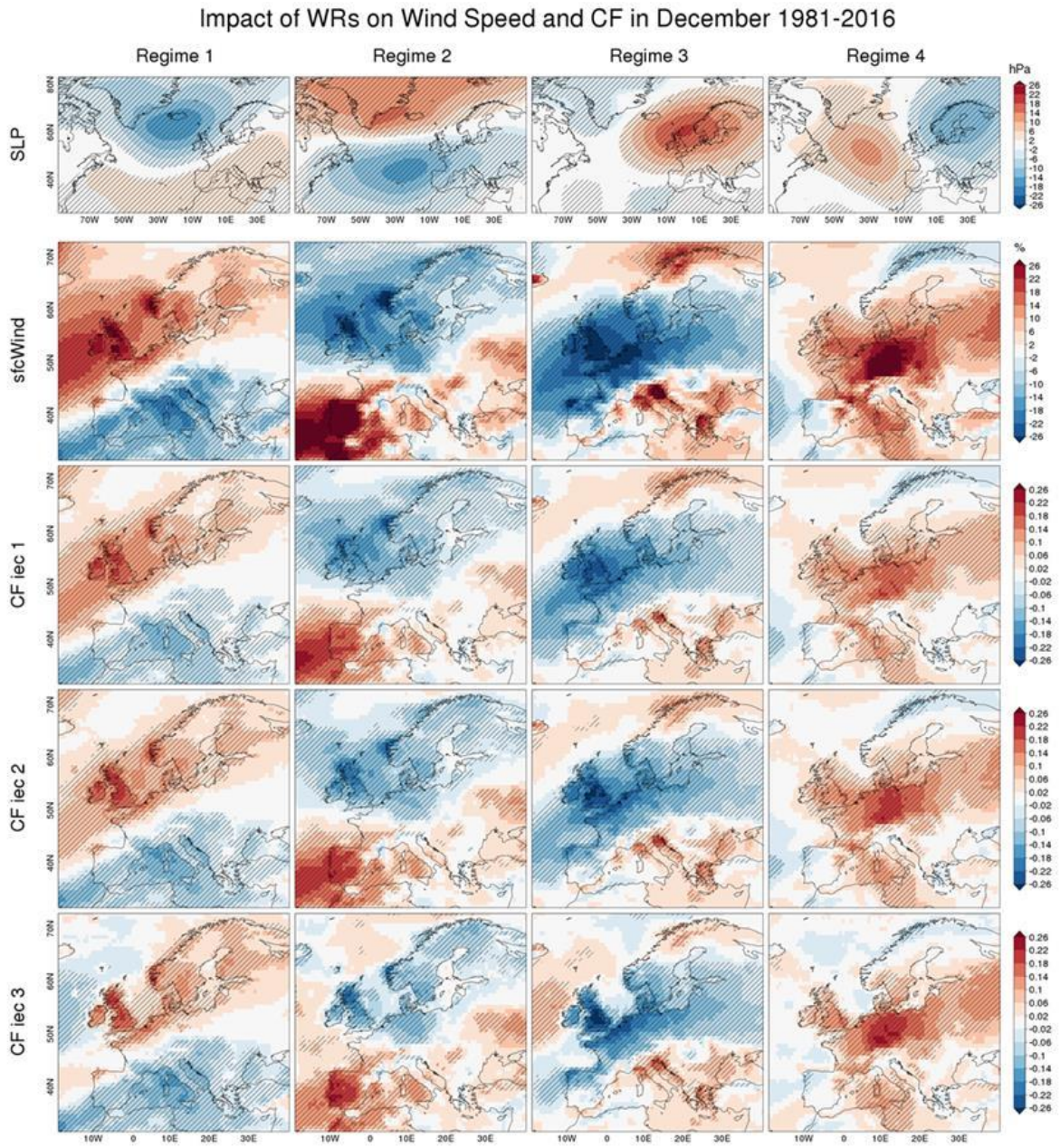

Figure 65: Impact of weather regimes (columns) derived from k-means on surface wind speed (sfcWind) and capacity factors (CFs) during December 1981-2016. Values ranges from -1 to 1 for both wind speed and CF. Impact on surface wind speed is expressed in relative anomalies (with respect to the average wind speed).

ANNEX C: Influence of climate variability on monthly solar generation

C.1: Impact of EATc on solar generation related variables and capacity factors

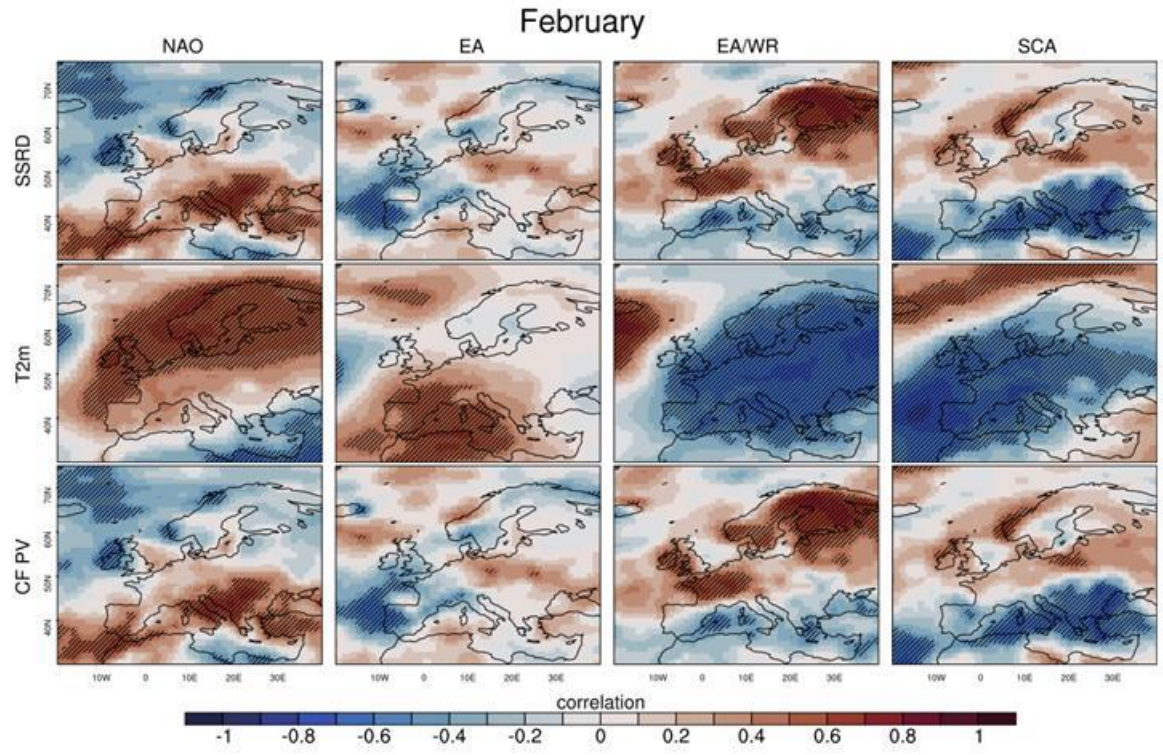

Figure 66: Impact of February teleconnection indices on surface solar radiation, 2 meters temperature and solar power capacity factor. Each image shows the correlation between the four Euro-Atlantic Teleconnection indices (columns) and surface solar radiation (SSRD), 2 meters Temperature (T2m), the capacity factor indicator (CF PV). Hatches indicate statistical significance at 99% confidence level.

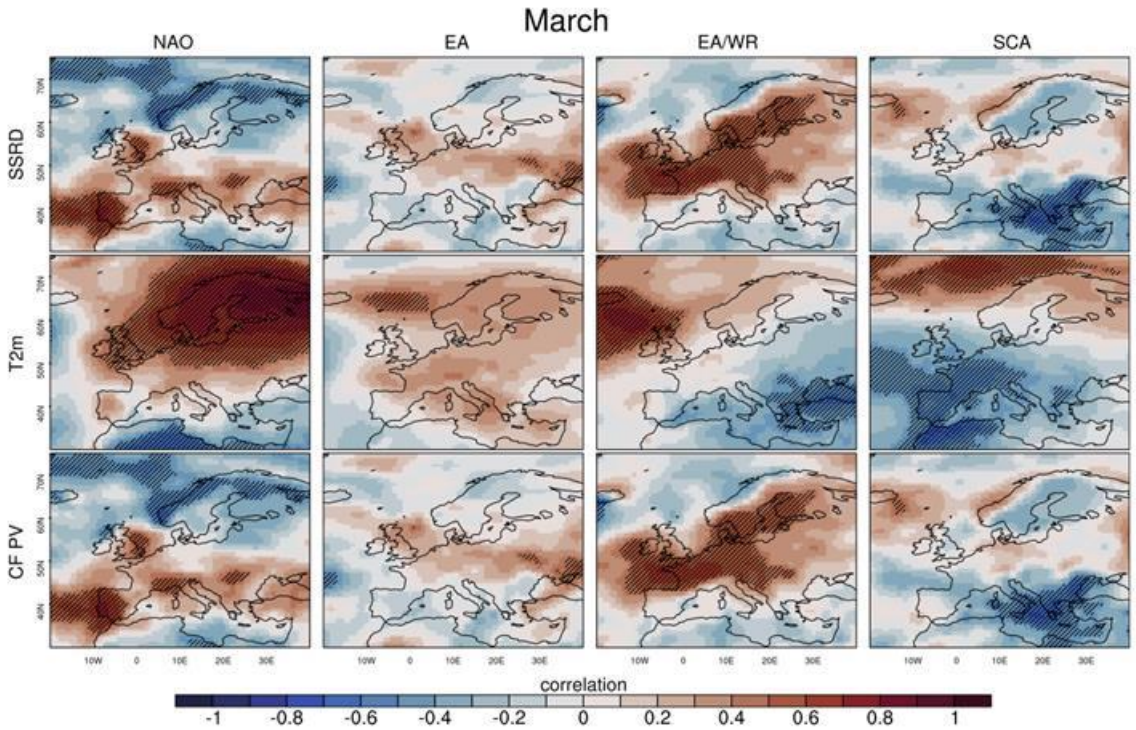

Figure 67: Impact of March teleconnection indices on surface solar radiation, 2 meters temperature and solar power capacity factor. Each image shows the correlation between the four Euro-Atlantic Teleconnection indices (columns) and surface solar radiation (SSRD), 2 meters Temperature (T2m), the capacity factor indicator (CF PV). Hatches indicate statistical significance at 99% confidence level.

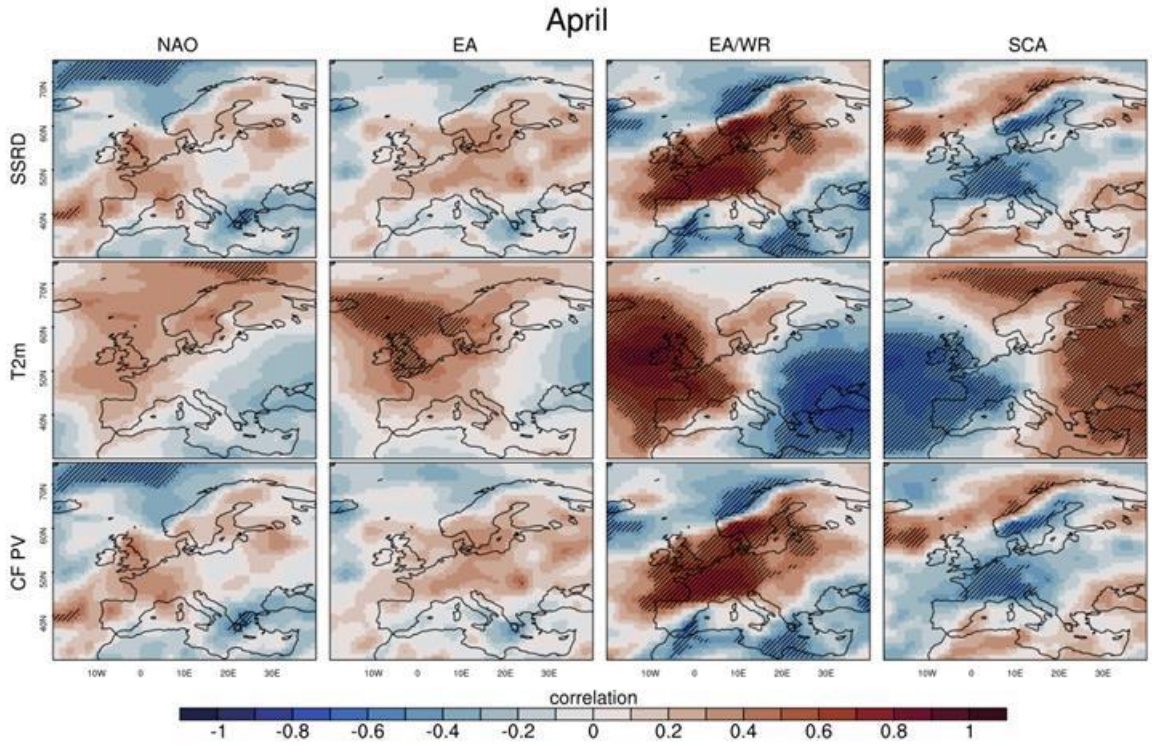

Figure 68: Impact of April teleconnection indices on surface solar radiation, 2 meters temperature and solar power capacity factor. Each image shows the correlation between the four Euro-Atlantic Teleconnection indices (columns) and surface solar radiation (SSRD), 2 meters Temperature (T2m), the capacity factor indicator (CF PV). Hatches indicate statistical significance at 99% confidence level.

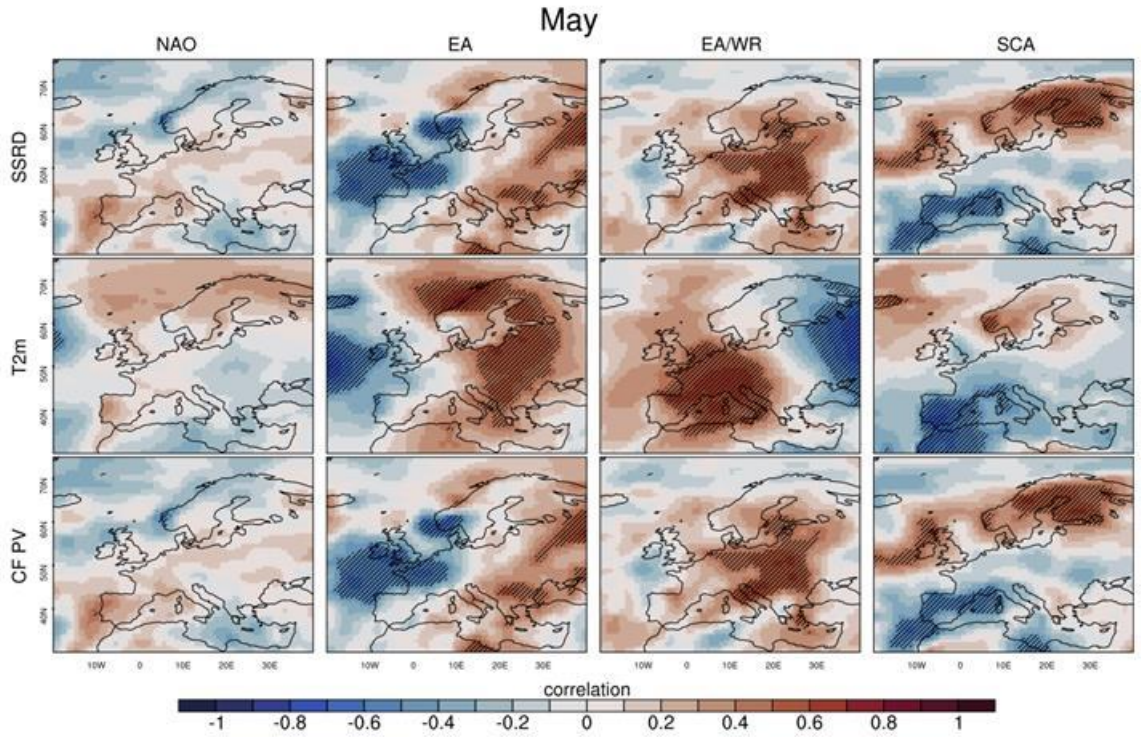

Figure 69: Impact of May teleconnection indices on surface solar radiation, 2 meters temperature and solar power capacity factor. Each image shows the correlation between the four Euro-Atlantic Teleconnection indices (columns) and surface solar radiation (SSRD), 2 meters Temperature (T2m), the capacity factor indicator (CF PV). Hatches indicate statistical significance at 99% confidence level.

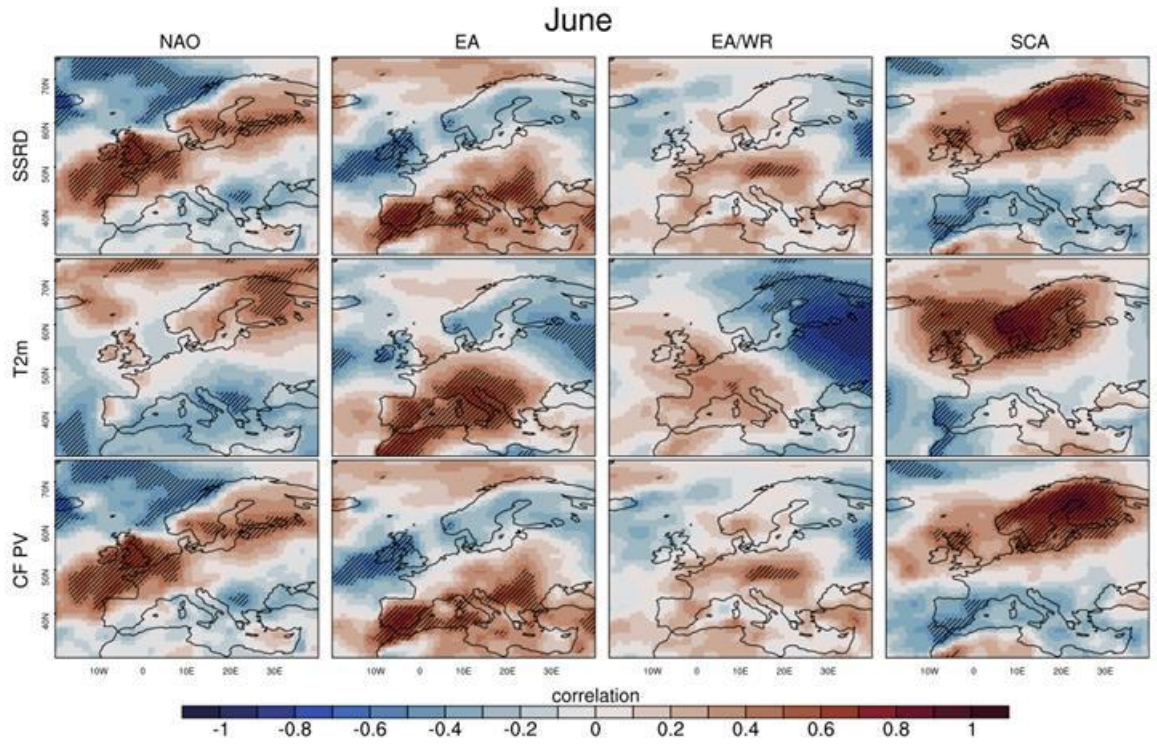

Figure 70: Impact of June teleconnection indices on surface solar radiation, 2 meters temperature and solar power capacity factor. Each image shows the correlation between the four Euro-Atlantic Teleconnection indices (columns) and surface solar radiation (SSRD), 2 meters Temperature (T2m), the capacity factor indicator (CF PV). Hatches indicate statistical significance at 99% confidence level.

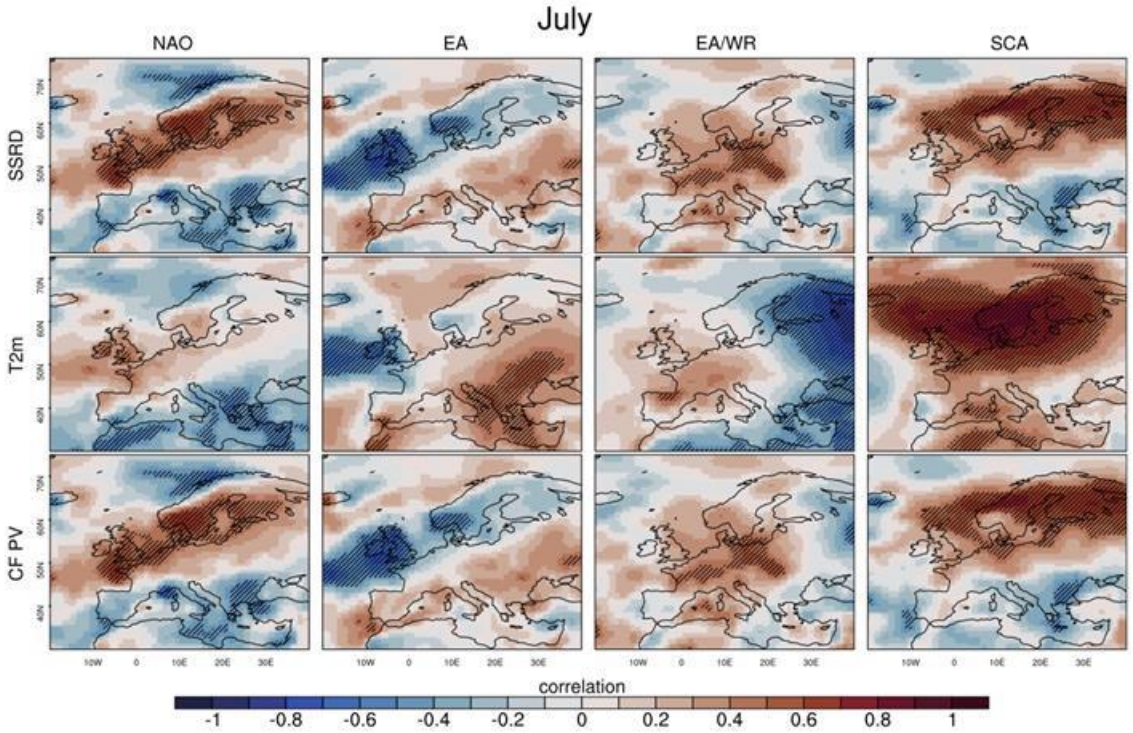

Figure 71: Impact of July teleconnection indices on surface solar radiation, 2 meters temperature and solar power capacity factor. Each image shows the correlation between the four Euro-Atlantic Teleconnection indices (columns) and surface solar radiation (SSRD), 2 meters Temperature (T2m), the capacity factor indicator (CF PV). Hatches indicate statistical significance at 99% confidence level.

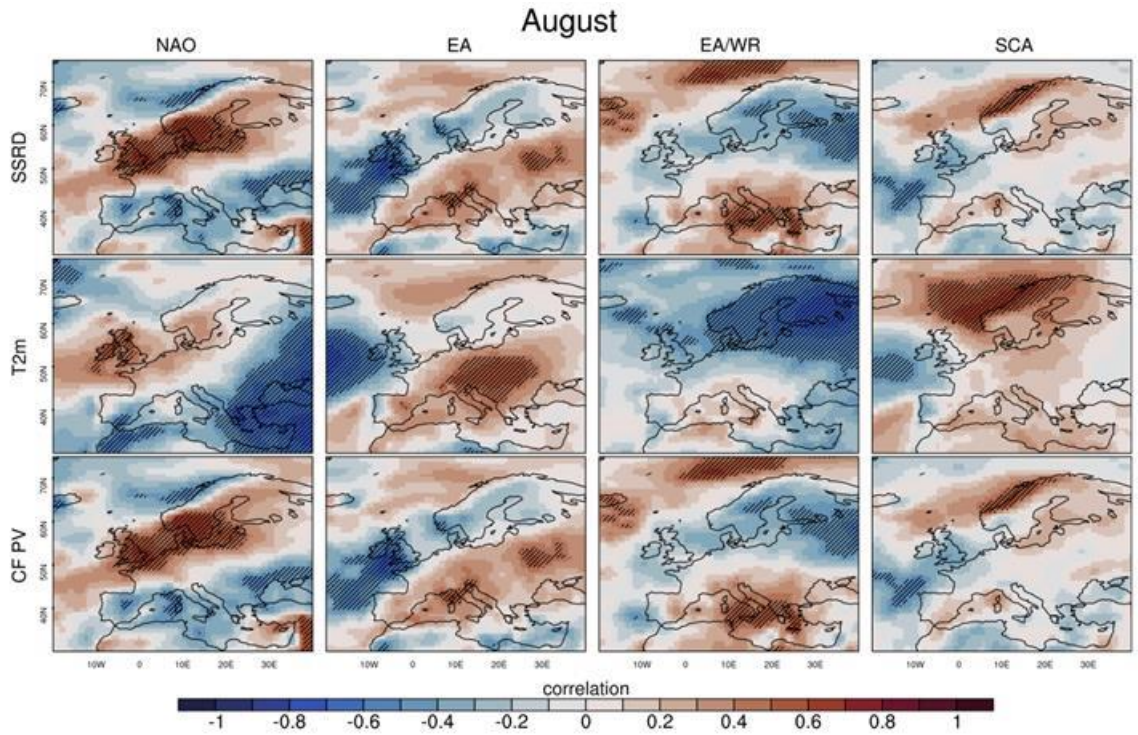

Figure 72: Impact of August teleconnection indices on surface solar radiation, 2 meters temperature and solar power capacity factor. Each image shows the correlation between the four Euro-Atlantic Teleconnection indices (columns) and surface solar radiation (SSRD), 2 meters Temperature (T2m), the capacity factor indicator (CF PV). Hatches indicate statistical significance at 99% confidence level.

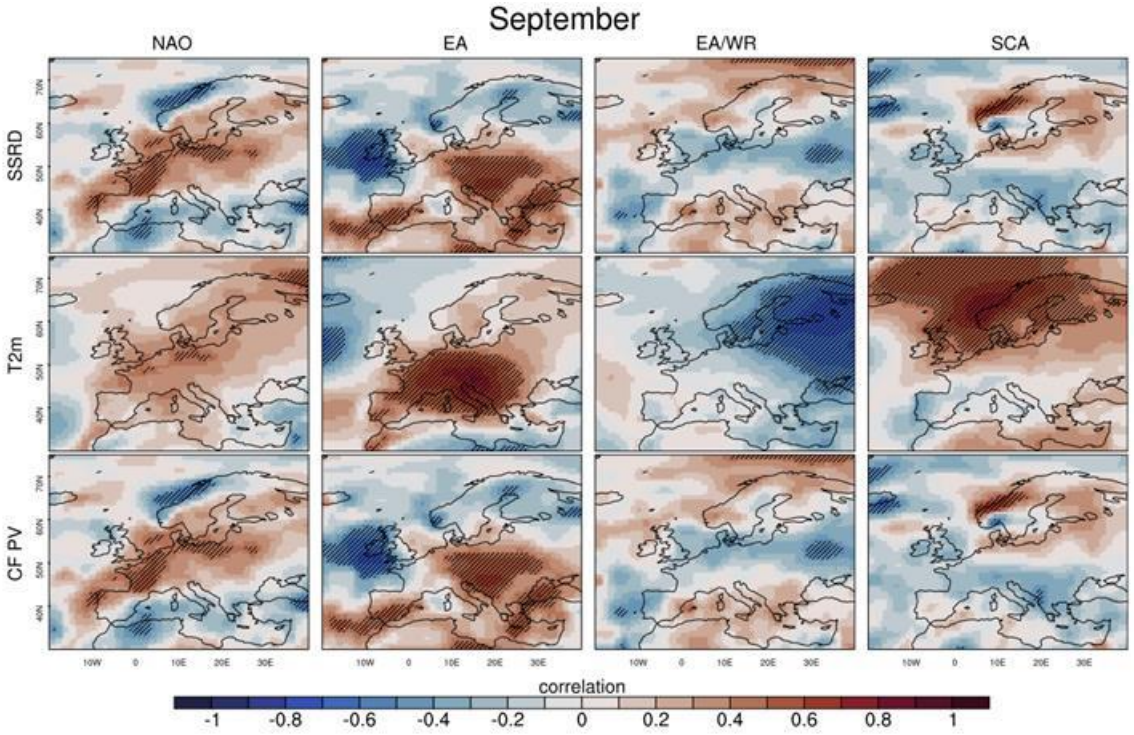

Figure 73: Impact of September teleconnection indices on surface solar radiation, 2 meters temperature and solar power capacity factor. Each image shows the correlation between the four Euro-Atlantic Teleconnection indices (columns) and surface solar radiation (SSRD), 2 meters Temperature (T2m), the capacity factor indicator (CF PV). Hatches indicate statistical significance at 99% confidence level.

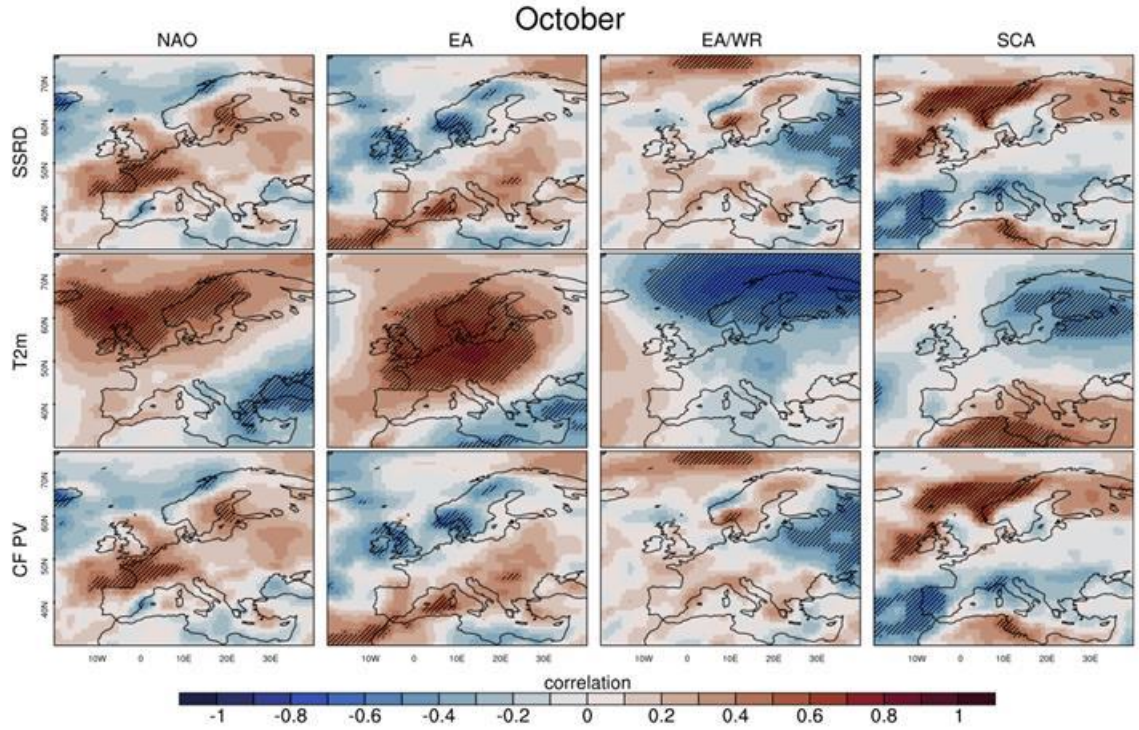

Figure 74: Impact of October teleconnection indices on surface solar radiation, 2 meters temperature and solar power capacity factor. Each image shows the correlation between the four Euro-Atlantic Teleconnection indices (columns) and surface solar radiation (SSRD), 2 meters Temperature (T2m), the capacity factor indicator (CF PV). Hatches indicate statistical significance at 99% confidence level.

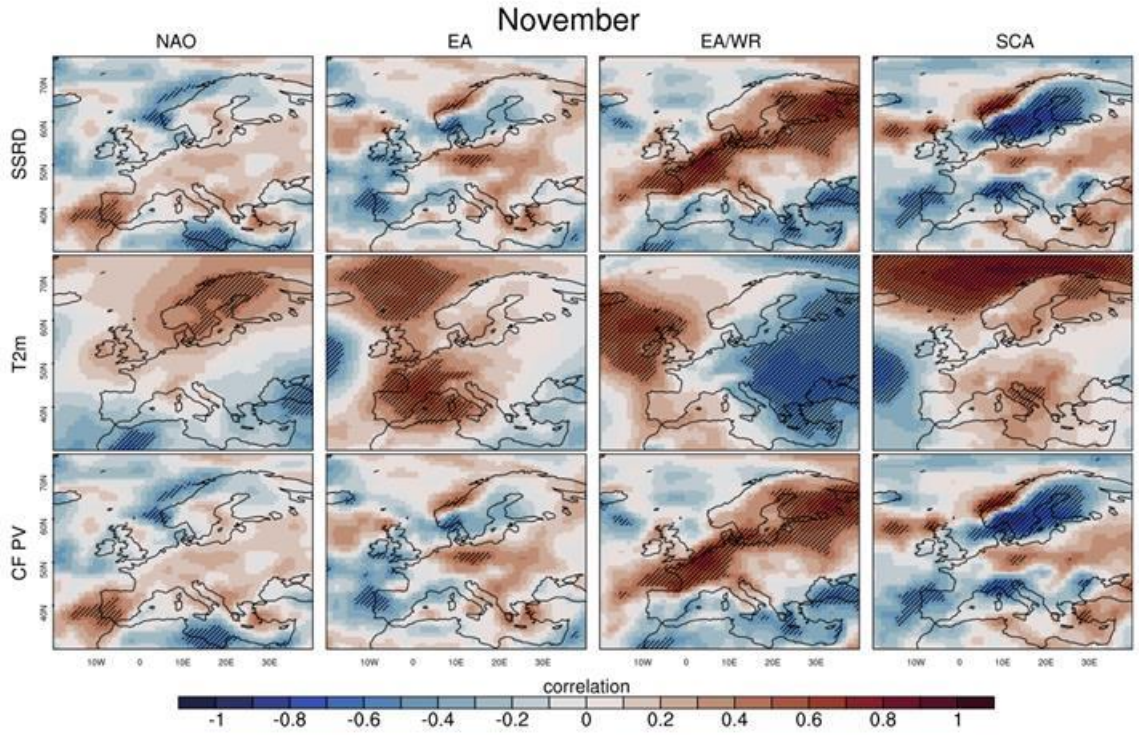

Figure 75: Impact of November teleconnection indices on surface solar radiation, 2 meters temperature and solar power capacity factor. Each image shows the correlation between the four Euro-Atlantic Teleconnection indices (columns) and surface solar radiation (SSRD), 2 meters Temperature (T2m), the capacity factor indicator (CF PV). Hatches indicate statistical significance at 99% confidence level.

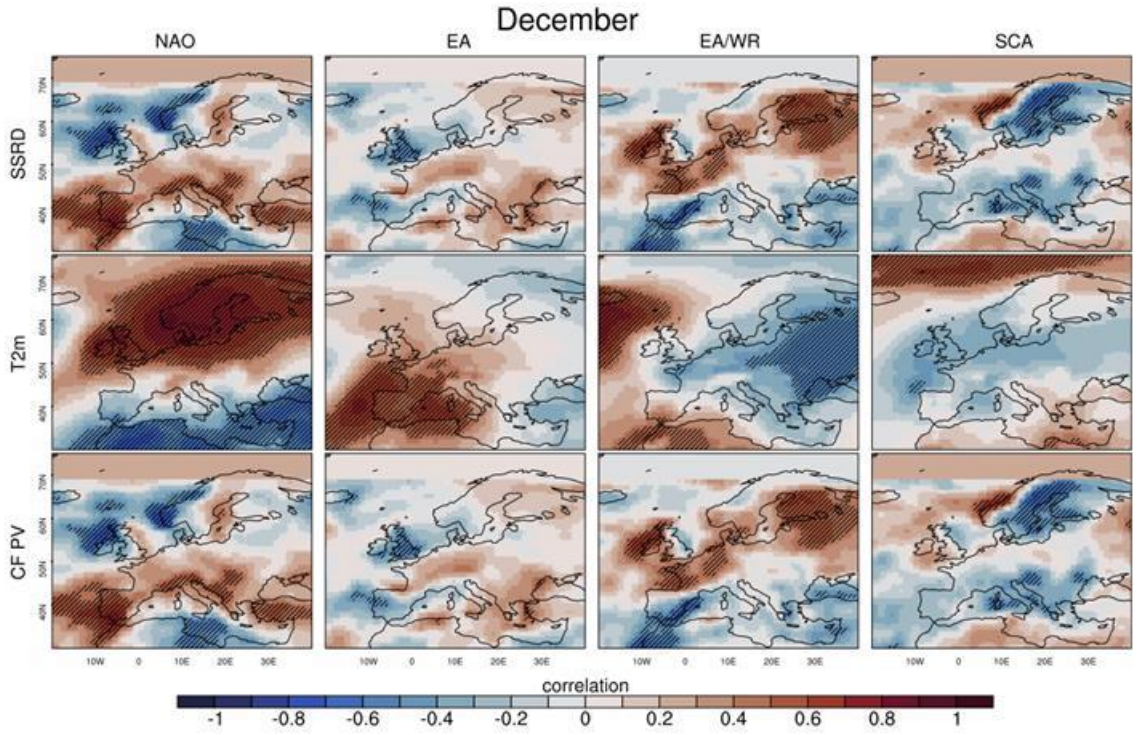

Figure 76: Impact of December teleconnection indices on surface solar radiation, 2 meters temperature and solar power capacity factor. Each image shows the correlation between the four Euro-Atlantic Teleconnection indices (columns) and surface solar radiation (SSRD), 2 meters Temperature (T2m), the capacity factor indicator (CF PV). Hatches indicate statistical significance at 99% confidence level.

C.2: Impact of WRs on solar generation related variables and capacity factors

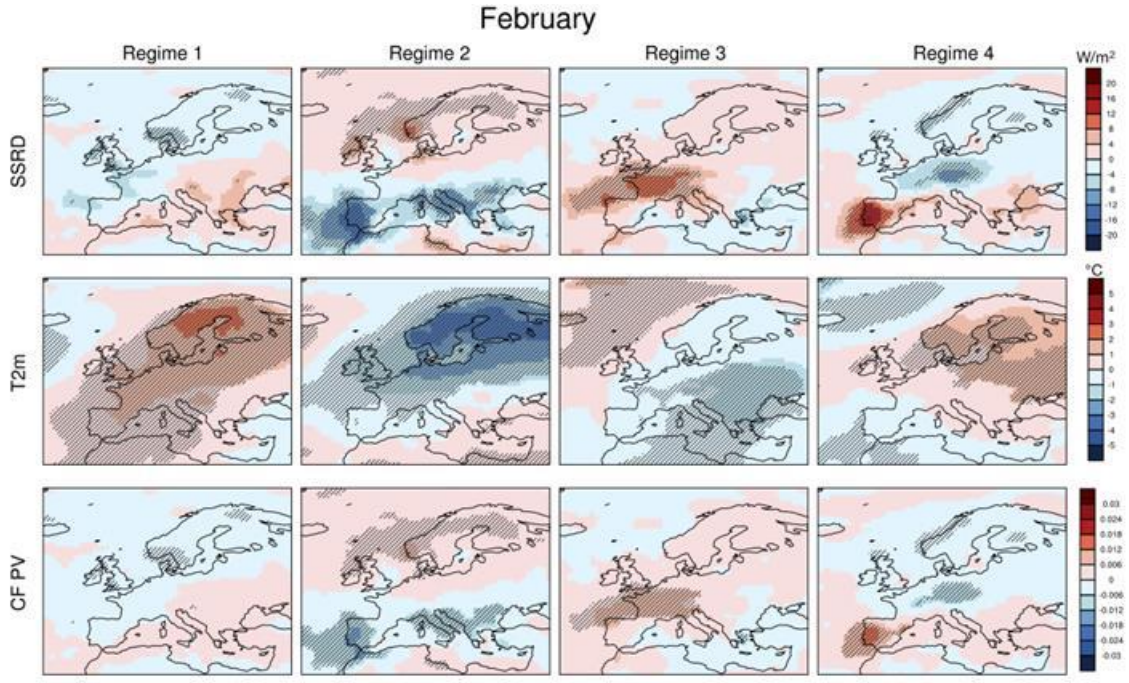

Figure 77: Impact of Euro-Atlantic weather regimes on SSRD (first row), 2 meters temperature (second row) and CF (third row) during February 1981-2016. Hatches indicate that anomalies are significant at the 95% confidence level.

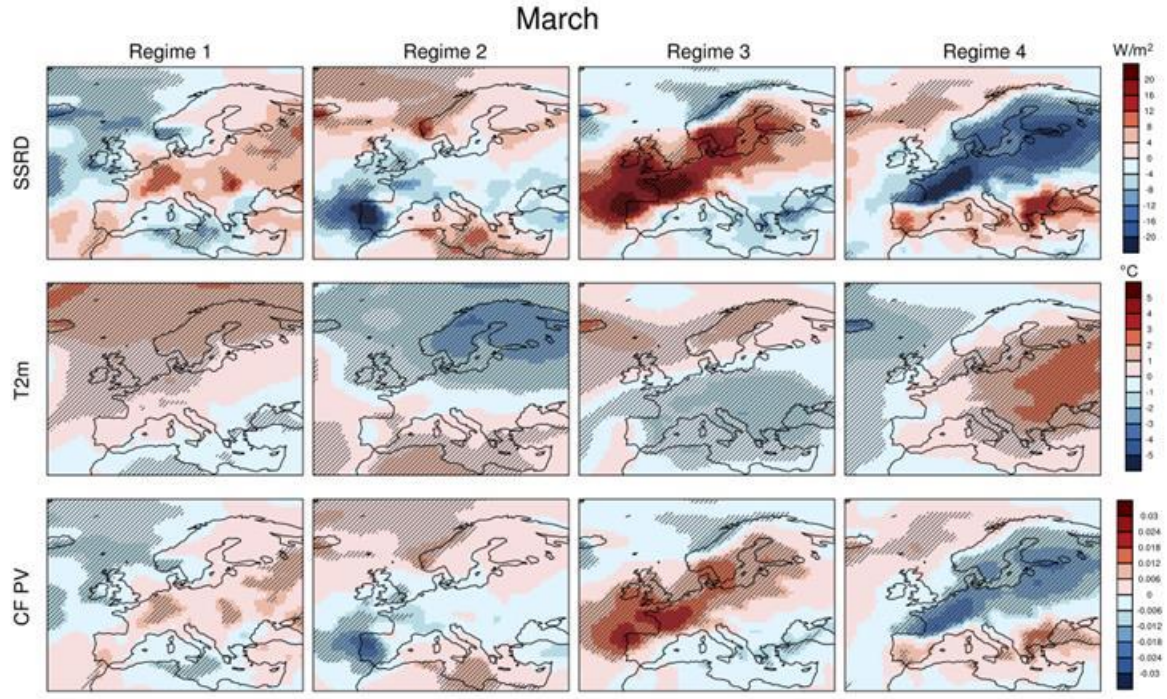

Figure 78: Impact of Euro-Atlantic weather regimes on SSRD (first row), 2 meters temperature (second row) and CF (third row) during March 1981-2016. Hatches indicate that anomalies are significant at the 95% confidence level.

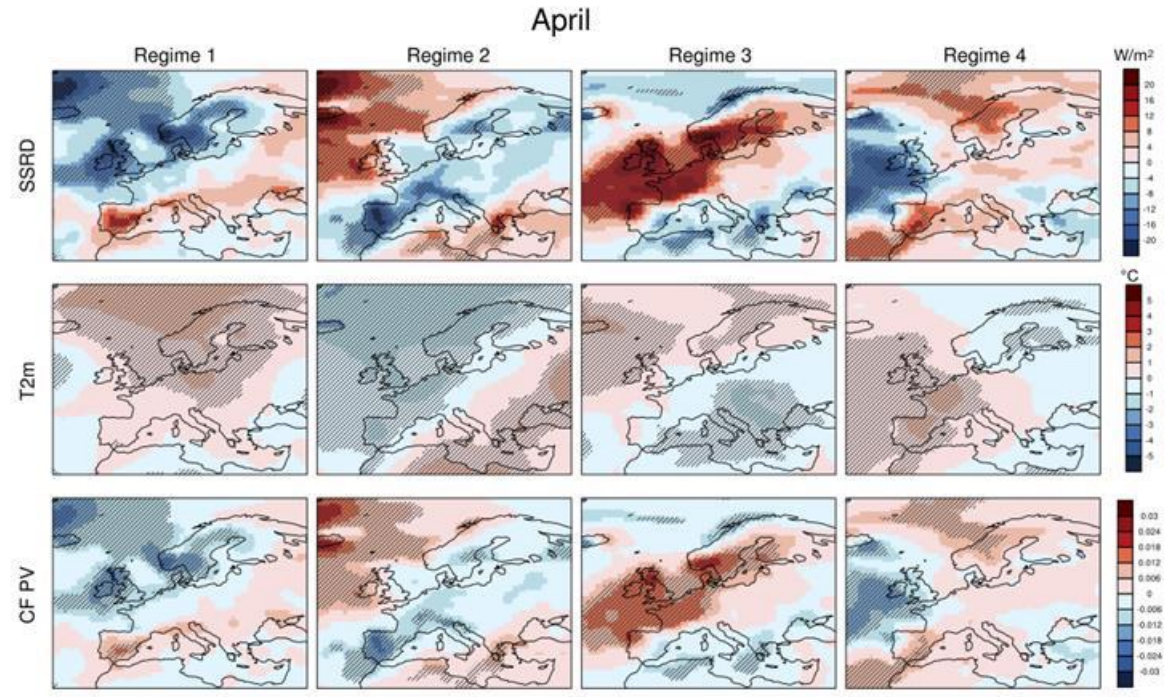

Figure 79: Impact of Euro-Atlantic weather regimes on SSRD (first row), 2 meters temperature (second row) and CF (third row) during April 1981-2016. Hatches indicate that anomalies are significant at the 95% confidence level.

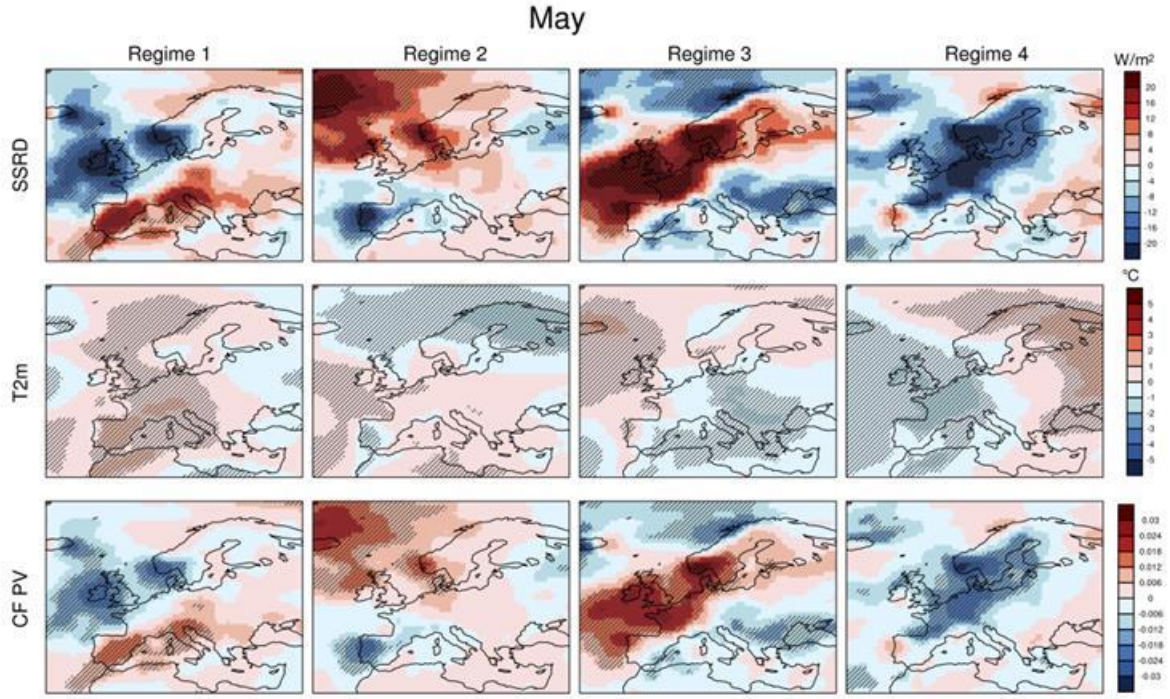

Figure 80: Impact of Euro-Atlantic weather regimes on SSRD (first row), 2 meters temperature (second row) and CF (third row) during May 1981-2016. Hatches indicate that anomalies are significant at the 95% confidence level.

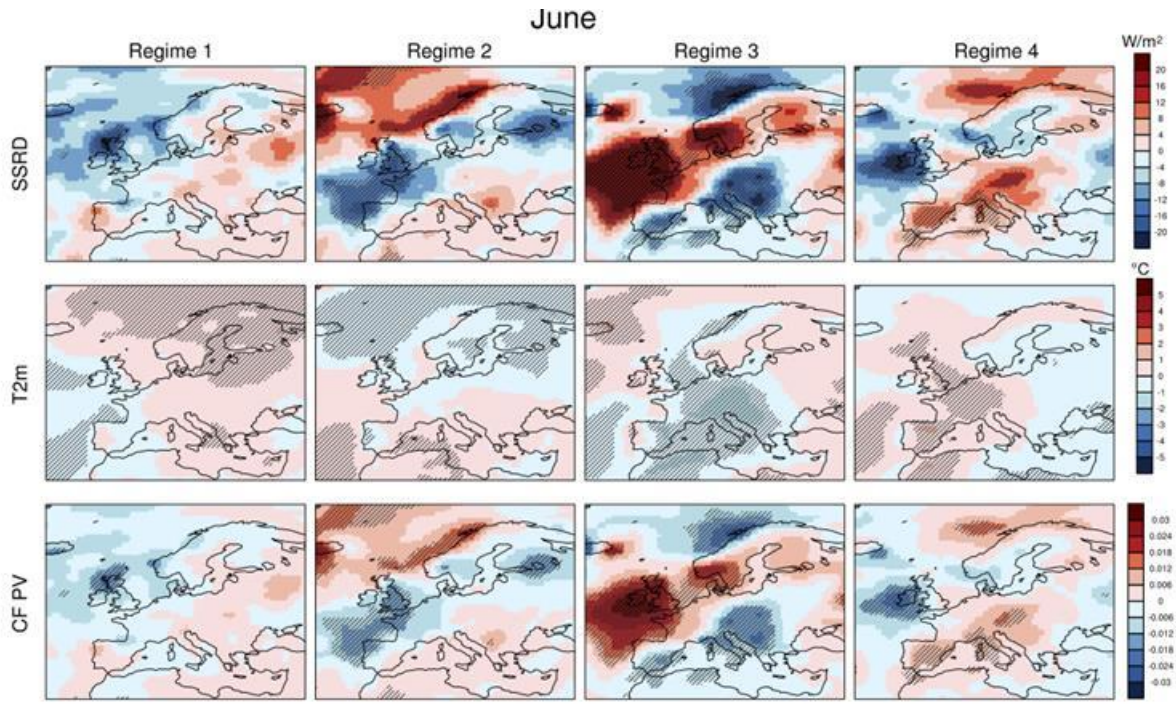

Figure 81: Impact of Euro-Atlantic weather regimes on SSRD (first row), 2 meters temperature (second row) and CF (third row) during June 1981-2016. Hatches indicate that anomalies are significant at the 95% confidence level.

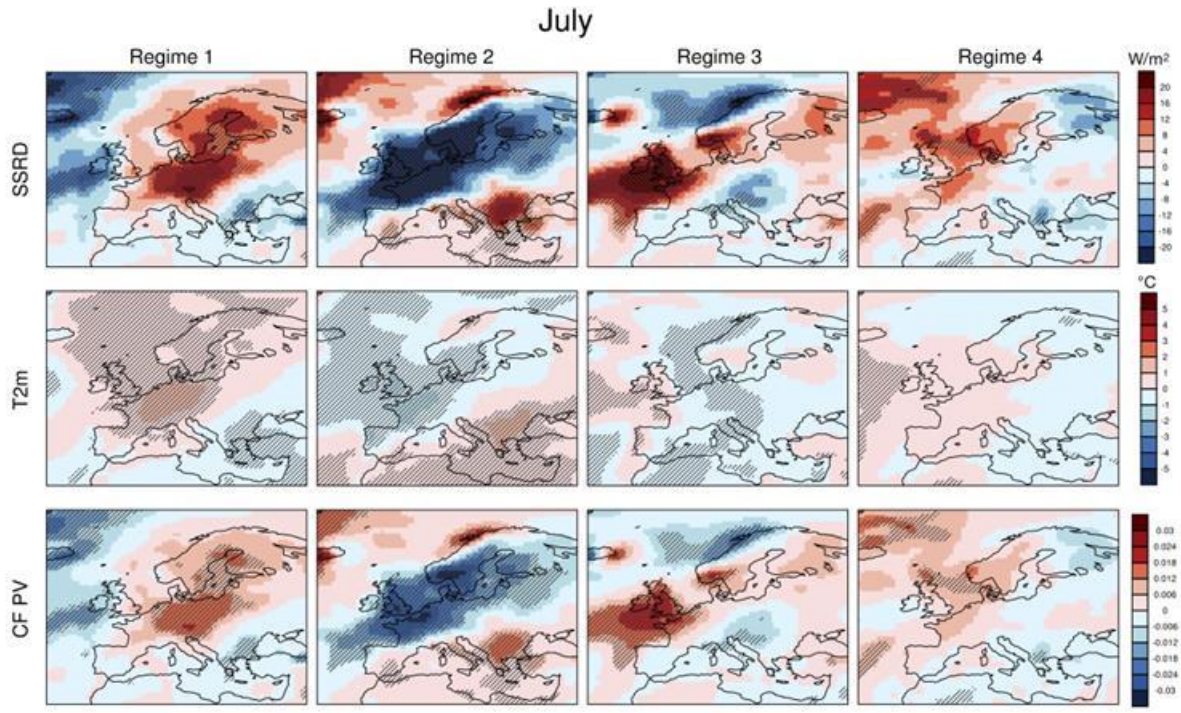

Figure 82: Impact of Euro-Atlantic weather regimes on SSRD (first row), 2 meters temperature (second row) and CF (third row) during July 1981-2016. Hatches indicate that anomalies are significant at the 95% confidence level.

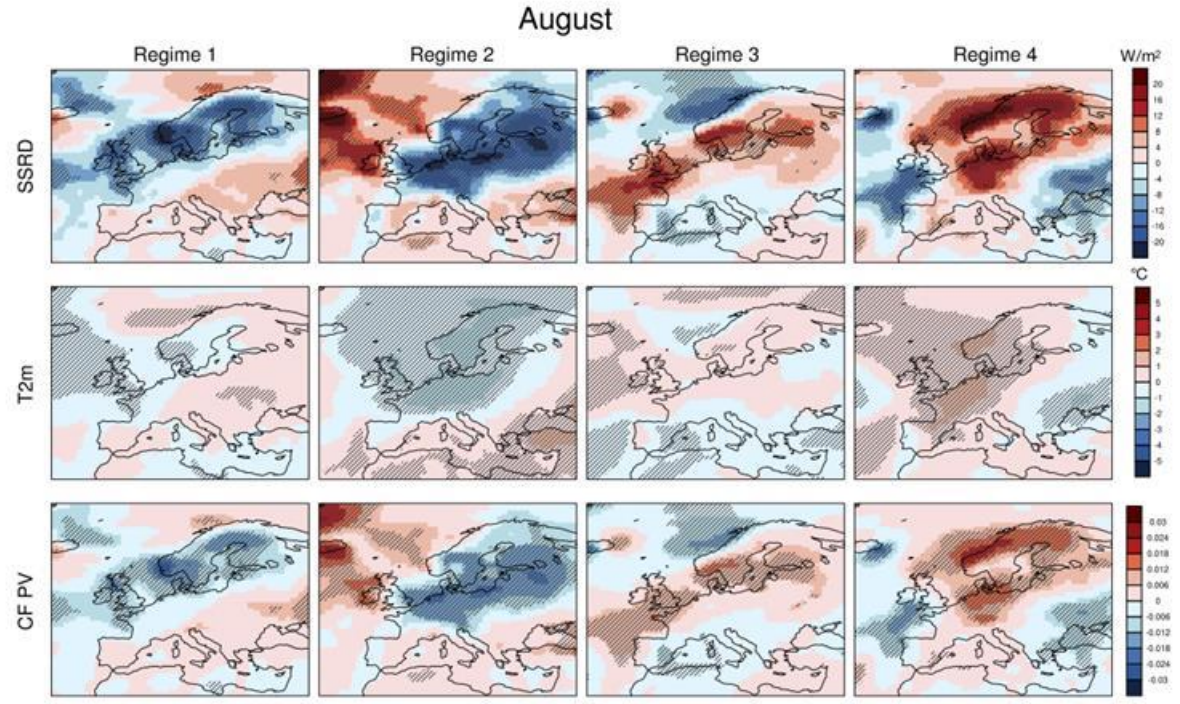

Figure 83: Impact of Euro-Atlantic weather regimes on SSRD (first row), 2 meters temperature (second row) and CF (third row) during August 1981-2016. Hatches indicate that anomalies are significant at the 95% confidence level.

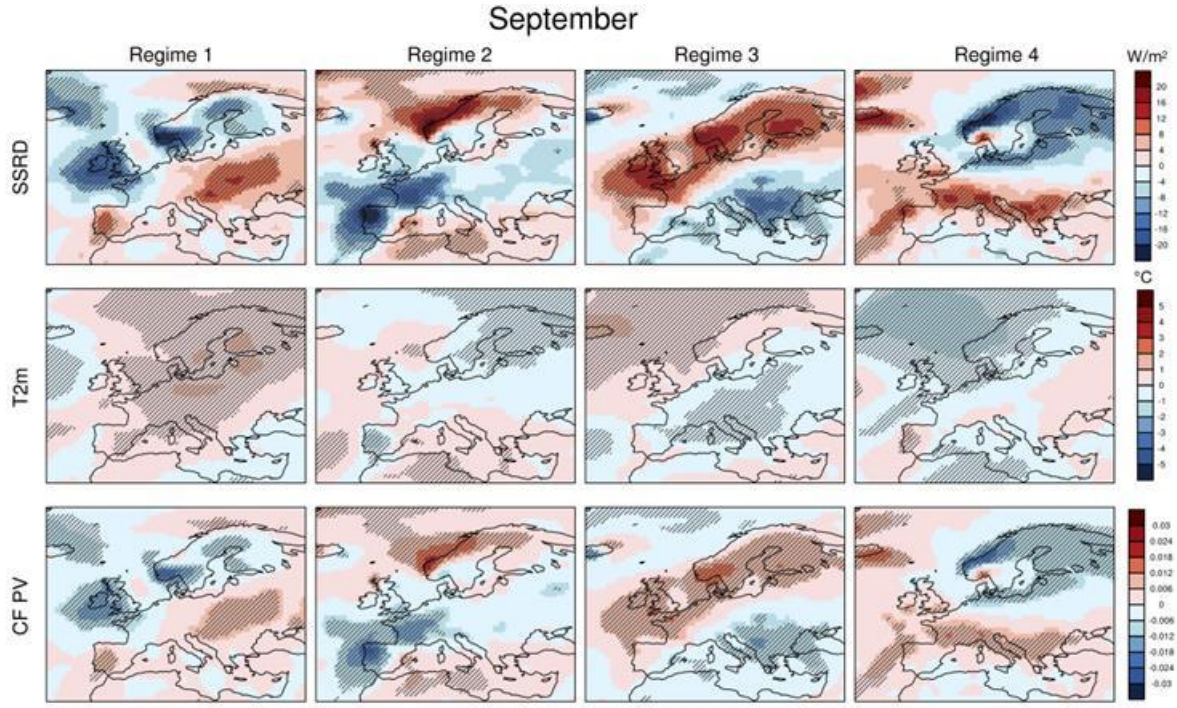

Figure 84: Impact of Euro-Atlantic weather regimes on SSRD (first row), 2 meters temperature (second row) and CF (third row) during September 1981-2016. Hatches indicate that anomalies are significant at the 95% confidence level.

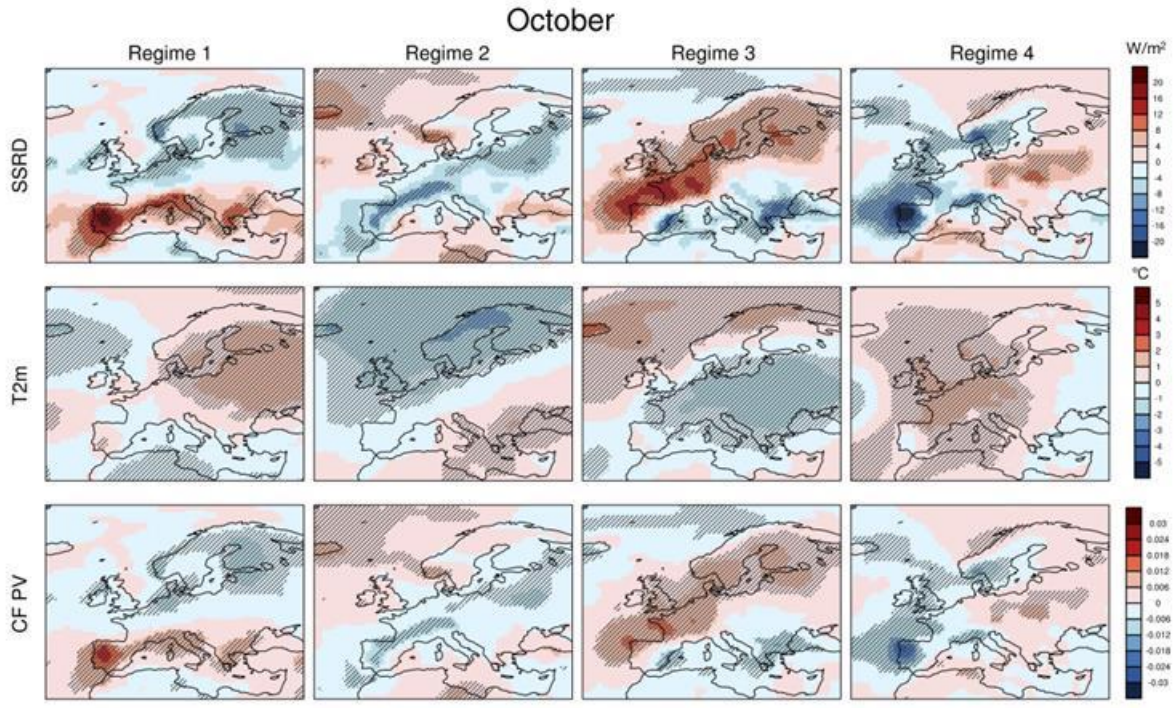

Figure 85: Impact of Euro-Atlantic weather regimes on SSRD (first row), 2 meters temperature (second row) and CF (third row) during October 1981-2016. Hatches indicate that anomalies are significant at the 95% confidence level.

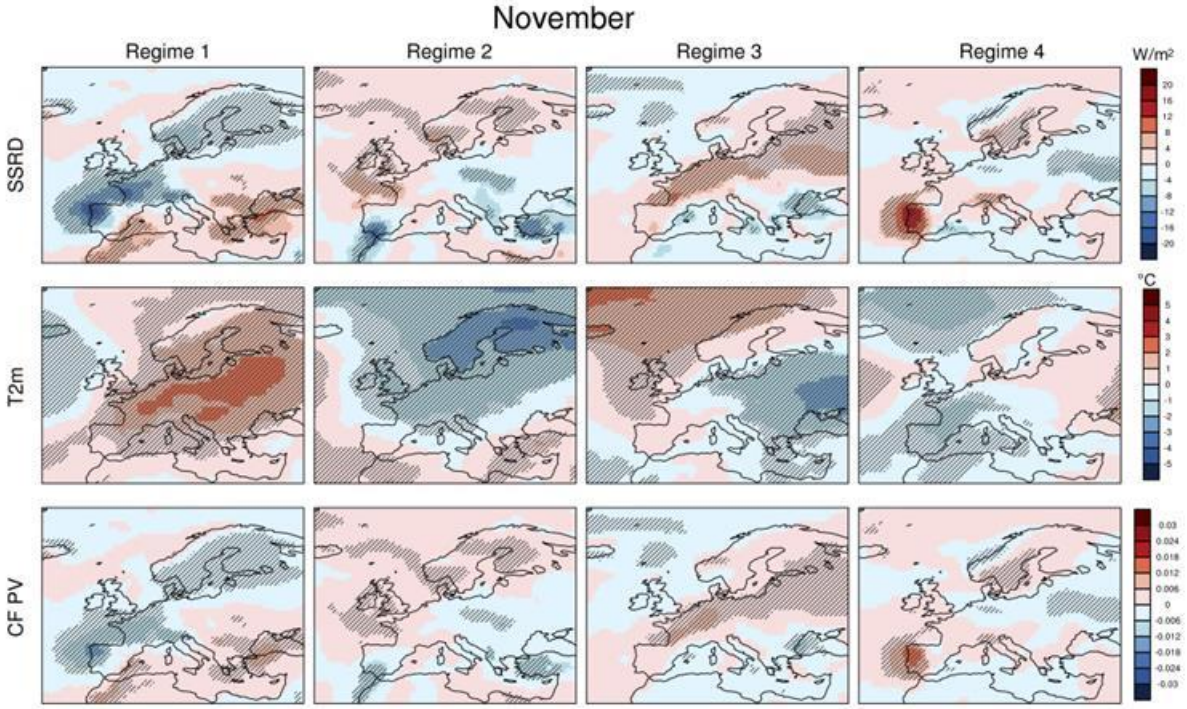

Figure 86: Impact of Euro-Atlantic weather regimes on SSRD (first row), 2 meters temperature (second row) and CF (third row) during November 1981-2016. Hatches indicate that anomalies are significant at the 95% confidence level.

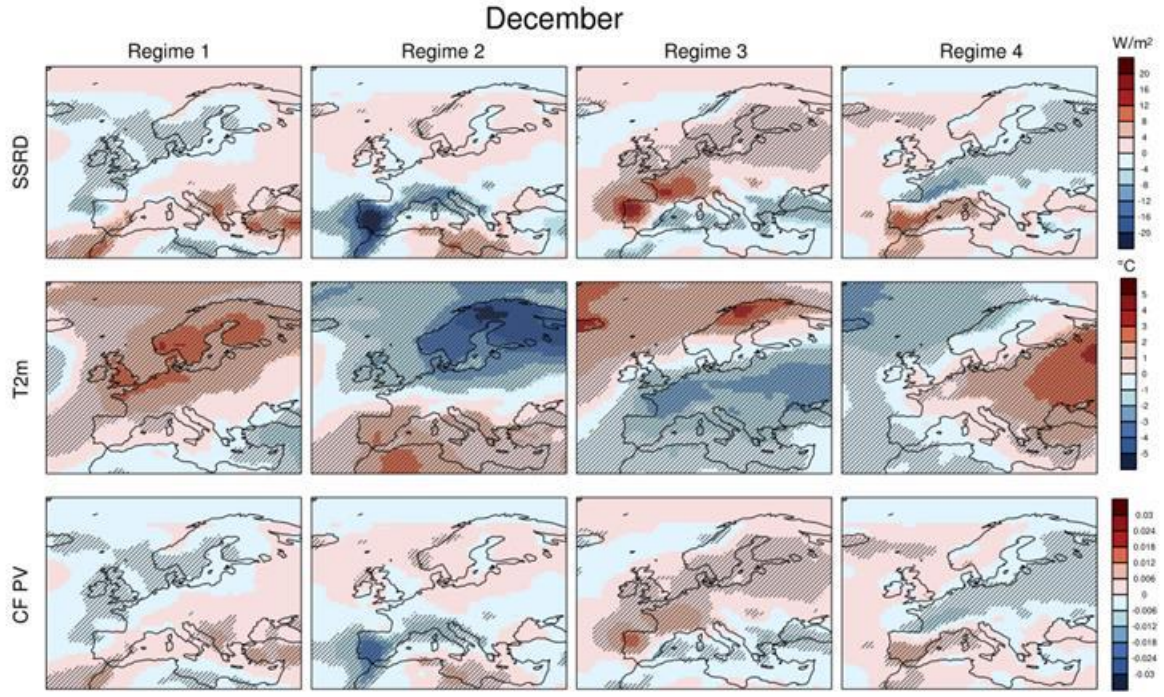

Figure 87: Impact of Euro-Atlantic weather regimes on SSRD (first row), 2 meters temperature (second row) and CF (third row) during December 1981-2016. Hatches indicate that anomalies are significant at the 95% confidence level.

ANNEX D: Influence of climate variability on hydropower generation

D.1 Impacts of modelled seasonal inflow volumes conditioned using teleconnections.

Table 5: Bootstrapped MAESS (mean absolute error skill score) for modelled seasonal inflow volumes conditioned using teleconnections averaged over all sub-basins. Values above zero indicate that conditioned seasonal inflows have skill over the unconditioned reference approach; values below zero indicate no skill.

	Lead time								
	1	2	3	4	5	6	7	8	9
Jan	-0.013	-0.022	0.002	-0.033	0.002	-0.033	0.005	0.004	-0.003
Feb	0.004	0.003	0.002	0.006	0.007	0.002	0.007	0.007	0.006
Mar	-0.041	0.045	0.002	-0.013	-0.009	-0.014	0.010	-0.006	-0.008
Apr	0.025	-0.008	-0.001	0.014	0.000	0.011	-0.012	0.004	0.011
Maj	0.060	0.025	0.036	0.021	0.044	0.054	0.005	0.009	0.025
Jun	0.048	0.025	0.018	0.025	0.022	0.029	0.022	0.031	0.023
Jul	0.015	0.007	-0.002	0.003	0.002	0.029	0.004	0.026	0.011
Aug	0.016	0.007	0.009	0.010	0.008	0.009	0.013	0.011	0.010
Sep	0.009	0.008	0.003	0.013	-0.007	0.001	0.012	0.015	0.011
Okt	0.003	0.004	0.006	0.003	0.002	0.004	0.005	0.000	0.005
Nov	0.009	0.008	0.014	0.018	0.017	0.016	0.011	0.012	0.012
Dec	0.008	0.009	0.008	0.010	0.007	0.002	0.005	0.009	0.008

Table 6: Bootstrapped FY^{+} (frequency of years), for modelled seasonal inflow volumes conditioned using teleconnections averaged over all sub-basins. Values above 50% indicate that conditioned seasonal inflows perform better than the unconditioned reference approach more often than not.

	Lead time								
	1	2	3	4	5	6	7	8	9
Jan	44.4	50.0	50.0	44.4	50.0	50.0	50.0	50.0	50.0
Feb	55.6	50.0	50.0	55.6	55.6	50.0	55.6	55.6	55.6
Mar	44.4	55.6	50.0	50.0	50.0	50.0	55.6	50.0	55.6
Apr	50.0	50.0	50.0	55.6	50.0	50.0	50.0	50.0	50.0
Maj	55.6	55.6	55.6	55.6	55.6	61.1	55.6	55.6	55.6
Jun	61.1	55.6	55.6	55.6	55.6	55.6	55.6	55.6	55.6
Jul	50.0	55.6	50.0	50.0	50.0	55.6	50.0	55.6	50.0
Aug	55.6	55.6	55.6	55.6	55.6	55.6	55.6	61.1	55.6
Sep	61.1	55.6	55.6	55.6	50.0	55.6	61.1	61.1	61.1

Okt	61.1	61.1	72.2	66.7	61.1	61.1	61.1	55.6	66.7
Nov	66.7	66.7	72.2	77.8	83.3	77.8	77.8	77.8	77.8
Dec	66.7	66.7	66.7	72.2	72.2	61.1	66.7	72.2	66.7

D.2 Impacts of modelled seasonal inflow volumes conditioned using hydrological weather regimes.

Table 7: Bootstrapped MAESS (mean absolute error skill score) for modelled seasonal inflows conditioned using weather regimes averaged over all sub-basins. Values above zero indicate that conditioned seasonal inflows have skill over the unconditioned reference approach; values below zero indicate no skill.

	Lead time								
	1	2	3	4	5	6	7	8	9
Jan	-0.043	-0.048	-0.034	-0.043	-0.008	-0.038	-0.026	0.007	-0.045
Feb	0.006	0.005	0.006	0.006	0.006	0.007	0.007	0.009	0.008
Mar	0.005	0.000	0.021	-0.046	-0.007	-0.016	-0.008	0.011	0.012
Apr	0.005	0.015	0.033	0.000	0.004	0.020	0.005	0.029	0.025
Maj	0.014	0.054	0.056	0.050	0.063	0.033	0.028	0.030	0.033
Jun	0.040	0.000	0.073	0.051	0.048	0.024	0.047	0.034	0.046
Jul	0.012	0.006	-0.002	0.000	0.018	0.004	0.014	0.018	0.008
Aug	0.035	0.026	0.007	0.037	0.024	0.014	0.012	0.014	0.015
Sep	0.006	0.009	0.008	0.002	0.005	0.011	0.007	0.004	0.005
Okt	0.003	0.002	0.004	0.002	0.000	0.002	0.001	0.005	0.000
Nov	0.018	0.011	0.010	0.017	0.012	0.003	0.006	0.006	0.008
Dec	0.011	0.010	0.003	0.015	0.005	0.013	0.007	0.010	0.008

Table 8: Bootstrapped FY+ (frequency of years), for modelled seasonal inflows conditioned using teleconnections averaged over all sub-basins. Values above 50% indicate that conditioned seasonal inflows perform better than the unconditioned reference approach more often than not.

	Lead time								
	1	2	3	4	5	6	7	8	9
Jan	44.4	44.4	44.4	44.4	44.4	50.0	44.4	50.0	44.4
Feb	50.0	55.6	55.6	50.0	50.0	55.6	55.6	55.6	55.6
Mar	55.6	50.0	55.6	50.0	55.6	50.0	50.0	50.0	55.6
Apr	50.0	55.6	55.6	50.0	50.0	55.6	50.0	55.6	55.6
Maj	55.6	61.1	55.6	55.6	55.6	55.6	55.6	55.6	55.6
Jun	55.6	50.0	55.6	55.6	55.6	55.6	55.6	55.6	55.6
Jul	55.6	50.0	55.6	55.6	50.0	50.0	50.0	55.6	50.0
Aug	55.6	55.6	55.6	55.6	55.6	55.6	55.6	55.6	55.6
Sep	55.6	55.6	61.1	55.6	55.6	55.6	55.6	55.6	61.1
Okt	66.7	55.6	61.1	61.1	55.6	61.1	55.6	55.6	50.0
Nov	77.8	66.7	72.2	77.8	77.8	61.1	66.7	66.7	66.7
Dec	66.7	66.7	55.6	77.8	66.7	72.2	66.7	72.2	72.2

ANNEX F: Influence of climate variability on energy demand

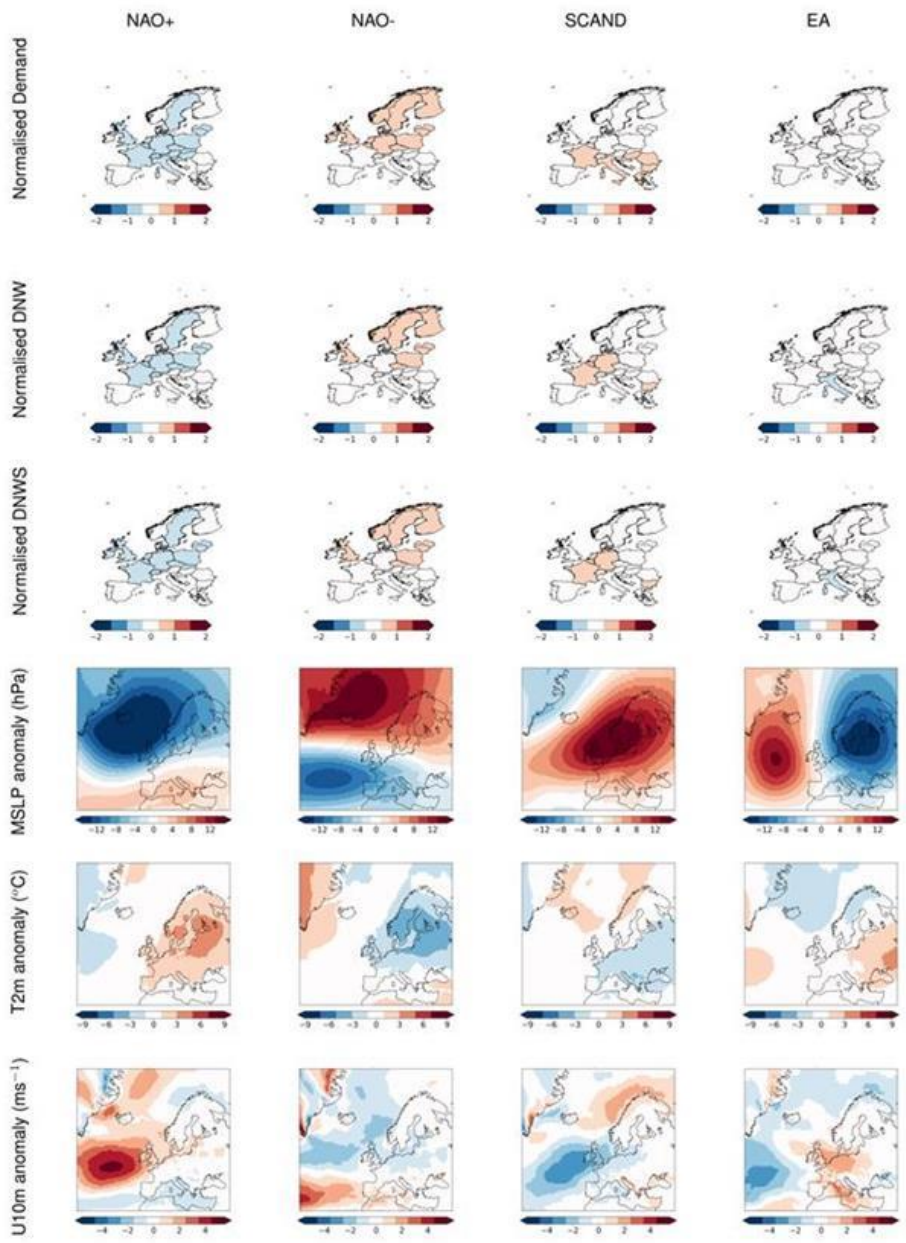

Figure 88: February normalised anomalies of demand, demand-net-wind (DNW) and demand-net-renewables (DNWS) associated with each of the traditional weather regimes: The two phases of the North Atlantic Oscillation (NAO+, NAO-), Scandinavian Blocking (SCAND) and the East Atlantic Pattern (EA). MSLP, 2m temperature and 10m wind speed anomalies for each regime are also presented (expressed as composites of fields relative to the 1981-2016 mean).

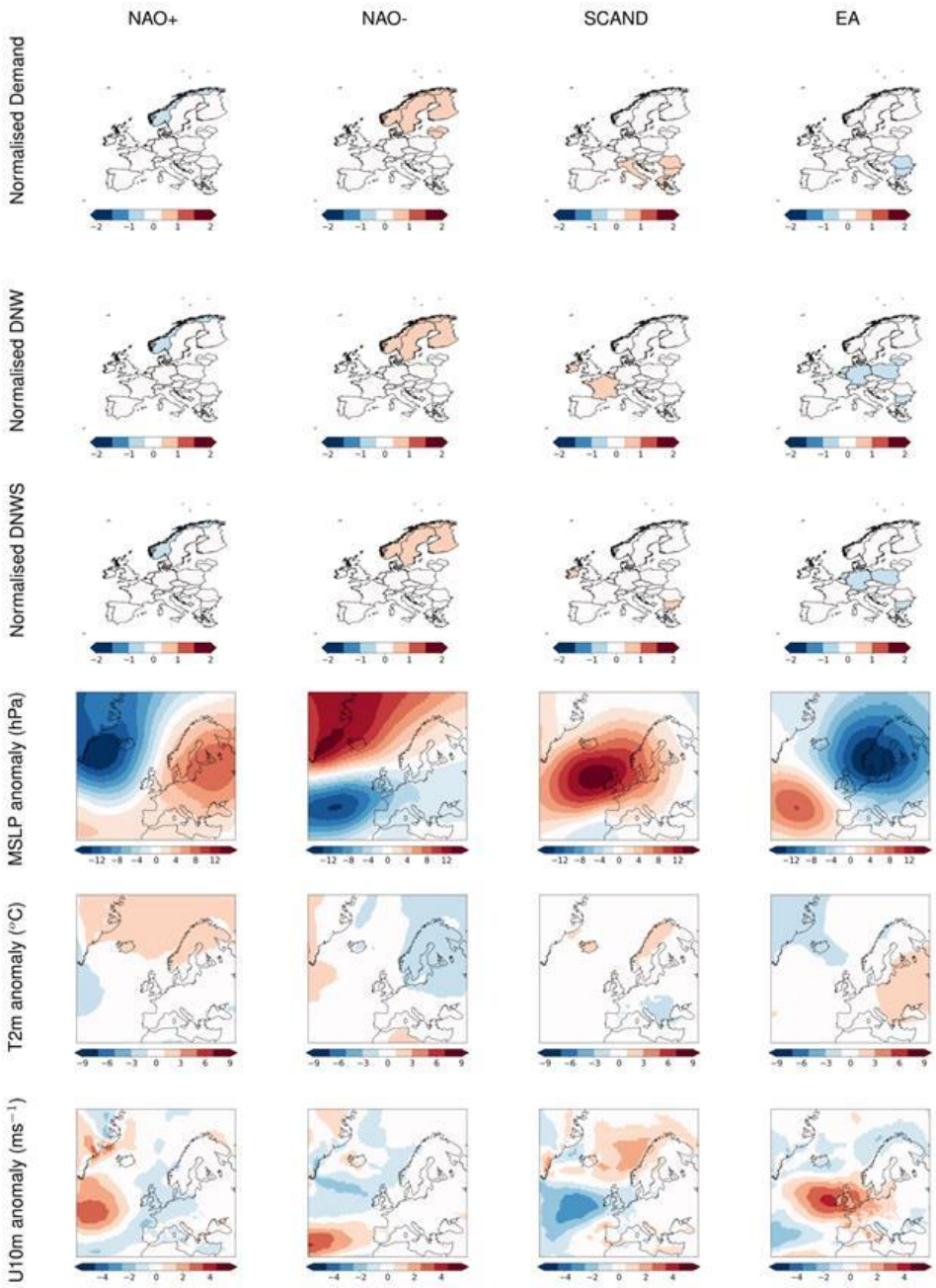

Figure 89: March normalised anomalies of demand, demand-net-wind (DNW) and demand-net-renewables (DNWS) associated with each of the traditional weather regimes: The two phases of the North Atlantic Oscillation (NAO+, NAO-), Scandinavian Blocking (SCAND) and the East Atlantic Pattern (EA). MSLP, 2m temperature and 10m wind speed anomalies for each regime are also presented (expressed as composites of fields relative to the 1981-2016 mean).

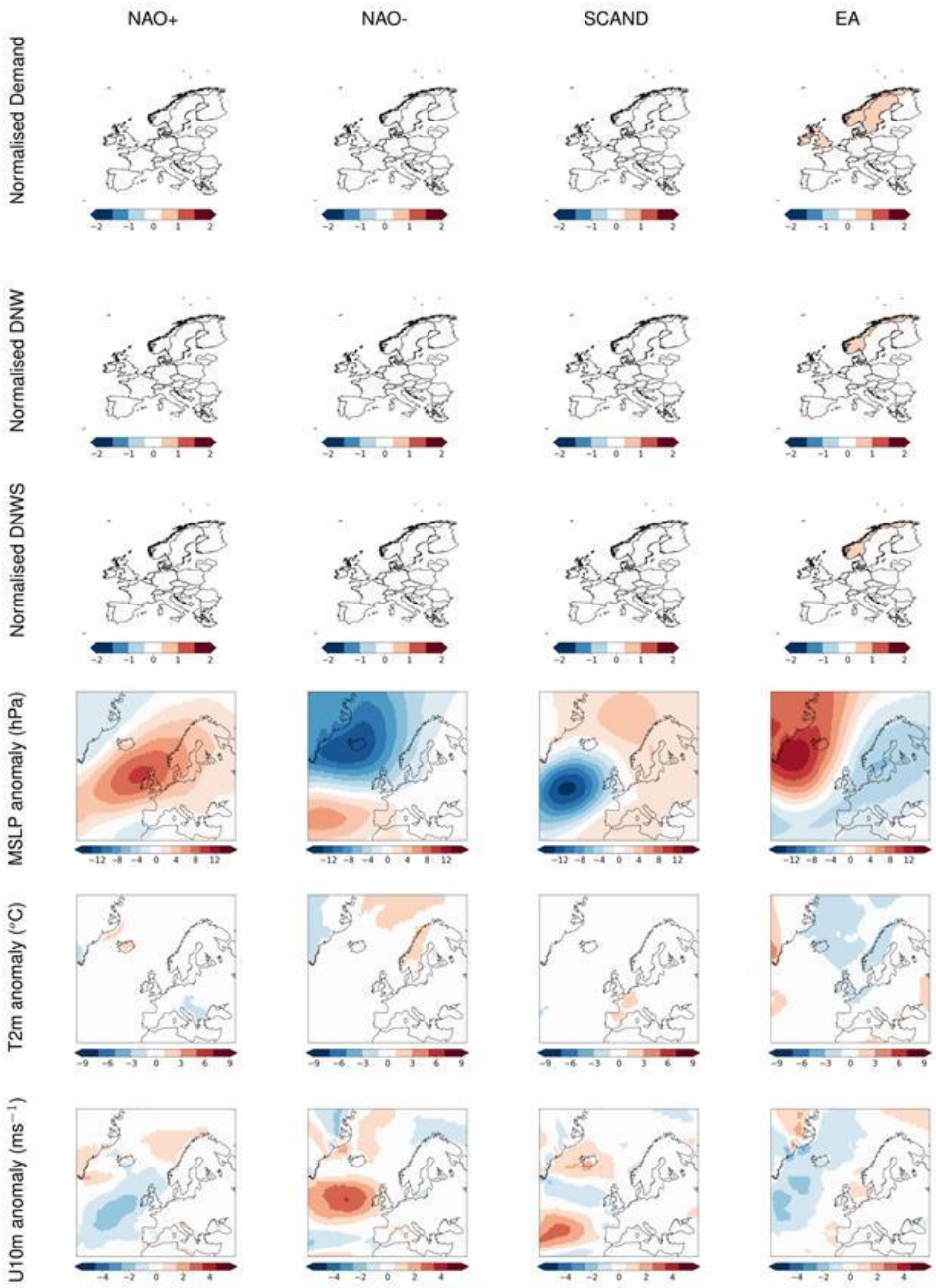

Figure 90: April normalised anomalies of demand, demand-net-wind (DNW) and demand-net-renewables (DNWS) associated with each of the traditional weather regimes: The two phases of the North Atlantic Oscillation (NAO+, NAO-), Scandinavian Blocking (SCAND) and the East Atlantic Pattern (EA). MSLP, 2m temperature and 10m wind speed anomalies for each regime are also presented (expressed as composites of fields relative to the 1981-2016 mean).

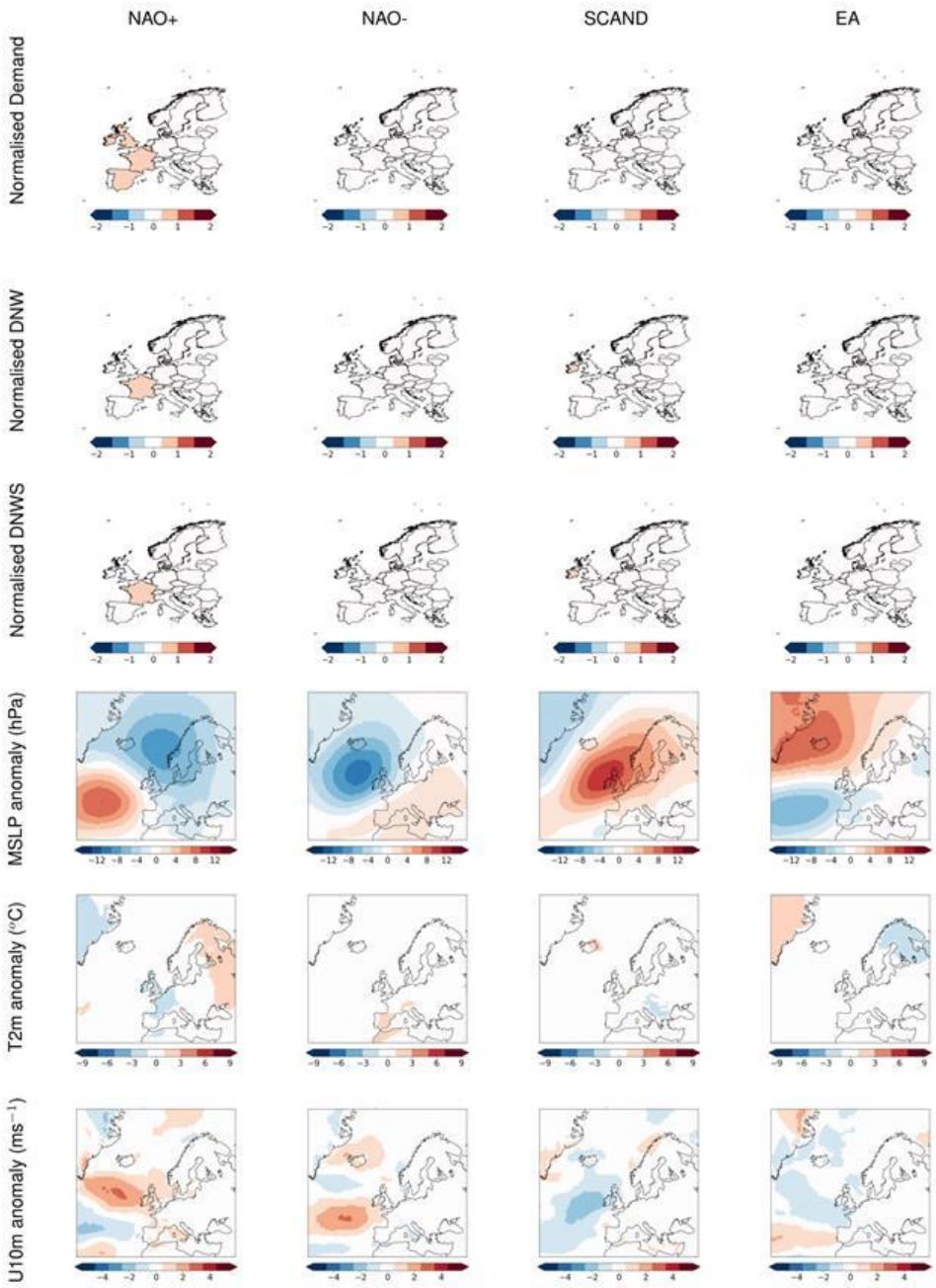

Figure 91: May normalised anomalies of demand, demand-net-wind (DNW) and demand-net-renewables (DNWS) associated with each of the traditional weather regimes: The two phases of the North Atlantic Oscillation (NAO+, NAO-), Scandinavian Blocking (SCAND) and the East Atlantic Pattern (EA). MSLP, 2m temperature and 10m wind speed anomalies for each regime are also presented (expressed as composites of fields relative to the 1981-2016 mean).

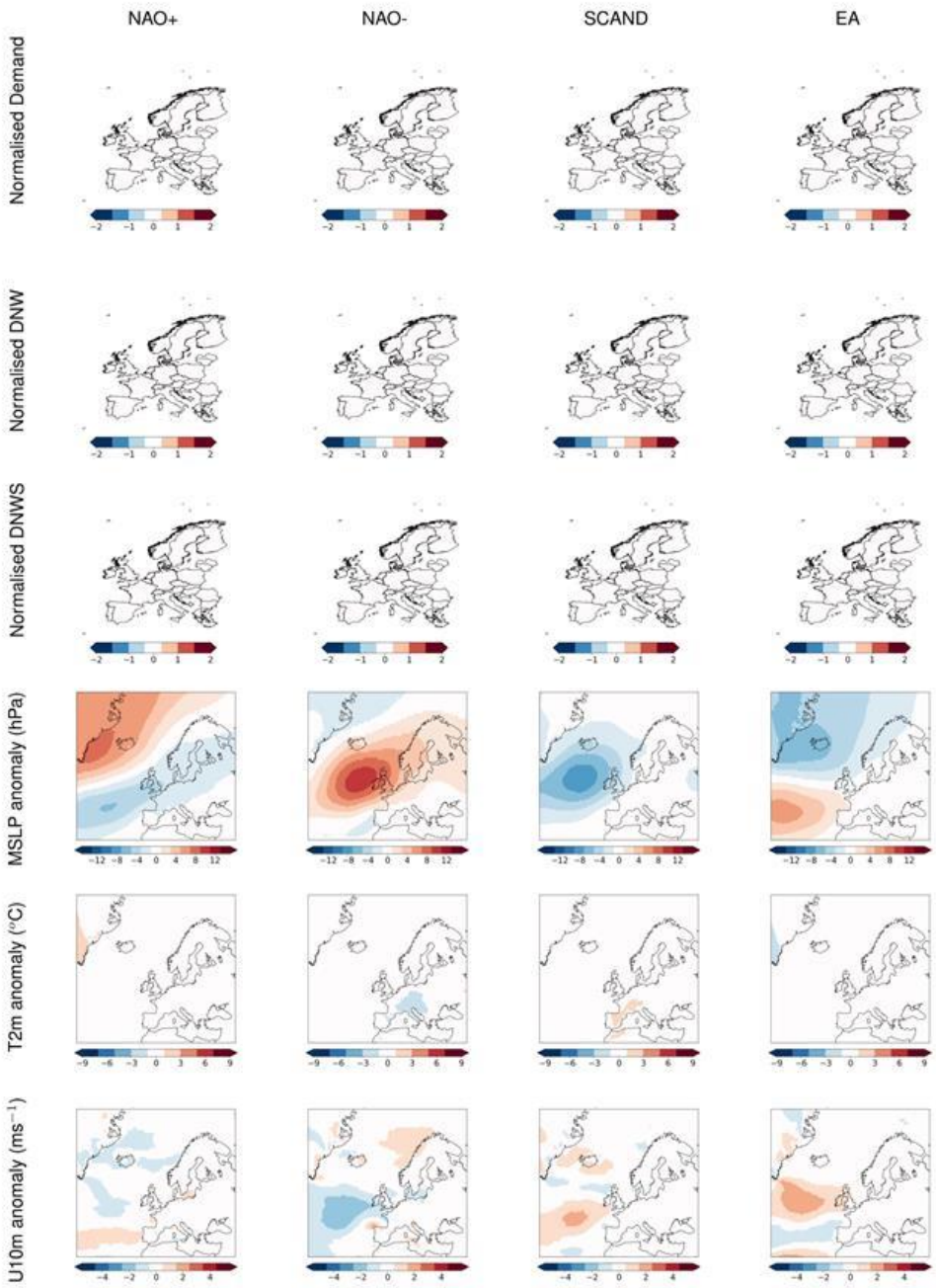

Figure 92: June normalised anomalies of demand, demand-net-wind (DNW) and demand-net-renewables (DNWS) associated with each of the traditional weather regimes: The two phases of the North Atlantic Oscillation (NAO+, NAO-), Scandinavian Blocking (SCAND) and the East Atlantic Pattern (EA). MSLP, 2m temperature and 10m wind speed anomalies for each regime are also presented (expressed as composites of fields relative to the 1981-2016 mean).

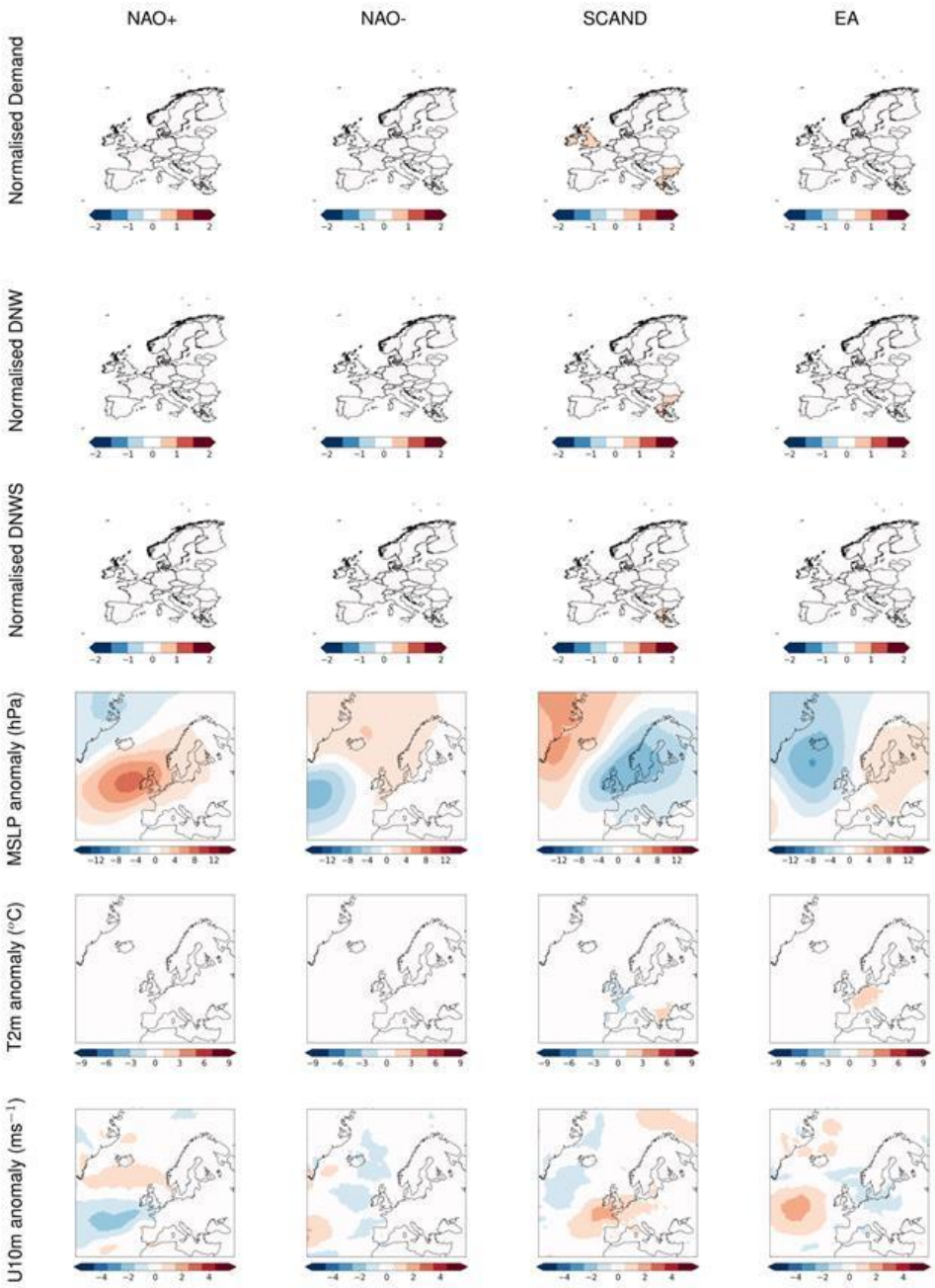

Figure 93: July normalised anomalies of demand, demand-net-wind (DNW) and demand-net-renewables (DNWS) associated with each of the traditional weather regimes: The two phases of the North Atlantic Oscillation (NAO+, NAO-), Scandinavian Blocking (SCAND) and the East Atlantic Pattern (EA). MSLP, 2m temperature and 10m wind speed anomalies for each regime are also presented (expressed as composites of fields relative to the 1981-2016 mean).

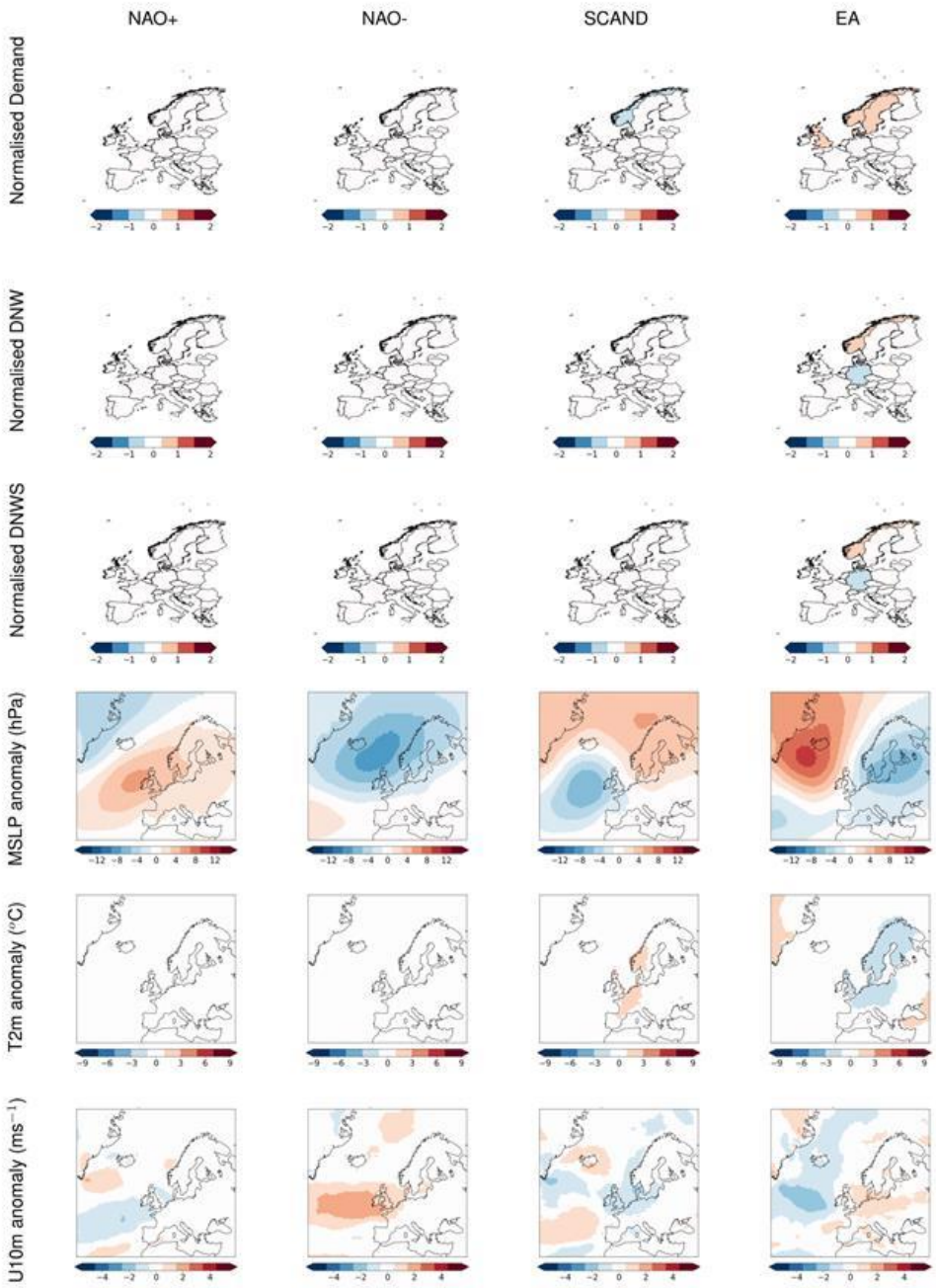

Figure 94: August normalised anomalies of demand, demand-net-wind (DNW) and demand-net-renewables (DNWS) associated with each of the traditional weather regimes: The two phases of the North Atlantic Oscillation (NAO+, NAO-), Scandinavian Blocking (SCAND) and the East Atlantic Pattern (EA). MSLP, 2m temperature and 10m wind speed anomalies for each regime are also presented (expressed as composites of fields relative to the 1981-2016 mean).

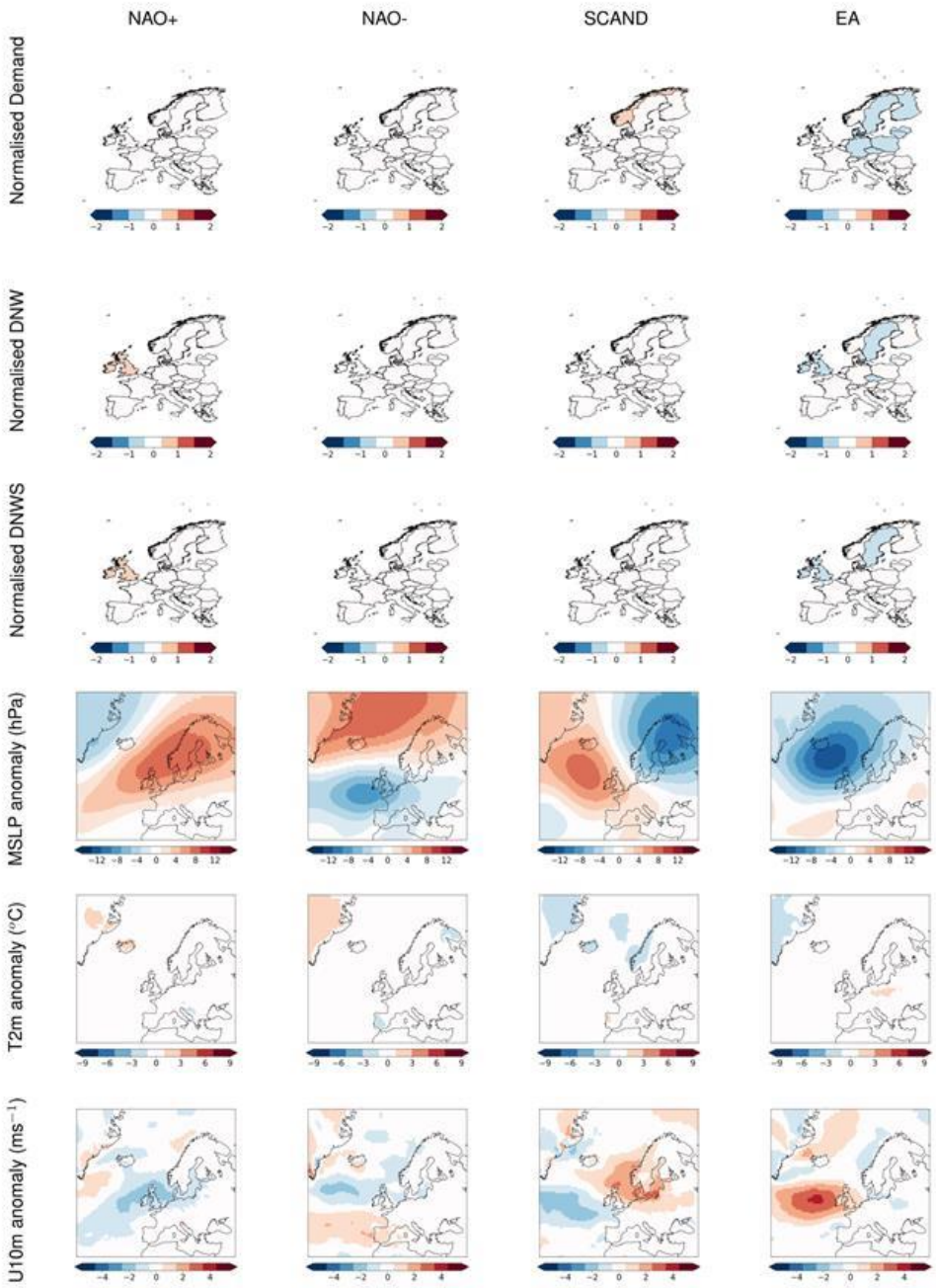

Figure 95: September normalised anomalies of demand, demand-net-wind (DNW) and demand-net-renewables (DNWS) associated with each of the traditional weather regimes: The two phases of the North Atlantic Oscillation (NAO+, NAO-), Scandinavian Blocking (SCAND) and the East Atlantic Pattern (EA). MSLP, 2m temperature and 10m wind speed anomalies for each regime are also presented (expressed as composites of fields relative to the 1981-2016 mean).

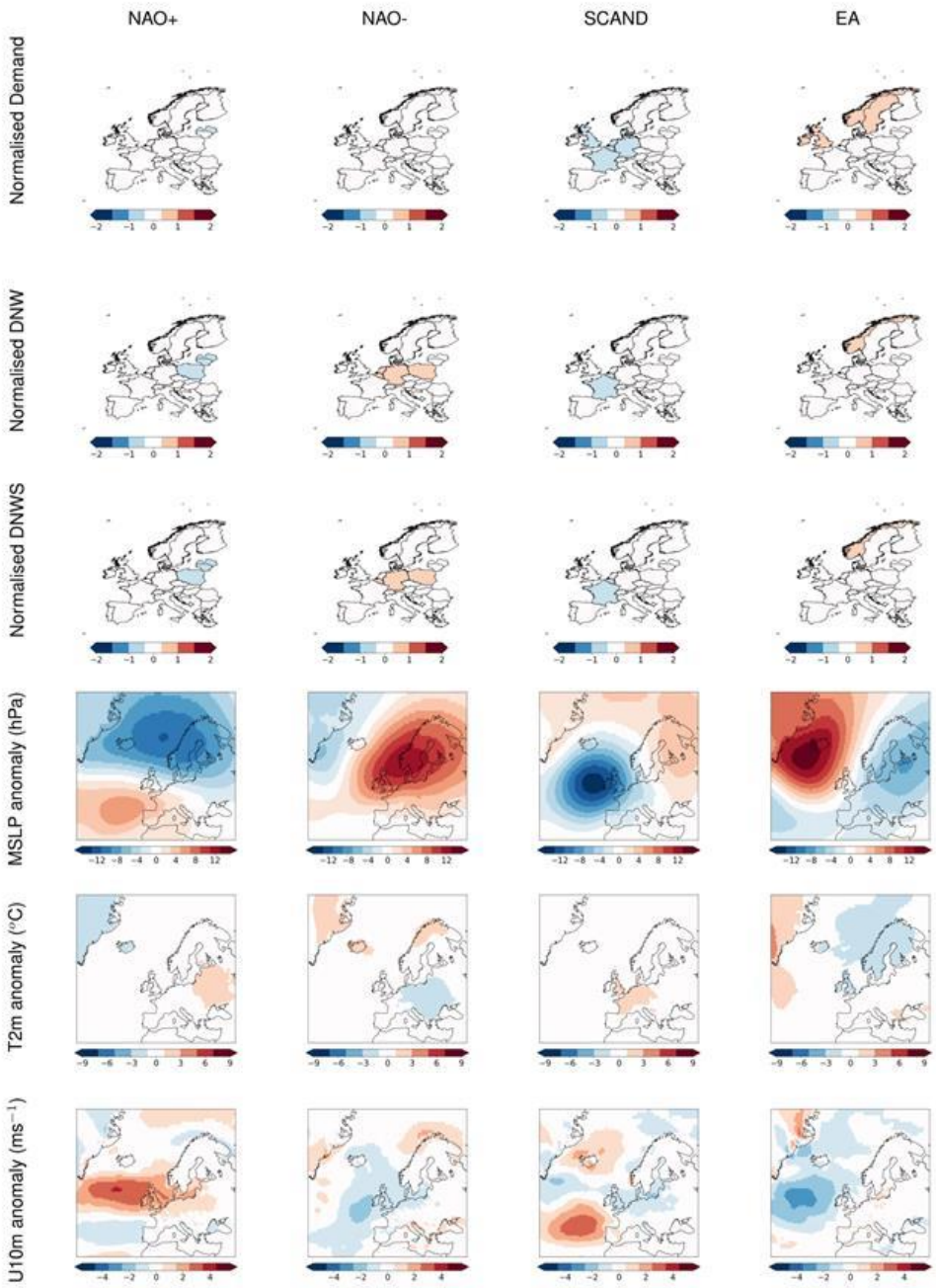

Figure 96: October normalised anomalies of demand, demand-net-wind (DNW) and demand-net-renewables (DNWS) associated with each of the traditional weather regimes: The two phases of the North Atlantic Oscillation (NAO+, NAO-), Scandinavian Blocking (SCAND) and the East Atlantic Pattern (EA). MSLP, 2m temperature and 10m wind speed anomalies for each regime are also presented (expressed as composites of fields relative to the 1981-2016 mean).

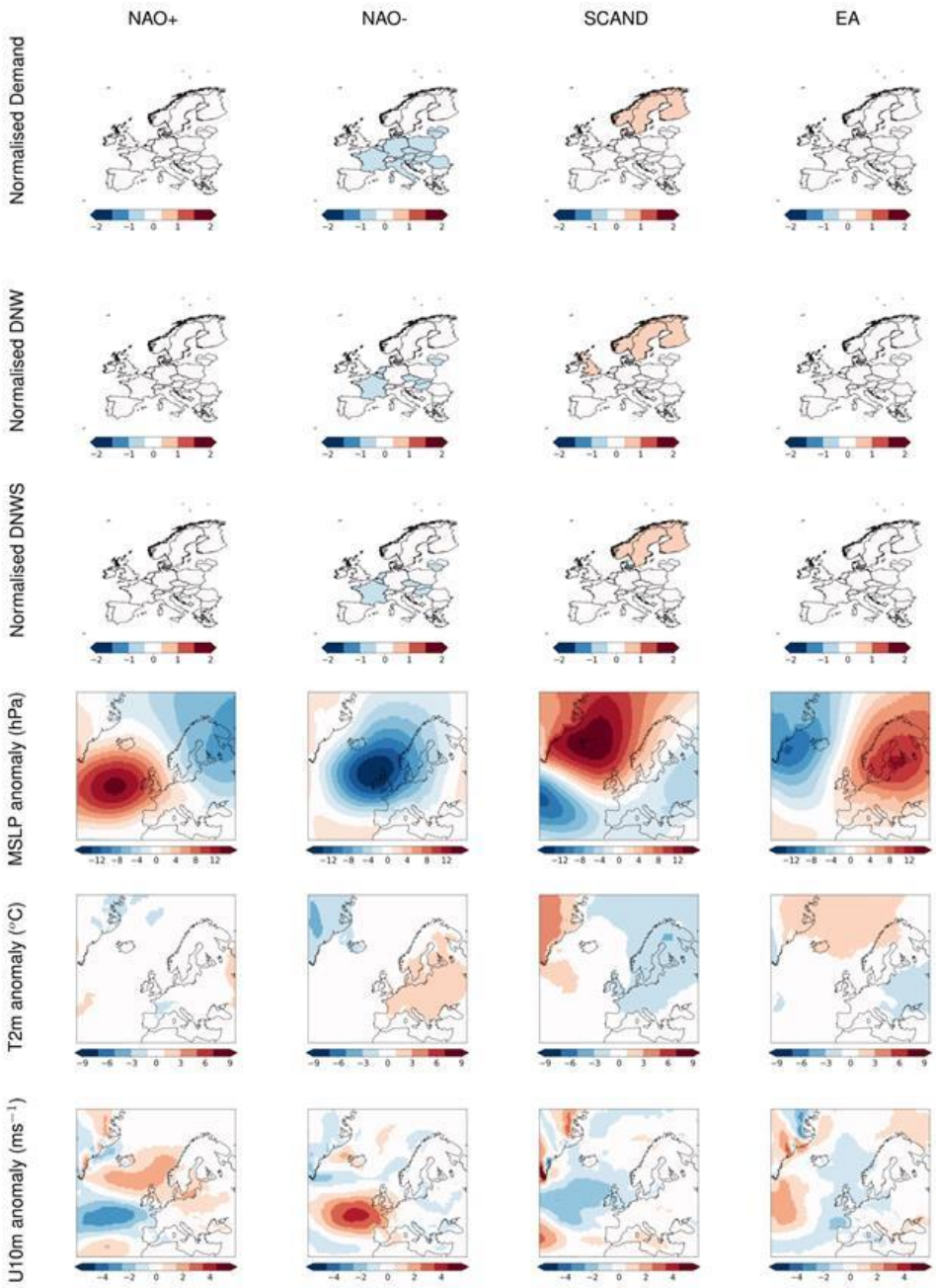

Figure 97: November normalised anomalies of demand, demand-net-wind (DNW) and demand-net-renewables (DNWS) associated with each of the traditional weather regimes: The two phases of the North Atlantic Oscillation (NAO+, NAO-), Scandinavian Blocking (SCAND) and the East Atlantic Pattern (EA). MSLP, 2m temperature and 10m wind speed anomalies for each regime are also presented (expressed as composites of fields relative to the 1981-2016 mean).

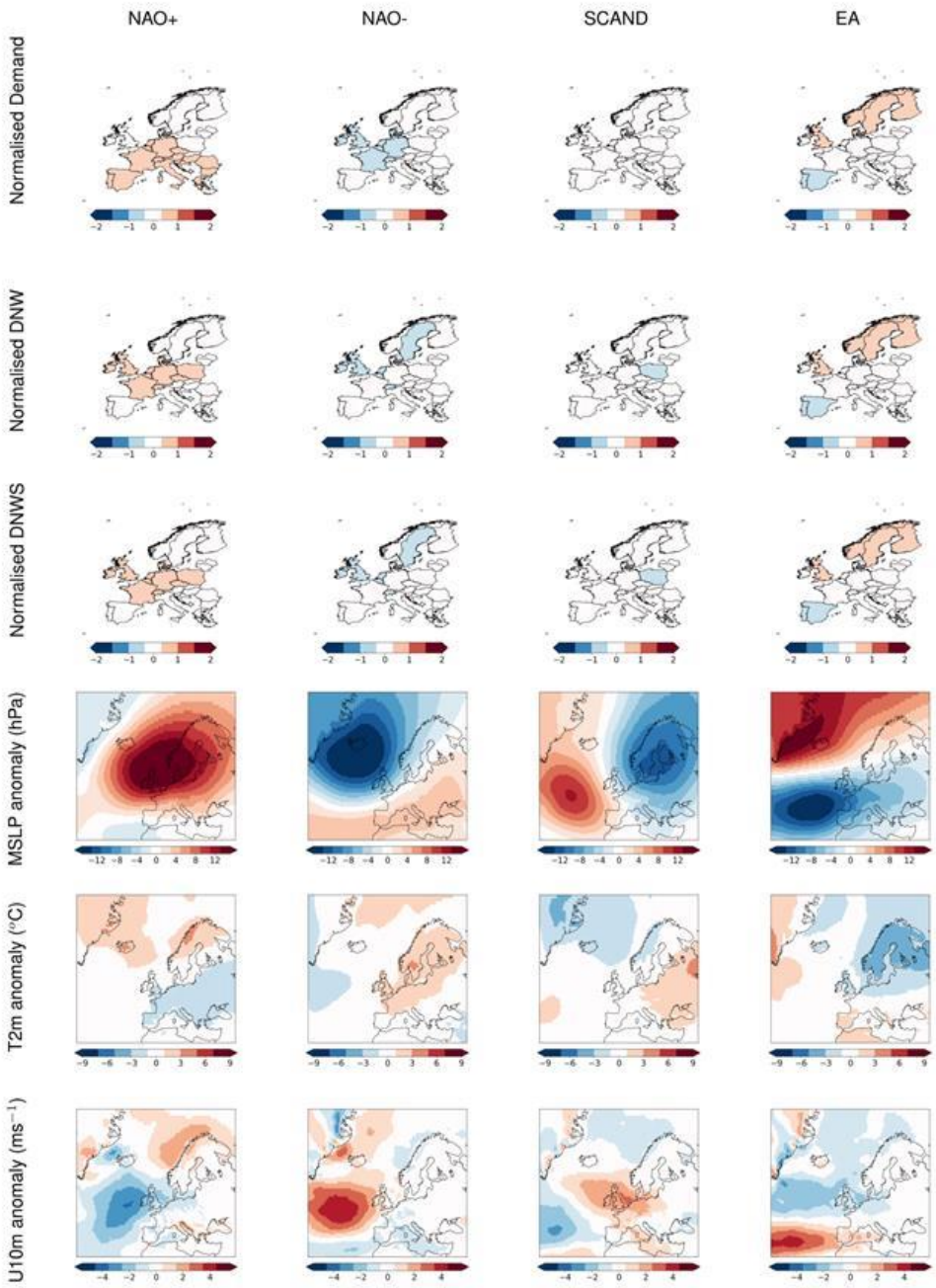

Figure 98: December normalised anomalies of demand, demand-net-wind (DNW) and demand-net-renewables (DNWS) associated with each of the traditional weather regimes: The two phases of the North Atlantic Oscillation (NAO+, NAO-), Scandinavian Blocking (SCAND) and the East Atlantic Pattern (EA). MSLP, 2m temperature and 10m wind speed anomalies for each regime are also presented (expressed as composites of fields relative to the 1981-2016 mean).

ANNEX G: The impact of impact regimes

G.1: Normalized demand anomalies

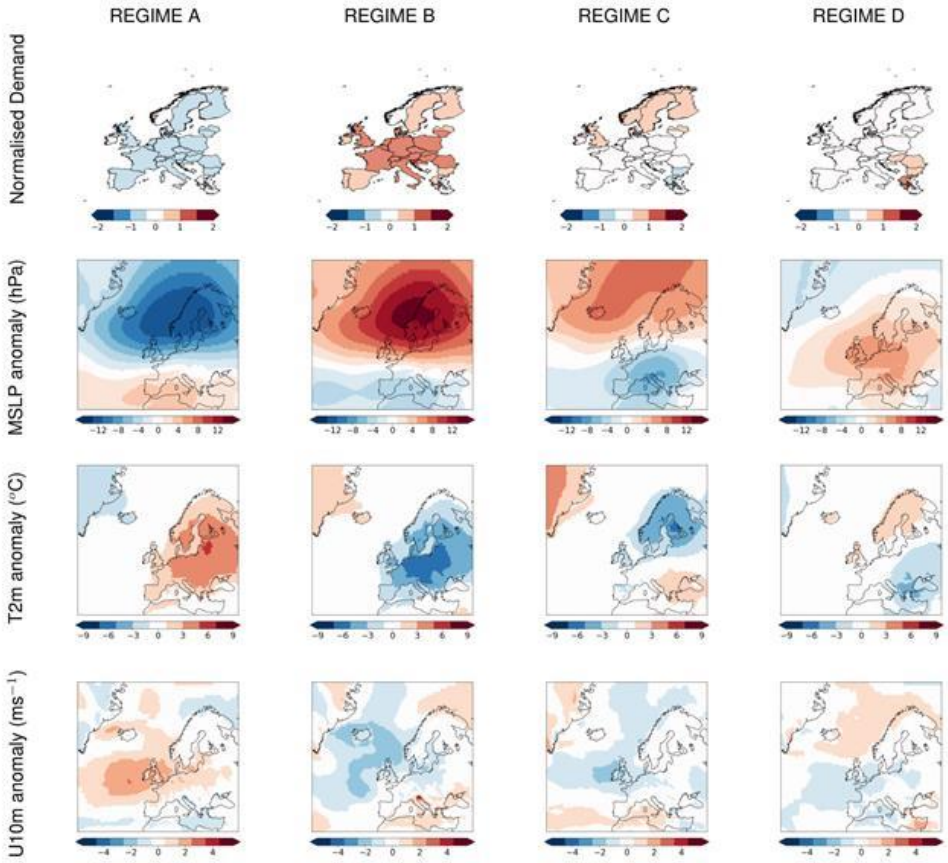

Figure 99: Impact regimes constructed from February normalized daily demand anomalies. Corresponding anomaly composites of meteorological fields relative to the climatological mean (1981-2016) for MSLP, 2m temperature, 10m surface wind speed are given below the relevant regime.

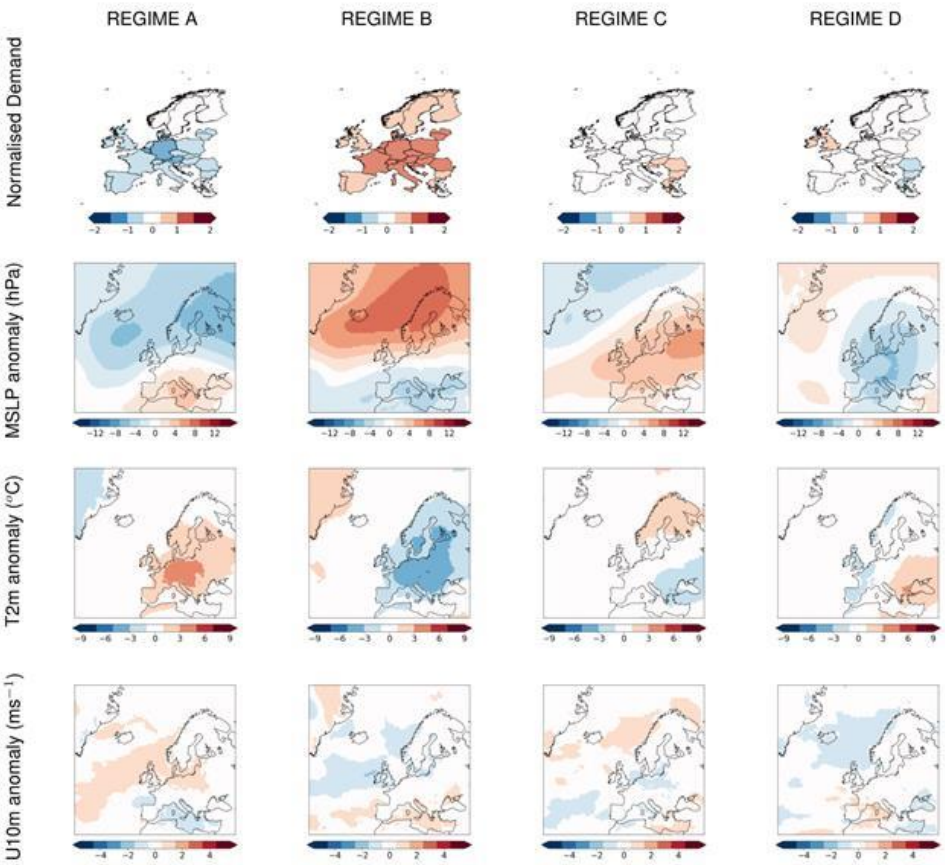

Figure 100: Impact regimes constructed from March normalized daily demand anomalies. Corresponding anomaly composites of meteorological fields relative to the climatological mean (1981-2016) for MSLP, 2m temperature, 10m surface wind speed are given below the relevant regime.

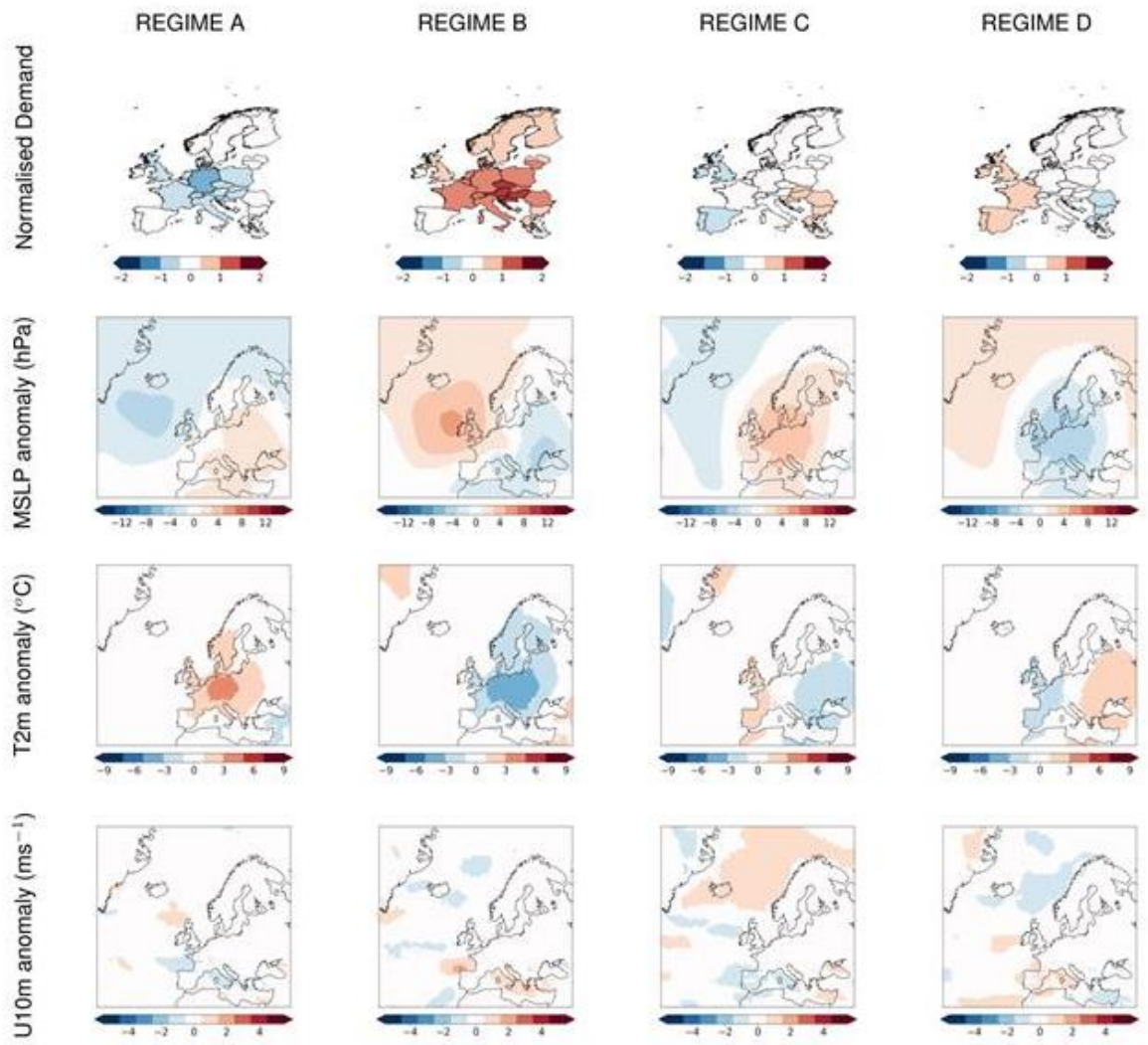

Figure 101: Impact regimes constructed from April normalized daily demand anomalies. Corresponding anomaly composites of meteorological fields relative to the climatological mean (1981-2016) for MSLP, 2m temperature, 10m surface wind speed are given below the relevant regime.

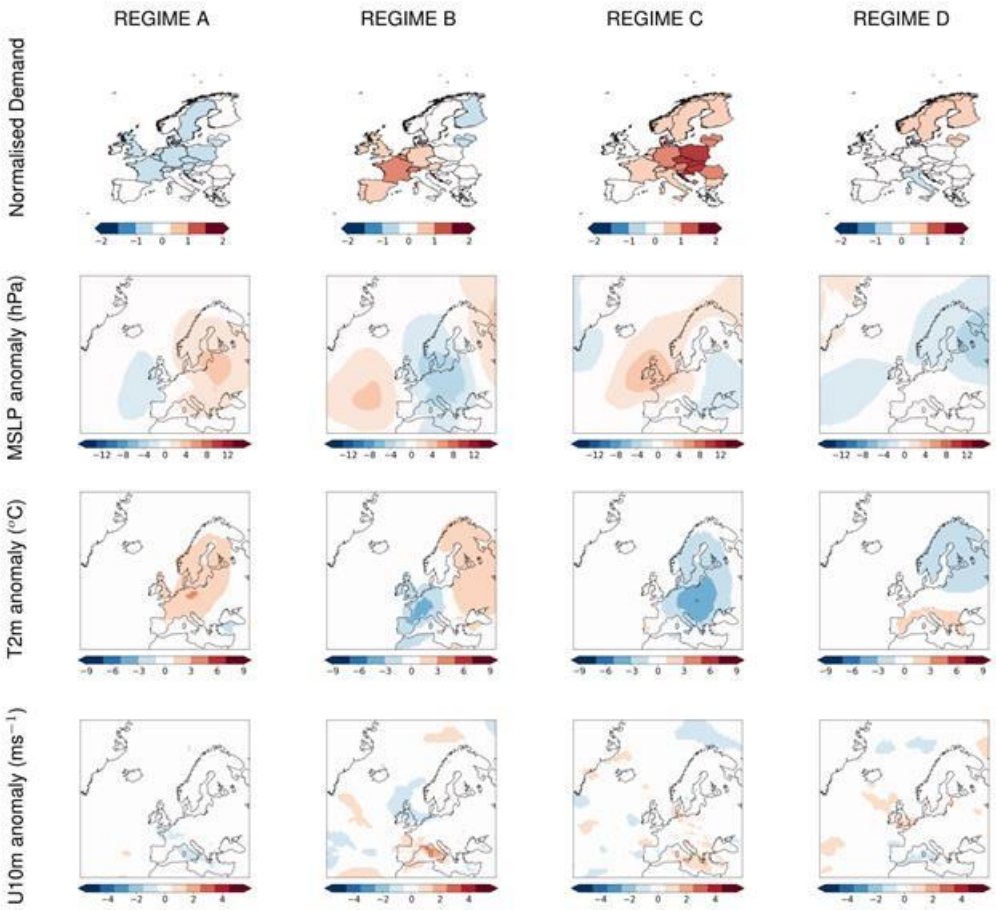

Figure 102: Impact regimes constructed from May normalized daily demand anomalies. Corresponding anomaly composites of meteorological fields relative to the climatological mean (1981-2016) for MSLP, 2m temperature, 10m surface wind speed are given below the relevant regime.

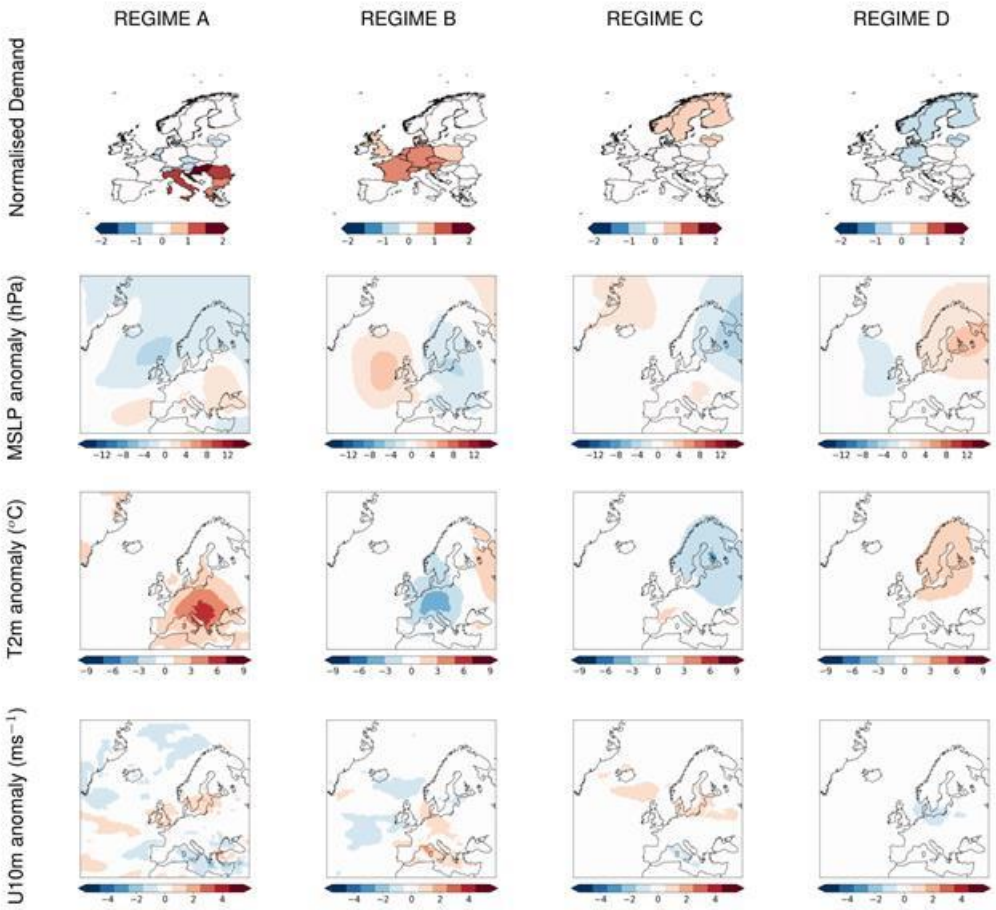

Figure 103: Impact regimes constructed from June normalized daily demand anomalies. Corresponding anomaly composites of meteorological fields relative to the climatological mean (1981-2016) for MSLP, 2m temperature, 10m surface wind speed are given below the relevant regime.

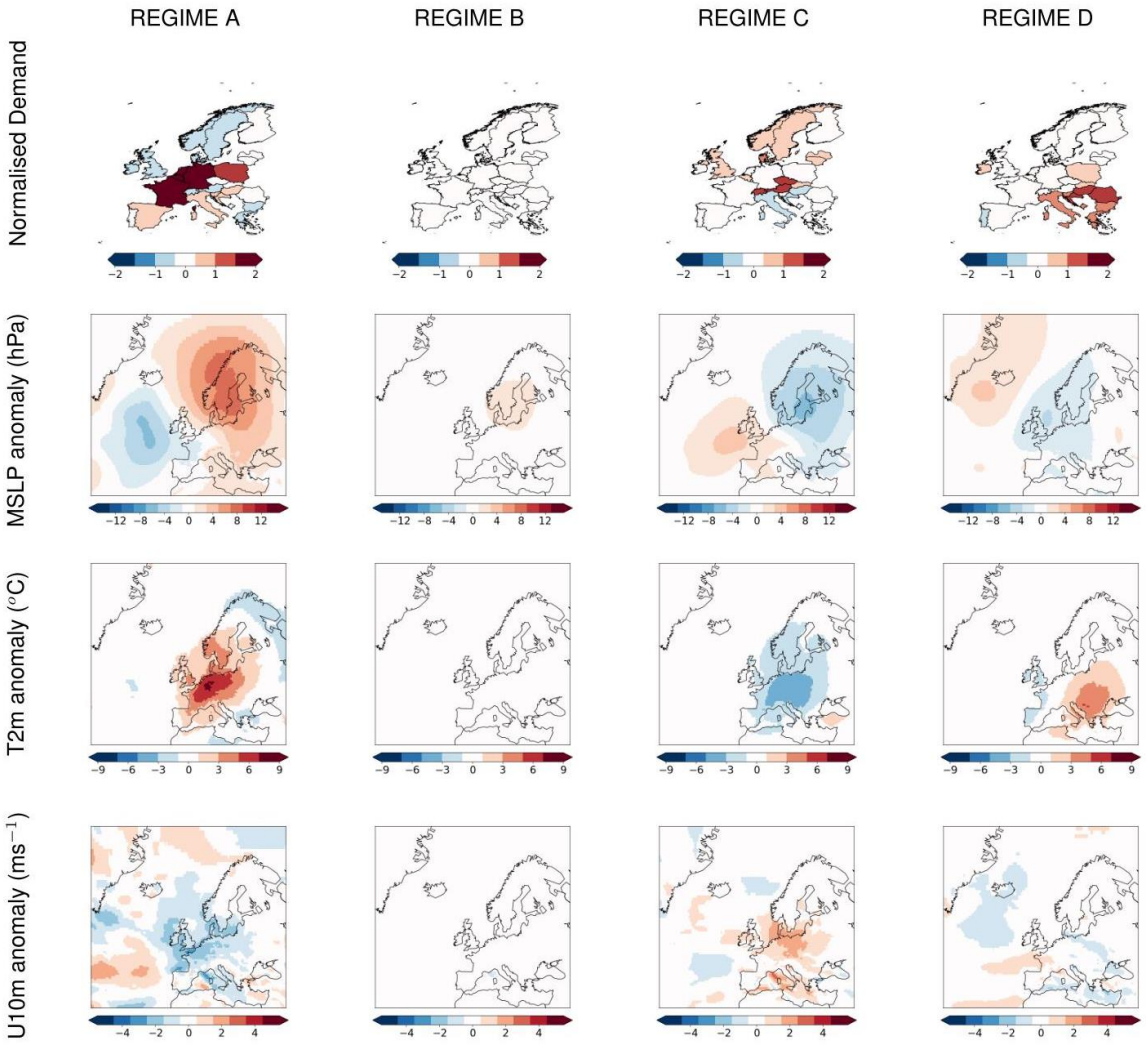

Figure 104: Impact regimes constructed from July normalized daily demand anomalies. Corresponding anomaly composites of meteorological fields relative to the climatological mean (1981-2016) for MSLP, 2m temperature, 10m surface wind speed are given below the relevant regime.

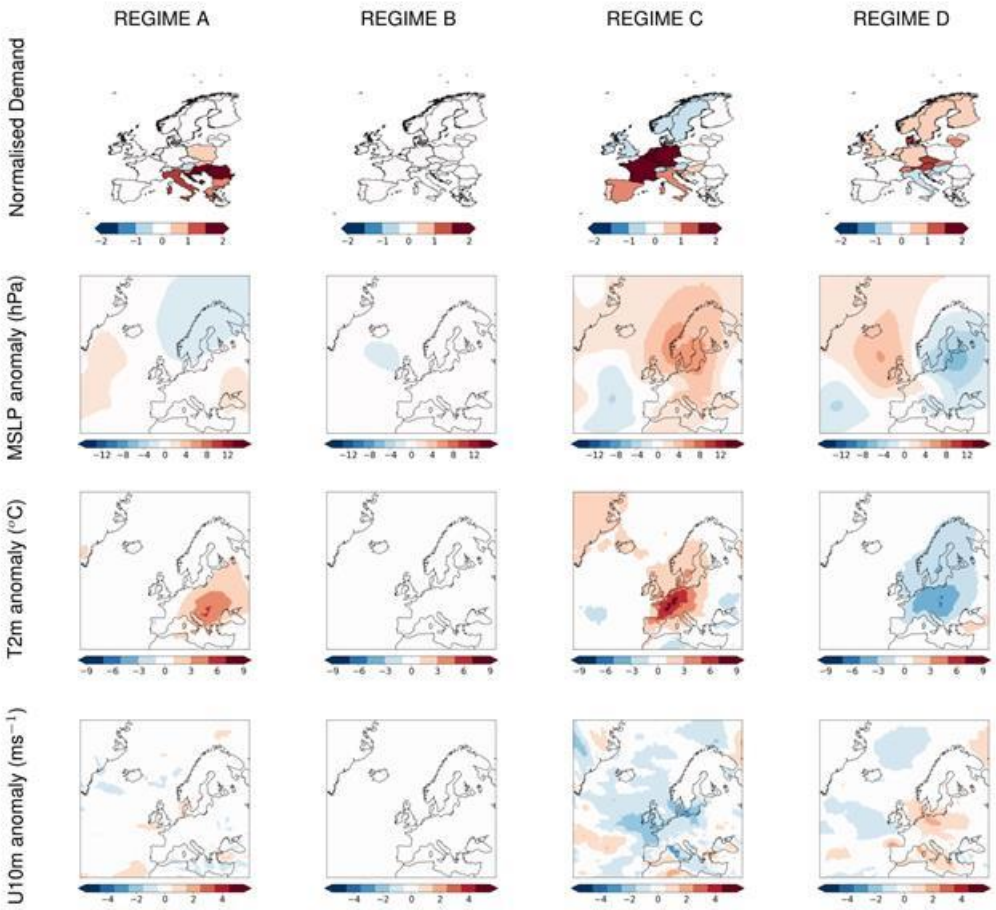

Figure 105: Impact regimes constructed from August normalized daily demand anomalies. Corresponding anomaly composites of meteorological fields relative to the climatological mean (1981-2016) for MSLP, 2m temperature, 10m surface wind speed are given below the relevant regime.

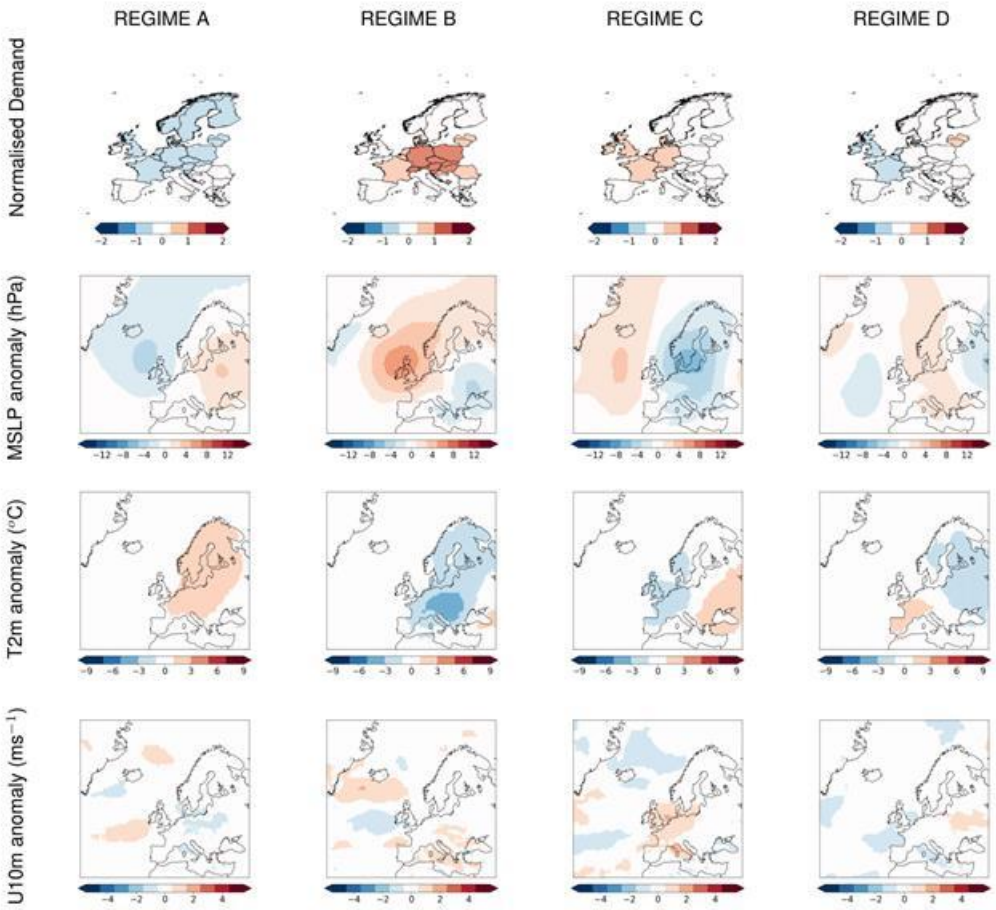

Figure 106: Impact regimes constructed from September normalized daily demand anomalies. Corresponding anomaly composites of meteorological fields relative to the climatological mean (1981-2016) for MSLP, 2m temperature, 10m surface wind speed are given below the relevant regime.

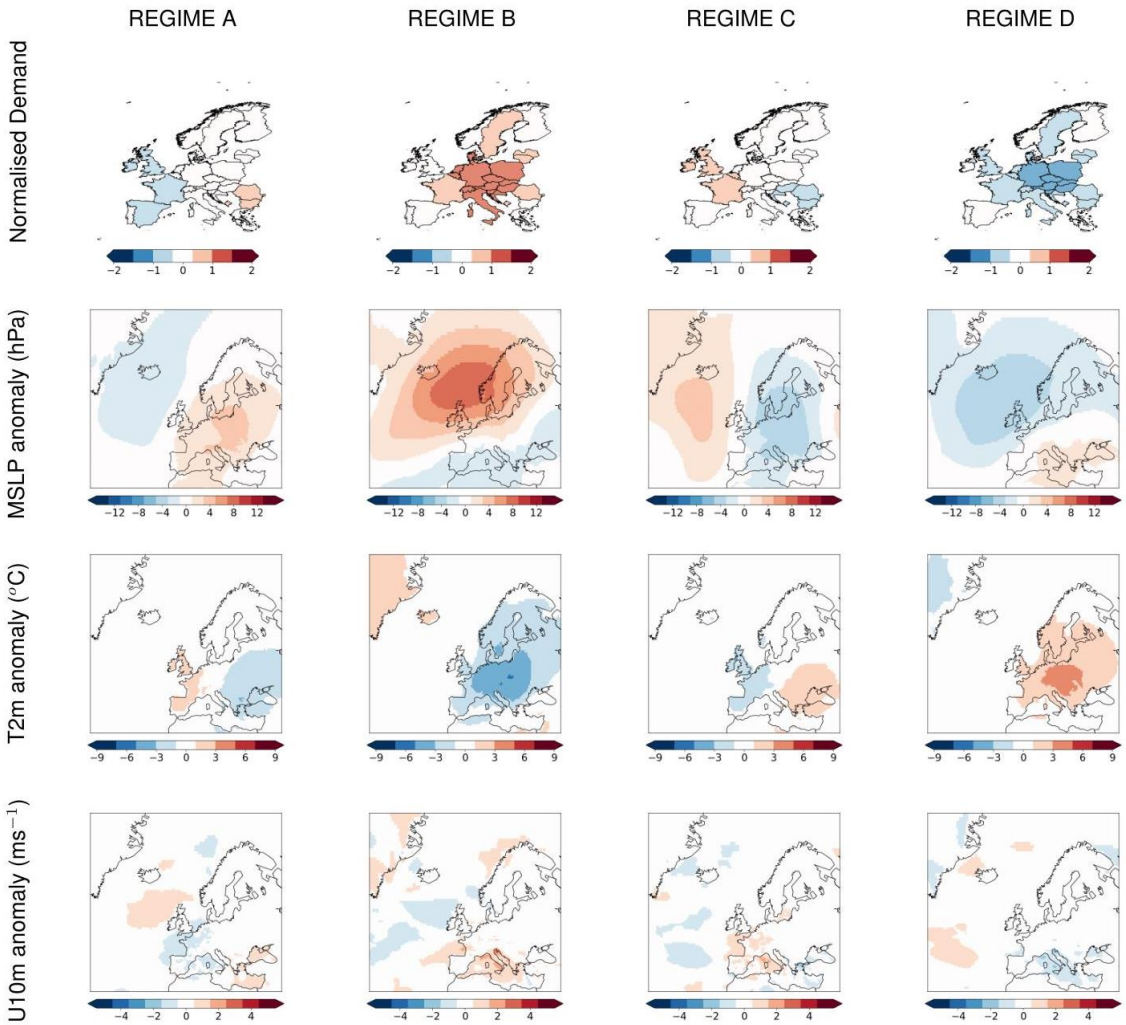

Figure 107: Impact regimes constructed from October normalized daily demand anomalies. Corresponding anomaly composites of meteorological fields relative to the climatological mean (1981-2016) for MSLP, 2m temperature, 10m surface wind speed are given below the relevant regime.

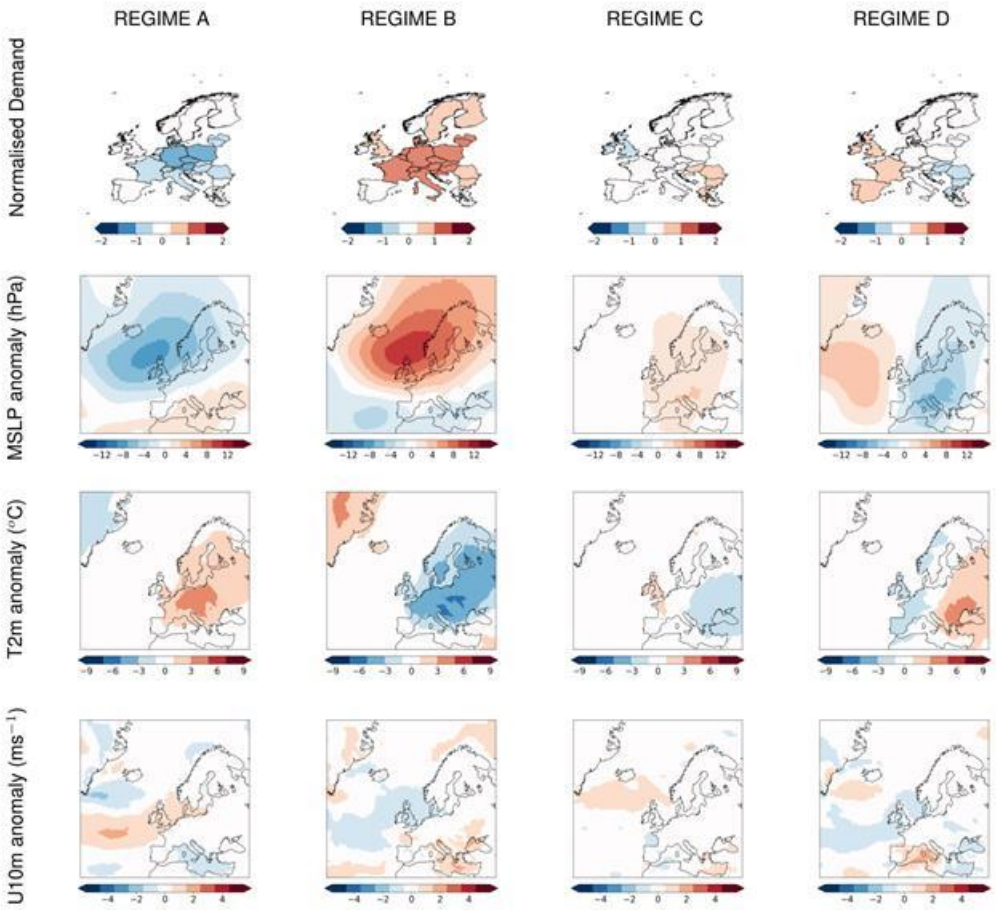

Figure 108: Impact regimes constructed from November normalized daily demand anomalies. Corresponding anomaly composites of meteorological fields relative to the climatological mean (1981-2016) for MSLP, 2m temperature, 10m surface wind speed are given below the relevant regime.

Figure 109: Impact regimes constructed from December normalized daily demand

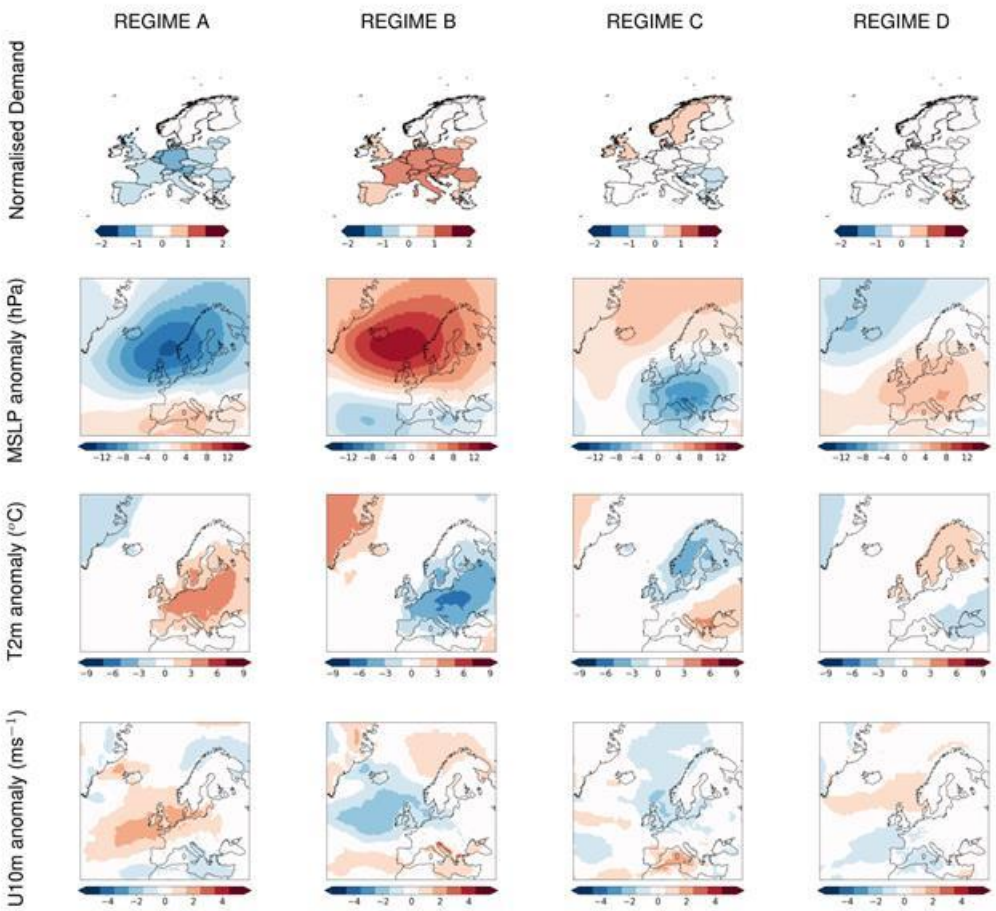

anomalies. Corresponding anomaly composites of meteorological fields relative to the climatological mean (1981-2016) for MSLP, 2m temperature, 10m surface wind speed are given below the relevant regime.

G.2: Normalized demand-net-wind

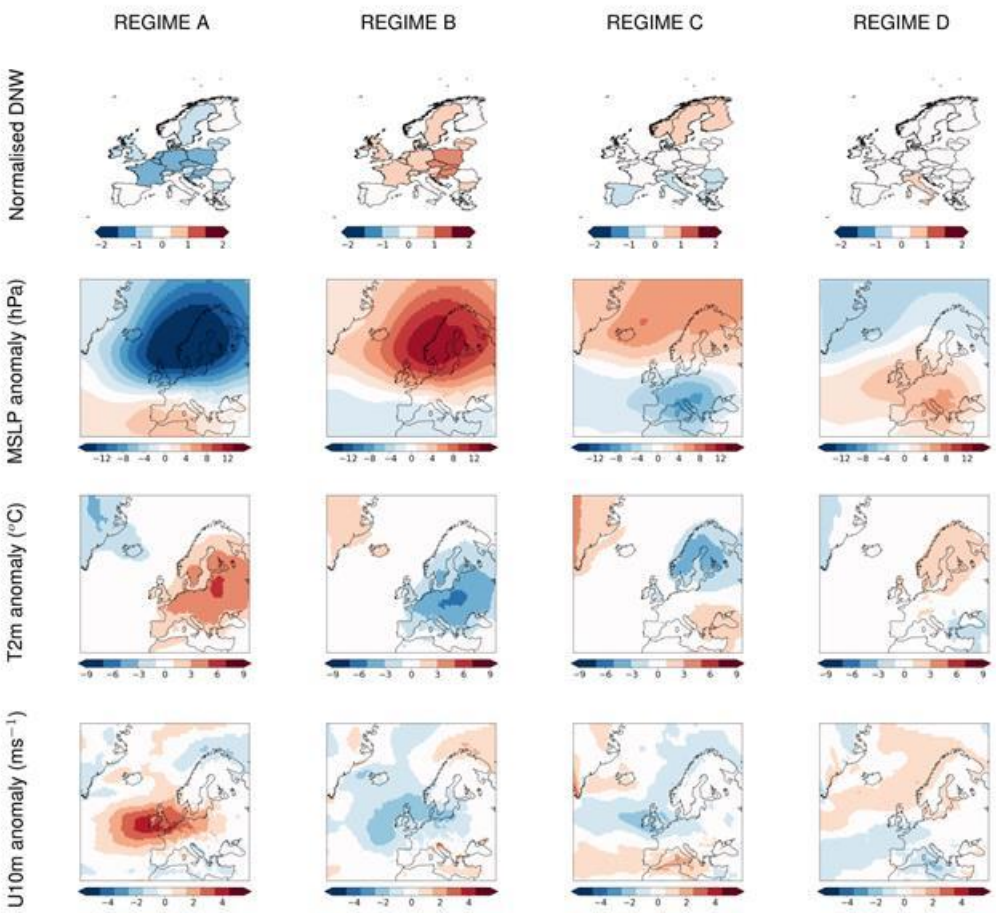

Figure 110: Impact regimes constructed from February normalized daily demand-net-wind (DNW) anomalies. Corresponding anomaly composites of meteorological fields

relative to the climatological mean (1981-2016) for MSLP, 2m temperature, 10m surface wind speed are given below the relevant regime.

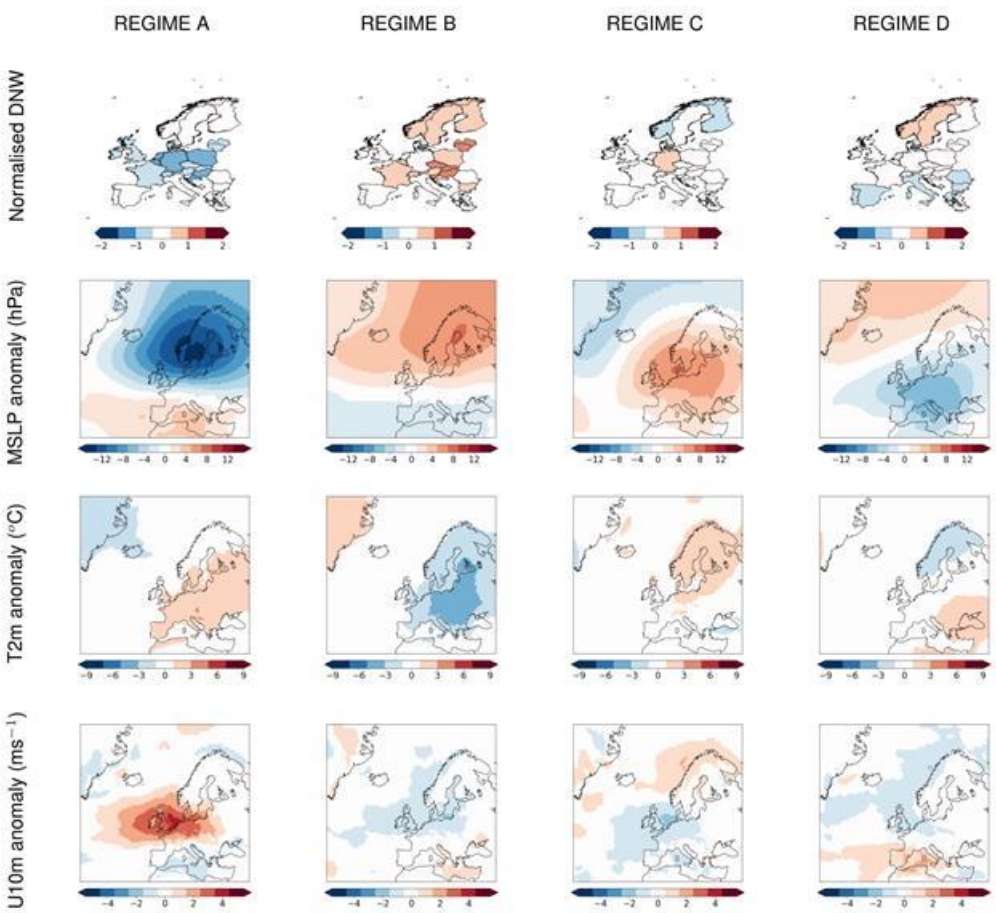

Figure 111: Impact regimes constructed from March normalized daily demand-net-wind (DNW) anomalies. Corresponding anomaly composites of meteorological fields

relative to the climatological mean (1981-2016) for MSLP, 2m temperature, 10m surface wind speed are given below the relevant regime.

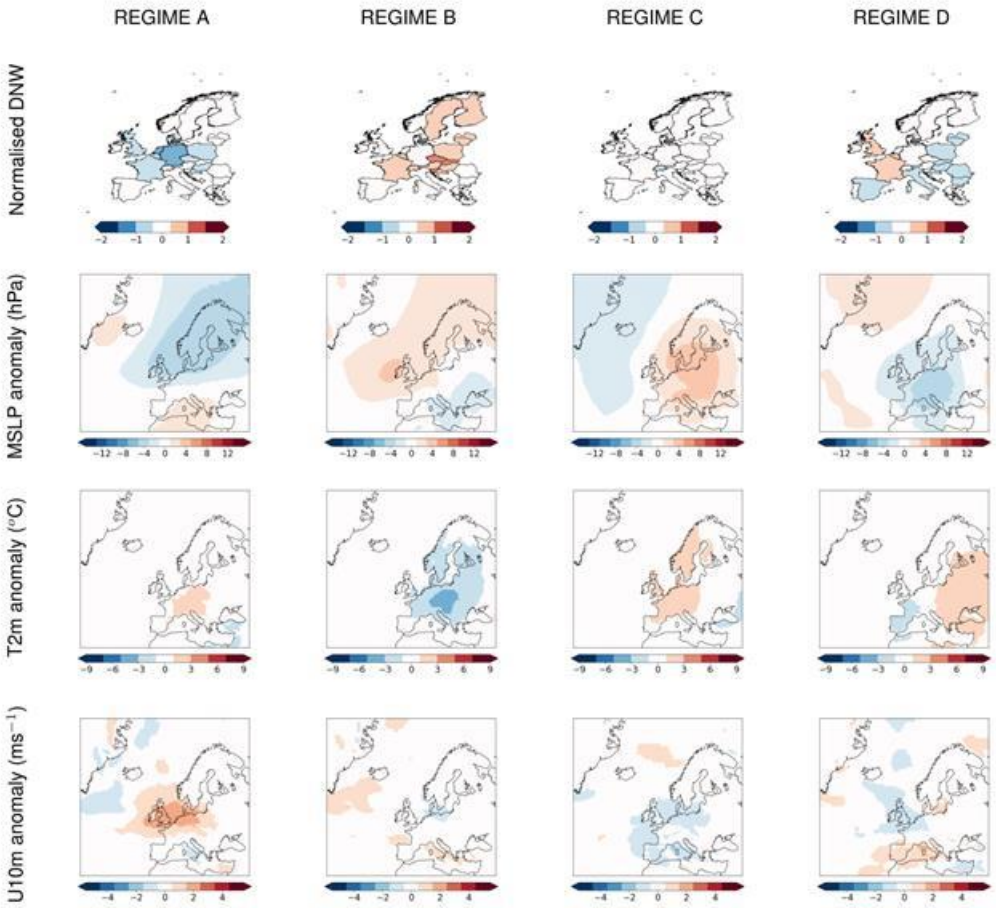

Figure 112: Impact regimes constructed from April normalized daily demand-net-wind (DNW) anomalies. Corresponding anomaly composites of meteorological fields relative to the climatological mean (1981-2016) for MSLP, 2m temperature, 10m surface wind speed are given below the relevant regime.

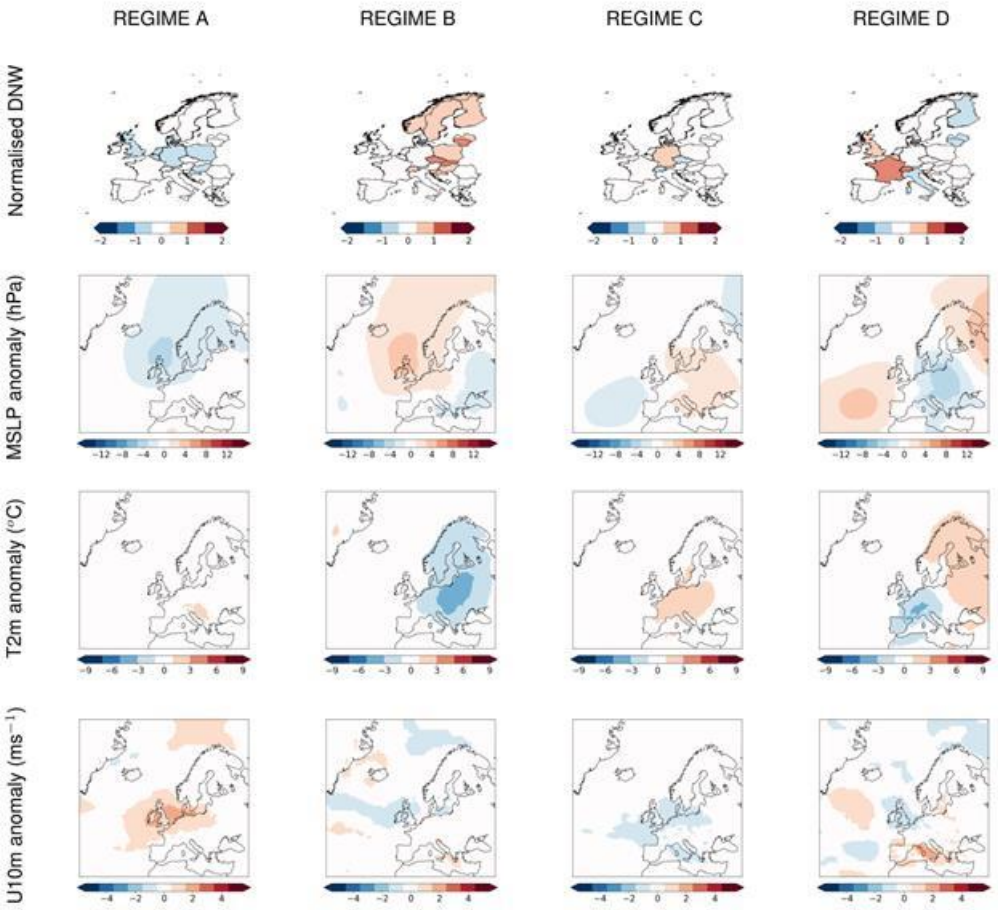

Figure 113: Impact regimes constructed from May normalized daily demand-net-wind (DNW) anomalies. Corresponding anomaly composites of meteorological fields relative to the climatological mean (1981-2016) for MSLP, 2m temperature, 10m surface wind speed are given below the relevant regime.

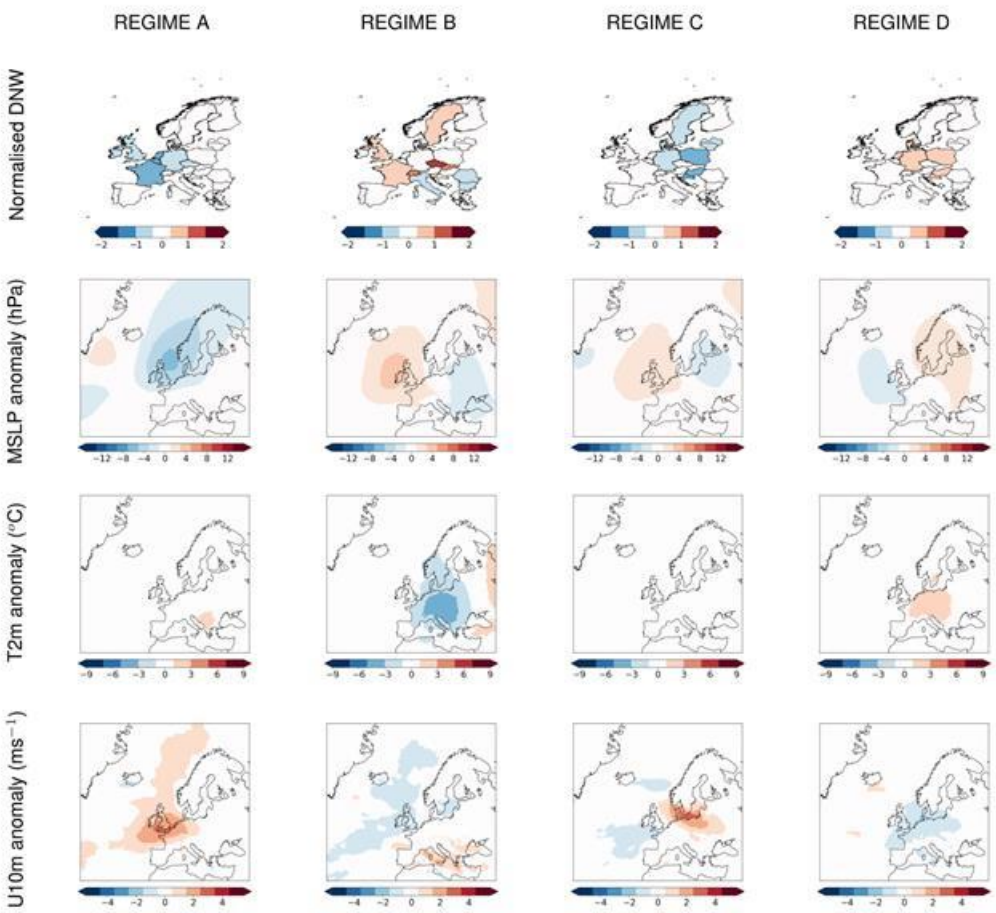

Figure 114: Impact regimes constructed from June normalized daily demand-net-wind (DNW) anomalies. Corresponding anomaly composites of meteorological fields relative to the climatological mean (1981-2016) for MSLP, 2m temperature, 10m surface wind speed are given below the relevant regime.

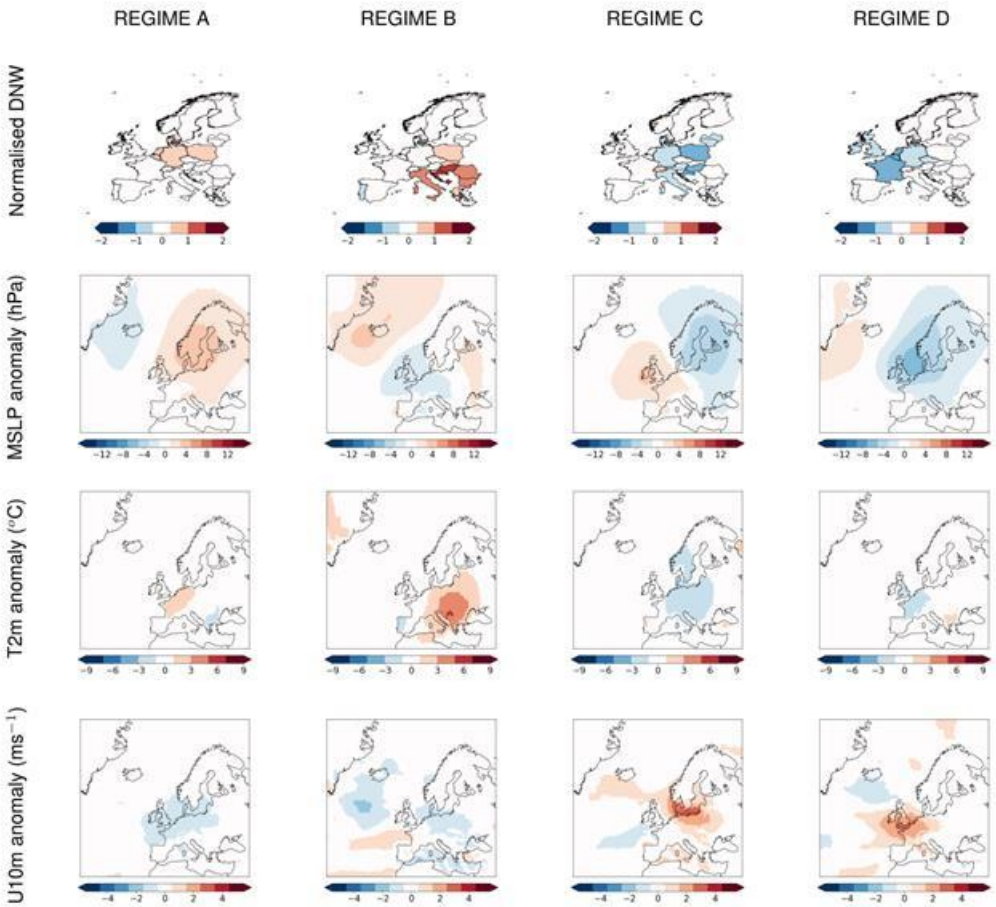

Figure 115: Impact regimes constructed from July normalized daily demand-net-wind (DNW) anomalies. Corresponding anomaly composites of meteorological fields relative to the climatological mean (1981-2016) for MSLP, 2m temperature, 10m surface wind speed are given below the relevant regime.

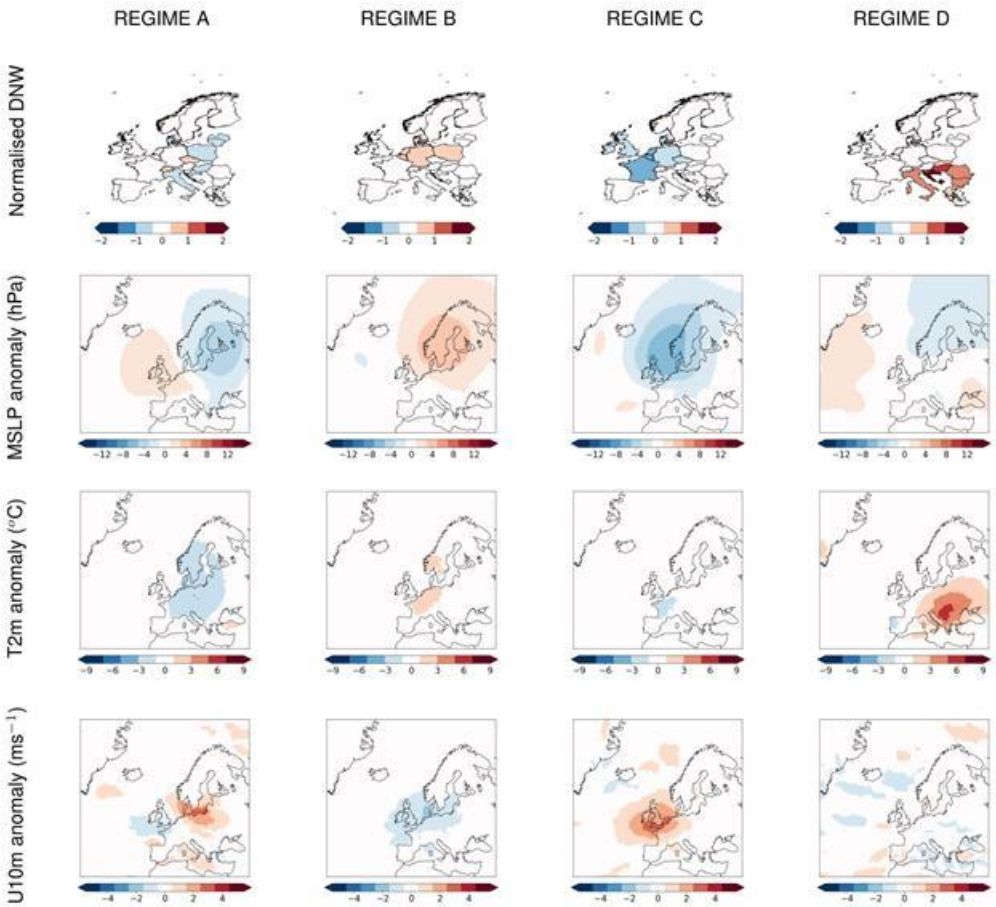

Figure 116: Impact regimes constructed from August normalized daily demand-net-wind (DNW) anomalies. Corresponding anomaly composites of meteorological fields relative to the climatological mean (1981-2016) for MSLP, 2m temperature, 10m surface wind speed are given below the relevant regime.

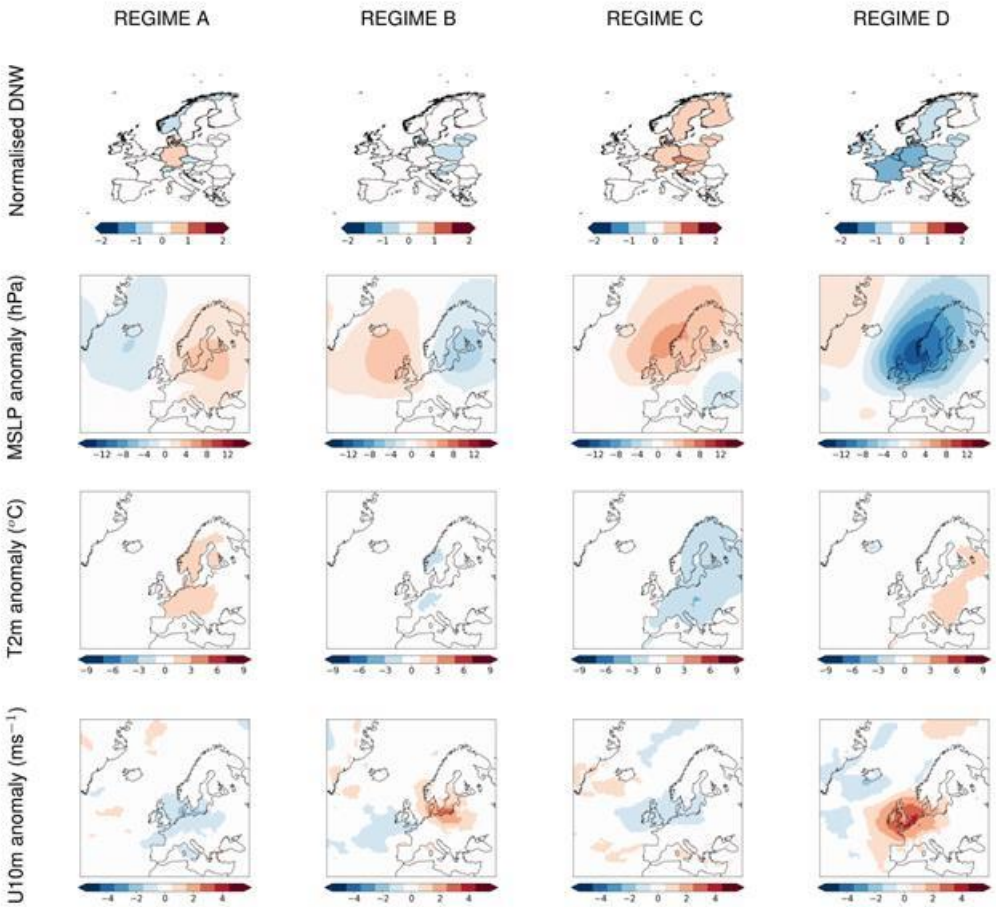

Figure 117: Impact regimes constructed from September normalized daily demand-net-wind (DNW) anomalies. Corresponding anomaly composites of meteorological fields relative to the climatological mean (1981-2016) for MSLP, 2m temperature, 10m surface wind speed are given below the relevant regime.

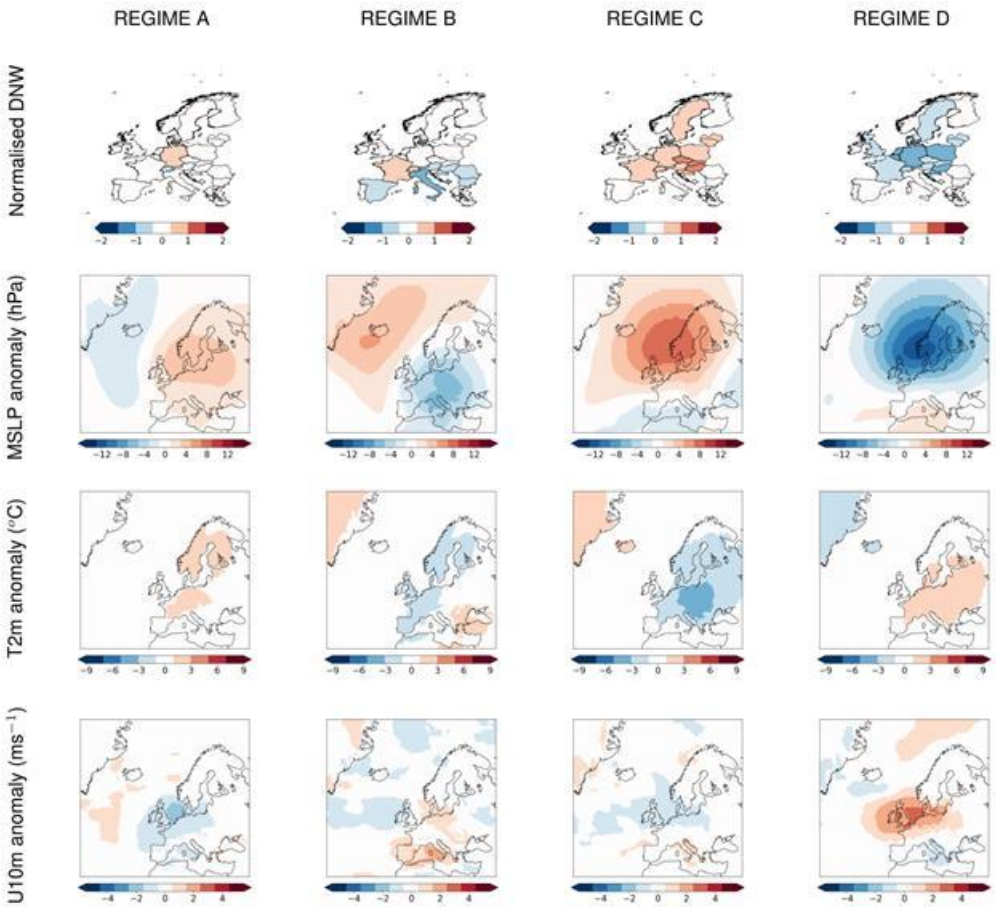

Figure 118: Impact regimes constructed from October normalized daily demand-net-wind (DNW) anomalies. Corresponding anomaly composites of meteorological fields relative to the climatological mean (1981-2016) for MSLP, 2m temperature, 10m surface wind speed are given below the relevant regime.

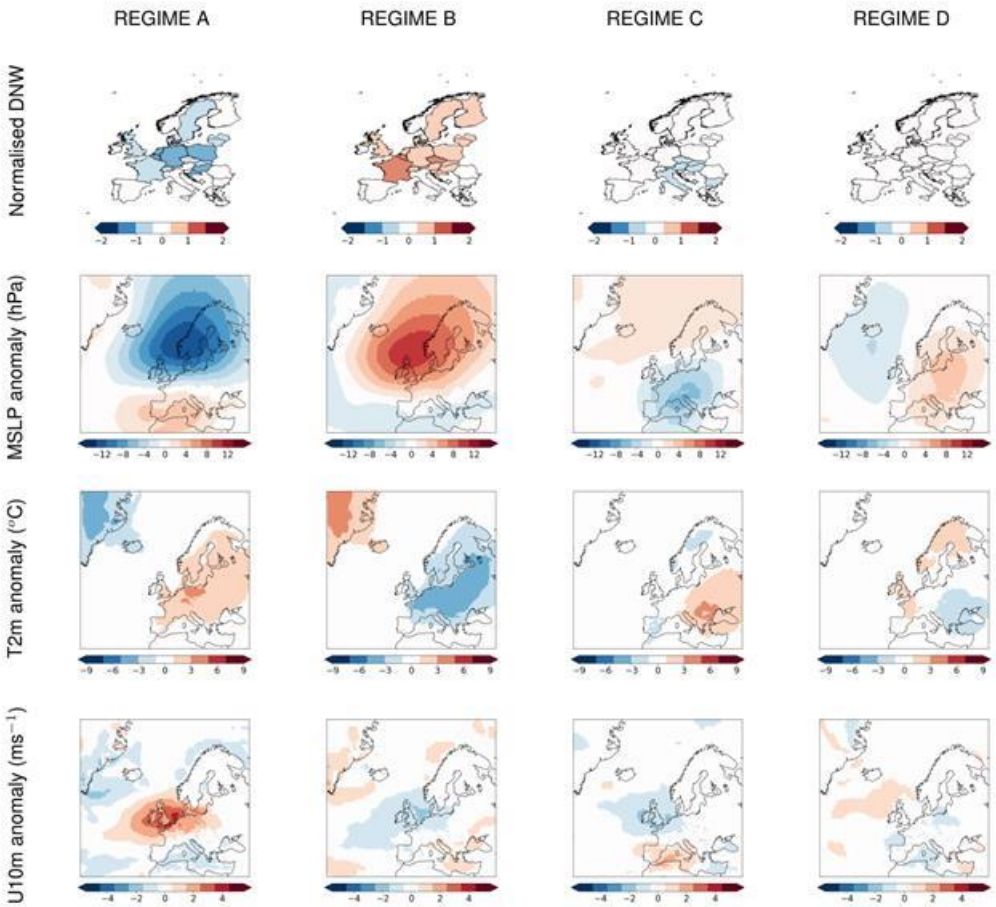

Figure 119: Impact regimes constructed from November normalized daily demand-net-wind (DNW) anomalies. Corresponding anomaly composites of meteorological fields relative to the climatological mean (1981-2016) for MSLP, 2m temperature, 10m surface wind speed are given below the relevant regime.

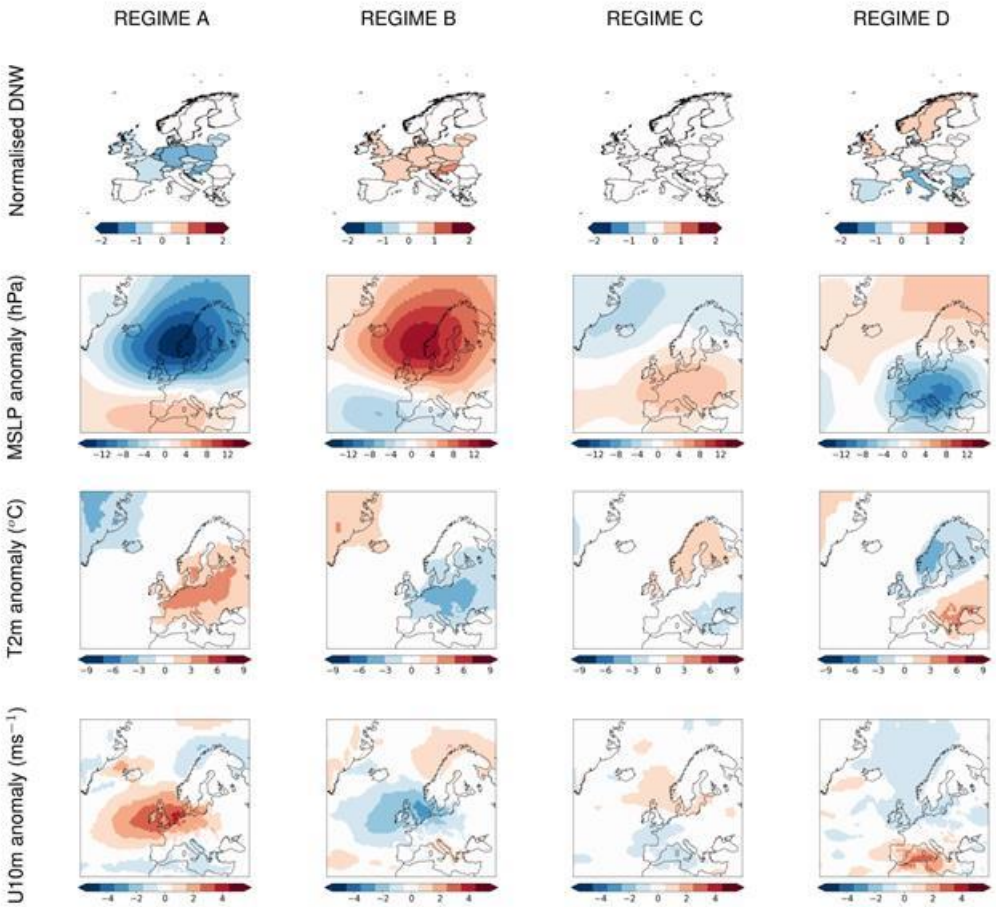

Figure 120: Impact regimes constructed from December normalized daily demand-net-wind (DNW) anomalies. Corresponding anomaly composites of meteorological fields relative to the climatological mean (1981-2016) for MSLP, 2m temperature, 10m surface wind speed are given below the relevant regime.